Title

Energetics of Rare Earth Solids Containing Hydroxide and Halide Ions

Author

Yang, Shuhao

Publication Date

2022

Energetics of Rare Earth Solids Containing Hydroxide and Halide Ions

By

SHUHAO YANG
DISSERTATION

Submitted in partial satisfaction of the requirements for the degree of

DOCTOR OF PHILOSOPHY

in

Chemistry

in the

OFFICE OF GRADUATE STUDIES

of the

UNIVERSITY OF CALIFORNIA

DAVIS

Approved:

Alexandra Navrotsky, Chair

Susan Kauzlarich

Ricardo H. R. Castro

Committee in Charge

2022

Abstract

Rare earth (RE) materials have widespread applications and constitute an indispensable part of modern lives. Tailored electrical, optical, and magnetic properties can be achieved by various RE elements in isomorphic structures, providing materials with the desired properties for specific applications. However, the processing of RE materials encounters difficulties in separation and recycling of RE elements due to the similar physical and chemical properties. For better utilization of REs, including mining, recovery, and incorporation into devices, it is essential to have comprehensive knowledge about thermodynamic properties of RE compounds.

The present work comprises not only new experimental thermodynamic studies on selected RE compounds but also a fundamental understanding of the energetics of RE compounds. By means of high temperature oxide melt solution calorimetry, formation enthalpies of RE oxycompounds (REOOH, REOF, and REOCl) and ternary sodium fluorides ($NaREF_4$) were measured to provide reliable data for energetic assessments of REs in diverse structures. NaF–NdF_3 nanocrystals and $Ca_{1-x}RE_xF_{2+x}$ solid solutions were also investigated to shed light on the energetics of RE fluoride nanocrystals and solid solutions containing defect clusters. Combining other published thermochemical data, lattice energies of numerous RE compounds were evaluated to reveal the correlations between the energetics and structures of RE materials.

RE oxycompounds are important components of RE precipitates and play a key role in the leaching of RE elements. By different synthesis methods, high-purity single-phase REOOH, REOF, and REOCl with various REs were prepared and characterized by powder X-ray diffraction (PXRD). The formation enthalpies from binary components, determined by high temperature oxide melt solution calorimetry, are all negative but become less exothermic from light to heavy RE elements. They confirm the thermodynamic stability of these RE compounds relative to binary oxides and/or halides, The thermal decomposition of REOOH and a structural phase transition in YbOF were studied by differential scanning calorimetry (DSC).

Mixed cation (alkali or alkaline earth) RE fluorides have drawn extensive research interest due to their unique luminescent properties and potential applications in phosphors and laser hosts, but limited thermodynamic studies hinder the rational design and synthesis of these materials. The formation enthalpies of $NaREF_4$ follow an opposite trend compared to most ternary RE oxide compounds, becoming increasingly negative for heavier REs. Energetic studies of NaF–NdF_3 nanocrystals coupled with chemical analysis and structural characterizations indicate that the $\alpha \rightarrow \beta$ phase conversion in aqueous solutions is associated with compositional variations and distinct from the $\beta \rightarrow \alpha$ transition driven by temperature for stoichiometric $NaNdF_4$. Formation enthalpies of $Ca_{1-x}RE_xF_{2+x}$ (RE = La, Pr, and Nd) solid solutions were measured and the relationships between the energetics and structures were discussed.

Based on experimental thermodynamic studies, an energetic evaluation of RE crystalline compounds was conducted to identify correlations between structures and thermodynamics. Lattice energies were calculated by Born–Haber cycles, which highly depend on ionic strength and increase in magnitude (becoming more exothermic) from light to heavy RE elements. The slopes of lines relating lattice energies to RE ionic radii are related to RE coordination numbers, contributing to the opposite trends in formation enthalpies for RE oxides and fluorides. A correlation between the magnitude of lattice energies and the structures occurring in RE compounds across the RE series was identified.

Acknowledgements

First and foremost, I would like to thank my advisor Professor Alexandra Navrotsky, who gave me the chance to embark this journey on thermodynamics and gave consistent support and guidance during my doctoral studies. Her profound knowledge and broad views inspire me to think from different perspectives, her dedication and rigorous approach to science urge me to have a higher academic pursuit, and her humorous and friendly personalities bring sunshine into our lives. She is a captain who leads by example, and there is too much I need to learn from her.

I sincerely thank Susan Kauzlarich and Ricardo Castro as my dissertation committee members. Susan provided a lot of help during my job search. I am also thankful to Frank Osterloh for being the committee chair of my qualifying exam and other committee members Alan Balch, Ting Guo, and Scott McCormack.

I am grateful to all the past and present members of our group, which used to be Peter A. Rock Thermochemistry Laboratory at UC Davis and currently ThermotU Laboratory as part of Navrotsky Eyring Center for Materials of the Universe at ASU. Tamilarasan Subramani was my mentor when I joined the lab and taught me how to conduct high temperature oxide melt solution calorimetry experiments. Sergey Ushakov gave me much technical support and talks with him were always interesting. Jayanthi Kumar and I worked together and helped each other in many projects. There were many fruitful results from the discussion with Albert Voskanyan. I would also thank Kristina Lilova, Xin Guo, and Mykola Abramchuk at both UC Davis and ASU; Benjamin Brugman, Kevin Meisner, Michael Bustamante, Gerson Leonel, Laura Bonatti, Megan Householder, William Kanitz, Ramandeep Mandia, Tanya Palit, and Shari Rogers at ASU; Lili Wu, Katherine Armstrong, Bin Wang, Novendra Novendra, Pinghui Zhang, Andy Lam, Can

Agca, Casey Sugie, Krasen Kovachev and William Cook at UC Davis. All your efforts contribute to maintenance and operation of the lab, and my research really benefited from your excellent works.

Many science advances come from communication and cooperation. It was a pleasure to work together with Richard Riman, Paul Antonick (Rutgers University) and Andre Anderko (OLI Systems) on rare earth projects. Joseph Kolis (Clemson University) and David Corbin (University of Kansas) helped the preparation of rare earth oxyhydroxide and zeolite samples, respectively. Heat capacity measurements collaborating with Brian Woodfield from Brigham Young University and thermodynamic studies of proton electrolytes with Aleksandra Mielewczyk-Gryń from Gdańsk University of Technology broadened my research scope.

The dissertation research was financially supported by Critical Materials Institute (CMI), a U.S. Department of Energy (DOE) Energy Innovation Hub, under the subaward number DE-AC02-07CH11358. It was a fascinating experience to attend the CMI annual meeting at Colorado School of Mines.

Finally, I would like to give my deepest gratitude to my parents. Their love and support are the most important reason I can get this far. And I gratefully appreciated everyone who contributed to fighting the COVID-19 epidemic. Hope the pandemic ends soon.

Table of Contents

List of Publications

The dissertation includes the following papers:

1. **Yang, S.**; Powell, M.; Kolis, J. W.; Navrotsky, A. Thermochemistry of rare earth oxyhydroxides, REOOH (RE = Eu to Lu). *J. Solid State Chem.* **2020**, 287, 121344.
2. **Yang, S.**; Anderko, A.; Riman, R. E.; Navrotsky, A. Thermochemistry of stoichiometric rare earth oxyfluorides REOF. *J. Am. Ceram. Soc.* **2022**, 105, 1472–1480.
3. **Yang, S.**; Anderko, A.; Riman, R. E.; Navrotsky, A. Thermochemistry of 3D and 2D rare earth oxychlorides (REOCl). *Inorg. Chem.* **2022**, DOI: 10.1021/acs.inorgchem.2c00763.
4. **Yang, S.**; Anderko, A.; Riman, R. E.; Navrotsky, A. Thermochemistry of sodium rare earth ternary fluorides, $NaREF_4$. *Acta Mater.* **2021**, *220*, 117289.
5. **Yang, S.**; Jayanthi, K.; Anderko, A.; Riman, R. E.; Navrotsky, A. Thermochemical investigation of the stability and conversion of nanocrystalline and high-temperature phases in sodium neodymium fluorides. *Chem. Mater.* **2021**, *33*, 9571–9579.
6. **Yang, S.**; Anderko, A.; Riman, R. E.; Navrotsky, A. Energetics of anion excess $Ca_{1-x}RE_xF_{2+x}$ (RE = La, Pr, and Nd) solid solutions. **2022**, to be submitted.

In addition, I have published the following publication during Ph.D.'s study.

1. **Yang, S.**; Guo, X.; Verma, A.; Shiflett, M. B.; Corbin, D. R.; Navrotsky, A. Thermochemical insights into stability and hydration of ion-exchanged zeolite ZK-5 (KFI framework). *J. Phys. Chem. C* **2020**, 287, 121344.

List of Tables

List of Figures

Chapter 1

Introduction – Experimental Thermodynamic Studies of Rare Earth Solids Containing Hydroxide and Halide Ions

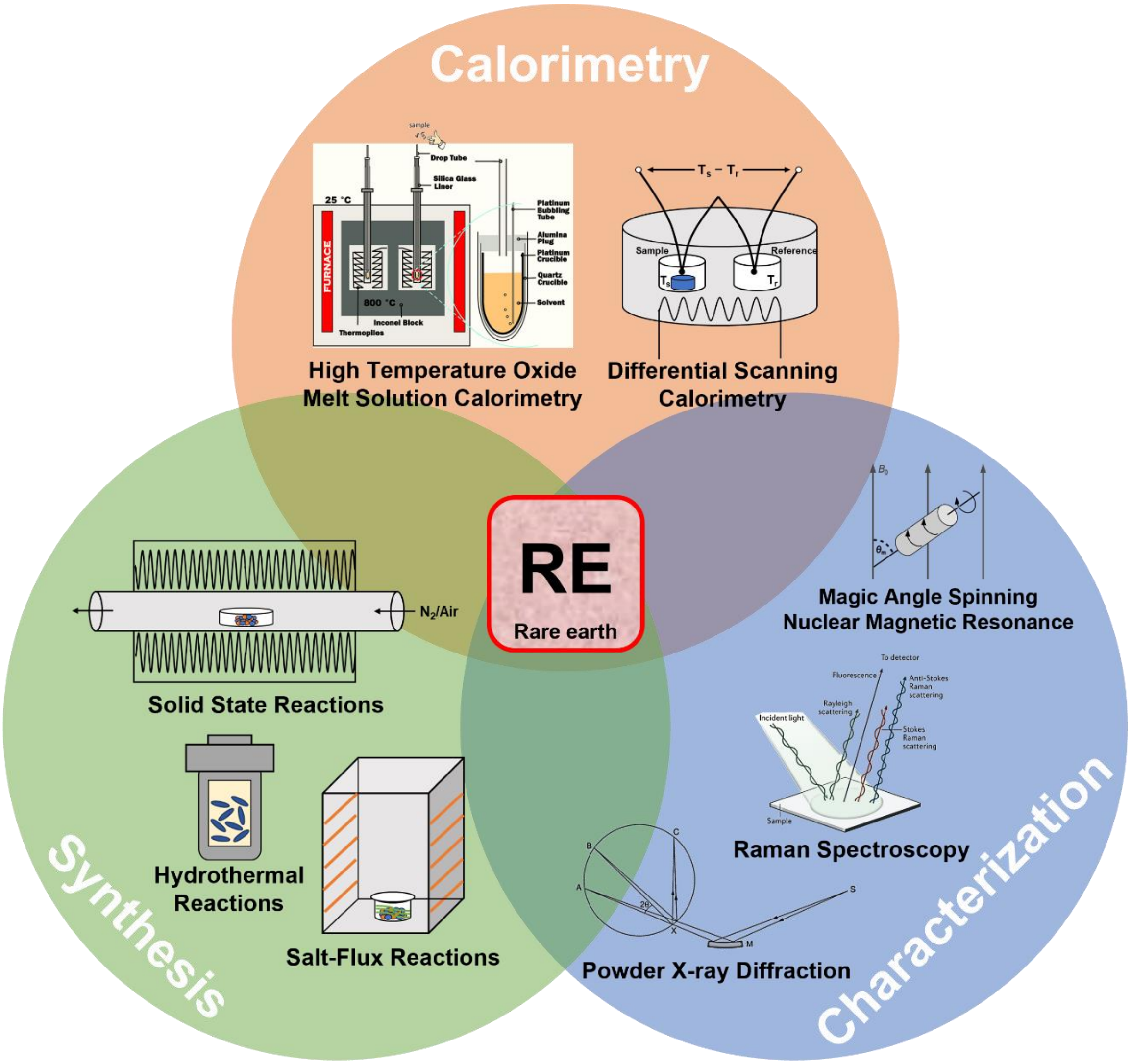

1.1 General Remarks

Rare earth (RE) elements, including lanthanide elements (La–Lu) plus scandium (Sc) and yttrium (Y), have a wide variety of technological uses and constitute an indispensable part of modern life. From mobile phones to electric motors, RE containing materials and devices can be found everywhere. Many technologies benefit from the unique physical, chemical, luminescent, and magnetic properties of RE elements and materials. For example, Nd is of importance to hard magnetic materials and Nd-Fe-B magnets represent the strongest permanent magnet.[1] By virtue of appealing luminescent properties, RE doped materials are widely used in optoelectronics such as solid-state lasers and light emitting diodes (LED).[2–4] Recently, with the development of nanotechnologies, RE nanocrystals have attracted extensive research interest for biomedical applications.[5] Moreover, Ce is not only a critical ingredient in many catalysts[6] but also an excellent addition in metal alloys[7] to improve their mechanical properties.

Despite intermediate overall abundance in the Earth's crust, RE elements have few concentrated occurrences and limited economic minerals. Due to the uneven distribution of minerals and supply chains, RE materials are considered "critical materials" possessing strategic value. However, their similar physical and chemical properties make the extraction, separation, and recycling of RE elements a big challenge. Their mining and extraction are usually accompanied by high energy consumption and pollution.[8,9] Hence, improving the efficiency of RE processing becomes a vital task in industrial production and environmental protection.

Thermodynamics governs phase stability and plays a key role in material manufacturing and processing. Fundamental studies of thermodynamic properties are essential in developing RE materials, understanding their stability, and optimizing the production process. Complete thermodynamic data of RE materials are also required for sustainable mining, ore handling, and recirculation of RE. In this regard, many studies have been carried out on thermodynamics of RE oxide compounds,[10,11] but RE halides and related compounds have received relatively attention, hindering the rational design, synthesis, and utilization of these materials.

1.2 Scope of Dissertation

This dissertation addresses the energetics of RE oxycompounds (REOX, X = OH, F, and Cl) and ternary RE fluorides ($NaREF_4$, NaF–NdF_3, and $Ca_{1-x}RE_xF_{2+x}$), which are intermediate phases during RE separation and have potential applications as functional materials with various luminescent properties.[12,13] With the help of high temperature oxide melt solution calorimetry, formation enthalpies of REOOH (Chapter 2), REOF (Chapter 3), REOCl (Chapter 4), and $NaREF_4$ (Chapter 5) were determined to evaluate their thermodynamic stability. These studies not only fill the thermodynamic data gap for RE materials but also deepen fundamental understanding of energetics of RE materials with diverse compositions and structures.

Besides stoichiometric RE compounds, thermochemical properties of NaF–NdF_3 nanocrystals (Chapter 6) and $Ca_{1-x}RE_xF_{2+x}$ solid solutions (Chapter 7) were also investigated. The study on NaF–NdF_3 nanocrystals reveals that the $\beta \rightarrow \alpha$ phase conversion of nanocrystals in aqueous solution is different from a typical phase transition driven by temperature ($\alpha \rightarrow \beta$ for stoichiometric $NaREF_4$) because it is accompanied by compositional changes. Solution calorimetry experiments indicate that $Ca_{1-x}RE_xF_{2+x}$ (RE = La, Pr, and Nd), solid solutions with anion interstitials are entropy-stabilized at synthesis temperature with endothermic formation enthalpies. Effects of RE concentration, ionic size, and annealing temperature on the structure and energetics of $Ca_{1-x}RE_xF_{2+x}$ were determined by combining structural characterizations and experimental thermodynamic studies.

Throughout this study, much effort is devoted to two issues: (i) the trend of formation enthalpies across the RE series for various RE compounds and (ii) different phases adopted by RE compounds with varying RE or “phase transitions” driven by RE ionic size. By calculating lattice energies using Born–Haber cycles, the energetics of RE compounds is evaluated and the coordination number of RE ions is found pivotal in slopes of lattice energies versus RE ionic radii, determining the trend of formation enthalpies from binary compounds. The structural difference thanks to different sized RE ions can also be explained from an energetic perspective. These new findings based on recent results of REOX and $NaREF_4$ and previously published thermochemical data on RE oxide compounds are expounded in Chapter 8.

1.3 Synthesis

High quality samples are the key to success of calorimetry experiments, where purity of compositions and phases is paramount. All reactant chemicals were analytical grade and checked by powder X-ray diffraction (PXRD) to confirm their phase purity. RE sesquioxides (RE_2O_3) were annealed at 1000 °C in air to remove any hydroxide and carbonate impurities. RE trichlorides ($RECl_3$) were unpacked, stored, and processed in a glovebox filled with N_2 ($H_2O < 1$ ppm) to avoid moisture absorption. Other chemicals and samples were stored in desiccators when not in use.

The solid-state reaction method was employed for the synthesis of REOF, $NaREF_4$, and $Ca_{1-x}RE_xF_{2+x}$ due to its simplicity and ease to control compositions. The binary fluorides (NaF, CaF_2 and REF_3) and oxides (RE_2O_3) were used as the precursors and mixed in stoichiometric ratios by hand in an agate mortar. Then, the powder mixtures were pelletized and transferred to covered Pt crucibles and heated in a tube furnace at the specified temperature under an Ar or N_2 atmosphere. The weight before and after the reaction was recorded to confirm that no weight change happened during the reaction, so the chemical composition of the product was the same as that of the precursor. Before cooling to room temperature, $NaREF_4$ samples were annealed at a relatively low temperature (450 or 500 °C) to avoid high temperature phases.[14,15] Two series of $Ca_{1-x}RE_xF_{2+x}$ samples were prepared at different annealing temperatures to investigate the effect of temperature on defect aggregation.[16,17] For the system containing kinetically controlled phases such as rhombohedral YbOF, the cooling process was carefully controlled to produce the thermodynamically stable phase (monoclinic YbOF).[18]

REOOH crystals were obtained from collaborators (Matthew Powell and Joseph W. Kolis) at Clemson University, which were prepared by high temperature hydrothermal reactions.[19,20] Coprecipitation and hydrothermal methods were used to synthesize $NaF–NdF_3$ nanocrystals, in which pH and temperature were adjusted to get nanocrystals with different phases, shapes, and sizes.[21-23] Their chemical composition was determined by inductively coupled plasma mass spectrometry (ICP-MS).

Although REOCl with light RE elements can be synthesized by the thermal decomposition of RE chloride hydrates[24,25] or the chlorination reaction[26] between RE_2O_3 and NH_4Cl, it is hard to obtain REOCl with heavy RE elements as a pure phase using these methods. Thus, a salt-flux method was adopted to prepare single-phase REOCl samples, where $RECl_3$ served as both the reactant and the flux.[27] A triple molar excess of $RECl_3$ was ground with RE_2O_3 in the glovebox and heated above the melting temperature of $RECl_3$ for 2 days under a N_2 atmosphere. After cooling to room temperature, excess $RECl_3$ was washed out with deionized water and the residue was separated and dried as crystalline REOCl.

1.4 Characterization

The synthesized samples were characterized by various techniques, not only to corroborate the composition and the phase but also to examine the structure which is closely related to thermodynamic properties. For all samples, PXRD was used to determine the phase composition. Based on peak positions of PXRD patterns, lattice parameters were calculated using MDI Jade software.[28] For REOF, $NaREF_4$, and NaF–NdF_3 samples, PXRD patterns were also analyzed by the Rietveld method implemented in the software GSAS-II to further determine atomic coordinates,[29] and refinement profiles are attached in Appendix A. NaF–NdF_3 and $Ca_{1-x}RE_xF_{2+x}$ samples were also characterized by Raman spectroscopy to identify the phase composition.[30] Local structural information, especially within the layers of SmSI structure-type REOCl, was gained by means of RE ionic size dependence of Raman shifts.[31] To shed light on defect clusters, ^{19}F magic-angle spinning (MAS) nuclear magnetic resonance (NMR) measurements were conducted on $Ca_{1-x}La_xF_{2+x}$ samples,[32] and the results were discussed in the context of previous research of structure and ionic conductivity.[33–41]

1.5 Calorimetry

Differential scanning calorimetry (DSC) was used to study phase transitions and other reactions driven by temperature, and thermogravimetric analysis (TGA) was coupled with DSC in TG-DSC instruments (Netzsch 449 and Setaram LabSYS Evo) to measure the weight change at the same time as heat effects. The temperature and sensitivity of the instruments were calibrated by measuring the temperature and heat of melting of several metals (e.g., In, Sn, Al, Ag, and Au). The water content of NaF–NdF_3 nanocrystals was measured by TGA, and phase transitions and/or reactions during the heating process were also recognized by DSC. TG-DSC experiments were carried out on REOOH to determine the enthalpy of the dehydration (decomposition) reaction from REOOH to RE_2O_3 and H_2O. The obtained results were compared to those from parallel high temperature drop solution calorimetry experiments and showed good consistency. Different phases of YbOF were studied by DSC, showing that the monoclinic phase is the thermodynamic stable phase, but the transition from the high temperature phase (cubic phase) is slow and easily generates the rhombohedral phase. The enthalpy of the monoclinic–cubic phase transition of YbOF was measured for the first time.

High temperature oxide melt solution calorimetry was heavily used and played an irreplaceable role in these experimental thermodynamic studies. This well-established calorimetric technique can overcome the problem that many solid compounds do not readily dissolve in aqueous solutions, which has given reliable thermodynamic data on oxides, nitrides, carbides, and sulfides.[42–44] High temperature oxide melt solution calorimetry has been successfully applied to RE oxides,[45] and this study expanded its scope to RE fluorides and chlorides. A Setaram AlexSYS Tian-Calvet twin microcalorimeter was calibrated against the heat content of high-purity α-Al_2O_3 (99.99%) and used to measure drop solution enthalpies (ΔH_{ds}) of samples in molten sodium molybdate ($3NaO\cdot4MoO_3$) at 800 °C. The results are listed in Appendix B. All experiments were flushed with O_2 at 60 mL min^{-1} and bubbled through the solvent at 5 mL min^{-1} to aid dissolution, prevent local saturation of the solvent, and sweep evolved gas out of the calorimeter. Enthalpies of exchange reactions between RE_2O_3 and NaF or NaCl were calculated based on the ΔH_{ds}. These are equal to reaction enthalpies calculated from thermodynamic tables within experimental error. The agreement indicates the complete dissolution of fluorides or chlorides and no specific interaction between dissolved components in the dilute molten solution. Through thermodynamic cycles, the formation enthalpies of RE compounds from binary compounds ($\Delta H^\circ_{f,\,bc}$) or elements ($\Delta H^\circ_{f,\,el}$) at 25 °C were calculated.

The obtained thermodynamic data was further discussed with the structure information from characterizations to reveal correlations between structures and energetics of RE compounds, which will be described in the subsequent chapters.

1.6 References

(1) Gutfleisch, O.; Willard, M. A.; Brück, E.; Chen, C. H.; Sankar, S. G.; Liu, J. P. Magnetic materials and devices for the 21st century: stronger, lighter, and more energy efficient. *Adv. Mater.* **2011**, *23,* 821–842.

(2) Kenyon, A. J. Recent developments in rare-earth doped materials for optoelectronics. *Prog. Quant. Electron.* **2002**, *26*, 225−284.

(3) Eliseeva, S. V.; Bünzli, J.-C. G. Lanthanide luminescence for functional materials and bio-sciences. *Chem. Soc. Rev.* **2010**, *39*, 189–227.

(4) Li, G.; Tian, Y.; Zhao, Y.; Lin, J. Recent progress in luminescence tuning of Ce^{3+} and Eu^{2+}-activated phosphors for pc-WLEDs. *Chem. Soc. Rev.* **2015**, *44*, 8688–8713.

(5) Gai, S.; Li, C.; Yang, P.; Lin, J. Recent progress in rare earth micro/nanocrystals: soft chemical synthesis, luminescent properties, and biomedical applications. *Chem. Rev.* **2014**, *114*, 2343−2389.

(6) Trovarelli, A. Catalytic properties of ceria and CeO_2-containing materials. *Catal. Rev.* **1996**, *38*, 439–520.

(7) Czerwinski, F. Cerium in aluminum alloys. *J. Mater. Sci.* **2020**, *55*, 24–72.

(8) Binnemans, K.; Jones, P. T.; Blanpain, B.; Van Gerven, T.; Yang, Y.; Walton, A.; Buchert, M. Recycling of rare earths: a critical review. *J. Clean. Prod.* **2013**, *51*, 1−22.

(9) Balaram, V. Rare earth elements: a review of applications, occurrence, exploration, analysis, recycling, and environmental impact. *Geosci. Front.* **2019**, *10*, 1285–1303.

(10) Zinkevich, M. Thermodynamics of rare earth sesquioxides. *Prog. Mater. Sci.* **2007**, *52*, 597−647.

(11) Navrotsky, A.; Lee, W.; Mielewczyk-Gryn, A.; Ushakov, S. V.; Anderko, A.; Wu, H.; Riman, R. E. Thermodynamics of solid phases containing rare earth oxides. *J. Chem. Thermodyn.* **2015**, *88*, 126–141.

(12) Udayakantha, M.; Schofield, P.; Waetzig, G. R.; Banerjee, S. A full palette: crystal chemistry, polymorphism, synthetic strategies, and functional applications of lanthanide oxyhalides. *J. Solid State Chem.* **2019**, *270*, 569–592.

(13) Chong, S.; Riley, B. J.; Nelson, Z. J. Crystalline compounds for remediation of rare-earth fission products: a review. *J. Rare Earths* **2022**, *40*, 365–380.

(14) Thoma, R. E.; Insley, H.; Hebert, G. M. The sodium fluoride-lanthanide trifluoride systems. *Inorg. Chem.* **1966**, *5*, 1222–1229.

(15) Fedorov, P. Systems of alkali and rare-earth metal fluorides. *Russ. J. Inorg. Chem.* **1999**, *44*, 1703–1727.

(16) Laval, J. P.; Mikou, A.; Frit, B.; Roult, G. Short-range order in heavily doped $CaF_2:Ln^{3+}$ fluorites: a powder neutron diffraction study. *J. Solid State Chem.* **1988**, *28-30*, 1300–1304.

(17) Laval, J. P.; Abaouz, A.; Frit, B. Short-range order in the $Ca_{1-x}La_xF_{2+x}$ solid solution: 1:0:3 or 1:0:4 clusters? *J. Solid State Chem.* **1989**, *81*, 271–277.

(18) Taoudi, A.; Laval, J. P.; Frit, B. Synthesis and crystal structure of three new rare earth oxyfluorides related to baddeleyite [LnOF; Ln=Tm,Yb,Lu]. *Mater. Res. Bull.* **1994**, *29*, 1137–1147.

(19) Byrappa, K.; Yoshimura, M. *Handbook of Hydrothermal Technology*; Elsevier, 2011.

(20) McMillen, C. D.; Kolis, J. W. Hydrothermal synthesis as a route to mineralogically-inspired structures. *Dalton Trans.* **2016**, *45*, 2772–2784.

(21) Li, C.; Yang, J.; Quan, Z.; Yang, P.; Kong, D.; Lin, J. Different microstructures of β-$NaYF_4$ fabricated by hydrothermal process: effects of pH values and fluoride sources. *Chem. Mater.* **2007**, *19*, 4933–4942.

(22) Li, C.; Zhang, C.; Hou, Z.; Wang, L.; Quan, Z.; Lian, H.; Lin, J. β-$NaYF_4$ and β-$NaYF_4$:Eu^{3+} microstructures: morphology control and tunable luminescence properties. *J. Phys. Chem. C* **2009**, *113*, 2332–2339.

(23) Zhang, F.; Li, J.; Shan, J.; Xu, L.; Zhao, D. Shape, size, and phase-controlled rare-earth fluoride nanocrystals with optical up-conversion properties. *Chem. Eur. J.* **2009**, *15*, 11010–11019.

(24) Wendlandt, W. W. The thermal decomposition of yttrium, scandium, and some rare-earth chloride hydrates. *J. Inorg. Nucl. Chem.* **1957**, *5*, 118−122.

(25) Wendlandt, W. W. The thermal decomposition of the heavier rare earth metal chloride hydrates. *J. Inorg. Nucl. Chem.* **1959**, *9*, 136−139.

(26) Hölsä, J.; Niinistö, L. Thermoanalytical study on the reactions of selected rare earth oxides with ammonium halides. *Thermochim. Acta* **1980**, *37*, 155−160.

(27) Brandt, G.; Diehl, R. Preparation, powder data and crystal structure of YbOCl. *Mater. Res. Bull.* **1974**, *9*, 411−419.

(28) *JADE 9.5*; Materials Data: Livermore, CA, 2019.

(29) Toby, B. H.; Von Dreele, R. B. GSAS-II: the genesis of a modern open-source all purpose crystallography software package. *J. Appl. Cryst.* **2013**, *46*, 544−549.

(30) Lage, M. M.; Moreira, R. L.; Matinaga, F. M.; Gesland, J.-Y. Raman and infrared reflectivity determination of phonon modes and crystal structure of czochralski-grown $NaLnF_4$ (Ln = La, Ce, Pr, Sm, Eu, and Gd) single crystals. *Chem. Mater.* **2005**, *17*, 4523–4529.

(31) Yao, Y.; Zhang, Y.; Xiong, W.; Wang, Z.; Sendeku, M. G.; Li, N.; Wang, J.; Huang, W.; Wang, F.; Zhan, X.; et al. Growth and raman scattering investigation of a new 2D MOX material: YbOCl. *Adv. Funct. Mater.* **2019**, *29*, 1903017.

(32) Harris, R. K.; Jackson, P. High-resolution fluorine-19 magnetic resonance of solids. *Chem. Rev.* **1991**, *91*, 1427−1440.

(33) Cheetham, A. K.; Fender, B. E. F.; Cooper, M. J. Defect structure of calcium fluoride containing excess anions I. Bragg scattering. *J. Phys. C: Solid State Phys.* **1971**, *4*, 3107–3121.

(34) Steele, D.; Childs, P. E.; Fender, B. E. F. Defect structure of calcium fluoride containing excess anions II. Diffuse scattering. *J. Phys. C: Solid State Phys.* **1972**, *5*, 2677–2688.

(35) Catlow, C. R. A.; Chadwick, A. V.; Corish, J. The defect structure of anion excess CaF_2. *J. Solid State Chem.* **1983**, *48*, 65–76.

(36) Catlow, C. R. A.; Chadwick, A. V.; Greaves, G. N.; Moroney, L. M. Direct observations of the dopant environment in fluorites using EXAFS. *Nature* **1984**, *312*, 601–604.

(37) Ivanov-Shits, A. K.; Sorokin, N. I.; Fedorov, P. P.; Sobolev, B. P. Specific features of ionic transport in nonstoichiometric fluorite-type $Ca_{1-x}R_xF_{2+x}$ (R = La–Lu, Y, Sc) phases. *Solid State Ion.* **1990**, *37*, 125–137.

(38) Hull, S.; Wilson, C. C. The defect structure of anion-excess $(Ca_{1-x}Y_x)F_{2+x}$ with x = 0.06. *J. Solid State Chem.* **1992**, *100*, 101–114.

(39) Wang, F.; Grey, C. P. Probing the defect structure of anion-excess $Ca_{1-x}Y_xF_{2+x}$ (x = 0.03−0.32) with high-resolution ^{19}F magic-angle spinning nuclear magnetic resonance spectroscopy. *Chem. Mater.* **1998**, *10*, 3081–3091.

(40) Grover, V.; Achary, S. N.; Patwe, S. J.; Tyagi, A. K. Synthesis and characterization of $M_{1-x}Nd_xF_{2+x}$ ($M = Sr^{2+}$, Ca^{2+}; $0.00 \leq x \leq 1.00$). *Mater. Res. Bull.* **2003**, *38*, 1413–1422.

(41) Ma, F.; Su, F.; Zhou, R.; Ou, Y.; Xie, L.; Liu, C.; Jiang, D.; Zhang, Z.; Wu, Q.; Su, L.; Liang, H. The defect aggregation of RE^{3+} (RE = Y, La ∼ Lu) in MF_2 (M = Ca, Sr, Ba) fluorites. *Mater. Res. Bull.* **2020**, *125*, 110788.

(42) Navrotsky, A. Progress and new directions in high temperature calorimetry. *Phys. Chem. Miner.* **1977**, *2*, 89–104.

(43) Navrotsky, A. Progress and new directions in high temperature calorimetry revisited. *Phys. Chem. Miner.* **1997**, *24*, 222–241.

(44) Navrotsky, A. Progress and new directions in calorimetry: a 2014 perspective. *J. Am. Ceram. Soc.* **2014**, *97*, 3349–3359.

(45) Helean, K. B.; Navrotsky, A. Oxide melt solution calorimetry of rare earth oxides. *J. Therm. Anal. Calorim.* **2002**, *69*, 751–771.

Chapter 2

Thermochemistry of Rare Earth Oxyhydroxides, REOOH (RE = Eu to Lu)

Shuhao Yang,[†] Matthew Powell,[‡] Joseph W. Kolis,[‡] Alexandra Navrotsky[*,†,§]

[†]Peter A. Rock Thermochemistry Laboratory and NEAT ORU, University of California, Davis CA 95616, United States

[‡]Department of Chemistry and Center for Optical Materials Science and Engineering Technologies (COMSET), Clemson University, Clemson, South Carolina 29634-0973, United States

[§]School of Molecular Sciences and Center for Materials of the Universe, Arizona State University, Tempe AZ 85287, United States

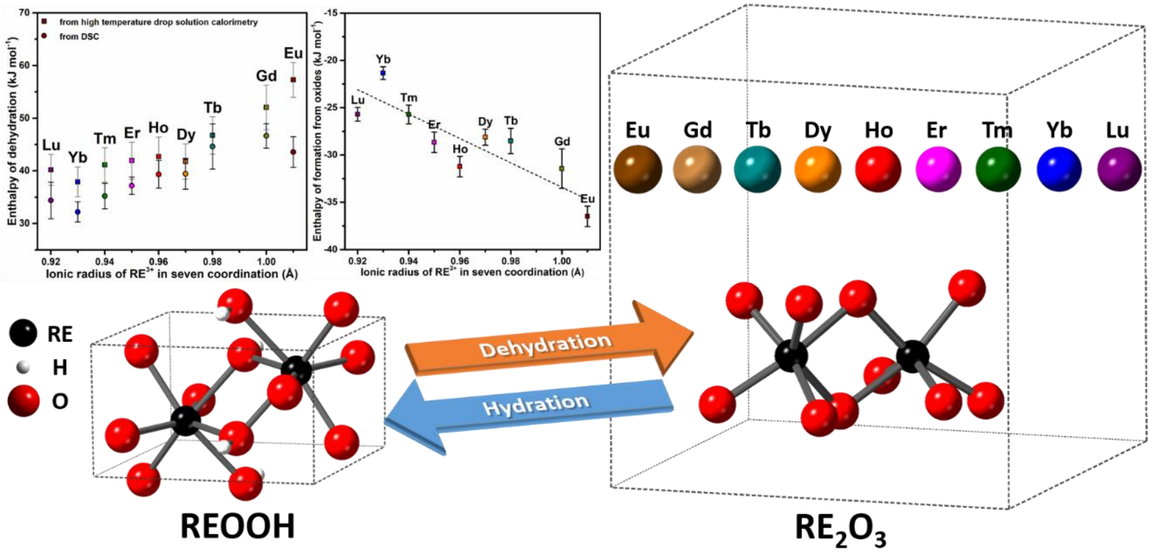

J. Solid State Chem. **2020**, *287*, 121344.

2.1 Abstract

As intermediate products of the dehydration of hydroxides or the hydration of oxides, rare earth oxyhydroxides (REOOH) have important implications for synthesis and potential applications in luminescent devices. Using high temperature oxide melt solution calorimetry and thermal analysis, thermodynamic properties of REOOH (RE = Eu to Lu), including enthalpies of dehydration and formation, were determined. The exothermic enthalpies of formation from oxides and endothermic enthalpies of dehydration demonstrate that oxyhydroxides are not only synthetic but also thermodynamic intermediates in rare earth oxide – water systems. The linear relationship between enthalpies of formation from oxides and ionic radius of RE^{3+} confirms the key role of cation size in the stability of REOOH, and reveals that REOOH with lighter rare earth elements are easier to form and harder to dehydrate, both thermodynamically and kinetically.

2.2 Introduction

Rare earth oxyhydroxides (REOOH), whose unique luminescence properties make them appealing materials in optical devices,[1–4] are one of the hydrated forms of rare earth element (RE) oxides. In terms of synthesis, REOOH phases appear as a by-product in the hydrothermal preparation of RE oxide crystals[5] and can be used as a convenient synthetic precursor for RE nanophase oxides with high surface area.[6,7] Since the first report of REOOH in 1938,[8] their crystal structure,[4,9–14] optical,[1–3] magnetic,[11] and electrical[15] characteristics have been studied, but relatively little work has been done concerning their thermodynamic properties,[15–18] especially enthalpies of formation. This data gap limits our understanding and restricts rational design of the synthesis of these and related materials. Thus, the aim of this paper is to determine the thermodynamic properties of REOOH and provide energetic insight into the conversion between

REOOH and RE_2O_3. Since rare earth sesquioxides have hexagonal ($P\bar{3}m1$), monoclinic ($C2/m$) and cubic ($Ia\bar{3}$) structures (denoted as A-, B-, and C-types, respectively) with different coordination numbers of cations,[19,20] this work focuses only on oxyhydroxides with rare earth metals forming oxides with the C-type structure at room temperature. The enthalpies of formation and dehydration show the systematic influence of the RE ions on the thermodynamic stability of REOOH and clarify the thermodynamic relationships among RE oxides, oxyhydroxides, and hydroxides.

2.3 Experimental Methods

2.3.1 Material Preparation

Polycrystalline rare earth oxyhydroxide samples, REOOH (RE = Eu to Lu), were grown hydrothermally using an Inconel 718 Tuttle cold-seal autoclave with 27 mL internal volume.[21,22] Silver ampoules (LeachGarner, 99.99%) having a diameter of 9.5 mm and 70 mm length were used as noble metal liners to house the reactions. Sesquioxide (RE_2O_3) powders (Dy - Strem, 99.9%; Er, Gd, Sm - Alfa Aesar REaction, 99.9%; Eu, Ho, Tm, Yb, Lu - HEFA Rare Earth, 99.99%) were used as the lanthanide source. Tb_4O_7 (HEFA Rare Earth, 99.99%) was used due to the lack of a stable pure-phase Tb(III) oxide. A mineralizer of 20 M KOH was used to facilitate bulk oxyhydroxide growth and was prepared by dissolving KOH pellets (Alfa Aesar, 99.98%) in deionized (DI) water in a 1:1 ratio. Ampoules were closed by an Ar-TIG welded Mercedes crimp on one end before the addition of 0.8 mL 20 M KOH mineralizer and 0.4 g oxide powder. An additional 0.04 mL $N_2H_4 \cdot H_2O$ (Alfa Aesar, 99%) was added to facilitate Tb(IV) reduction in the Tb_4O_7 reaction and prevent oxidative silver attack. Then, the other end of the ampoule was also sealed. Three ampoules were placed into an autoclave containing DI water to balance the pressure within the ampoules. Autoclaves were surrounded by vermiculite insulation, maintained at a pressure of 100 MPa, heated by ceramic band heaters to 650 °C, and held at that temperature for 14 days before cooling to room temperature in air over 4 h. After recovering and opening the ampoules, products were filtered and washed thoroughly with DI water. REOOH crystals as plates and slabs were collected and subjected to sonication in DI water and filtration to remove any unreacted RE_2O_3 and hydroxide ($RE(OH)_3$). To remove $RE(OH)_3$ mixed in EuOOH and GdOOH samples, initial samples were heated at 325 °C for 0.5 h to obtain purified REOOH samples. In the following experiments, large crystalline and purified samples were ground into fine powder for calorimetry.

2.3.2 Powder X-ray Diffraction

Powder X-ray diffraction (PXRD) patterns were obtained using a Bruker AXS D8 Advance diffractometer operated with Cu Kα radiation ($\lambda = 1.54$ Å). The data were collected in the 2θ range of 5–90°, with a step size of 0.02° and a dwell time of 1 s per step. Analysis of the XRD patterns using Jade 6.5 software was conducted for phase identification and lattice parameter determination.

2.3.3 Thermogravimetry and Differential Scanning Calorimetry

Thermogravimetry and differential scanning calorimetry (TG-DSC) was performed using a Netzsch STA 449 instrument. In each measurement, ~ 25 mg of sample was hand-pressed into a pellet, placed in a Pt crucible, and heated from 30 to 1200 °C (10 °C min^{-1}) under O_2 (Praxair, 99.999%) flow (40 mL min^{-1}), but TbOOH was heated under Ar (Praxair, 99.999%, $O_2/H_2O < 3$ ppm) flow (40 mL min^{-1}). The calorimeter was calibrated against the heat content of a sapphire standard and a buoyancy correction was performed with an empty crucible prior to the experiment.

Three TG-DSC measurements including baseline, sapphire standard, and sample were carried out in turn for the determination of specific heat capacity (C_p) according to the following equation:

$$C_p(s) = \frac{m_{std}}{m_s} \times \frac{DSC_s - DSC_{bl}}{DSC_{std} - DSC_{bl}} \times C_p(std) \qquad (2.1)$$

where $C_p(s)$ is the specific heat capacity of the sample, $C_p(std)$ is the specific heat capacity of the sapphire standard, m_{std} is the mass of the sapphire standard, m_s is the mass of the sample, DSC_s is the value of DSC signal from the sample curve, DSC_{std} is the value of DSC signal from the sapphire standard curve, and DSC_{bl} is the value of DSC signal from the baseline. For REOOH samples, the integral of the obtained C_p from room temperature to observed temperature of dehydration was calculated as the heat capacity effect ($\Delta H°_{Td} - \Delta H°_{298.15}$).

2.3.4 High Temperature Oxide Melt Solution Calorimetry

High temperature oxide melt solution calorimetry experiments were carried out using a Tian-Calvet twin calorimeter using methods standard to our laboratory and described previously.[23–25] The calorimeter was calibrated against the heat content of 5 mg pellets of high purity α-Al_2O_3 (99.997%). Pressed sample pellets (~5 mg) were dropped from ambient temperature into the calorimeter at 803 °C containing the solvent, molten sodium molybdate ($3Na_2O\cdot4MoO_3$), in a platinum crucible. All experiments were flushed with O_2 at 50 mL min^{-1} with bubbling through the solvent at 5 mL min^{-1} to aid dissolution and provide oxidizing conditions. The measurement was repeated at least eight times on each sample composition. In the case of TbOOH, because of its possible tendency to oxidize, the samples were pelletized in a glove box filled with nitrogen and transported to the calorimeter in glass vials, limiting contact with laboratory air to a few seconds.

2.4 Results and Discussion

A series of REOOH (RE = Eu to Lu) samples was obtained from the hydrothermal method. According to PXRD patterns (Figure 2.1) and TG-DSC scans (Figure 2.2), some $RE(OH)_3$ was present in the EuOOH and GdOOH samples, namely 8 and 4 wt %, respectively. To remove the $RE(OH)_3$ impurities, samples were heated at 325 °C for 0.5 h in air,[4] which purified REOOH samples very well based on PXRD and TG-DSC results.

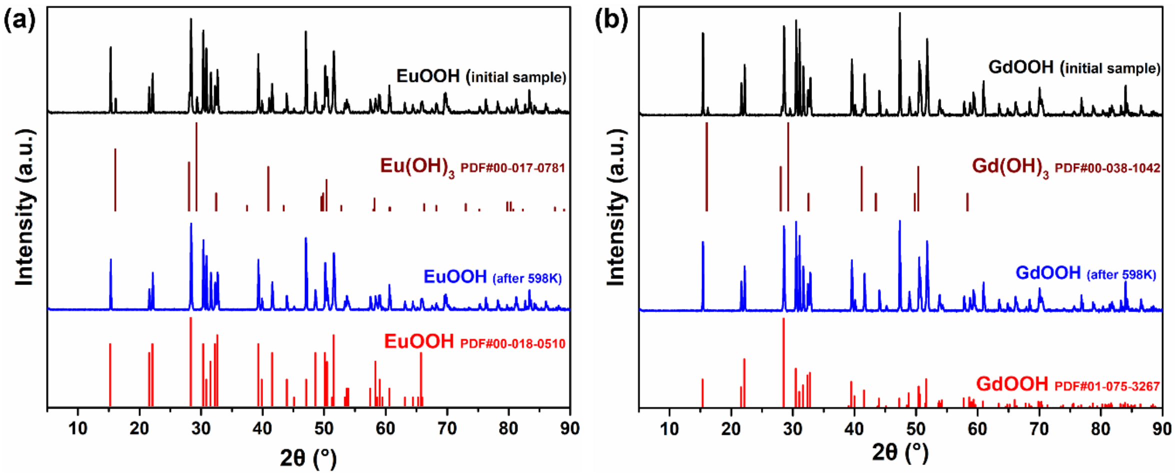

Figure 2.1 PXRD patterns of (a) EuOOH and (b) GdOOH samples with the Powder Diffraction File (PDF) cards.[4,14,15]

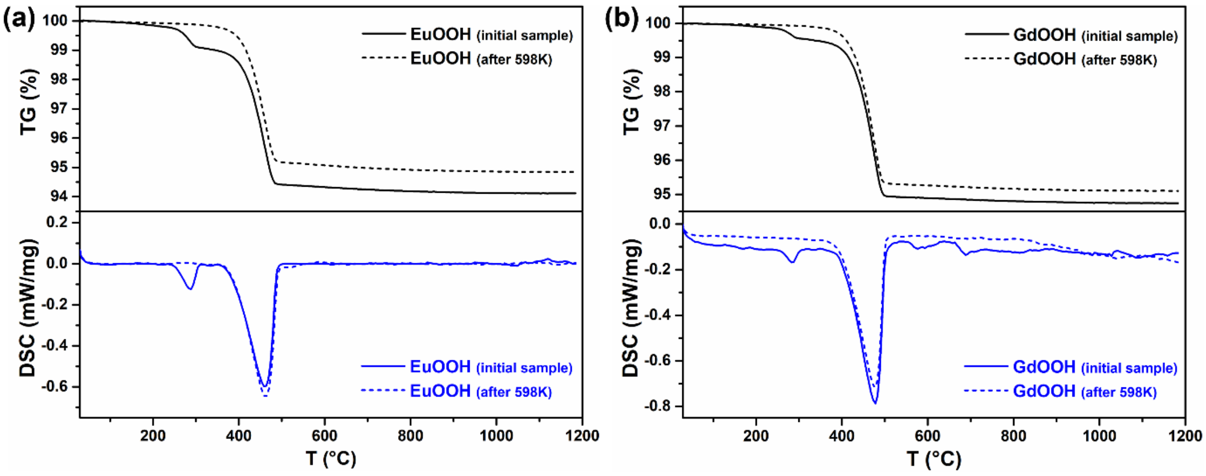

Figure 2.2 TG-DSC scans of (a) EuOOH and (b) GdOOH samples.

PXRD patterns shown in Figure 2.3 reveal that all REOOH samples crystallized as a single phase with monoclinic structure in the $P2_1/m$ space group. Thermal conversion of samples above 500 °C always led to dehydration and the formation of oxides. To avoid any change of oxidation state of rare earth ions (RE^{3+}), an oxygen atmosphere was chosen for the process of dehydration, but TbOOH was heated in Ar as trivalent terbium is easily oxidized to terbium (III,IV) oxide in O_2 (Figure 2.4).[26] Using these procedures, rare earth oxides (RE_2O_3) were obtained as the products of dehydration (Figure 2.5).

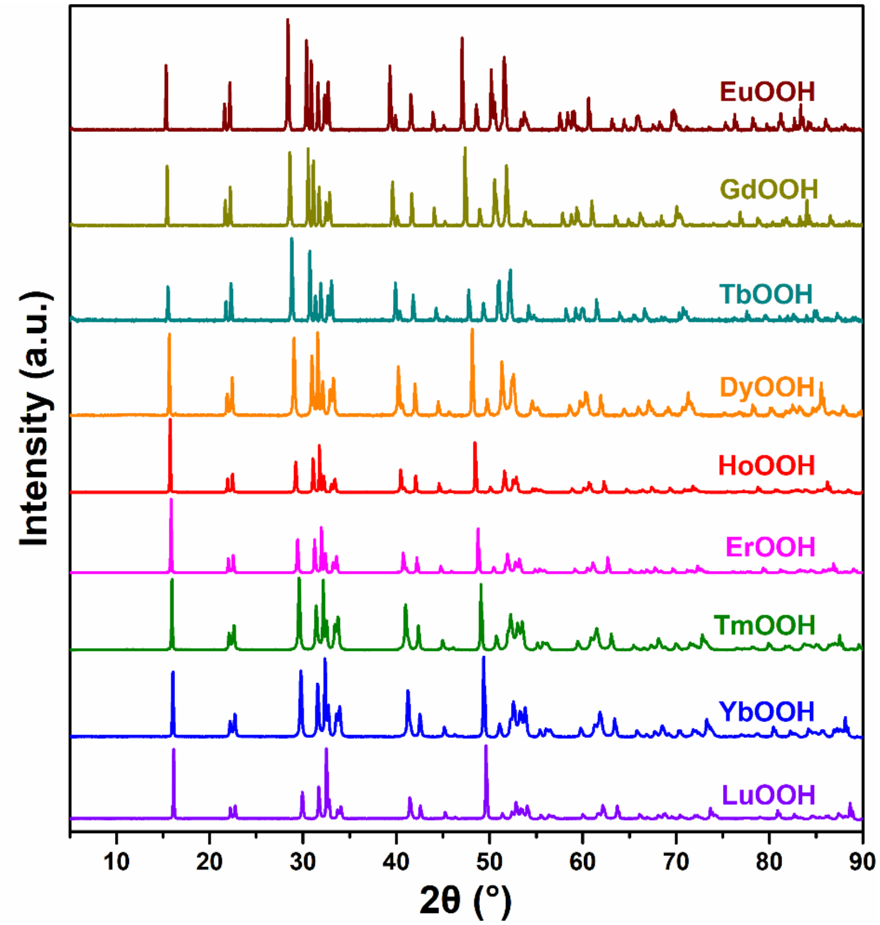

Figure 2.3 PXRD patterns of REOOH samples.

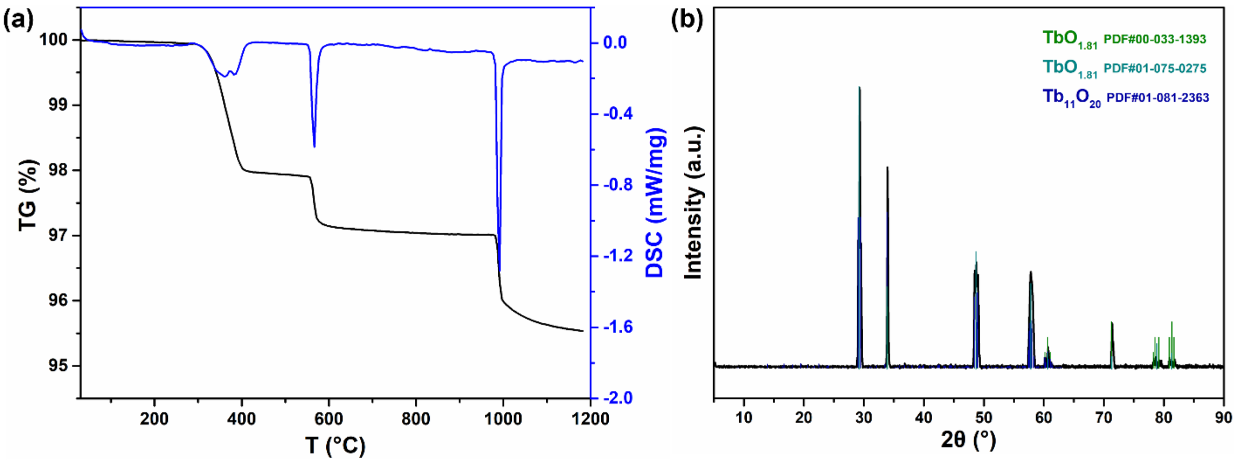

Figure 2.4 (a) The TG-DSC scan of TbOOH sample in O_2 and (b) the PXRD pattern of the sample quenched from 1200 °C under O_2 atmosphere with the PDF cards.

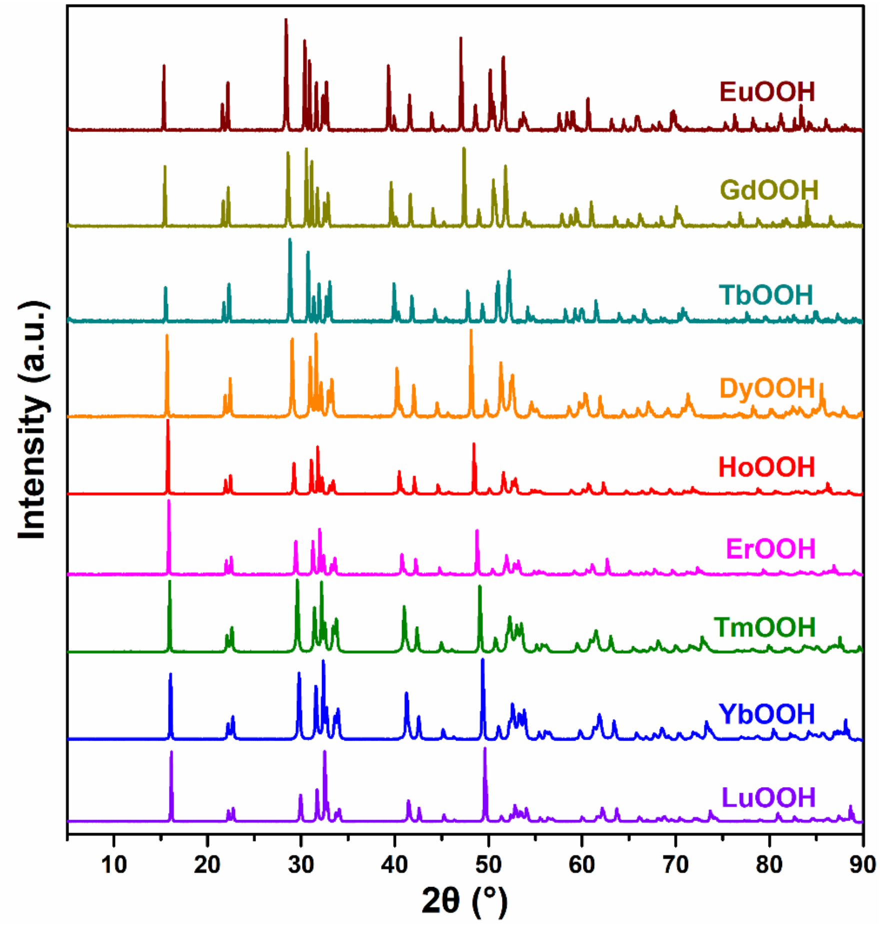

Figure 2.5 PXRD patterns of RE_2O_3 samples.

Based on peak positions of PXRD patterns and monoclinic structural model for REOOH (space group $P2_1/m$) or cubic structural model for RE_2O_3 (space group $Ia\bar{3}$), the unit cell parameters and volumes were determined (Table 2.1). Considering the coordination number of RE^{3+} is different in oxyhydroxides and oxides, two series of ionic radii[27] are adopted in the comparation of the unit cell volumes of REOOH and RE_2O_3 as plotted in Figure 2.6. As heavier lanthanide elements have smaller ionic radius, the unit cell volume of oxyhydroxides and oxides decreases from Eu to Lu, following a linear relationship with ionic radius. A similar trend has been observed in rare earth phosphates,[28] confirming that the contraction of 4f orbitals in lanthanide series dominates the cell size of rare earth compounds.

Table 2.1 Crystal structure and calculated lattice parameters of samples.

Sample	Crystal structure	a (Å)	b (Å)	c (Å)	β (°)	Volume (Å^3)
Rare earth oxyhydroxides						
EuOOH	Monoclinic, $P2_1/m$	6.1099 (4)	3.745 (1)	4.3470 (5)	108.60 (1)	94.27 (4)
GdOOH	Monoclinic, $P2_1/m$	6.0786 (5)	3.720 (1)	4.3404 (6)	108.76 (1)	92.92 (5)
TbOOH	Monoclinic, $P2_1/m$	6.0310 (4)	3.691 (1)	4.3211 (2)	108.85 (1)	91.04 (4)
DyOOH	Monoclinic, $P2_1/m$	5.9928 (8)	3.664 (1)	4.3040 (9)	108.97 (1)	89.38 (7)
HoOOH	Monoclinic, $P2_1/m$	5.9607 (4)	3.641 (1)	4.2961 (1)	109.06 (1)	88.12 (6)
ErOOH	Monoclinic, $P2_1/m$	5.9263 (4)	3.615 (1)	4.2823 (5)	109.10 (1)	86.70 (7)
TmOOH	Monoclinic, $P2_1/m$	5.8923 (3)	3.596 (1)	4.2680 (9)	109.18 (1)	85.42 (6)
YbOOH	Monoclinic, $P2_1/m$	5.8611 (4)	3.573 (4)	4.2522 (9)	109.22 (1)	84.10 (6)
LuOOH	Monoclinic, $P2_1/m$	5.8392 (4)	3.556 (2)	4.2467 (9)	109.34 (2)	83.21 (9)
Rare earth oxides						
Eu_2O_3	Cubic, $Ia\bar{3}$	10.8616 (6)				1281.37 (21)
Gd_2O_3	Cubic, $Ia\bar{3}$	10.8093 (4)				1262.96 (15)
Tb_2O_3	Cubic, $Ia\bar{3}$	10.7223 (5)				1232.71 (16)
Dy_2O_3	Cubic, $Ia\bar{3}$	10.6551 (1)				1209.68 (3)
Ho_2O_3	Cubic, $Ia\bar{3}$	10.5968 (6)				1189.86 (21)
Er_2O_3	Cubic, $Ia\bar{3}$	10.5386 (7)				1170.44 (25)
Tm_2O_3	Cubic, $Ia\bar{3}$	10.4767 (1)				1149.96 (3)
Yb_2O_3	Cubic, $Ia\bar{3}$	10.4259 (5)				1133.29 (17)
Lu_2O_3	Cubic, $Ia\bar{3}$	10.3808 (6)				1118.65 (20)

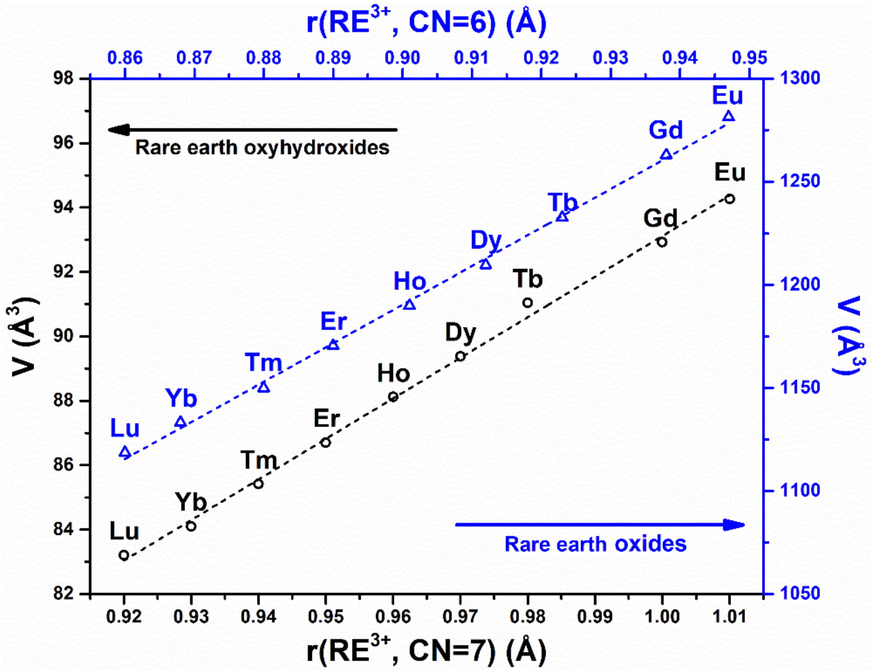

Figure 2.6 Variation of the unit cell volume (V) versus the ionic radius (r) of the RE^{3+} in oxyhydroxides (circle) and oxides (triangle).

The dehydration process was investigated by TG-DSC to provide a thermodynamic view of the transition from oxyhydroxides to oxides. The results indicate that all REOOH samples dehydrate between 340 and 500 °C, along with a mass loss in TG curves (Figure 2.7) and an endothermic peak in DSC curves (Fig. 2.8). The experimental mass losses from 4.92 wt% for EuOOH to 4.28 wt% for LuOOH correspond to the theoretical values of the conversion from REOOH to RE_2O_3 (ranging from 4.87 to 4.33 wt%). Therefore, the dehydration process follows the following chemical equation:

$$\text{REOOH (s, } T_d) \rightarrow 1/2\text{RE}_2\text{O}_3 \text{ (s, } T_d) + 1/2\text{H}_2\text{O (g, } T_d) \qquad (2.2)$$

Where T_d is the dehydration temperature. Here, onset temperatures in DSC curves are used to compare the dehydration temperatures of oxyhydroxides with different cations because of their smaller dependence on heating rate and sample mass.[29] Dehydration temperature decreases gradually with decreasing ionic radius as shown in Figure 2.9, demonstrating the important role of metal cations in the transformation and durability of REOOH. The deviation of GdOOH from the trend may be due to the electronic configuration of Gd^{3+} with its half-filled 4f subshell ($4f^7$).[19]

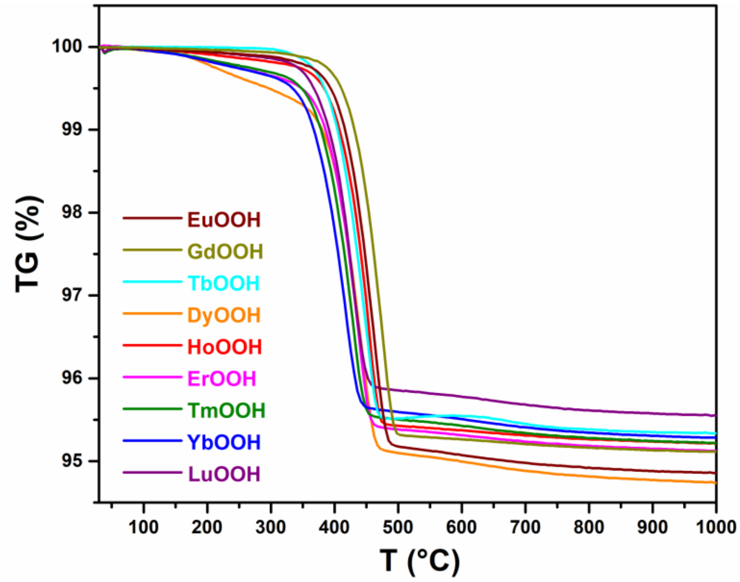

Figure 2.7 TG curves of REOOH samples.

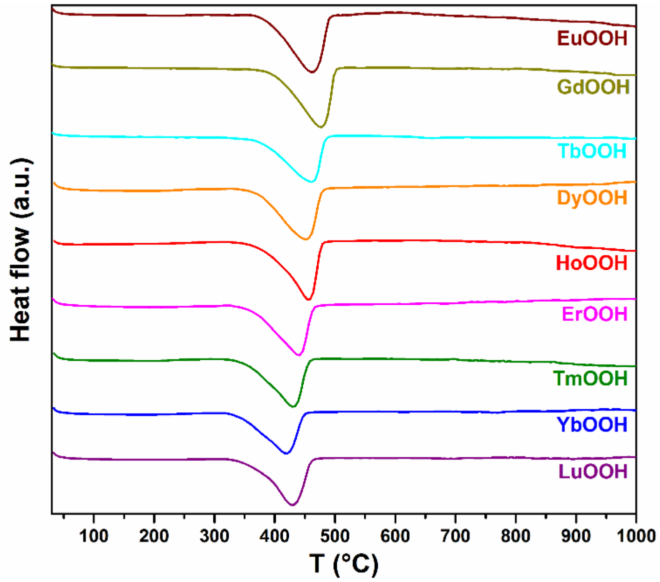

Figure 2.8 DSC curves of REOOH samples.

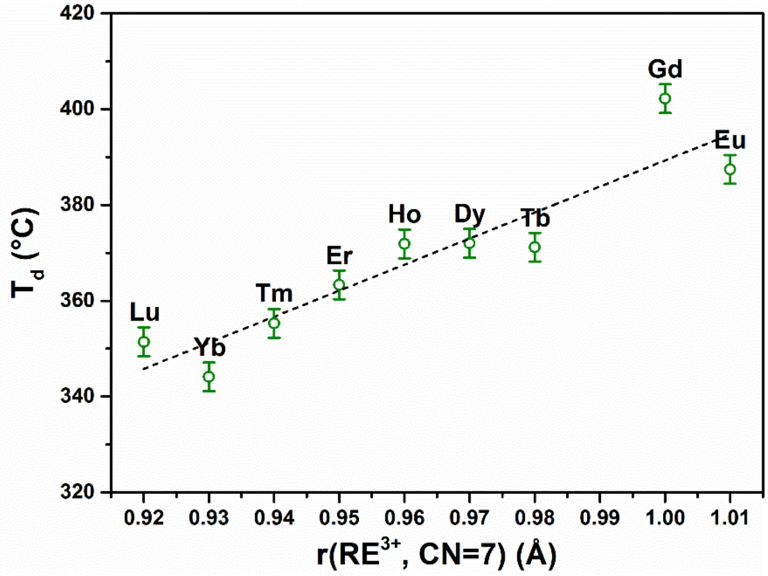

Figure 2.9 Variation of observed temperature of dehydration (T_d) of REOOH versus the ionic radius (r) of the RE^{3+}.

To better understand the dehydration process, two methods were applied to estimate the enthalpies of dehydration. First, through integrating the area of the endothermic peak, the reaction enthalpies of the transformation from REOOH to RE_2O_3 were measured by DSC as follows.

$$\Delta H^{DSC}_{deh}\ (\mathrm{kJ\ mol^{-1}}) = \Delta H_{integral}\ (\mathrm{J\ g^{-1}}) \times M\ (\mathrm{g\ mol^{-1}}) / 1000 \qquad (2.3)$$

Second, the enthalpies of dehydration are calculated from the enthalpies of drop solution (ΔH_{ds}) of REOOH, which were obtained from high temperature oxide melt solution calorimetry (described in more detail below) using the following relation:

$$\begin{tikzcd}
\mathrm{REOOH\ (s,\ 25\ °C)} \arrow[r, "\Delta H_1"] \arrow[d, "\Delta H_6"] & \mathrm{1/2RE_2O_3\ (sol,\ 803\ °C)} & + & \mathrm{1/2H_2O\ (g,\ 803\ °C)} \\
\mathrm{REOOH\ (s,\ T_d)} \arrow[r, "\Delta H^{ox\text{-}melt}_{deh}"] & \mathrm{1/2RE_2O_3\ (s,\ T_d)} \arrow[u, "1/2\Delta H_5"] & + & \mathrm{1/2H_2O\ (g,\ T_d)} \arrow[u, "1/2\Delta H_7"] \\
& \mathrm{1/2RE_2O_3\ (s,\ 25\ °C)} \arrow[u, "1/2\Delta H_4"] \arrow[uu, bend right, "1/2\Delta H_2"'] & &
\end{tikzcd} \qquad (2.4)$$

Table 2.2 Thermodynamic cycles used to calculate the formation enthalpies of REOOH from RE_2O_3 and H_2O ($\Delta H^{\circ}_{f,\ ox}$), dehydration enthalpies of REOOH estimated from high temperature oxide melt solution calorimetry ($\Delta H^{ox\text{-}melt}_{deh}$), and hydration enthalpies of RE_2O_3 to REOOH at 25 °C estimated from DSC (ΔH^{DSC}_{hyd}).

Reactions	ΔH
REOOH (s, 25 °C) → $1/2RE_2O_3$ (soln, 803 °C) + $1/2H_2O$ (g, 803 °C)	$\Delta H_1 = \Delta H_{ds}$
RE_2O_3 (s, 25 °C) → RE_2O_3 (soln, 803 °C)	ΔH_2
H_2O (l, 25 °C) → H_2O (g, 803 °C)	ΔH_3 [30]
$1/2RE_2O_3$ (s, 25 °C) + $1/2H_2O$ (l, 25 °C) → REOOH (s, 25 °C)	$\Delta H^{\circ}_{f,\ ox}$
$\Delta H^{\circ}_{f,\ ox} = -\Delta H_1 + 1/2\Delta H_2 + 1/2\Delta H_3$	
REOOH (s, 25 °C) → $1/2RE_2O_3$ (soln, 803 °C) + $1/2H_2O$ (g, 803 °C)	$\Delta H_1 = \Delta H_{ds}$
RE_2O_3 (s, 25 °C) → RE_2O_3 (soln, 803 °C)	ΔH_2
RE_2O_3 (s, 25 °C) → RE_2O_3 (s, T_d)	ΔH_4 [31]
RE_2O_3 (s, T_d) → RE_2O_3 (soln, 803 °C)	$\Delta H_5 = \Delta H_2 - \Delta H_4$
REOOH (s, 25 °C) → REOOH (s, T_d)	ΔH_6
H_2O (g, T_d) → H_2O (g, 803 °C)	ΔH_7 [30]
REOOH (s, T_d) → $1/2RE_2O_3$ (s, T_d) + $1/2H_2O$ (g, T_d)	$\Delta H^{ox\text{-}melt}_{deh}$
$\Delta H^{ox\text{-}melt}_{deh} = \Delta H_1 - 1/2\Delta H_5 - \Delta H_6 - 1/2\Delta H_7$	
REOOH (s, T_d) → $1/2RE_2O_3$ (s, T_d) + $1/2H_2O$ (g, T_d)	$\Delta H_8 = \Delta H^{DSC}_{deh}$
RE_2O_3 (s, 25 °C) → RE_2O_3 (s, T_d)	ΔH_4 [31]
REOOH (s, 25 °C) → REOOH (s, T_d)	ΔH_6
H_2O (l, 25 °C) → H_2O (g, T_d)	ΔH_9 [30]
$1/2RE_2O_3$ (s, 25 °C) + $1/2H_2O$ (l, 25 °C) → REOOH (s, 25 °C)	ΔH^{DSC}_{hyd}
$\Delta H^{DSC}_{hyd} = 1/2\Delta H_4 - \Delta H_6 - \Delta H_8 + 1/2\Delta H_9$	

This enthalpy refers to the observed temperature of dehydration, and thermodynamic cycles are listed in Table 2.2. The values calculated by the two approaches are gathered in Table 2.3 and depicted in Figure 2.10. Overall, the agreement is reasonable and the difference between the values gained from DSC and high temperature oxide melt solution, such as the case of Eu, can be attributed to systematic and random errors during DSC experiments resulting from accuracy of the instrument and integration errors. The dehydration process is endothermic by 32.2–46.7 (ΔH^{DSC}_{deh}) or 37.9–57.3 kJ mol^{-1} ($\Delta H^{ox\text{-}melt}_{deh}$) for all REOOH compounds, which suggests that oxyhydroxides are energetically stable with respect to oxides plus water. In addition, the enthalpies of dehydration from both experiments follow a similar trend versus ionic radius of RE^{3+}, i.e., the dehydration of REOOH becomes less endothermic with heavier and smaller cations. Combining the dehydration temperatures and enthalpies of dehydration, the thermodynamics of dehydration indicates that oxyhydroxides have a stronger thermodynamic driving force to dehydrate during the heating process when the rare earth ion shrinks in size. The general trend for the dehydration of rare earth oxyhydroxides reflects the strength of ionic bonds in REOOH, which become weaker with the decrease of ionic radius of cations.

Table 2.3 Enthalpies of drop solution (ΔH_{ds}), enthalpies of dehydration estimated from DSC (ΔH^{DSC}_{deh}) and high temperature drop solution calorimetry ($\Delta H^{ox\text{-}melt}_{deh}$) for REOOH, and heat capacity effects of REOOH from 25 °C to observed dehydration temperature ($\Delta H^\circ_{Td} - \Delta H^\circ_{298.15}$).

Lanthanide oxyhydroxides	ΔH_{ds}[a] (kJ mol^{-1})	ΔH^{DSC}_{deh} (kJ mol^{-1})	$\Delta H^{o}_{Td} - \Delta H^{o}_{298.15}$ (kJ mol^{-1})	$\Delta H^{ox\text{-}melt}_{deh}$ (kJ mol^{-1})
EuOOH	11.85 ± 0.18 (8)	43.59 ± 2.90	32.19 ± 2.25	57.28 ± 3.33
GdOOH	7.54 ± 0.49 (9)	46.65 ± 2.32	30.08 ± 2.10	52.04 ± 4.19
TbOOH	8.03 ± 0.66 (11)	44.62 ± 4.29	31.63 ± 2.21	46.74 ± 3.53
DyOOH	10.64 ± 0.25 (8)	39.42 ± 2.92	35.94 ± 2.51	41.76 ± 3.35
HoOOH	13.06 ± 0.34 (8)	39.34 ± 2.64	37.75 ± 2.63	42.73 ± 3.72
ErOOH	11.65 ± 0.38 (8)	37.17 ± 1.64	34.79 ± 2.43	41.95 ± 3.52
TmOOH	13.32 ± 0.52 (8)	35.23 ± 2.41	32.92 ± 2.30	41.14 ± 3.28
YbOOH	12.57 ± 0.47 (8)	32.21 ± 1.93	30.83 ± 2.15	37.90 ± 2.82
LuOOH	12.30 ± 0.32 (8)	34.38 ± 3.47	31.95 ± 2.23	40.20 ± 2.94

[a] Error is two standard deviations of the mean, and value in parentheses is the number of experiments.

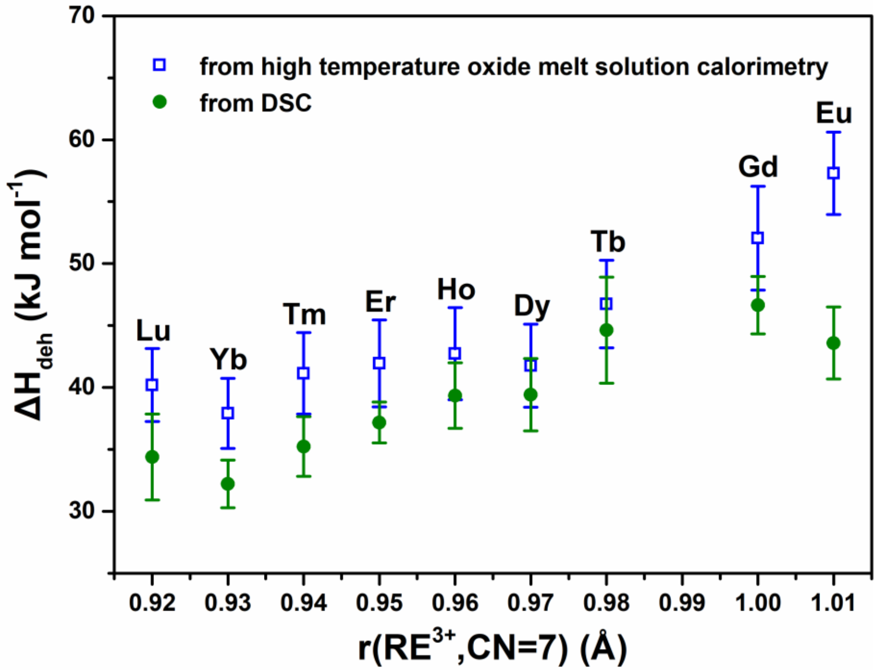

Figure 2.10 Enthalpies of dehydration (ΔH_{deh}) of REOOH as a function of ionic radius (r) of RE^{3+} estimated from high temperature oxide melt solution calorimetry (blue trace) and DSC (green trace).

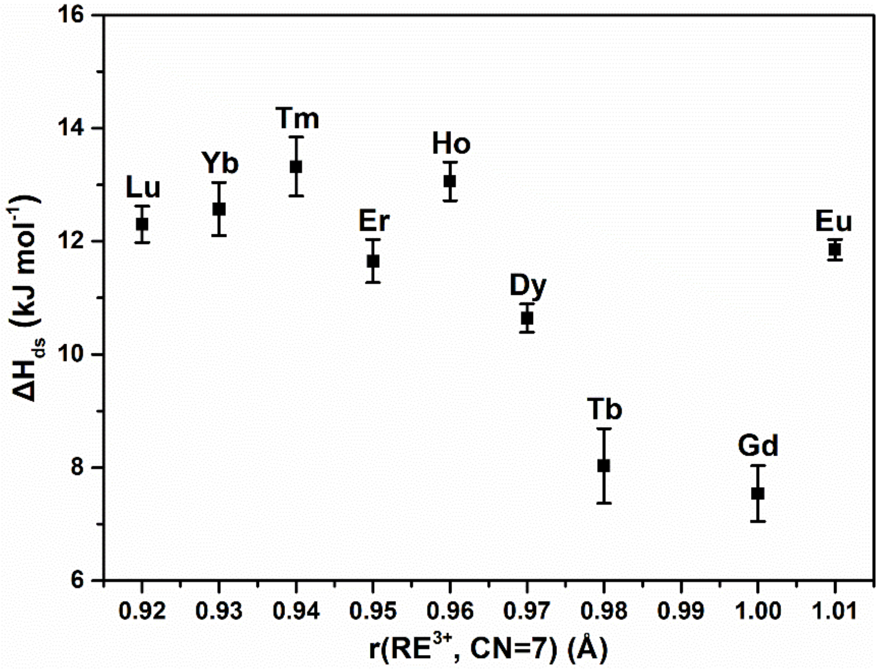

Figure 2.11 Enthalpies of drop solution (ΔH_{ds}) of REOOH in $3Na_2O \cdot 4MoO_3$ at 803 °C.

To evaluate the stability of REOOH at room temperature, the enthalpies of formation were measured by means of high temperature oxide melt solution calorimetry, in which samples were dropped into $3Na_2O\cdot4MoO_3$ at 803 °C and enthalpies of drop solution (ΔH_{ds}) were measured (Figure 2.11 and Table 2.3). Thermodynamic cycles employed to calculate the enthalpies of formation from oxides ($\Delta H^\circ_{f,\,ox}$) are presented in Table 2.2 following the relation:

$$\begin{tikzcd}
\text{REOOH (s, 25 °C)} \arrow[r, "\Delta H_1"] & 1/2RE_2O_3\text{ (sol, 803 °C)} & + & 1/2H_2O\text{ (g, 803 °C)} \\
 & 1/2RE_2O_3\text{ (s, 25 °C)} \arrow[u, "1/2\Delta H_2"'] \arrow[ul, "\Delta H^\circ_{f,\,ox}"] & + & 1/2H_2O\text{ (l, 25 °C)} \arrow[u, "1/2\Delta H_3"']
\end{tikzcd} \tag{2.5}$$

The data used to calculate $\Delta H^\circ_{f,\,ox}$ and enthalpies of formation from elements ($\Delta H^\circ_{f,\,el}$) are given in Table 2.4. The DSC dehydration enthalpies ($\Delta H^{DSC}{}_{deh}$) are calculated back to room temperature as enthalpies of hydration from RE_2O_3 to REOOH estimated from DSC ($\Delta H^{DSC}{}_{hyd}$) by subtracting the heat capacity effects ($\Delta H^\circ_{Td} - \Delta H^\circ_{298.15}$):

$$\begin{tikzcd}
\text{REOOH (s, } T_d) \arrow[r, "\Delta H_8"] & 1/2RE_2O_3\text{ (s, }T_d) & + & 1/2H_2O\text{ (g, }T_d) \\
\text{REOOH (s, 25 °C)} \arrow[u, "\Delta H_6"'] & 1/2RE_2O_3\text{ (s, 25 °C)} \arrow[u, "1/2\Delta H_4"'] \arrow[l, "\Delta H^{DSC}{}_{hyd}"'] & + & 1/2H_2O\text{ (l, 25 °C)} \arrow[u, "1/2\Delta H_9"']
\end{tikzcd} \tag{2.6}$$

The results are shown in Table 2.5.

Table 2.4 Enthalpies of drop solution (ΔH_{ds}) of rare earth oxides in molten sodium molybdate at 800–805 °C with their enthalpies of formation from elements ($\Delta H^\circ_{f,\,el}$).

Rare earth oxides	ΔH_{ds} (kJ mol^{-1})	$\Delta H^\circ_{f,\,el}$ (kJ mol^{-1})
Eu_2O_3	−122.46 ± 1.80 (8) [32]	−1662.5 ± 6.0 [31]
Gd_2O_3	−121.00 ± 3.20 (7) [33]	−1819.7 ± 3.6 [31]
Tb_2O_3[a]	−114.15 ± 1.33 (8) [32]	−1865.2 ± 6.0 [31]
Dy_2O_3	−108.11 ± 1.68 (8)[34]	−1863.4 ± 5.0 [31]
Ho_2O_3	−109.51 ± 1.50 (6) [35]	−1883.3 ± 8.2 [31]
Er_2O_3	−107.20 ± 1.42 (6) [35]	−1900.1 ± 6.5 [31]

Tm_2O_3	−97.97 ± 0.93 (6) [35]	−1889.3 ± 5.7 [31]
Yb_2O_3	−90.71 ± 0.40 (8)[b]	−1814.5 ± 6.0 [31]
Lu_2O_3	−99.98 ± 0.79 (9)[b]	−1877.0 ± 7.7 [31]

Error is two standard deviations of the mean, and value in parentheses is the number of experiments.

[a] The prior experiments[32] on Tb took into account the ease of oxidation of Tb_2O_3 to Tb_4O_7 to provide a reliable value for the enthalpy of drop solution of the sesquioxide, with Tb trivalent when dissolved in the molten sodium molybdate.

[b] The ΔH_{ds} of Yb_2O_3 and Lu_2O_3 at 803 °C are measured in this work.

Table 2.5 Enthalpies of formation from oxides ($\Delta H°_{f,\ ox}$) and elements ($\Delta H°_{f,\ el}$) at 25 °C for REOOH, and enthalpies of hydration from RE_2O_3 to REOOH estimated from DSC (ΔH^{DSC}_{hyd}), plus enthalpies of formation from oxides ($\Delta H°_{f,\ ox}$) at 25 °C for $RE(OH)_3$.

Lanthanide oxyhydroxides	$\Delta H°_{f,\ ox}$ (kJ mol^{-1})	ΔH^{DSC}_{hyd} (kJ mol^{-1})	$\Delta H°_{f,\ el}$ (kJ mol^{-1})	Lanthanide hydroxides	$\Delta H°_{f,\ ox}$ [36,37] (kJ mol^{-1})
EuOOH	−36.49 ± 1.08	−22.80 ± 5.14	−1010.6 ± 4.1	$Eu(OH)_3$	−59.15 ± 13.15
GdOOH	−31.45 ± 2.09	−26.06 ± 4.42	−1084.2 ± 3.9	$Gd(OH)_3$	−70.35 ± 11.95
TbOOH	−28.52 ± 1.33	−26.40 ± 6.49	−1104.0 ± 4.4	$Tb(OH)_3$	−53.50 ± 13.15
DyOOH	−28.11 ± 0.85	−25.76 ± 5.43	−1102.7 ± 3.4	$Dy(OH)_3$	−68.00 ± 12.65
HoOOH	−31.23 ± 1.09	−27.84 ± 5.27	−1115.8 ± 5.2	$Ho(OH)_3$	−60.75 ± 14.25
ErOOH	−28.66 ± 1.09	−24.02 ± 4.71	−1121.6 ± 4.4	$Er(OH)_3$	−53.75 ± 13.40
TmOOH	−25.72 ± 0.99	−19.81 ± 4.70	−1113.3 ± 3.9	$Tm(OH)_3$	−47.75 ± 13.00
YbOOH	−21.34 ± 0.67	−15.64 ± 4.08	−1071.5 ± 3.7	$Yb(OH)_3$	−59.55 ± 13.15
LuOOH	−25.70 ± 0.72	−19.88 ± 5.70	−1107.1 ± 4.6	$Lu(OH)_3$	−59.80 ± 14.00

Figure 2.12 shows the enthalpies of formation of REOOH from RE_2O_3 and water at 25 °C, ranging from −36.49 ± 1.08 (EuOOH) to −21.34 ± 0.67 (YbOOH) kJ mol^{-1}. And the enthalpies of hydration from RE_2O_3 to REOOH estimated from DSC (Figure 2.13) vary from −27.84 ± 5.43 (HoOOH) to −15.64 ± 4.08 (YbOOH) kJ mol^{-1}. The negative values confirm the thermodynamic

stability of oxyhydroxides relative to oxides at ambient temperature since it is unlikely that entropy effects will overpower the significant negative enthalpy of formation, especially when

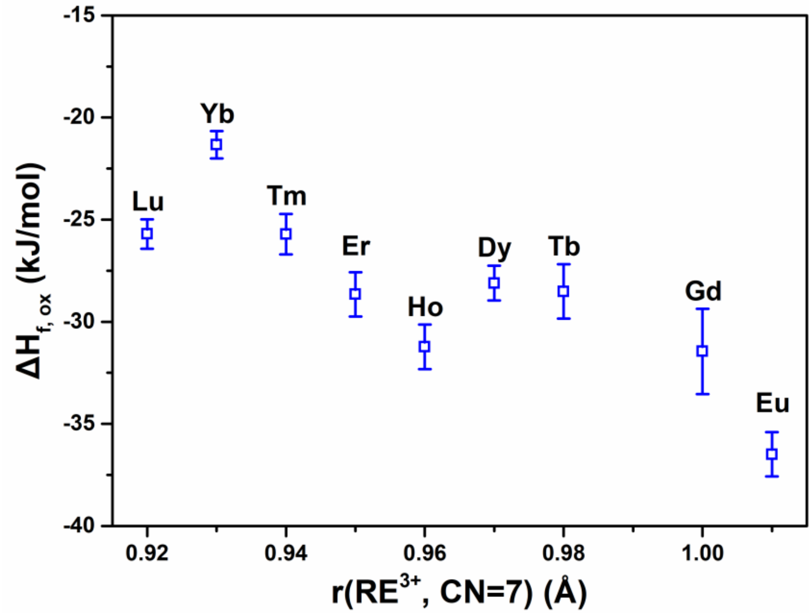

Figure 2.12 Enthalpies of formation from oxides ($\Delta H^{\circ}_{f,\,ox}$) at 25 °C of REOOH measured by high temperature oxide melt solution calorimetry.

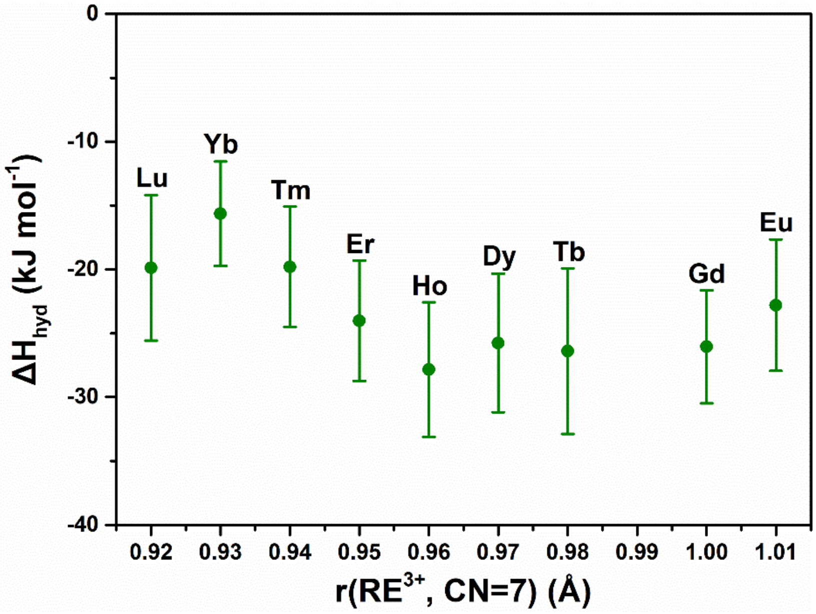

Figure 2.13 Enthalpies of hydration (ΔH_{hyd}) from RE_2O_3 to REOOH estimated from DSC.

the reference state of water is liquid. A roughly linear relationship is seen between these enthalpy values and the ionic radius of the lanthanide, and enthalpies of formation from oxides become more negative with increasing ionic radius of RE^{3+}. This trend can be ascribed to the decrease of basicity of RE_2O_3 across the rare earth series, and weaker acid-base interaction between water and RE_2O_3.

With further hydration of RE oxides, hydroxides will form as products.

$$\mathrm{REO_{1.5}\ (s, 25\ °C)} \xrightarrow{1/2\mathrm{H_2O}} \mathrm{REOOH\ (s, 25\ °C)} \xrightarrow{\mathrm{H_2O}} \mathrm{RE(OH)_3 (s, 25\ °C)} \qquad (2.7)$$

Their enthalpies of formation from oxides are listed in Table 2.5. A complete picture of the thermochemistry of rare earth oxide – water systems for whole lanthanide series is illustrated in Figure 2.14.[18,36–39] The enthalpies of formation from oxides become more exothermic with increasing hydration, so the energetic stability follows the order: $REO_{1.5} < REOOH < RE(OH)_3$, where oxyhydroxides serve as thermodynamic “intermediates” between oxides and hydroxides.

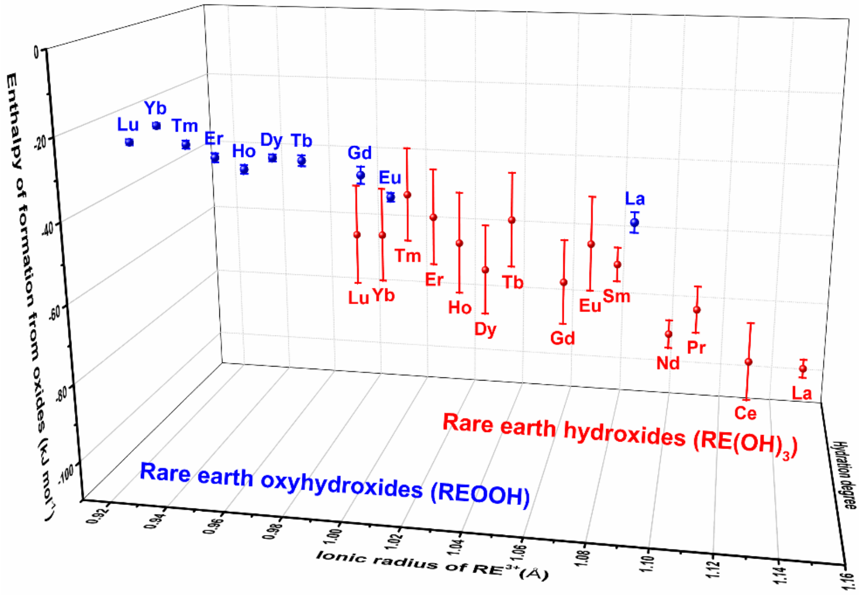

Figure 2.14 Enthalpies of formation of rare earth oxyhydroxides (blue trace) and hydroxides (red trace) from corresponding oxides at 25 °C.

2.5 Conclusions

The enthalpies of formation of a series of REOOH were measured by high temperature oxide melt solution calorimetry and the energetics of dehydration were determined both by high temperature oxide melt solution calorimetry and by DSC. Combined with heat capacity effects, enthalpies of conversion between REOOH and RE_2O_3 were determined at room temperature and dehydration temperature. From the perspective of thermodynamics, oxyhydroxides are more energetically stable than oxides plus water in the rare earth series and act as intermediates between hydroxides and oxides. For different rare earth elements, the thermodynamic stability of REOOH decreases with decreasing ionic radius of RE^{3+}. Hence, oxyhydroxides with lighter rare earth elements are more likely to form and more difficult to be removed during the preparation of rare earth oxides, especially for the hydrothermal synthesis.

2.6 Acknowledgements

The calorimetric studies at UC Davis were funded by the U.S. Department of Energy Critical Materials Institute Hub under subaward number SC-18-474. Shuhao Yang would like to thank Tamilarasan Subramani and Novendra Novendra for help in calorimetric experiments, and Albert A. Voskanyan for fruitful discussions. The synthesis work was performed at Clemson University and supported by Department of Energy award BES DE-SC0020071.

2.7 References

(1) Hölsä, J.; Chateau, C.; Leskelä, T.; Leskelä, M. Optical study of phase transformations in rare earth oxyhydroxides. *Acta Chem. Scand.* **1985**, *39*, 415−421.

(2) Holsa, J.; Leskela, T.; Leskela, M. Luminescence properties of europium(3+)-doped rare-earth oxyhydroxides. *Inorg. Chem.* **1985**, *24*, 1539−1542.

(3) Holsa, J. Simulation of crystal field effect in monoclinic rare earth oxyhydroxides doped with trivalent europium. *J. Phys. Chem.* **1990**, *94*, 4835−4838.

(4) Chang, C.; Zhang, Q.-A.; Mao. D. The hydrothermal preparation, crystal structure and photoluminescent properties of GdOOH nanorods. *Nanotechnology* **2006**, *17*, 1981−1985.

(5) McMillen, C. D.; Sanjeewa, L. D.; Moore, C. A.; Brown, D. C.; Kolis, J. W. Crystal growth and phase stability of Ln:Lu_2O_3 (Ln=Ce, Pr, Nd, Sm, Eu, Tb, Dy, Ho, Er, Tm, Yb) in a higher-temperature hydrothermal regime. *J. Cryst. Growth* **2016**, *452*, 146−150.

(6) Zhang, X.; Wang, Y.; Cheng, F.; Zheng, Z.; Du, Y. Ultrathin lanthanide oxides nanomaterials: synthesis, properties and applications. *Sci. Bull.* **2016**, *61*,1422−1434.

(7) Amrute, A. P.; Łodziana, Z.; Schreyer, H.; Weidenthaler, C.; Schüth, F. High-surface-area corundum by mechanochemically induced phase transformation of boehmite. *Science* **2019**, *366*, 485−489.

(8) Weiser, H. B.; Milligan, W. O. The hydrous oxides of some rarer elements. *J. Phys. Chem.* **1938**, *42*, 673−678.

(9) Milligan, W. O.; Mullica, D. F.; Hall, M. A. Structural refinement of lutetium hydroxide oxide. *Acta Crystallogr. B* **1980**, *36*, 3086−3088.

(10) Christensen, A. N. On the crystal structures of HoOOH, ErOOH, and YbOOH. *Acta Chem. Scand.* **1965**, *19*, 1391−1396.

(11) Christensen, A. N.; Lebech, B. Magnetic transition temperature of terbium hydroxide oxide. Structure of ytterbium hydroxide oxide. *Acta Crystallogr. B* **1981**, *37*, 425−427.

(12) Seck, H. A.; Dachille, F.; Roy, R. High-pressure polymorphism and reactions of dysprosium sesquioxide. *Inorg. Chem.* **1969**, *8*, 165−167.

(13) Gondrand, M.; Christensen, A. N. Hydrothermal and high pressure preparation of some rare earth trihydroxides and some rare earth oxide hydroxides. *Mater. Res. Bull.* **1971**, *6*, 239−246.

(14) Bärnighausen, H. Die Elementarzelle und Raumgruppe von EuOOH. *Acta Crystallogr.* **1965**, *19*, 1047.

(15) Yamamoto, O.; Takeda, Y.; Kanno, R.; Fushimi, M. Thermal decomposition and electrical conductivity of $M(OH)_3$ and MOOH (M=Y, lanthanide). *Solid State Ion.* **1985**, *17*, 107−114.

(16) Shafer, M. W.; Roy, R. Rare-earth polymorphism and phase equilibria in rare-earth oxide-water systems. *J. Am. Ceram. Soc.* **1959**, *42*, 563−570.

(17) Neumann, A.; Walter, D. The thermal transformation from lanthanum hydroxide to lanthanum hydroxide oxide. *Thermochim. Acta* **2006**, *445*, 200−204.

(18) Cordfunke, E. H. P.; Konings, R. J. M.; Ouweltjes, W. The standard enthalpies of formation of hydroxides IV. $La(OH)_3$ and LaOOH. *J. Chem. Thermodyn.* **1990**, *22*, 449−452.

(19) Adachi, G.-y.; Imanaka, N. The binary rare earth oxides. *Chem. Rev.* **1998**, *98*, 1479−1514.

(20) Navrotsky, A.; Lee, W.; Mielewczyk-Gryn, A.; Ushakov, S. V.; Anderko, A.; Wu, H.; Riman, R. E. Thermodynamics of solid phases containing rare earth oxides. *J. Chem. Thermodyn.* **2015**, *88*, 126−141.

(21) Tuttle, O. F. A new hydrothermal quenching apparatus. *Am. J. Sci.* **1948**, *246*, 628−635.

(22) Byrappa, K.; Yoshimura, M. 3 - Apparatus. In *Handbook of Hydrothermal Technology*, 2nd ed.; William Andrew Publishing, 2001; pp 82−160.

(23) Navrotsky, A. Progress and new directions in high temperature calorimetry. *Phys. Chem. Miner.* **1977**, *2*, 89−104.

(24) Navrotsky, A. Progress and new directions in high temperature calorimetry revisited. *Phys. Chem. Miner.* **1997**, *24*, 222−241.

(25) Navrotsky, A. Progress and new directions in calorimetry: a 2014 perspective. *J. Am. Ceram. Soc.* **2014**, *97*, 3349−3359.

(26) Burnham, D. A.; Eyring, L.; Kordis, J. High-temperature X-ray diffraction studies of the terbium oxide-oxygen and mixed cerium terbium oxide-oxygen systems. *J. Phys. Chem.* **1968**, *72*, 4424−4431.

(27) Jia, Y. Q. Crystal radii and effective ionic radii of the rare earth ions. *J. Solid State Chem.* **1991**, *95*, 184−187.

(28) Shelyug, A.; Mesbah, A.; Szenknect, S.; Clavier, N.; Dacheux, N.; Navrotsky, A. Thermodynamics and stability of rhabdophanes, hydrated rare earth phosphates $REPO_4 \cdot n\ H_2O$. *Front. Chem.* **2018**, *6*, 604.

(29) Sarge, S. M.; Höhne, G. W. H.; Hemminger, W. Measurements and evaluation. In *Calorimetry: Fundamentals, Instrumentation and Applications*; Wiley-VCH Verlag GmbH & Co. KGaA, 2014; pp 81−122.

(30) Chase, M. W. J., *NIST-JANAF Thermochemical Tables*. 4th ed.; J. Phys. Chem. Ref. Data, Monograph, 1998; Vol. 9, pp 1–1951.

(31) Konings, R. J. M.; Beneš, O.; Kovács, A.; Manara, D.; Sedmidubský, D.; Gorokhov, L.; Iorish, V. S.; Yungman, V.; Shenyavskaya, E.; Osina, E. The thermodynamic properties of the f-elements and their compounds. Part 2. The lanthanide and actinide oxides. *J. Phys. Chem. Ref. Data* **2014**, *43*, 013101.

(32) Mielewczyk-Gryn, A.; Navrotsky, A. Enthalpies of formation of rare earth niobates, RE_3NbO_7. *Am. Mineral.* **2015**, *100*, 1578−1583.

(33) Hayun, S.; Navrotsky, A. Formation enthalpies and heat capacities of rear earth titanates: RE_2TiO_5 (RE=La, Nd and Gd). *J. Solid State Chem.* **2012**, *187*, 70−74.

(34) Subramani, T.; Navrotsky, A. Energetics of formation and disordering in rare earth weberite RE_3TaO_7 materials. *Inorg. Chem.* **2019**, *58*, 16126−16133.

(35) Qi, J.; Guo, X.; Mielewczyk-Gryn, A.; Navrotsky, A. Formation enthalpies of $LaLn'O_3$ (Ln′=Ho, Er, Tm and Yb) interlanthanide perovskites. *J. Solid State Chem. 2015*, *227*, 150−154.

(36) Diakonov, I. I.; Ragnarsdottir, K. V.; Tagirov, B. R. Standard thermodynamic properties and heat capacity equations of rare earth hydroxides: II. Ce(III)-, Pr-, Sm-, Eu(III)-, Gd-, Tb-, Dy-, Ho-, Er-, Tm-, Yb-, and Y-hydroxides. Comparison of thermochemical and solubility data. *Chem. Geol.* **1998**, *151*, 327−347.

(37) Alvero, R.; Bernal, A.; Carrizosa, I.; Odriozola, J. A.; Trillo, J. M. Lanthanide oxides: thermochemical approach to hydration. *J. Mater. Sci. 1987*, *22*, 1517−1520.

(38) Morss, L. R.; Hall, J. P. Standard molar enthalpies of formation and solubility product constants of samarium and praseodimium hydroxides $Sm(OH)_3$ and $Pr(OH)_3$. In *49th Annual Calorimetric Conference*, Santa Fe, NM, USA, 1994; pp 63.

(39) Merli, L.; Lambert, B.; Fuger, J. Thermochemistry of lanthanum, neodymium, samarium and americium trihydroxides and their relation to the corresponding hydroxycarbonates. *J. Nucl. Mater.* **1997**, *247*, 172−176.

Chapter 3

Thermochemistry of Stoichiometric Rare Earth Oxyfluorides REOF

Shuhao Yang,[†,‡] Andre Anderko,[‖] Richard E. Riman,[§] Alexandra Navrotsky[*,†]

[†]Navrotsky Eyring Center for Materials of the Universe, School of Molecular Sciences, Arizona State University, Tempe, Arizona 85287, United States

[‡]Department of Chemistry, University of California, Davis, California 95616, United States

[‖]OLI Systems, Inc., Parsippany, New Jersey 07054, United States

[§]Department of Materials Science and Engineering, Rutgers, The State University of New Jersey, Piscataway, New Jersey 08854, United States

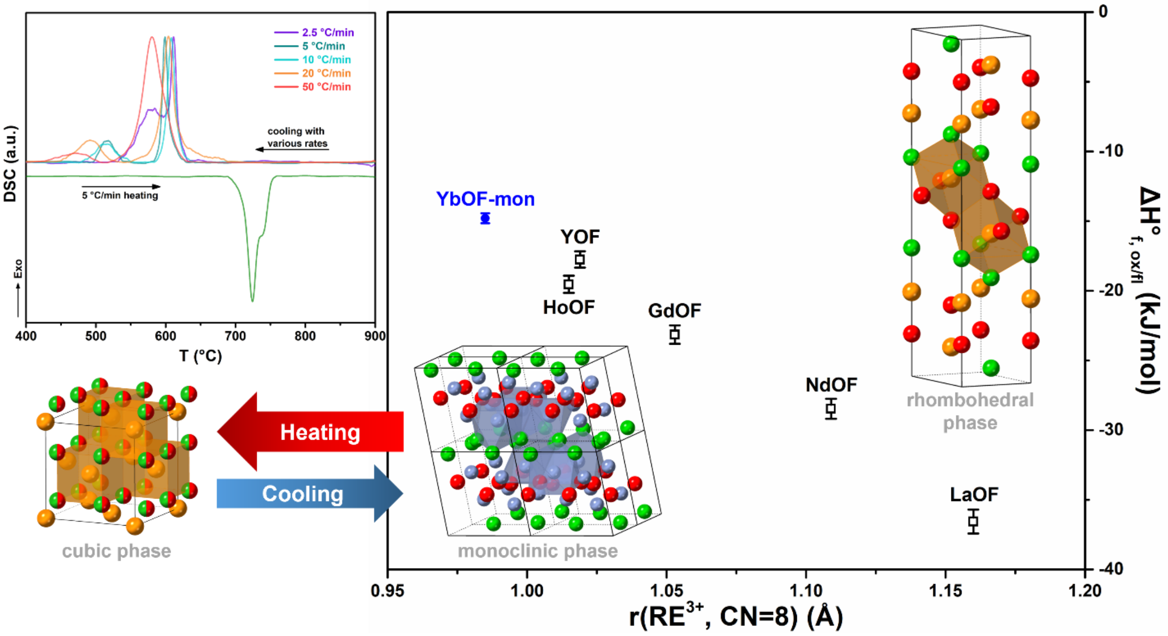

J. Am. Ceram. Soc. **2022**, *105*, 1472–1480.

3.1 Abstract

Rare earth oxyfluorides (REOF) have potential applications in luminescent devices and energy storage and are important for synthesis and properties of RE-doped oxyfluoride glasses. This study evaluates the thermodynamic properties of stoichiometric REOF with varying RE (RE = La, Nd, Gd, Ho, Y, and Yb) elements using high temperature oxide melt solution calorimetry and investigates the phase transitions of YbOF by differential scanning calorimetry. The formation enthalpies from binary oxides and fluorides are exothermic and become less exothermic with the decrease of ionic radius of RE^{3+}, showing that REOF compounds are energetically stable relative to equal molar mixtures of RE_2O_3 and REF_3 and the RE–O interactions contribute to most of their thermodynamic stabilities. Different from REOF with large RE ions (La–Er and Y) having the rhombohedral phase, REOF with small cations (e.g., Yb) possesses the monoclinic structure as the more energetically stable phase at room temperature. However, the slow transition between the monoclinic and cubic phases easily generates the rhombohedral phase, which is favored by kinetics.

3.2 Introduction

Rare earth oxyfluorides (REOF) are examples of mixed-anion RE compounds. Owing to unique luminescent properties and variable structures, they are regarded as promising host lattices for RE luminescent materials. [1–4] RE oxyfluorides also show changeable electric and ionic conductivity varying with ratios of O and F anions,[5,6] which may be of interest for energy applications. As potential components in oxyfluoride glasses, formation and crystallization of RE oxyfluorides have great effects on the manufacture and properties of RE-doped glasses.[7,8] Due to their wide applications and important places in RE materials chemistry, many studies have been conducted to investigate crystal structures and synthetic methods of RE oxyfluorides.

By means of X-ray and neutron diffraction,[9–17] thermal analysis,[6,18] and spectroscopy,[19,20] crystal structures and relationships between various structures at different temperatures and compositions have been determined for most RE oxyfluorides. For the stoichiometric compound with equal molar O^{2-} and F^{-} (REOF), a distorted fluorite structure (rhombohedral β phase, space group: $R\bar{3}m$) is adopted for most RE elements as the phase which appears to be stable at room temperature. With temperature increasing, a reversible phase transition leads to a fluorite-type structure (cubic α phase, space group: $Fm\bar{3}m$) as the high temperature phase. However, for the last three lanthanide elements (Tm, Yb, and Lu), a monoclinic structure (isostructural to α-ZrO_2, space group: $P2_1/c$) is found and proposed as the more stable phase for these REOF compounds.[21] When the content of F is higher than that of O, nonstoichiometric oxyfluorides $REO_{1-x}F_{1+2x}$ have tetragonal and orthorhombic structures (Vernier phases) for light and heavy RE elements, respectively.[11,12]

Generally, there are three methods to synthesize bulk RE oxyfluoride crystals: (i) solid-state reaction between RE oxides and fluorides, which is the most straightforward way; (ii) hydrolysis of RE fluorides above 900°C;[22] and (iii) low temperature solid-state synthesis using polytetrafluoroethylene (PTFE), which is a recently developed method.[23,24] It is worth to note that the last two methods require careful control of synthetic conditions during the synthesis of stoichiometric REOF compounds. Otherwise, nonstoichiometric RE oxyfluoride compounds and RE oxides may form as side products.[4,25]

Despite the above studies, no work has reported thermodynamic stability of RE oxyfluorides, especially enthalpies of formation for stoichiometric REOF compounds. Regarding various RE elements, trends of thermodynamic stability of RE compounds along RE series have been determined for many RE oxide systems[26] and recently for ternary sodium RE fluorides[27]. In addition, with respect to heavy RE elements (Tm, Yb, and Lu), the reason why the monoclinic phase is preferred compared to the rhombohedral phase and energetic stabilities of these phases remain to be studied. All these thermodynamic data and research gaps limit the understanding and utilization of RE oxyfluoride materials. In this paper, using high temperature oxide melt solution calorimetry, the thermodynamic stability of stoichiometric REOF with varying RE elements relative to binary oxides and fluorides, RE_2O_3 and REF_3, are determined to better define conditions under which they may form or decompose. Further, to achieve a better understanding of thermodynamic stability and phase transitions in oxyfluorides of heavy RE elements, differential scanning calorimetry (DSC) is used for YbOF in combination with oxide melt solution calorimetry.

3.3 Experimental Methods

3.3.1 Material Preparation

Before using, rare earth sesquioxides (RE_2O_3), including La_2O_3 (99.999 %, Aldrich), Nd_2O_3 (99.9 %, Apache Chemicals), Gd_2O_3 (99.99 %, Aldrich), Ho_2O_3 (99.99 %, Alfa-Aesar), Yb_2O_3 (99.99 %, Alfa-Aesar), and Y_2O_3 (99.99 %, Alfa-Aesar), were annealed at 1000 °C for several hours in air to destroy any hydroxides and carbonates which are common impurities during storage at ambient conditions. Rare earth trifluorides (REF_3), including LaF_3 (99.99 %), NdF_3 (99.9 %), GdF_3 (99.9 %), HoF_3 (99.99 %), YbF_3 (99.99 %), and YF_3 (99.9 %) were purchased from Alfa-Aesar and dried at 200 °C under vacuum overnight. All chemicals have been checked by powder X-ray diffraction to confirm the phase purity.

Rare earth oxyfluorides (REOF, RE = La, Nd, Gd, Ho, and Y) were prepared by solid-state reactions, in which equal molar ratio of RE_2O_3 and REF_3 were mixed, pelletized, reacted at 1000 °C (or 950 °C for Ho, Yb, and Y) for 2 days, and then annealed at 500 °C for 1 day in Pt crucibles under Ar atmosphere. No weight change was observed during the reaction, so the composition of the rare earth oxyfluorides is the same as the precursors, namely REOF.

For ytterbium oxyfluoride (YbOF), the phases of samples highly depend on cooling rates, so different cooling processes were applied to prepare YbOF samples after solid-state reactions at 950 °C for 1 day. (I) The sample annealed at decreasing various temperatures down to 400 °C in a week was termed as YbOF-mon; (II) The sample slowly cooled down to room temperature with a cooling rate of ~1 °C min^{-1} was termed as YbOF-mon/rhd; (III) The sample fast cooled down to room temperature using a tube furnace with a movable sample stage was designated as YbOF-quenching, and the cooling process was done by moving samples out of the heating area under Ar flow and the cooling time was estimated to be less than 5 min total, with a much shorter time (1 min or less) to reach a temperature below 500 °C, at which point any further phase transformation is unlikely. No weight change was observed during these reactions, so the composition of all samples is the same as the precursor, namely YbOF.

3.3.2 Powder X-ray Diffraction

Powder X-ray diffraction (PXRD) patterns were obtained using a Bruker D2 Phaser diffractometer operated with Cu Kα radiation ($\lambda = 1.54184$ Å). The data for REOF samples were collected in the 2θ range of 10−120° with a step size of 0.02° and a dwell time of 5 s per step, which were analyzed using the Rietveld method implemented in the program GSAS-II.[28] The data for RE_2O_3, REF_3, and samples after DSC measurements were collected in the 2θ range of 10−80° with a step size of 0.02° and a dwell time of 0.45 s per step.

3.3.3 High Temperature Oxide Melt Solution Calorimetry

High temperature oxide melt solution calorimetry experiments were carried out using a Setaram AlexSYS Tian-Calvet twin microcalorimeter using methods standard to our laboratory and described previously.[29–31] The calorimeter was calibrated against the heat content of high purity α-Al_2O_3 (99.997 %). Pressed sample pellets (∼10 mg) were dropped from ambient temperature into the calorimeter containing the solvent, molten sodium molybdate ($3Na_2O\cdot4MoO_3$), in a Pt crucible at 800 °C. All experiments were flushed with O_2 at 60 ml min^{-1} with bubbling through the solvent at 5 ml min^{-1} to aid dissolution and prevent local saturation of the solvent. The measurement was repeated at least eight times on each sample.

3.3.4 Differential Scanning Calorimetry

Differential scanning calorimetry (DSC) measurements were performed in a Setaram LabSYS Evo calorimeter. The temperature and enthalpy calibration of the instrument was performed by measuring the temperature (T_m) and heat (ΔH_m) of melting of the following metals: Pb (T_m = 327.47 °C, ΔH_m = 23.00 J g^{-1}), Zn (T_m = 419.56 °C, ΔH_m = 107.4 J g^{-1}), Al (T_m = 660.33 °C, ΔH_m = 401.3 J g^{-1}), Ag (T_m = 961.78 °C, ΔH_m = 104.8 J g^{-1}), and Au (T_m = 1064.18 °C, ΔH_m = 64.5 J g^{-1}). In each measurement, ~50 mg of the YbOF-mon sample was pressed into a pellet, placed in a Pt crucible with a lid, and an empty Pt crucible with a lid was used as the reference. The heating was performed from 30 to 900 °C at a rate of 5 °C min^{-1}. After keeping at 900 °C for 1 h, the cooling was performed at different rates from 2.5 to 50 °C min^{-1}. All experiments were conducted under an inert atmosphere by flowing with 20 ml min^{-1} Ar. The empty Pt crucible is measured in the same conditions for the blank experiment subtraction to reduce the influence of unavoidable asymmetries. The peak onset temperatures observed on heating were considered as the transition temperature (T_{tr}), and the peak areas were integrated as enthalpies of phase transitions (ΔH_{tr}). The result is based on the average value of three measurements.

3.4 Results

As shown in Figure 3.1, there are three crystal structures for stoichiometric REOF. The rhombohedral and the monoclinic structure are the low temperature phase for light (La–Er and Y) and heavy (Tm, Yb, and Lu) RE elements, respectively, and can be considered originating from the cubic structure for the high temperature phase of REOF. The rhombohedral structure (Figure 3.1a) is also called the β phase, in which oxygen and fluorine anions are distributed in alternating layers along the z axis, and RE cations lie between two triangular pyramids consisting of O and F anions, respectively. Each RE^{3+} is eightfold coordinated to four O^{2-} and four F^{-} in a distorted cube. In the monoclinic structure (Figure 2.1b), each RE cation has sevenfold coordination in a REF_3O_4 polyhedron instead of eightfold coordination for larger RE cations in the rhombohedral structure. This monoclinic structure is also known as baddeleyite (α-ZrO_2). As a mixed-anion compound, the cationic sublattice distortion from the fluorite structure is accompanied by shorter RE–O distance than RE–F distance to balance the charge difference of the anions rather than to balance the valence bond deficiency in ZrO_2.[21] A similar position shift of cations, that is, RE ions are closer to O plane nets and further from F plane nets, also exists in the rhombohedral structure of REOF. Although O^{2-} and F^{-} are shown as randomly distributed on the anion sublattice in the cubic structure (Figure 2.1c), some thermodynamic studies imply that this fluorite-like structure is made up of random REO_4F_4 polyhedra.[18]

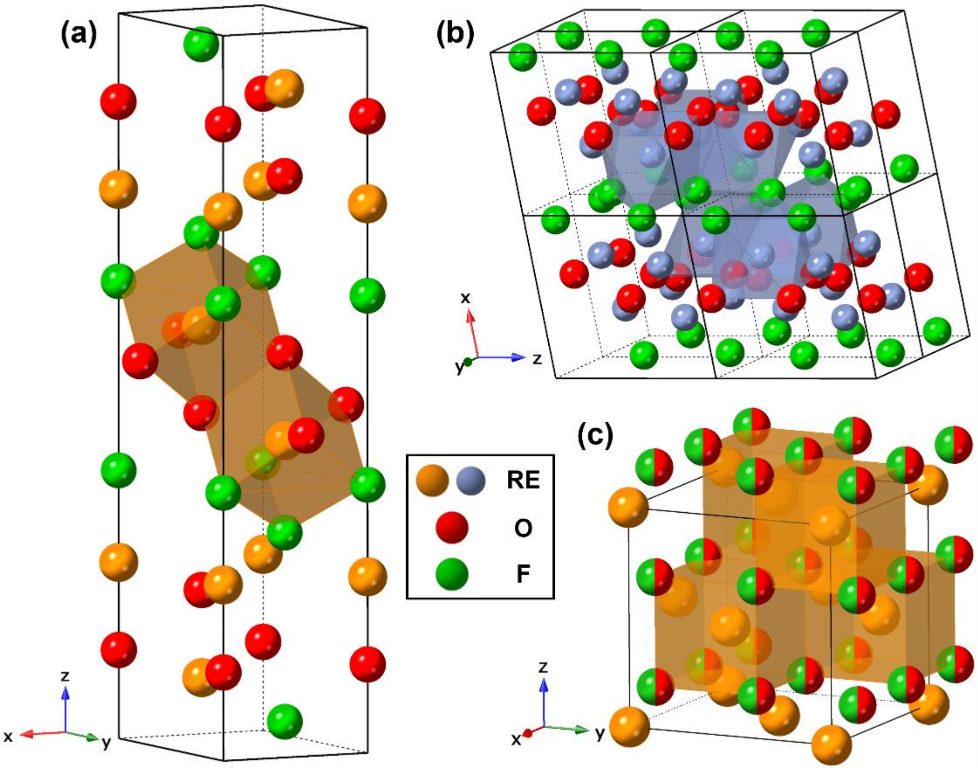

Figure 3.1 The crystal structure of REOF with the (a) rhombohedral (β phase), (b) monoclinic, and (c) cubic (α phase) structures, in which the last three lanthanide elements (Tm, Yb, and Lu) are represented by pastel blue balls in the monoclinic structure.

To obtain the stochiometric RE oxyfluorides (REOF) without composition variations, all samples were prepared by solid-state reactions between RE sesquioxides (RE_2O_3) and RE trifluorides (REF_3). All starting materials were checked by PXRD, which shows that light and heavy RE elements have different structures for their oxides (Figures 3.2) and fluorides (Figures 3.3). The sesquioxides, La_2O_3 and Nd_2O_3 adopt the A-type structure (space group: P$\bar{3}$m1) compared to the C-type structure (space group: Ia$\bar{3}$) for Gd_2O_3, Ho_2O_3, Y_2O_3, and Yb_2O_3. LaF_3 and NdF_3 have the "LaF_3" structure (space group: P$\bar{3}$c1) compared to the "YF_3" structure (space group: Pnma) for the rest of RE fluorides. These structure differences are consistent with the previous thermodynamic studies of RE oxide and fluoride compounds.[26,27]

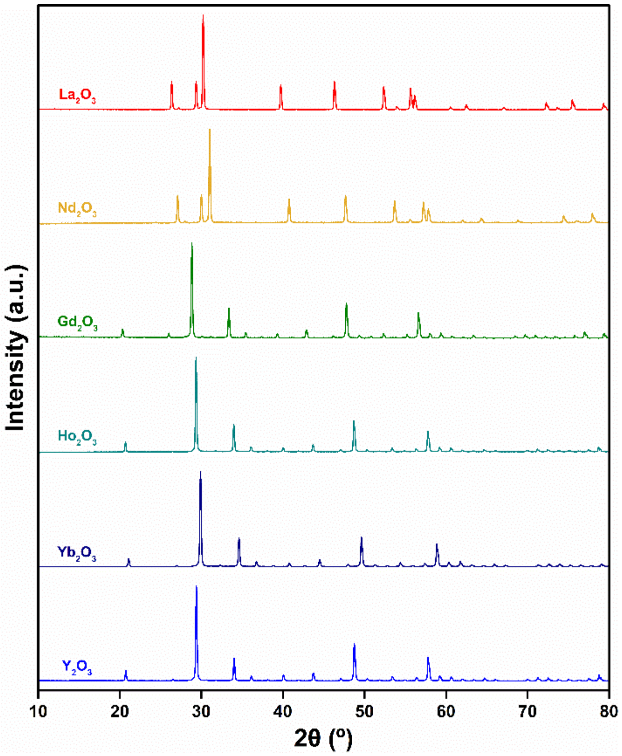

Figure 3.2 PXRD patterns of RE$_2$O$_3$.

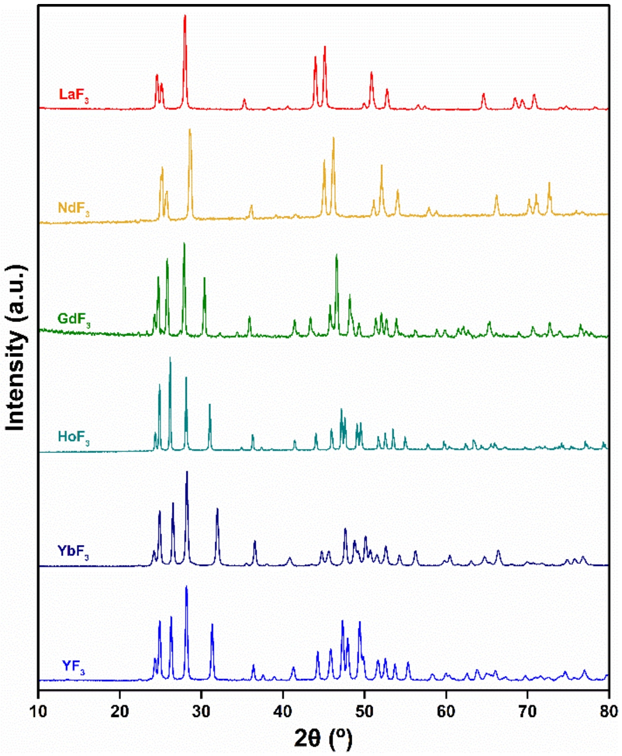

Figure 3.3 PXRD patterns of REF$_3$.

According to PXRD characterizations (Figure 3.4), except for YbOF, all REOF samples show the rhombohedral structure (β phase). Rietveld analysis of the PXRD patterns (Tables 3.1 and 3.2, Figure A.1–A.5) shows that the lattice parameters decrease from light to heavy RE elements when ionic size of RE^{3+} also diminishes.

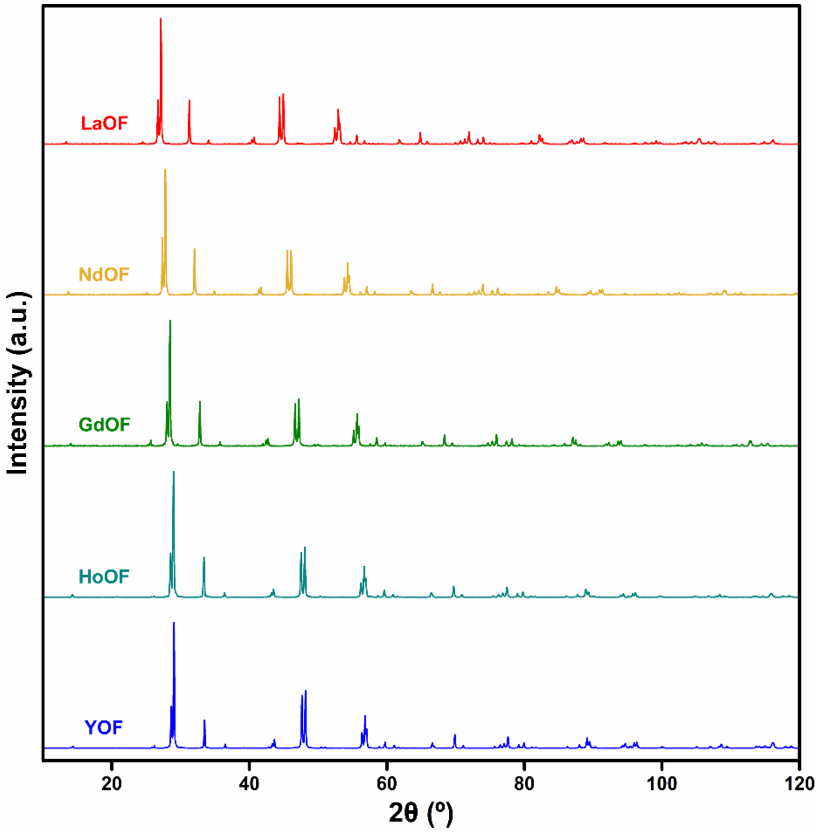

Figure 3.4 PXRD patterns of REOF in the rhombohedral structure (β phase).

Table 3.1 Lattice parameters of REOF in the space group of $R\bar{3}m$ (Z = 6) obtained from Rietveld refinements of PXRD patterns.

Sample	a (Å)	c (Å)	V (Å^3)	R	wR	GOF
LaOF	4.0521(1)	20.2109(3)	287.40(1)	2.68%	4.88%	2.34
NdOF	3.95484(5)	19.7111(2)	266.993(4)	3.88%	3.29%	2.37
GdOF	3.8680(1)	19.2693(4)	249.67(1)	2.86%	7.34%	2.12
HoOF	3.80358(9)	18.9354(3)	237.241(9)	2.20%	3.34%	2.79
YOF	3.79814(7)	18.8861(2)	235.947(7)	2.08%	5.58%	3.57

Table 3.2 Atomic coordinates and isotropic displacement parameters in REOF.

Sample	Atom	Wyckoff	x	y	z	SOF	U_{iso}
LaOF	La	6c	0	0	0.24237	1	0.01
	O	6c	0	0	0.36833	1	0.01
	F	6c	0	0	0.11903	1	0.01
NdOF	Nd	6c	0	0	0.24194	1	0.01
	O	6c	0	0	0.11429	1	0.01
	F	6c	0	0	0.37373	1	0.01
GdOF	Gd	6c	0	0	0.74191	1	0.01
	O	6c	0	0	0.61851	1	0.01
	F	6c	0	0	0.86856	1	0.01
HoOF	Ho	6c	0	0	0.74172	1	0.01
	O	6c	0	0	0.61912	1	0.01
	F	6c	0	0	0.86975	1	0.01
YOF	Y	6c	0	0	0.74174	1	0.01
	O	6c	0	0	0.61990	1	0.01
	F	6c	0	0	0.86920	1	0.01

As shown in Figure 3.5, three YbOF samples were prepared by solid-state reactions and the phases of the products formed appear to mainly depend on the cooling processes. A mixture of the monoclinic and rhombohedral phases (YbOF-mon/rhd) was obtained when the sample was cooled slowly to room temperature at ~1 °C min^{-1}. The amount of the rhombohedral phase decreases as cooling time increases, and a sample with nearly pure monoclinic phase (YbOF-mon) was acquired after a week of stepwise cooling. On the other hand, a mixture of rhombohedral and another phase(s) (possibly cubic and/or defect cubic) was formed when the sample was quickly quenched from 950°C in several minutes. Except for YbOF-mon with the monoclinic phase, extra peaks were detected in the XRD patterns compared to the ideal rhombohedral or cubic structure, which is possibly associated with defect structures and lower symmetry during fast quenching and phase transitions.[4]

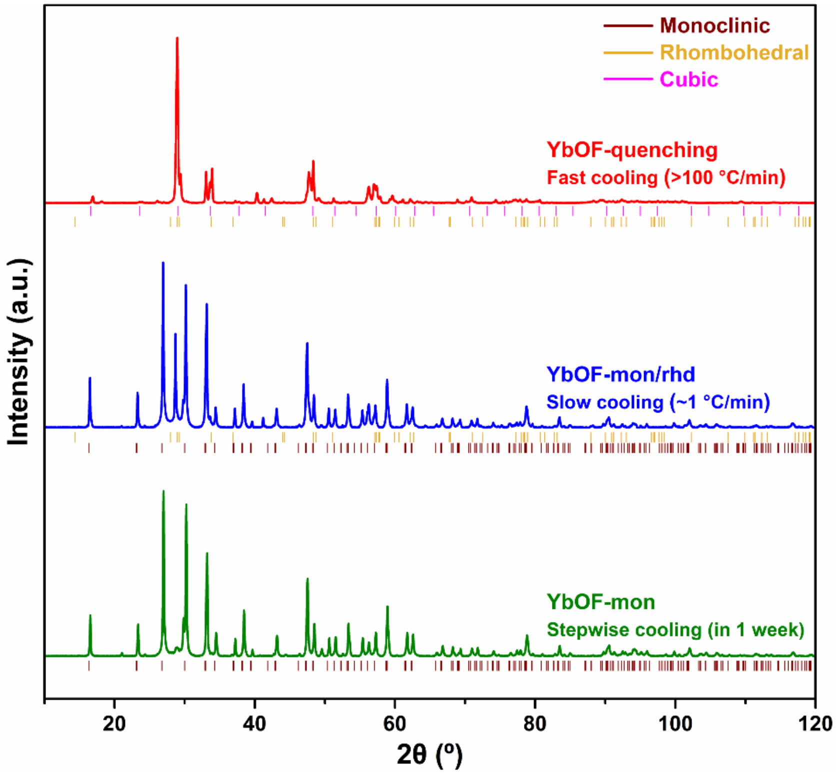

Figure 3.5 PXRD patterns of YbOF samples from different cooling processes.

Table 3.3 Drop solution enthalpies (ΔH_{ds}) in molten $3Na_2O\cdot4MoO_3$ at 800 °C and enthalpies of formation from elements ($\Delta H^\circ_{f,\,el}$) at 25 °C of binary rare earth oxides and fluorides.

Element	$\Delta H_{ds}(RE_2O_3)$ (kJ mol^{-1})	$\Delta H_{ds}(REF_3)$ (kJ mol^{-1})	$\Delta H^\circ_{f,\,el}(RE_2O_3)$ (kJ mol^{-1})	$\Delta H^\circ_{f,\,el}(REF_3)$ (kJ mol^{-1})
La	−221.81 ± 2.25 [32]	154.89 ± 0.58 [27]	−1791.6 ± 2.0 [33]	−1731.8 ± 5.0 [34]
Nd	−156.95 ± 1.05 [35]	151.02 ± 1.32 [27]	−1806.9 ± 3.0 [33]	−1712.9 ± 4.2 [34]
Gd	−134.48 ± 1.70 [35]	145.72 ± 0.66 [27]	−1819.7 ± 3.6 [33]	−1713.3 ± 4.6 [34]
Ho	−109.51 ± 1.50 [35]	140.89 ± 0.72 [27]	−1883.3 ± 8.2 [33]	−1714.2 ± 6.3 [34]
Y	−116.34 ± 1.21 [35]	146.69 ± 0.56 [27]	−1932.8 ± 5.2 [36]	−1718.4 ± 3.3 [34]
Yb	−90.71 ± 0.40 [37]	126.94 ± 0.51 [27]	−1814.5 ± 6.0 [33]	−1656.9 ± 10.0[a] [34]

The enthalpies of formation of REOF were determined by high temperature oxide melt solution calorimetry. Samples were dropped in molten sodium molybdate ($3Na_2O\cdot4MoO_3$) at

800 °C to measure their drop solution enthalpies (ΔH_{ds}). The ΔH_{ds} values for RE_2O_3 and REF_3 are listed in Table 3.3 with their enthalpies of formation from elements ($\Delta H^\circ_{f,\,el}$). For REOF, their ΔH_{ds} values are shown in Table 3.4 with the enthalpies of formation from oxides and fluorides ($\Delta H^\circ_{f,\,ox/fl}$) or from elements ($\Delta H^\circ_{f,\,el}$) calculated from thermodynamic cycles in Table 3.5.

Table 3.4 Drop solution enthalpies (ΔH_{ds}), enthalpies of formation from oxides and fluorides ($\Delta H^\circ_{f,\,ox/fl}$) and from elements ($\Delta H^\circ_{f,\,el}$) of REOF.

Sample	ΔH_{ds} (kJ mol^{-1})	$\Delta H^\circ_{f,\,ox/fl}$ (kJ mol^{-1})	$\Delta H^\circ_{f,\,el}$ (kJ mol^{-1})
LaOF	14.25 ± 0.37 (8)	−36.56 ± 0.86	−1211.0 ± 2.0
NdOF	26.48 ± 0.45 (8)	−28.46 ± 0.72	−1201.7 ± 1.9
GdOF	26.89 ± 0.25 (8)	−23.14 ± 0.66	−1200.8 ± 2.1
HoOF	29.99 ± 0.25 (8)	−19.53 ± 0.61	−1218.7 ± 3.5
YOF	27.87 ± 0.37 (8)	−17.75 ± 0.58	−1234.8 ± 2.1
YbOF-mon	26.87 ± 0.29 (8)	−14.79 ± 0.36	−1171.9 ± 3.9

Table 3.5 Thermodynamic cycles to calculate enthalpies of formation from oxides and fluorides or elements for REOF.

Reaction	ΔH
REOF (s, 25 °C) → 1/3RE_2O_3 (soln, 800 °C) + 1/3REF_3 (soln, 800 °C)	$\Delta H_1 = \Delta H_{ds}(REOF)$
RE_2O_3 (s, 25 °C) → RE_2O_3 (soln, 800 °C)	$\Delta H_2 = \Delta H_{ds}(RE_2O_3)$
REF_3 (s, 25 °C) → REF_3 (soln, 800 °C)	$\Delta H_3 = \Delta H_{ds}(REF_3)$
1/3RE_2O_3 (s, 25 °C) + 1/3REF_3 (s, 25 °C) → REOF (s, 25 °C) $\Delta H^\circ_{f,\,ox/fl}(REOF) = -\Delta H_1 + 1/3\Delta H_2 + 1/3\Delta H_3$	$\Delta H^\circ_{f,\,ox/fl}(REOF)$
2RE (s, 25 °C) + 3/2O_2 (g, 25 °C) → RE_2O_3 (s, 25 °C)	$\Delta H_4 = \Delta H^\circ_{f,el}(RE_2O_3)$
RE (s, 25 °C) + 3/2F_2 (g, 25 °C) → REF_3 (s, 25 °C)	$\Delta H_5 = \Delta H^\circ_{f,el}(REF_3)$
RE (s, 25 °C) + 1/2O_2 (g, 25 °C) + 1/2F_2 (g, 25 °C) → REOF (s, 25 °C) $\Delta H^\circ_{f,el}(REOF) = \Delta H^\circ_{f,\,ox/fl}(REOF) + 1/3\Delta H_4 + 1/3\Delta H_5$	$\Delta H^\circ_{f,el}(REOF)$

As shown in Figure 3.6, $\Delta H°_{f,\ ox/fl}$ values of REOF become less exothermic for smaller RE ions, ranging from −36.6 (LaOF) to −14.8 (YbOF-mon) kJ mol^{-1}. These significantly exothermic values confirm thermodynamic stability for these oxyfluorides relative to oxides plus fluorides.

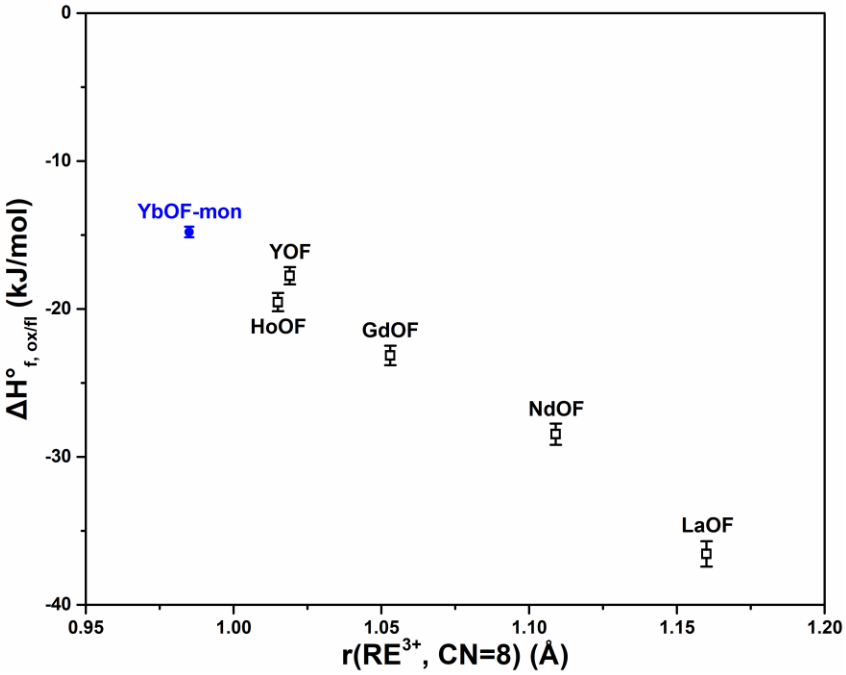

Figure 3.6 Enthalpies of formation from oxides and fluorides ($\Delta H°_{f,\ ox/fl}$) of REOF versus ionic radii of RE^{3+} in 8 coordination. Except for YbOF in the monoclinic structure, all REOF samples are in the rhombohedral structure.

The phase transitions of YbOF driven by temperature were studied by DSC. As demonstrated in Figure 3.7, when YbOF-mon is heated with a rate of 5 °C min^{-1}, an endothermic peak (onset temperature: 715°C) shows up with a shoulder at higher temperature (peak temperature: 740°C) in the DSC curve. The transition enthalpy (ΔH_{tr}) is 7539 ± 146 J mol^{-1} by integrating the peak area. After heating to 900°C and keeping for 1 h, cooling processes with rates ranging from 2.5 to 50 °C min^{-1} were monitored by DSC measurements and the obtained samples were checked by PXRD (Figure 3.8). At a cooling rate of 2.5 °C min^{-1}, there is a sharp exothermic peak along with a relatively wide exothermic peak as the side peak, leading to a mixture of monoclinic and rhombohedral phases. When the cooling rate increases, the first exothermic peak becomes broader while the second peak moves to lower temperature and shrinks. The content of the monoclinic phase decreases with the increasing of cooling rates. Finally, at the cooling rate of 50 °C min^{-1}, there is a broad exothermic peak from 650 to 500°C with a little exothermic peak afterward in the DSC profile, and the monoclinic phase disappears in the XRD pattern.

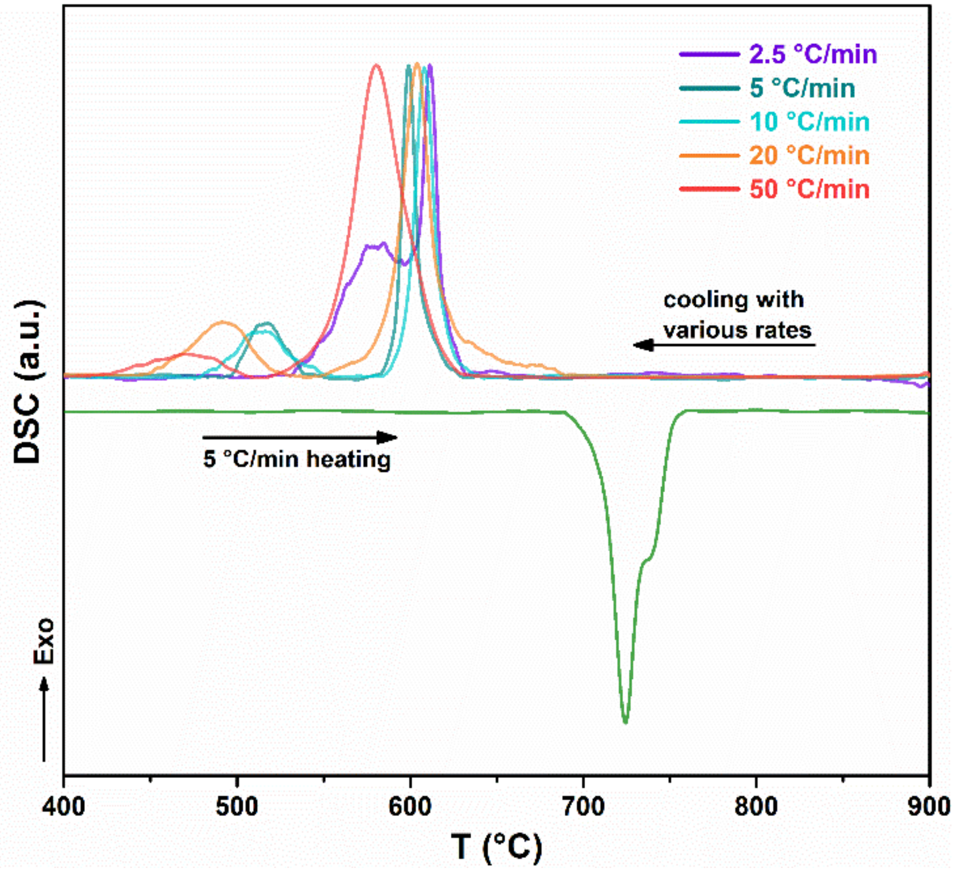

Figure 3.7 Normalized DSC curves of YbOF-mon with 5 °C min^{-1} heating rate and different cooling rates.

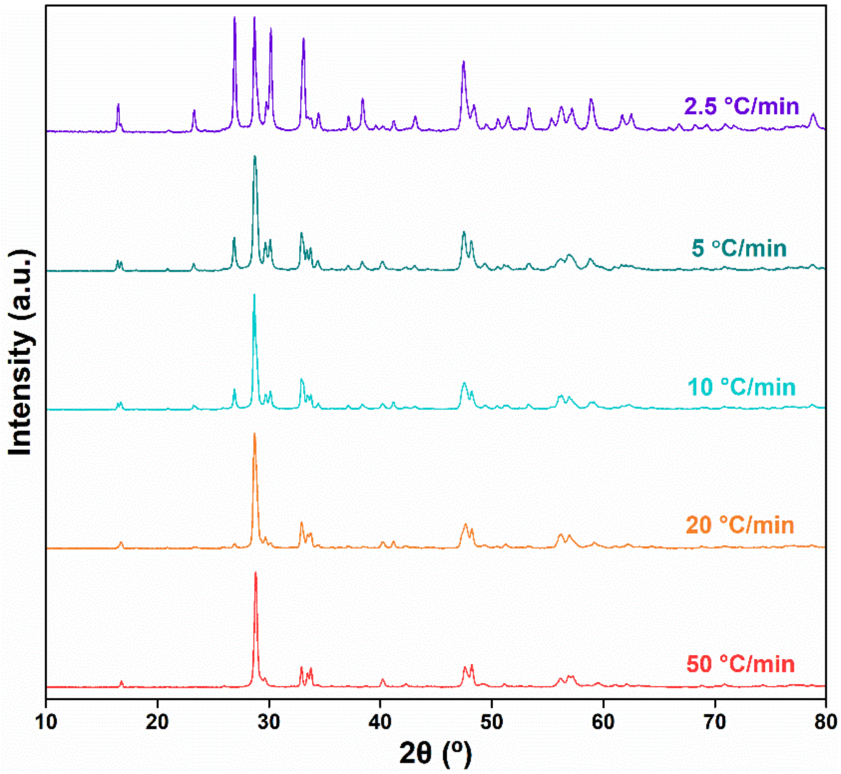

Figure 3.8 PXRD patterns of YbOF samples obtained from different cooling rates.

3.5 Discussion

Different from RE ternary oxides or fluorides containing various metal cations, REOF phases have the anion sublattice with half O^{2-} and half F^{-}, so the energies of REOF mainly come from the two cation–anion interactions between RE^{3+} and O^{2-} or F^{-}. Because O^{2-} possesses twice the charge of F^{-}, its electrostatic potential with RE^{3+} is double that of F^{-} at the same cation–anion distance, which is the main contribution to the lattice energies of REOF. By constructing Born–Haber cycles, lattice energies (U) of RE_2O_3, REF_3, and REOF are calculated from $\Delta H°_{f,\,el}$ (Tables 3.6–3.8). Although all of them become more exothermic when the ionic size of RE^{3+} decreases and the lattice contracts, the lattice energy differences for the formation of REOF from RE_2O_3 and REF_3 (U_D) become less exothermic from light to heavy rare earth elements (Figure 3.9), owing to the larger slope of U versus the ionic radius of RE^{3+} for RE_2O_3 than for REF_3 (see

Figure 3.9). Therefore, the trend of $\Delta H^{\circ}_{f,\,ox/fl}$ is more like enthalpies of formation from binary oxides ($\Delta H^{\circ}_{f,\,ox}$) for most ternary RE oxide compounds[26] than enthalpies of formation from binary fluorides ($\Delta H^{\circ}_{f,\,fl}$) for ternary RE fluoride compounds,[27] which is related to the increasing coordination of RE^{3+} from RE_2O_3 to REOF.

Table 3.6 Summary of reactions in Born–Haber cycles for the formation of REOF and RE_2O_3.

Reaction	ΔH (kJ mol^{-1})
RE (s, 25 °C) → RE (g, 25 °C)	$\Delta H_1 = \Delta H_{sub}$
RE (g, 25 °C) → RE^{3+} (g, 25 °C) + $3e^{-}$	$\Delta H_2 = (I_1+I_2+I_3)$
O_2 (g, 25 °C) → 2O (g, 25 °C)	$\Delta H_3 = 498.458 \pm 0.004$ [38]
O (g, 25 °C) + $2e^{-}$ → O^{2-} (g, 25 °C)	$\Delta H_4 = 703$ [39]
F_2 (g, 25 °C) → 2F (g, 25 °C)	$\Delta H_5 = 158.670 \pm 0.096$ [38]
F (g, 25 °C) + e^{-} → F^{-} (g, 25 °C)	$\Delta H_6 = -328.164$ [38]
RE (s, 25 °C) + $1/2O_2$ (g, 25 °C) + $1/2F_2$ (g, 25 °C) → REOF (s, 25 °C)	$\Delta H_7 = \Delta H^{\circ}_{f,\,el}$(REOF)
RE^{3+}(g, 25 °C) + O^{2-} (g, 25 °C) + F^{-} (g, 25 °C) → REOF (s, 25 °C)	U(REOF)
U(REOF) = $\Delta H_7 - \Delta H_1 - \Delta H_2 - 1/2\Delta H_3 - \Delta H_4 - 1/2\Delta H_5 - \Delta H_6$	
RE (s, 25 °C) → RE (g, 25 °C)	$\Delta H_1 = \Delta H_{sub}$
RE (g, 25 °C) → RE^{3+} (g, 25 °C) + $3e^{-}$	$\Delta H_2 = (I_1+I_2+I_3)$
O_2 (g, 25 °C) → 2O (g, 25 °C)	$\Delta H_3 = 498.458 \pm 0.004$ [38]
O (g, 25 °C) + $2e^{-}$ → O^{2-} (g, 25 °C)	$\Delta H_4 = 703$ [39]
2RE (s, 25 °C) + $3/2O_2$ (g, 25 °C) → RE_2O_3 (s, 25 °C)	$\Delta H_8 = \Delta H^{\circ}_{f,\,el}(RE_2O_3)$
$2RE^{3+}$(g, 25 °C) + $3O^{-}$ (g, 25 °C) → RE_2O_3 (s, 25 °C)	$U(RE_2O_3)$
$U(RE_2O_3) = \Delta H_8 - 2\Delta H_1 - 2\Delta H_2 - 3/2\Delta H_3 - 3\Delta H_4$	

Table 3.7 Enthalpies of sublimation (ΔH_{sub}) and ionization ($I_1+I_2+I_3$) of rare earth elements.

Element	ΔH_{sub} (kJ mol^{-1})	$(I_1+I_2+I_3)$ (kJ mol^{-1})
La	434.5 ± 3.0 [40]	3455 ± 5 [41]
Nd	325.6 ± 2.0 [40]	3694 ± 5 [41]
Gd	406.9 ± 2.0 [40]	3750 ± 5 [41]
Ho	305.5 ± 5.0 [40]	3924 ± 5 [41]
Y	421.3 ± 5.0 [42]	3777 ± 5 [41]
Yb	152.4 ± 1.0 [40]	4194 ± 5 [41]

Table 3.8 Lattice energies (U) of RE_2O_3, REF_3 and REOF calculated from Born–Haber cycles.

Element	U(RE_2O_3) (kJ mol^{-1})	U(REF_3) (kJ mol^{-1})	U(REOF) (kJ mol^{-1})
La	–12427.3 ± 11.8	–4874.8 ± 7.7 [27]	–5803.9 ± 6.2
Nd	–12702.8 ± 11.2	–4986.0 ± 6.8 [27]	–5924.7 ± 5.7
Gd	–12990.2 ± 11.4	–5123.7 ± 7.1 [27]	–6061.1 ± 5.8
Ho	–13199.0 ± 16.3	–5197.2 ± 9.5 [27]	–6151.6 ± 7.9
Y	–13186.1 ± 15.1	–5170.2 ± 7.8 [27]	–6136.5 ± 7.4
Yb	–13364.0 ± 11.8	–5256.8 ± 11.2 [27]	–6221.7 ± 6.4

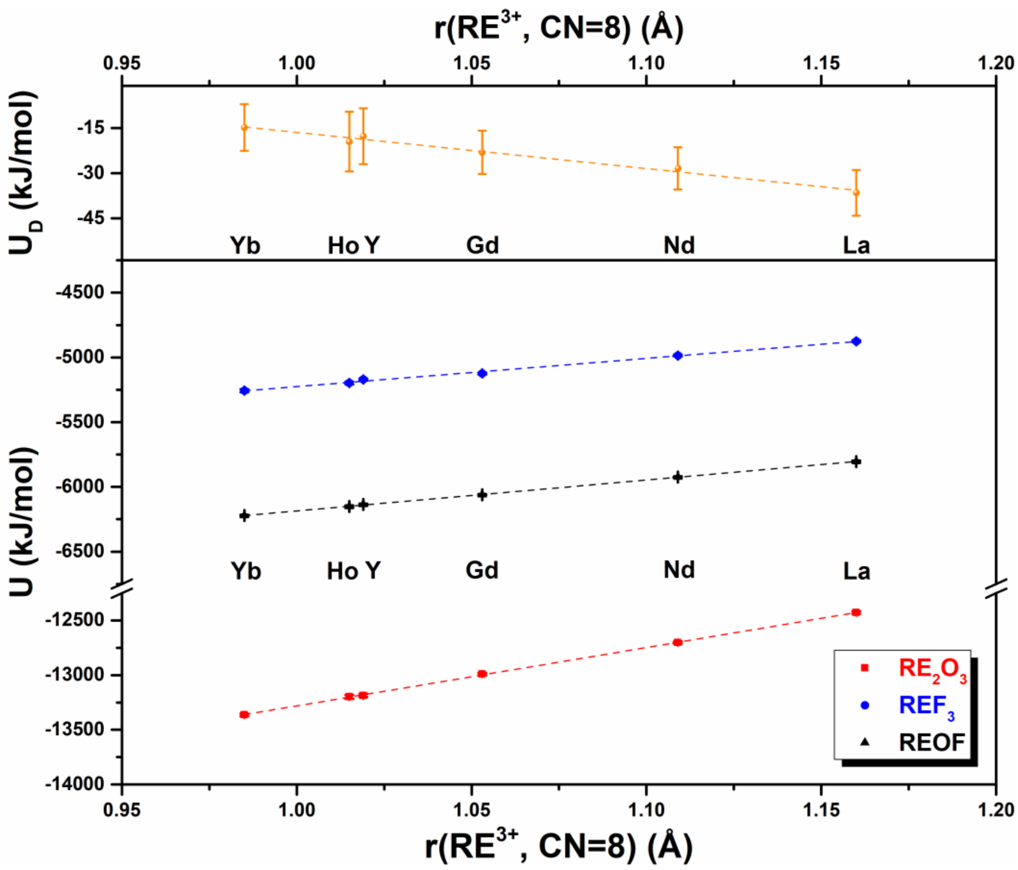

Figure 3.9 Lattice energies (U) of RE_2O_3, REF_3 and REOF with differences for the formation of REOF from RE_2O_3 and REF_3 (U_D = U(REOF) – U(RE_2O_3)/3 – U(REF_3)/3) versus ionic radius of RE^{3+}.

With RE ions shrinking in size, not only thermodynamic stability but also lattice parameters of REOF decrease from light to heavy RE elements. When reaching the small cations (i.e., Tm, Yb, and Lu), the monoclinic instead of the rhombohedral phase becomes the room temperature stable phase for their stoichiometric REOF compounds. Similar "phase transitions" driven by ionic size have been observed in many RE compound systems, like A-type → C-type for RE_2O_3 and "LaF_3" structure → "YF_3" structure for REF3 as ionic radius of RE^{3+} decreases. Along with these "phase transitions," generally, light RE ions have higher coordination than heavy RE ions resulting from their relatively large ionic size. The decrease of the coordination number of Yb^{3+} from 8 to 7 may explain the relative stability of the monoclinic structure compared with the rhombohedral structure considering its relatively small ionic radius. This is also supported by the trend of $\Delta H°_{f,\ ox/fl}$, which becomes less exothermic from large to small RE ions. The structural and energetic instability makes the rhombohedral phase the metastable phase in the stoichiometric YbOF system.

Considering that most REOF (RE = La–Er and Y) have the rhombohedral−cubic phase transition driven by temperature,[13,15] it is reasonable to assume that YbOF has a cubic structure as the high-temperature phase as well. Based on the ΔH_{tr} (7539 ± 146 J mol^{-1}) and the transition temperature (T_{tr} = 715°C), the transition entropy (ΔS_{tr}) of YbOF-mon is 7.63 ± 0.15 J mol^{-1} K^{-1}, which is comparable to the corresponding ΔS_{tr} of the rhombohedral−cubic phase transition for other REOF.[18] This value is also close to the configurational entropy of α-REOF as 8.83 J mol^{-1} K^{-1} in accordance with the disordered structure composed of random REO_4F_4 polyhedra. But the undercooling of transitions is over 50°C for YbOF at the scanning rate of 5°C min^{-1}, indicating the high activation energy for this transition. The slow kinetics of monoclinic−cubic transformation is also corroborated by incomplete transitions back to the monoclinic phase and the appearance of the metastable rhombohedral phase during fast cooling. Bond valence sum calculations show that there is considerable bond strain in the cubic phase, which can be relieved in the rhombohedral phase and results in the fast nonquenchable kinetics of the order−disorder phase transition for YOF.[17] Therefore, although the rhombohedral phase of YbOF is metastable in energetics, its formation is favored by kinetics and hard to be avoided in fast cooling processes.

3.6 Conclusions

Thermodynamic stabilities of stoichiometric REOF with varying RE elements have been determined by high temperature oxide melt solution calorimetry. The exothermic formation enthalpies of REOF confirm their energetic stabilities relative to the mixture of RE_2O_3 and REF_3. Enthalpies of formation become less exothermic with the decrease of the ionic size of RE^{3+}, reflecting that the RE–O interactions dominate in the energetics of REOF. Compared to the rhombohedral structure for most REOF (RE = La–Er and Y), the monoclinic phase is favored as the low temperature stable phase for small RE ions (Tm, Yb, and Lu) with lower coordination. However, the slow monoclinic−cubic transition can easily lead to the formation of the rhombohedral phase, especially after fast cooling.

3.7 Acknowledgements

We thank US Department of Energy Critical Materials Institute (CMI) Hub for financial support of this research (grant number DE-AC02-07CH11358). We acknowledge the use of facilities within the Eyring Materials Center at Arizona State University supported in part by NNCI-ECCS-2025490 and thank David Wright and Tamilarasan Subramani for help in sample preparation.

3.8 References

(1) Du, Y.-P.; Zhang, Y.-W.; Sun, L.-D.; Yan, C.-H. Luminescent monodisperse nanocrystals of lanthanide oxyfluorides synthesized from trifluoroacetate precursors in high-boiling solvents. *J. Phys. Chem. C* **2008**, *112*, 405–415.

(2) Armelao, L.; Bottaro, G.; Bovo, L.; Maccato, C.; Pascolini, M.; Sada, C.; Soini, E.; Tondello, E. Luminescent properties of Eu-doped lanthanum oxyfluoride sol−gel thin films. *J. Phys. Chem. C* **2009**, *113*, 14429–14434.

(3) Wen, T.; Luo, W.; Wang, Y.; Zhang, M.; Guo, Y.; Yuan, J.; Ju, J.; Wang, Y.; Liao, F.; Yang, B. Multicolour and up-conversion fluorescence of lanthanide doped Vernier phase yttrium oxyfluoride nanocrystals. *J. Mater. Chem. C* **2013**, *1*, 1995–2001.

(4) Wen, T.; Zhou, Y.; Guo, Y.; Zhao, C.;, Yang, B.; Wang, Y. Color-tunable and single-band red upconversion luminescence from rare-earth doped Vernier phase ytterbium oxyfluoride nanoparticles. *J. Mater. Chem. C* **2016**, *4*, 684–690.

(5) Fergus, J. W.; Chen, H. P. Structure and conductivity of tetragonal and rhombohedral lanthanum oxyfluoride compounds. *J. Electrochem. Soc.* **2000**, *147*, 4696–4704.

(6) Jacob, K. T.; Saji, V. S.; Waseda, Y. Lanthanum oxyfluoride: structure, stability, and ionic conductivity. *Int. J. Appl. Ceram. Technol.* **2006**, *3*, 312–321.

(7) de Pablos-Martín, A.; Durán, A.; Pascual, M. J. Nanocrystallisation in oxyfluoride systems: mechanisms of crystallisation and photonic properties. *Int. Mater. Rev.* **2012**, *57*, 165–186.

(8) Fedorov, P. P.; Luginina, A. A.; Popov, A. I. Transparent oxyfluoride glass ceramics. *J. Fluor. Chem.* **2015**, *172*, 22–50.

(9) Zachariasen, W. Crystal chemical studies of the 5f-series of elements. XIV. Oxyfluorides, XOF. *Acta Crystallogr.* **1951**, *4*, 231–236.

(10) Mann, A. W.; Bevan, D. J. M. The crystal structure of stoichiometric yttrium oxyfluoride, YOF. *Acta Crystallogr. B* **1970**, *26*, 2129–2131.

(11) Niihara, K.; Yajima, S. The crystal structure and nonstoichiometry of rare earth oxyfluoride. *Bull. Chem. Soc. Jpn.* **1971**, *44*, 643–648.

(12) Bevan, D. J. M.; Mohyla, J.; Hoskins, B. F.; Steen, R. J. The crystal structures of some Vernier phases in the yttrium oxide-fluoride system. *Eur. J. Solid State Inorg. Chem.* **1990**, *27*, 451–465.

(13) Müller, J. H.; Petzel, T. High-temperature X-ray diffraction study of the rhombohedral-cubic phase transition of ROF with R = Y, La, Pr, Nd, Sm–Er. *J. Alloys Compd.* **1995**, *224*, 18–21.

(14) Fergus, J. W. Crystal chemistry of neodymium oxyfluoride. *Mater. Res. Bull.* **1996**, *31*, 1317–1323.

(15) Achary, S. N.; Ambekar, B. R.; Mathews, M. D.; Tyagi, A. K.; Moorthy, P. N. Study of phase transition and volume thermal expansion in a rare-earth (RE) oxyfluoride system by high-temperature XRD (RE = La, Nd, Sm, Eu and Gd). *Thermochim. Acta* **1998**, *320*, 239–243.

(16) Beaury, L.; Derouet, J.; Hölsä, J.; Lastusaari, M.; Rodriguez-Carvajal, J. Neutron powder diffraction studies of stoichiometric NdOF between 1.5 and 300 K. *Solid State Sci.* **2002**, *4*, 1039–1043.

(17) Levin, I.; Huang, Q. Z.; Cook, L. P.; Wong-Ng, W. Nonquenchable chemical order−disorder phase transition in yttrium oxyfluoride. *Eur. J. Inorg. Chem.* **2005**, *2005*, 87–91.

(18) Petzel, T.; Marx, V.; Hormann, B. Thermodynamics of the rhombohedral-cubic phase transition of ROF with R ≡ Y, La, Pr, Nd, Sm–Er. *J. Alloys Compd.* **1993**, *200*, 27–31.

(19) Hölsä, J.; Piriou, B.; Räsänen, M. IR- and Raman-active normal vibrations of rare earth oxyfluorides, REOF; RE = Y, La, and Gd. *Spectrochim. Acta A.* **1993**, *49*, 465–470.

(20) Dabachi, J.; Body, M.; Dittmer, J.; Fayon, F.; Legein, C. Structural refinement of the RT LaOF phases by coupling powder X-Ray diffraction, ^{19}F and ^{139}La solid state NMR and DFT calculations of the NMR parameters. *Dalton Trans.* **2015**, *44*, 20675–20684.

(21) Taoudi, A.; Laval, J. P.; Frit, B. Synthesis and crystal structure of three new rare earth oxyfluorides related to baddeleyite [LnOF; Ln = Tm,Yb,Lu]. *Mater. Res. Bull.* **1994**, *29*, 1137–1147.

(22) Baenziger, N. C.; Holden, J. R.; Knudson, G. E.; Popov, A. I. Unit cell dimensions of some rare earth oxyfluorides. *J. Am. Chem. Soc.* **1954**, *76*, 4734–4735.

(23) Lee, J.; Zhang, Q.; Saito, F. Synthesis of nano-sized lanthanum oxyfluoride powders by mechanochemical processing. *J. Alloys Compd.* **2003**, *348*, 214–219.

(24) Dutton, S. E.; Hirai, D.; Cava, R. J. Low temperature synthesis of LnOF rare-earth oxyfluorides through reaction of the oxides with PTFE. *Mater. Res. Bull.* **2012**, *47*, 714–718.

(25) Yonezawa, S.; Jae-Ho, K.; Takashima, M. Pyrohydrolysis of rare-earth trifluorides in moist air. *Solid State Sci.* **2002**, *4*, 1481–1485.

(26) Navrotsky, A.; Lee, W.; Mielewczyk-Gryn, A.; Ushakov, S. V.; Anderko, A.; Wu, H.; Riman, R E. Thermodynamics of solid phases containing rare earth oxides. *J. Chem. Thermodyn.* **2015**, *88*, 126–141.

(27) Yang, S.; Anderko, A.; Riman, R. E.; Navrotsky, A. Thermochemistry of sodium rare earth ternary fluorides, $NaREF_4$. *Acta Mater.* **2021**, *220*, 117289.

(28) Toby, B. H.; Von Dreele, R. B. GSAS-II: the genesis of a modern open-source all purpose crystallography software package. *J. Appl. Crystallogr.* **2013**, *46*, 544–549.

(29) Navrotsky, A. Progress and new directions in high temperature calorimetry. *Phys. Chem. Miner.* **1977**, *2*, 89–104.

(30) Navrotsky, A. Progress and new directions in high temperature calorimetry revisited. *Phys. Chem. Miner.* **1997**, *24*, 222–241.

(31) Navrotsky, A. Progress and new directions in calorimetry: a 2014 perspective. *J. Am. Ceram. Soc.* **2014**, *97*, 3349–3359.

(32) Mielewczyk-Gryn, A.; Wachowski, S.; Lilova, K. I.; Guo, X.; Gazda, M.; Navrotsky, A. Influence of antimony substitution on spontaneous strain and thermodynamic stability of lanthanum orthoniobate. *Ceram. Int.* **2015**, *41*, 2128–2133.

(33) Konings, R. J. M.; Beneš, O.; Kovács, A.; Manara, D.; Sedmidubský, D.; Gorokhov, L.; Iorish, V. S.; Yungman, V.; Shenyavskaya, E.; Osina, E. The thermodynamic properties of the f-elements and their compounds. Part 2. The lanthanide and actinide oxides. *J. Phys. Chem. Ref. Data* **2014**, *43*, 013101.

(34) Glushko, V. P. *Thermochemical Constants of Substances.* Academy of Sciences of USSR, 1978.

(35) Mielewczyk-Gryn, A.; Navrotsky, A. Enthalpies of formation of rare earth niobates, RE_3NbO_7. *Am. Mineral.* **2015**, *100*, 1578–1583.

(36) Morss, L. R.; Day, P. P.; Felinto, C.; Brito, H. Standard molar enthalpies of formation of Y_2O_3, Ho_2O_3, and Er_2O_3 at the temperature 298.15 K. *J. Chem. Thermodyn.* **1993**, *25*, 415–422.

(37) Yang, S.; Powell, M.; Kolis, J. W.; Navrotsky, A. Thermochemistry of rare earth oxyhydroxides, REOOH (RE = Eu to Lu). *J. Solid State Chem.* **2020**, *287*, 121344.

(38) Rumble, J. R. *CRC Handbook of Chemistry and Physics*, 101st ed.; CRC Press/Taylor & Francis, 2020.

(39) Atkins, P.; de Paula, J.; Keeler, J. *Atkins' Physical Chemistry*, 11th ed.; Oxford University Press, 2018.

(40) Konings, R. J. M.; Beneš, O. The thermodynamic properties of the f-elements and their compounds. I. The lanthanide and actinide metals. *J. Phys. Chem. Ref. Data* **2010**, *39*, 043102.

(41) Cotton, S. *Lanthanide and Actinide Chemistry*; John Wiley & Sons, 2006.

(42) Morss, L. R. Thermochemical properties of yttrium, lanthanum, and the lanthanide elements and ions. *Chem. Rev.* **1976**, *76*, 827–841.

Chapter 4

Thermochemistry of 3D and 2D Rare Earth Oxychlorides (REOCls)

Shuhao Yang,[†,‡] Andre Anderko,[∥] Richard E. Riman,[§] Alexandra Navrotsky[*,†]

[†]Navrotsky Eyring Center for Materials of the Universe, School of Molecular Sciences, Arizona State University, Tempe, Arizona 85287, United States

[‡]Department of Chemistry, University of California, Davis, California 95616, United States

[∥]OLI Systems, Inc., Parsippany, New Jersey 07054, United States

[§]Department of Materials Science and Engineering, Rutgers, The State University of New Jersey, Piscataway, New Jersey 08854, United States

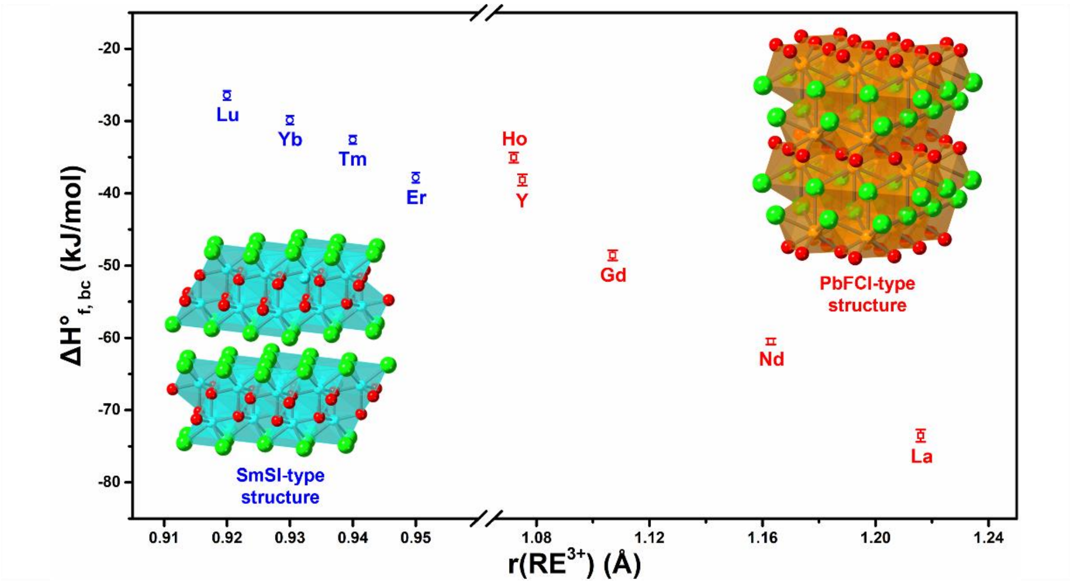

Inorg. Chem. **2022**, DOI: 10.1021/acs.inorgchem.2c00763.

4.1 Abstract

The thermodynamic stability of rare earth (RE) materials plays a key role in the design of separation and recycling processes for RE elements. Thermodynamic stability is fundamentally influenced by the lanthanide contraction, as observed in the systematic reduction of unit cell volumes with increasing atomic number. RE materials are found in the form of solids having primary bonds in three dimensions (3D materials) as well as ones with primary bonds in two dimensions (2D materials) whose layers are held together by weak van der Waals (vdW) forces. While studies of synthesis, structure, and physical properties of 2D RE materials are numerous, no systematic research has compared their thermodynamic stability to that of 3D materials. In the present work, RE oxychlorides (REOCls), which display a structural transition from a 3D-polyhedral network (PbFCl-type) to a vdW-bonded layered one (SmSI-type) as the RE size decreases, were all synthesized by the flux method. High temperature oxide melt solution calorimetry was used to determine their formation enthalpies to enable Born–Haber cycles to calculate lattice energies. Our results indicate that REOCl compounds are thermodynamically stable when compared to their binary oxides and chlorides. The lattice energies of 3D REOCls increase with decreasing RE size yet are insensitive to unit cell volumes for 2D REOCls. This is caused by interatomic interactions parallel and perpendicular to layers in the SmSI-type REOCls, causing a different structure response to the lanthanide contraction than 3D RE materials.

4.2 Introduction

Rare earth oxychlorides (REOCls) have attracted great research interest in recent years owing to potential applications as chloride ion conductors,[1,2] catalysts,[3–5] and luminescent materials.[6–9] As an important component in the RE_2O_3–$RECl_3$ system, REOCl compounds are

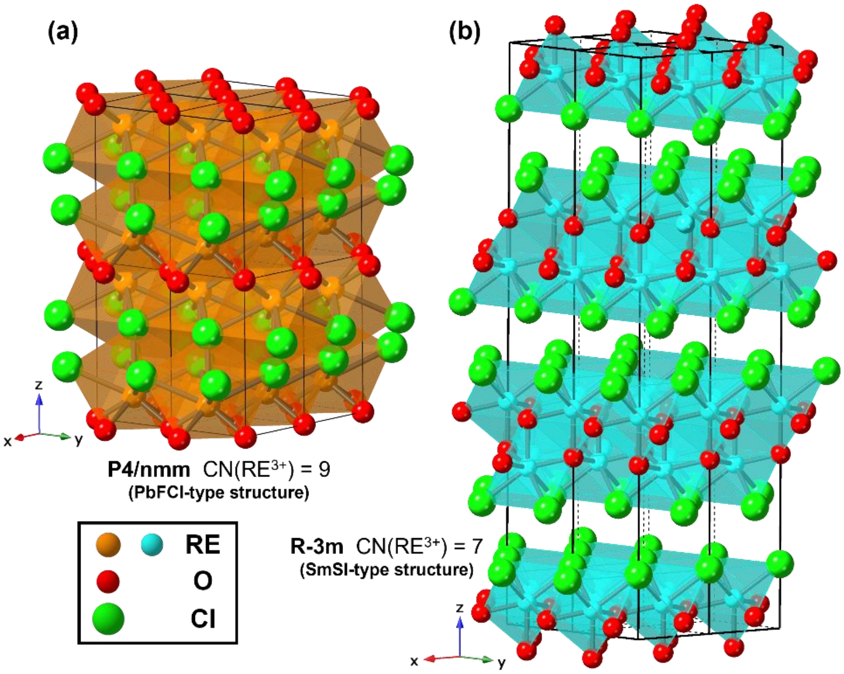

Figure 4.1 Crystal structures of REOCls adopting (a) the PbFCl-type structure and (b) the SmSI-type structure, in which large and small RE elements are indicated in orange or azure, respectively.

critical in the conversion and leaching of RE elements in aqueous solutions, which can be used for the separation and recycling of RE elements.[10,11] Two crystal structures are adopted by REOCls. As shown in Figure 4.1a, the majority of REOCls (RE = La–Ho, and Y) crystallize in a tetragonal PbFCl-type structure (P4/nmm), in which RE^{3+} is coordinated to four O^{2-} and four Cl^{-} in the neighboring layers with another Cl^{-} in the next nearest layer forming a REO_4Cl_5 square antiprism. A rhombohedral SmSI-type structure ($R\bar{3}m$) is favored by REOCls with heavier (smaller) RE ions (Figure 4.1b). Instead of three-dimensional (3D) polyhedral networks, the SmSI-type REOCl has a two-dimensional (2D) structure held together by van der Waals (vdW) forces, where RE^{3+} is coordinated to four O^{2-} and three Cl^{-} in each layer. The size difference of various RE ions enables RE compounds with the same stoichiometry to show diverse crystal structures. In general, coordination numbers decrease with smaller RE ions. For example, stoichiometric RE oxyfluorides (REOFs) have a distorted fluorite structure (rhombohedral) and a monoclinic structure with eightfold or sevenfold coordination for large and small RE, respectively.[12] However, the transition from 3D bulk materials to 2D materials sets REOCls apart from other RE ceramic materials. This transition not only introduces a new family of 2D RE materials with appealing properties[13,14] but also provides an opportunity to investigate the effect of ionic size on the energetics of 2D materials.[15,16]

In contrast to RE oxyfluorides having nonstoichiometric phases, REOCl is the only ternary phase composition in RE(III)–O–Cl systems.[17] Common synthesis methods include thermal decomposition reactions of RE chloride hydrates ($RECl_3 \cdot xH_2O$),[18,19] solid-state reactions between RE_2O_3 and $RECl_3$, and chlorination reactions of RE_2O_3 using NH_4Cl.[20] Some synthetic routes based on solvothermal reactions have also been developed for REOCl nanocrystals.[21,22] Although such methods work well for REOCls with light RE elements, it is more difficult to synthesize REOCl compounds containing heavy RE elements as a single phase. Specifically, HoOCl, YOCl, and ErOCl are reported to be dimorphic[23] and the YOF-type REOCls may form in low-temperature flux reactions.[24,25] It is not clear whether this phase progress arises from either kinetic reasons or a small thermodynamic driving force to form a 2D material. This paper seeks to answer this question.

Thermodynamic properties, especially formation enthalpies, of REOCls have not been studied extensively. The only available data was obtained from reaction or solution calorimetry at room temperature,[26,27] which could have very limited utility. This is because slow dissolution and the lack of precisely controlled reaction conditions could have introduced complexities, making this data less reliable.[28–30] Thermodynamic evaluations have been attempted on REOCl systems to estimate the formation enthalpies, but limited and ambiguous experimental data reduce the reliability of such studies and restrict them to compounds having the PbFCl-type structure.[31–33] In the present work, the formation enthalpies of REOCls were determined from light to heavy RE elements (La, Nd, Gd, Y, and Ho–Lu) by high temperature oxide melt solution calorimetry. This calorimetric technique has been widely employed in oxide compounds and was recently applied to fluoride and oxyfluoride systems.[12,34,35] The methodology was extended and proven to be effective for chloride and oxychloride compounds in this work. Experimental thermodynamic data were used in Born–Haber cycles to calculate the lattice energies of REOCls, shedding light on the effects of RE ionic size on the energetics of 3D and 2D RE materials.

4.3 Experimental Methods

4.3.1 Material Preparation

Rare earth sesquioxides (RE_2O_3) and rare earth trichlorides ($RECl_3$) were used as the starting materials in the flux synthesis. RE_2O_3, including La_2O_3 (99.999%, Aldrich), Nd_2O_3 (99.9%, Apache Chemicals), Gd_2O_3 (99.99%, Aldrich), Ho_2O_3 (99.99%, Alfa Aesar), Y_2O_3 (99.99%, Alfa Aesar), Er_2O_3 (99.9%, Alfa Aesar), Tm_2O_3 (99.99%, Alfa Aesar), Yb_2O_3 (99.99%, Alfa Aesar), and Lu_2O_3 (99.99%, Alfa Aesar), were annealed prior to use at 1000 °C for several hours in air to remove any hydroxide and carbonate impurities. $RECl_3$, including $LaCl_3$ (99.99%, Alfa Aesar), $NdCl_3$ (99.99%, Alfa Aesar), $GdCl_3$ (99.99%, Alfa Aesar), $HoCl_3$ (99.95%, Alfa Aesar), YCl_3 (99.99%, Alfa Aesar), $ErCl_3$ (99.9%, Alfa Aesar), $TmCl_3$ (99.9%, Sigma-Aldrich), $YbCl_3$ (99.99%, Alfa Aesar), and $LuCl_3$ (99.99%, Sigma-Aldrich), were unpacked and stored in a glovebox filled with N_2 (H_2O < 1 ppm) to avoid moisture absorption. NaCl (99.999%, Sigma-Aldrich) was used for solution calorimetry experiments without further purification. All chemicals were checked by powder X-ray diffraction to confirm the phase purity.

Rare earth oxychlorides (REOCls) were prepared by a flux-based method,[36,37] in which $RECl_3$ served as both reactant and flux. The RE_2O_3 and $RECl_3$ mixture in a molar ratio of 1:3 was ground by a mortar and pestle in a glovebox and kept in a covered Pt crucible, which was then placed into a tube furnace and heated at 1050 °C (heating rate: 5 °C min^{-1}) and held for 2 days under a N_2 atmosphere. After cooling to room temperature at 5 °C min^{-1}, the excess $RECl_3$ was washed out with deionized water and the residue was separated by vacuum filtration and oven-dried in air at 120 °C for several hours. The product, crystalline REOCl, was ground into a fine powder and dried at 300 °C under a high vacuum (< 1 mmHg) for 10 h.

4.3.2 Powder X-ray Diffraction

Powder X-ray diffraction (PXRD) patterns were obtained using a Bruker D2 Phaser diffractometer operated with Cu Kα radiation (λ = 1.54184 Å), 1.0 mm air scatter screen, and 0.6 mm divergency slit. The data were collected in the 2θ range of 5–90° with a step size of 0.02° and a dwell time of 5 s per step. $RECl_3$ powders were transferred to an airtight holder inside the glovebox to collect their PXRD patterns. Lattice parameters of REOCls were refined based on peak positions in the PXRD patterns using MDI Jade software.

4.3.3 Raman Spectroscopy

Raman spectra were collected at room temperature on a custom-built Raman spectrometer in a 180° geometry. The sample was excited using a 50 mW diode laser with a wavelength of 633 nm. The laser beam was focused onto the sample using a 50× APO Mitutoyo microscope objective with a numerical aperture of 0.42. The signal was isolated from the laser excitation source using a Kaiser laser band-pass filter combined with a Semrock RazorEdge ultrasteep longpass edge filter. The data were collected using an Andor 750 spectrometer combined with an iDus Back-thinned CCD detector. Raman spectra were calibrated according to the peak position and intensity of a quartz standard.

4.3.4 High Temperature Oxide Melt Solution Calorimetry

High temperature oxide melt solution calorimetry experiments were carried out using a Setaram AlexSYS Tian-Calvet twin microcalorimeter using methods standard to our laboratory and described previously.[38–40] The calorimeter was calibrated against the heat content of high-purity α-Al_2O_3 (99.99%). Pressed sample pellets (~3 mg) were dropped from ambient temperature into the calorimeter containing the solvent, molten sodium molybdate ($3Na_2O\cdot4MoO_3$), in a Pt crucible at 800 °C. Hygroscopic $RECl_3$ was pelletized in the glovebox and transported to the calorimeter in closed centrifuge tubes under N_2 atmosphere, limiting contact with laboratory air to a few seconds. All experiments were flushed with O_2 at 60 mL min^{-1} and bubbled through the solvent at 5 mL min^{-1} to aid dissolution and prevent local saturation of the solvent. The measurement was repeated at least eight times on each sample.

4.4 Results and Discussion

PXRD characterizations of synthesized materials (Figure 4.2) indicate the formation of two crystal structures. For the larger RE (La–Ho, and Y), PXRD patterns can be indexed to the PbFCl-type structure (P4/nmm). Despite SmSI-type and YOCl-type structures having the same space group ($R\bar{3}m$), (104) reflections, the distinguishing feature of the YOCl-type structure,[24,25] show very weak intensity and confirm the SmSI-type structure for REOCls with smaller RE size (Er–Lu). Similarly, different crystal structures are adopted by RE_2O_3 (A-type and C-type) and $RECl_3$ (UCl_3-type and $AlCl_3$-type) with varying RE elements (Figure 4.3 and 4.4). Significant preferred orientation along the [001] axis was observed in PbFCl-type REOCls, which is particularly obvious in HoOCl and YOCl. The anisotropic growth of REOCl crystals is not unusual in molten salt reactions.[41,42] As the ionic radius of RE^{3+} decreases, the lattice of REOCls shrinks and Cl–Cl distances become shorter with stronger anion–anion repulsion.[43] The strain concentrates in the Cl layer and finally leads to a transformation to the SmSI-type structure for smaller RE.

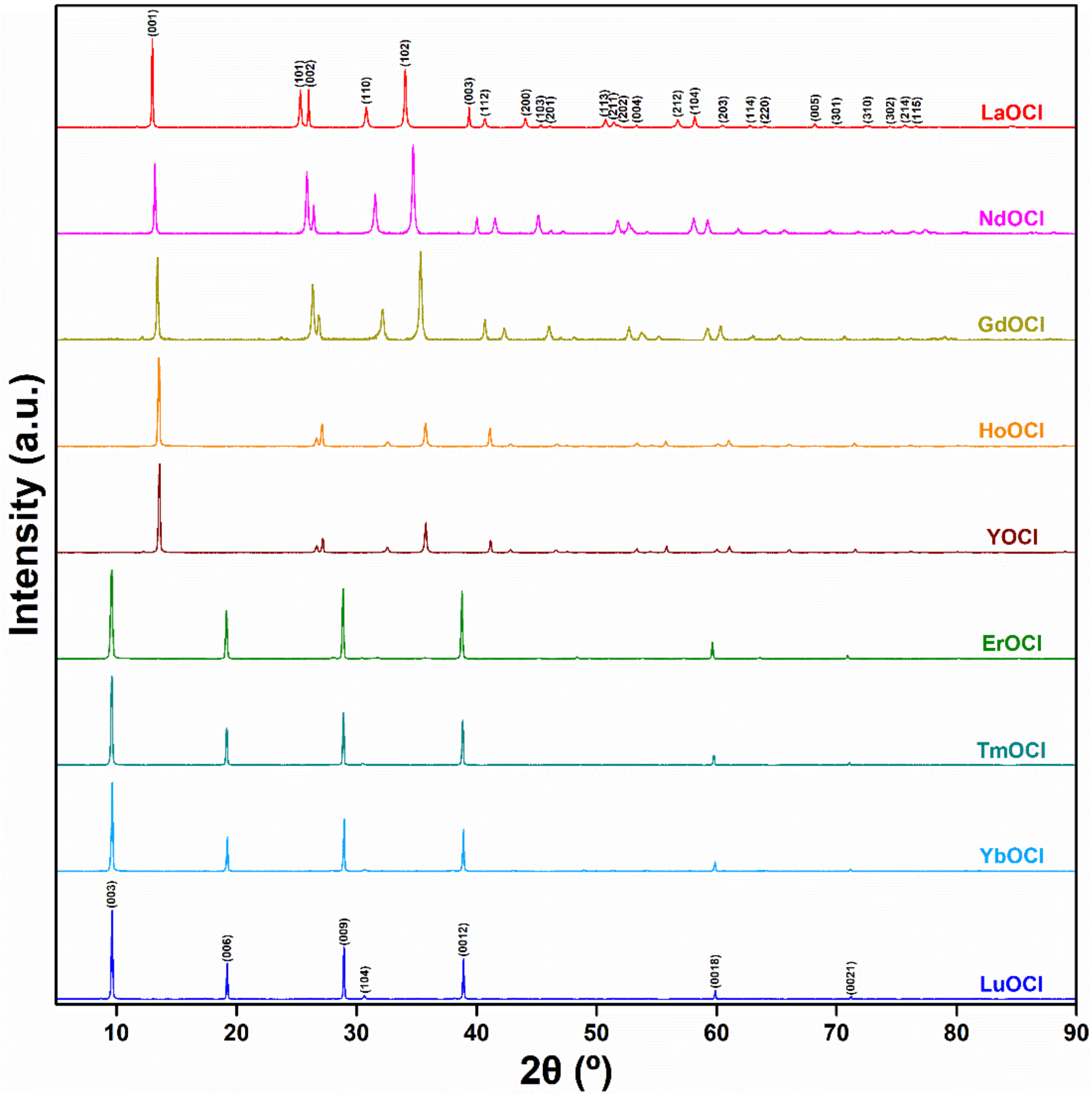

Figure 4.2 PXRD patterns of REOCls.

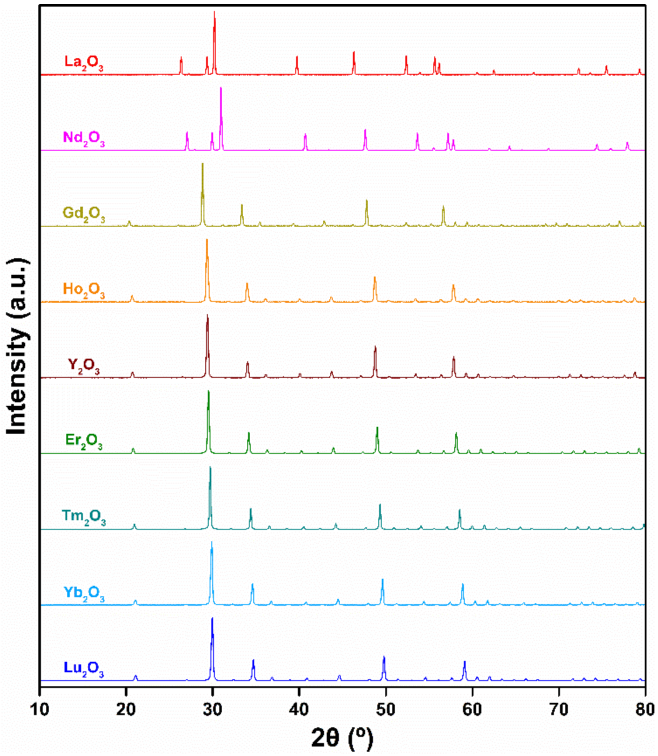

Figure 4.3 PXRD patterns of RE$_2$O$_3$.

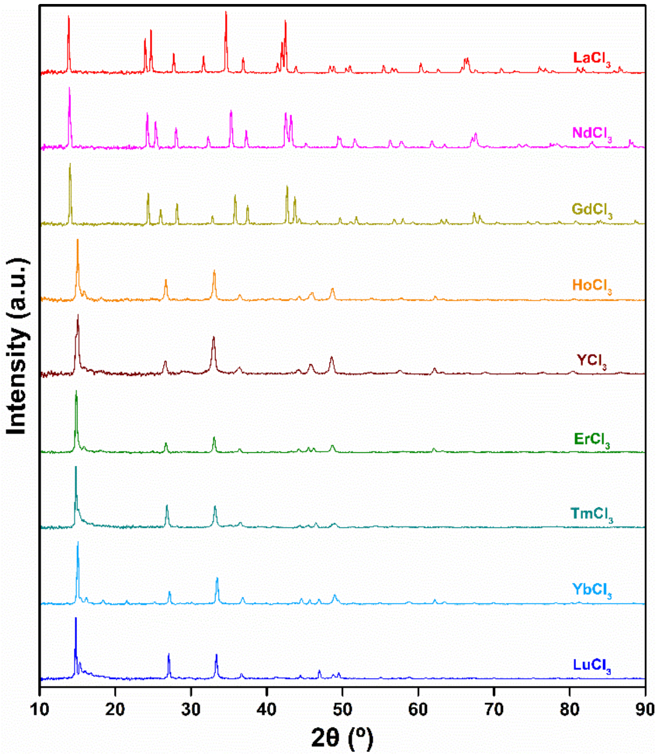

Figure 4.4 PXRD patterns of RECl$_3$.

Unit cell parameters (*a*, *c*, and *V*) of REOCl compounds were refined. The results are listed in Table 4.1 and plotted versus the ionic radii[44] of RE^{3+} in ninefold or sevenfold coordination in Figure 4.5 and 4.6. Considering the different *Z* values in the unit cell of PbFCl-type (*Z* = 2) and SmSI-type (*Z* = 6) REOCls, tripled lattice parameters (3*c* and 3*V*) of REOCls with the PbFCl-type structure are used for ease of comparison. As a result of the lanthanide contraction, lattice parameters and unit cell volumes of PbFCl-type REOCls decrease from light to heavy RE. In contrast, SmSI-type REOCl compounds are affected subtly by the variation of RE, i.e., the *a*–lattice parameter value decreases from Er to Lu, but *c*–lattice parameter and *V*–unit cell volume values change only slightly. This observation is consistent with the diverse interatomic interactions along different directions in SmSI-type REOCls. Within the layers, cations and anions are bound by ionic interactions, leading to decreasing *a* values for smaller RE ions, following the same trend as PbFCl-type REOCls; along the *c*-axis, the layers were held together by weak vdW interactions, giving rise to longer RE–RE distances. It appears that vdW forces are not notably affected by the RE size, so the almost unchanged *c* (~27.7 Å) and *V* (~332 $Å^3$) are seen in 2D REOCls.

Table 4.1 Lattice parameters of REOCls.

Sample	Space group	a (Å)	c (Å)	V ($Å^3$)
LaOCl	P4/nmm (No. 129)	4.107(2)	6.865(2)	115.8(2)
NdOCl		4.014(2)	6.756(4)	108.8(2)
GdOCl		3.937(2)	6.649(3)	103.1(2)
HoOCl		3.886(2)	6.591(1)	99.5(1)
YOCl		3.895(3)	6.584(1)	99.9(2)
ErOCl	$R\bar{3}m$ (No. 166)	3.725(2)	27.71(2)	332.9(5)
TmOCl		3.717(3)	27.69(2)	331.3(6)
YbOCl		3.723(4)	27.780(4)	333.4(7)
LuOCl		3.709(1)	27.779(3)	331.0(2)

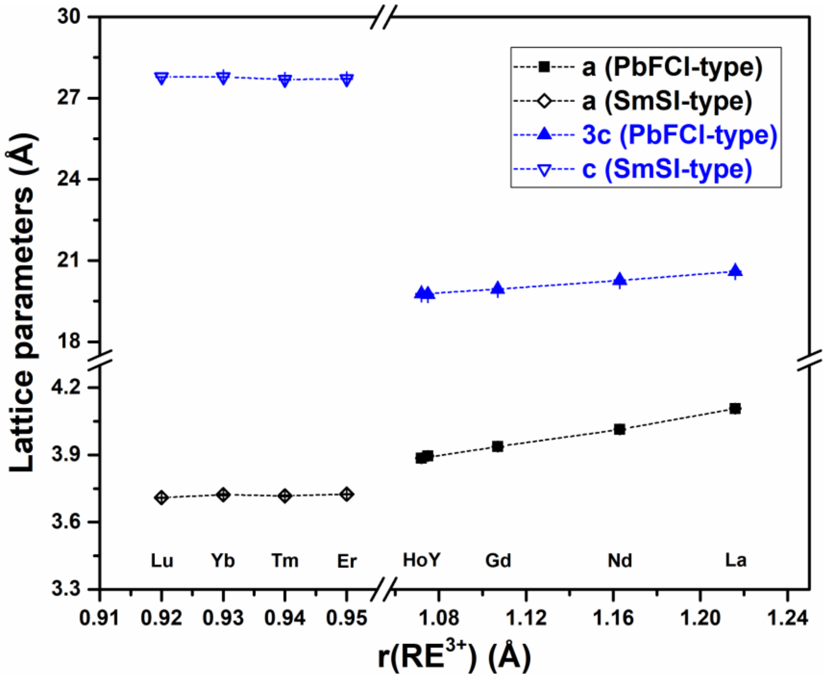

Figure 4.5 Lattice parameters of REOCls versus ionic radii of RE^{3+} in ninefold and sevenfold coordination for PbFCl-type and SmSI-type structures, respectively.

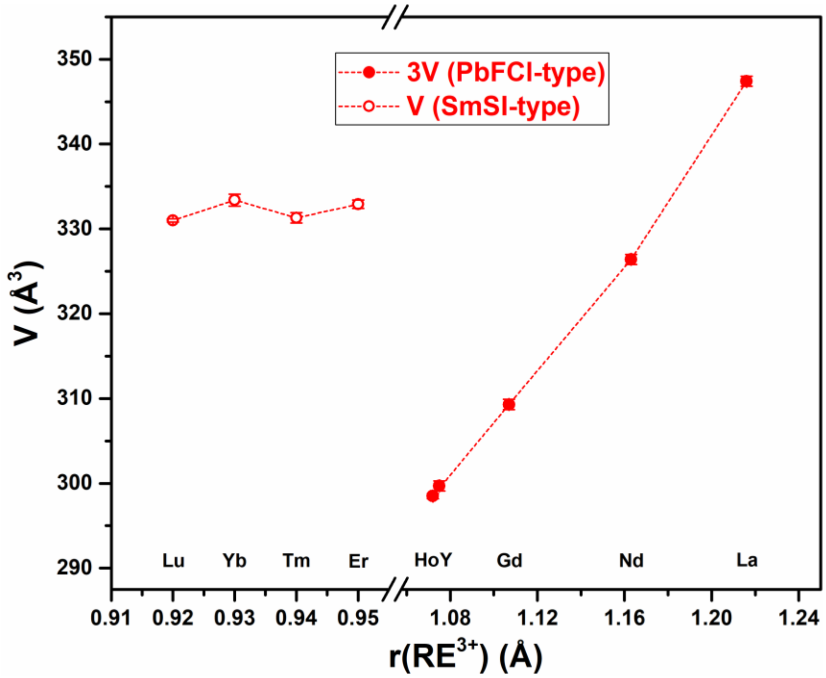

Figure 4.6 Unit cell volumes (*V*) of REOCls versus ionic radii of RE^{3+} in ninefold and sevenfold coordination for PbFCl-type and SmSI-type structures, respectively.

Raman spectra were obtained to investigate the local structure of REOCls with the SmSI-type structure (Figure 4.7). In the range from 50 to 300 cm^{-1}, three prominent Raman bands in accord with E_g and A_{1g} modes are observed.[13] The peak positions obtained by peak fitting are presented in Figure 4.8. Raman peaks of YbOCl show some deviations from those of the other SmSI-type REOCls, which may be due to the presence of divalent Yb^{2+} impurity in as-synthesized YbOCl.[45] The traces of Yb^{2+} and derived defects are probably correlated to the relatively large unit cell volume of YbOCl (Figure 4.6), but we did not investigate this further. Raman peak positions show a good linear dependence on ionic radii of RE^{3+}, except for YbOCl. When the ionic radius of RE^{3+} increases, a redshift is observed in the E_g mode located at 87 cm^{-1}, revealing the expansion along the layer plane. With larger RE cations, two A_{1g} modes (141 and 271 cm^{-1}) originating from different out-of-plane vibrations show a blueshift and a redshift, respectively, implying that the vertical expansion mainly happens between RE and Cl layers with concomitant shorter distances between O layers.

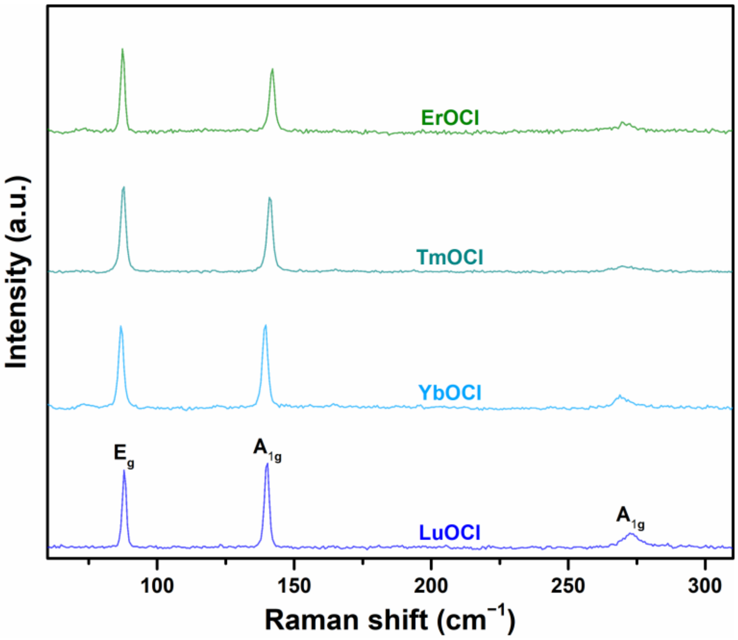

Figure 4.7 Raman spectra of SmSI-type REOCls.

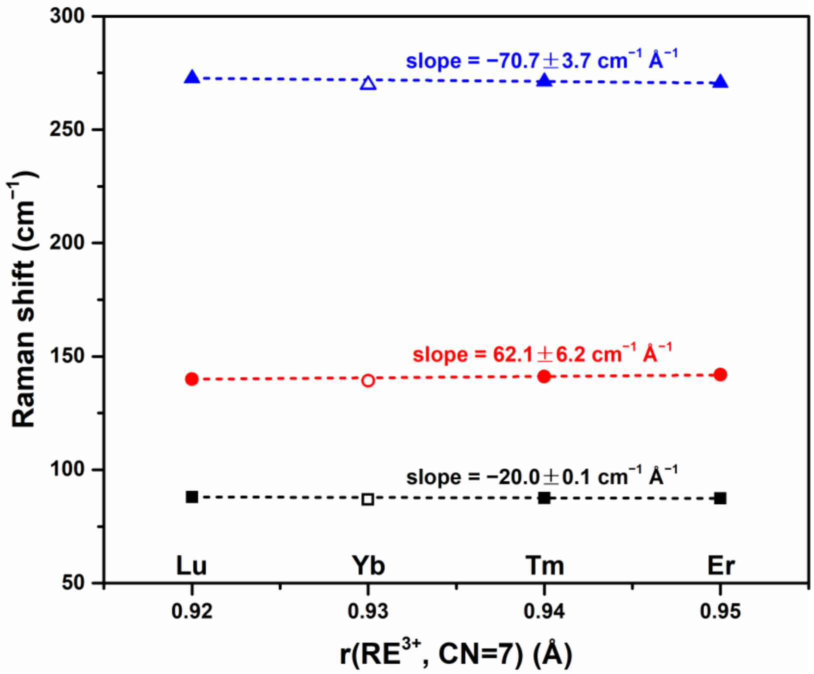

Figure 4.8 Raman frequencies of E_g and A_{1g} modes as a function of ionic radii of RE^{3+} in sevenfold coordination. The dashed lines are linear fitting of the peak positions of ErOCl, TmOCl, and LuOCl, which are represented by solid dots.

High temperature oxide melt solution calorimetry experiments were conducted to determine the formation enthalpies, in which drop solution enthalpies (ΔH_{ds}) corresponding to the heat effects of samples dropped from room temperature and dissolved in the molten solvent ($3Na_2O \cdot 4MoO_3$) at 800 °C were measured. To check the effectiveness of this method on RE chlorides, enthalpies of the exchange reactions between NaCl and RE_2O_3

$$6NaCl\ (s, 25\ °C) + RE_2O_3\ (s, 25\ °C) \rightarrow 3Na_2O\ (s, 25\ °C) + 2RECl_3\ (s, 25\ °C) \qquad (4.1)$$

were calculated based on ΔH_{ds} ($\Delta H_{exchange}$) (Table 4.2). As demonstrated in Table 4.3, $\Delta H_{exchange}$ values are equal to reaction enthalpies ($\Delta H_{reaction}$) calculated using formation enthalpies from elements ($\Delta H°_{f,\ el}$) within experimental error, suggesting complete dissolution of chlorides and no specific interaction between chloride components in the dilute molten solution. A similar methodology had been used to confirm reliable dissolution when developing oxide melt solution calorimetry for OH^- and F^--containing materials.[34,46] There were no unanticipated problems in calorimetric procedures.

Table 4.2 Thermodynamic cycles used to calculate enthalpies of the exchange reactions between NaCl and RE_2O_3.

Reaction	ΔH
NaCl (s, 25 °C) → NaCl (soln, 800 °C)	ΔH_1
RE_2O_3 (s, 25 °C) → RE_2O_3 (soln, 800 °C)	ΔH_2
Na_2O (s, 25 °C) → Na_2O (soln, 800 °C)	ΔH_3
$RECl_3$ (s, 25 °C) → $RECl_3$ (soln, 800 °C)	ΔH_4
6NaCl (s, 25 °C) + RE_2O_3 (s, 25 °C) → $3Na_2O$ (s, 25 °C) + $2RECl_3$ (s, 25 °C)	$\Delta H_{exchange}$
$\Delta H_{exchange} = 6\Delta H_1 + \Delta H_2 - 3\Delta H_3 - 2\Delta H_4$	
Na (s, 25 °C) + $1/2Cl_2$ (g, 25 °C) → NaCl (s, 25 °C)	ΔH_5
2RE (s, 25 °C) + $3/2O_2$ (g, 25 °C) → RE_2O_3 (s, 25 °C)	ΔH_6
2Na (s, 25 °C) + $1/2O_2$ (g, 25 °C) → Na_2O (s, 25 °C)	ΔH_7
RE (s, 25 °C) + $3/2Cl_2$ (g, 25 °C) → $RECl_3$ (s, 25 °C)	ΔH_8
6NaCl (s, 25 °C) + RE_2O_3 (s, 25 °C) → $3Na_2O$ (s, 25 °C) + $2RECl_3$ (s, 25 °C)	$\Delta H_{reaction}$
$\Delta H_{reaction} = -6\Delta H_5 - \Delta H_6 + 3\Delta H_7 + 2\Delta H_8$	

Table 4.3 Drop solution enthalpies in $3Na_2O\cdot4MoO_3$ at 800 °C of binary chlorides ($\Delta H_{ds\text{-}cl}$) and oxides ($\Delta H_{ds\text{-}ox}$), and formation enthalpies of binary chlorides ($\Delta H^\circ_{f,\ el\text{-}cl}$) and oxides ($\Delta H^\circ_{f,\ el\text{-}ox}$) from elements, plus reaction enthalpies of the exchange reactions between NaCl and RE_2O_3 calculated from ΔH_{ds} ($\Delta H_{exchange}$) or $\Delta H^\circ_{f,\ el}$ ($\Delta H_{reaction}$).

Element	$\Delta H_{ds\text{-}cl}$[a] (kJ mol^{-1})	$\Delta H_{ds\text{-}ox}$ (kJ mol^{-1})	$\Delta H^\circ_{f,\ el\text{-}cl}$ (kJ mol^{-1})	$\Delta H^\circ_{f,\ el\text{-}ox}$ (kJ mol^{-1})	$\Delta H_{exchange}$ (kJ mol^{-1})	$\Delta H_{reaction}$ (kJ mol^{-1})
Na	77.51 ± 0.30 (9)	−195.90 ± 4.23 [34]	−411.12 ± 0.34 [47]	−418.0 ± 4.2 [47]		

La	−16.41 ± 0.85 (8)	−221.81 ± 2.25 [48]	−1071.6 ± 1.5 [49]	−1791.6 ± 2.0 [50]	863.8 ± 13.1	861.1 ± 13.3
Nd	−26.13 ± 0.55 (8)	−156.95 ± 1.05 [51]	−1040.9 ± 1.0 [49]	−1806.9 ± 3.0 [50]	948.1 ± 12.9	937.8 ± 13.3
Gd	−50.24 ± 0.76 (8)	−134.48 ± 1.70 [51]	−1018.2 ± 1.5 [49]	−1819.7 ± 3.6 [50]	1018.8 ± 13.0	996.0 ± 13.6
Ho	−87.35 ± 0.91 (8)	−109.51 ± 1.50 [51]	−997.7 ± 2.5 [49]	−1883.3 ± 8.2 [50]	1118.0 ± 13.0	1100.6 ± 16.0
Y	−100.17 ± 0.73 (8)	−116.34 ± 1.21 [51]	−1018.4 ± 2.6 [52]	−1932.8 ± 5.2 [53]	1136.8 ± 13.0	1108.7 ± 14.7
Er	−96.85 ± 0.39 (8)	−107.2 ± 1.42 [54]	−994.4 ± 2.0 [49]	−1900.1 ± 6.5 [50]	1139.3 ± 12.9	1124.0 ± 14.9
Tm	−89.78 ± 0.46 (8)	−97.97 ± 0.93 [54]	−996.3 ± 2.5 [49]	−1889.3 ± 5.7 [50]	1134.4 ± 12.9	1109.4 ± 14.8
Yb	−90.33 ± 0.45 (8)	−90.71 ± 0.40 [55]	−959.5 ± 3.0 [49]	−1814.5 ± 6.0 [50]	1142.7 ± 12.9	1108.2 ± 15.3
Lu	−71.50 ± 0.73 (8)	−99.98 ± 0.79 [55]	−987.1 ± 2.5 [49]	−1877.0 ± 7.7 [50]	1095.8 ± 12.9	1115.5 ± 15.7

[a] Value is the mean of the number of experiments indicated in parentheses. Two standard deviations of the mean are given as errors.

ΔH_{ds} values of REOCl compounds in $3Na_2O\cdot4MoO_3$ at 800 °C are given in Table 4.4 with the standard formation enthalpies from binary compounds ($\Delta H^\circ_{f,\,bc}$) and $\Delta H^\circ_{f,\,el}$ calculated from the thermodynamic cycles in Table 4.5. As shown in Figure 4.9, $\Delta H^\circ_{f,\,bc}$ becomes less exothermic from light to heavy RE ions, ranging from −73.54 ± 0.85 (LaOCl) to −26.45 ± 0.63 (LuOCl) kJ mol^{-1}. The considerably exothermic $\Delta H^\circ_{f,\,bc}$ confirms the thermodynamic stability of REOCls relative to the mechanical mixture of binary oxides and chlorides. Compared to REOCls with light RE elements, REOCls containing heavy RE have less exothermic $\Delta H^\circ_{f,\,bc}$, which may account for the difficulties in their synthesis. Thus, it is reasonable to attribute the dimorphism of HoOCl, ErOCl, and YOCl to the close $\Delta H^\circ_{f,\,bc}$ values of REOCl located at the frontier between PbFCl-type and SmSI-type structures. Considering that YOF-type structure has a very similar local coordination environment as SmSI-type structure,[56] it is reasonable to conclude that they have similar energetic properties, which may explain the appearance of YOF-type REOCls in some synthesis experiments.[24,25]

Table 4.4 Drop solution enthalpies (ΔH_{ds}) in $3Na_2O\cdot4MoO_3$ at 800 °C, and formation enthalpies from binary compounds ($\Delta H°_{f,\,bc}$) and from elements ($\Delta H°_{f,el}$) at 25 °C of REOCls.

Sample	$\Delta H_{ds}{}^{a}$ (kJ mol^{-1})	$\Delta H°_{f,\,bc}$ (kJ mol^{-1})	$\Delta H°_{f,\,el}$ (kJ mol^{-1})
LaOCl	−5.87 ± 0.28 (8)	−73.54 ± 0.85	–1027.9 ± 1.2
NdOCl	−0.54 ± 0.15 (9)	−60.49 ± 0.42	–1009.8 ± 1.1
GdOCl	−13.00 ± 0.32 (8)	−48.57 ± 0.70	–994.5 ± 1.5
HoOCl	−30.58 ± 0.38 (8)	−35.04 ± 0.70	–995.4 ± 2.9
YOCl	−34.01 ± 0.61 (8)	−38.16 ± 0.77	–1021.9 ± 2.1
ErOCl	−30.19 ± 0.48 (8)	−37.83 ± 0.69	–1002.7 ± 2.4
TmOCl	−29.98 ± 0.48 (8)	−32.60 ± 0.59	–994.5 ± 2.2
YbOCl	−30.48 ± 0.55 (8)	−29.87 ± 0.59	–954.5 ± 2.3
LuOCl	−30.71 ± 0.52 (8)	−26.45 ± 0.63	–981.2 ± 2.8

[a] Value is the mean of the number of experiments indicated in parentheses. Two standard deviations of the mean are given as errors.

Table 4.5 Thermodynamic cycles used to calculate formation enthalpies from binary compounds ($\Delta H°_{f,\,bc}$) or elements ($\Delta H°_{f,\,el}$) of REOCls.

Reaction	ΔH
REOCl (s, 25 °C) → 1/3RE_2O_3 (soln, 800 °C) + 1/3$RECl_3$ (soln, 800 °C)	$\Delta H_1 = \Delta H_{ds}$
RE_2O_3 (s, 25 °C) → RE_2O_3 (soln, 800 °C)	$\Delta H_2 = \Delta H_{ds\text{-}ox}$
$RECl_3$ (s, 25 °C) → $RECl_3$ (soln, 800 °C)	$\Delta H_3 = \Delta H_{ds\text{-}cl}$
1/3RE_2O_3 (s, 25 °C) + 1/3$RECl_3$ (s, 25 °C) → REOCl (s, 25 °C)	$\Delta H°_{f,\,bc}$
$\Delta H°_{f,\,bc} = -\Delta H_1 + 1/3\Delta H_2 + 1/3\Delta H_3$	
2RE (s, 25 °C) + 3/2O_2 (g, 25 °C) → RE_2O_3 (s, 25 °C)	$\Delta H_4 = \Delta H°_{f,\,el\text{-}ox}$
RE (s, 25 °C) + 3/2Cl_2 (g, 25 °C) → $RECl_3$ (s, 25 °C)	$\Delta H_5 = \Delta H°_{f,\,el\text{-}cl}$
RE (s, 25 °C) + 1/2O_2 (g, 25 °C) + 1/2Cl_2 (g, 25 °C) → REOCl (s, 25 °C)	$\Delta H°_{f,\,el}$
$\Delta H°_{f,\,el} = \Delta H°_{f,\,bc} + 1/3\Delta H_4 + 1/3\Delta H_5$	

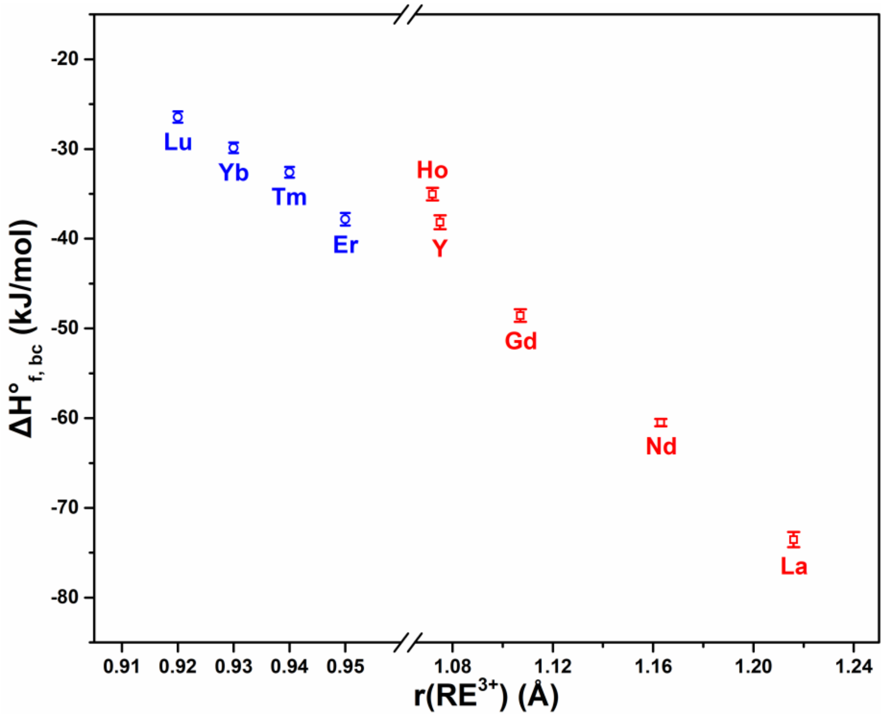

Figure 4.9 Formation enthalpies from binary compounds ($\Delta H^\circ_{f,\,bc}$) of REOCls at 25 °C versus ionic radii of RE^{3+} in ninefold and sevenfold coordination for PbFCl-type (red) and SmSI-type (blue) structures, respectively.

By means of Born–Haber cycles (Table 4.6–4.8), lattice energies (U) of REOCls and the corresponding binary oxides ($REO_{1.5}$) and chlorides ($RECl_3$) were calculated and shown in Figure 4.10. Ionic radii of RE^{3+} in eightfold coordination are used in Figure 4.10 to recognize the change in coordination number due to the lanthanide contraction. Since U is largely determined by Columbic interactions between cations and anions, higher charges and shorter cation–anion distances produce more exothermic U. As more O^{2-} anions are incorporated in the structure, the strength of U follows the sequence: $RECl_3 < REOCl < REO_{1.5}$. When varying RE, U increases in magnitude (becomes more exothermic) from light to heavy RE. This trend generally exists in RE compounds because smaller RE ions are packed more closely with other ions in the structure with shorter cation–anion distances and stronger ionic interactions.[12,34] Typically, U is correlated with the volume of the formula unit or molecular volume (V_m), which reflects the packing density and can be used as a factor to evaluate the cation–anion distance in complex ionic solids.[57] However, in spite of V_m comparable to that of NdOCl, U values of SmSI-type REOCls are much more exothermic than that of NdOCl and become more exothermic from ErOCl to LuOCl. The lack of dependence of U on volume can be ascribed to the vdW forces between the layers in the SmSI-type REOCls, which are minimally affected by the RE size but affect the volume. On the other hand, ionic interactions within the layers contribute strongly to the energetics of these 2D REOCls and become stronger for smaller RE ions, albeit having little impact on volumes. Different slopes of U against the RE size result in different trends of $\Delta H^\circ_{f,\,bc}$, which are related to the coordination numbers of RE^{3+} in binary and ternary RE compounds.[34] In the RE_2O_3–$RECl_3$ system, $REO_{1.5}$ and $RECl_3$ show larger slopes of U versus the ionic radius of RE^{3+} compared to REOCls because they have lower RE coordination, generating the less exothermic $\Delta H^\circ_{f,\,bc}$ of REOCls for smaller RE. The reduction of RE coordination in the structural conversion from PbFCl-type to SmSI-type leads to the similar $\Delta H^\circ_{f,\,bc}$ values of HoOCl, ErOCl, and YOCl.

Table 4.6 Summary of reactions in Born–Haber cycles for the formation of REOCl, $REO_{1.5}$, and $RECl_3$.

Reaction	ΔH (kJ mol^{-1})
RE (s, 25 °C) → RE (g, 25 °C)	$\Delta H_1 = \Delta H_{sub}$
RE (g, 25 °C) → RE^{3+} (g, 25 °C) + $3e^-$	$\Delta H_2 = (I_1+I_2+I_3)$
O_2 (g, 25 °C) → 2O (g, 25 °C)	$\Delta H_3 = 498.458 \pm 0.004$ [58]
O (g, 25 °C) + $2e^-$ → O^{2-} (g, 25 °C)	$\Delta H_4 = 703$ [59]
Cl_2 (g, 25 °C) → 2Cl (g, 25 °C)	$\Delta H_5 = 242.851 \pm 0.096$ [58]
Cl (g, 25 °C) + e^- → Cl^- (g, 25 °C)	$\Delta H_6 = -348.575 \pm 0.003$ [58]
RE (s, 25 °C) + $1/2O_2$ (g, 25 °C) + $1/2Cl_2$ (g, 25 °C) → REOCl (s, 25 °C)	$\Delta H_7 = \Delta H^\circ_{f,\,el}(REOCl)$

RE^{3+}(g, 25 °C) + O^{2-} (g, 25 °C) + Cl^{-} (g, 25 °C) → REOCl (s, 25 °C)	U(REOCl)
U(REOCl) = $- \Delta H_1 - \Delta H_2 - 1/2\Delta H_3 - \Delta H_4 - 1/2\Delta H_5 - \Delta H_6 + \Delta H_7$	
RE (s, 25 °C) → RE (g, 25 °C)	$\Delta H_1 = \Delta H_{sub}$
RE (g, 25 °C) → RE^{3+} (g, 25 °C) + $3e^{-}$	$\Delta H_2 = (I_1+I_2+I_3)$
O_2 (g, 25 °C) → 2O (g, 25 °C)	$\Delta H_3 = 498.458 \pm 0.004$ [58]
O (g, 25 °C) + $2e^{-}$ → O^{2-} (g, 25 °C)	$\Delta H_4 = 703$ [59]
2RE (s, 25 °C) + $3/2O_2$ (g, 25 °C) → RE_2O_3 (s, 25 °C)	$\Delta H_8 = \Delta H°_{f, el}(RE_2O_3)$ [50,53]
RE^{3+}(g, 25 °C) + $3/2O^{-}$ (g, 25 °C) → $REO_{1.5}$ (s, 25 °C)	$U(REO_{1.5})$
$U(REO_{1.5}) = - \Delta H_1 - \Delta H_2 - 3/4\Delta H_3 - 3/2\Delta H_4 + 1/2\Delta H_8$	
RE (s, 25 °C) → RE (g, 25 °C)	$\Delta H_1 = \Delta H_{sub}$
RE (g, 25 °C) → RE^{3+} (g, 25 °C) + $3e^{-}$	$\Delta H_2 = (I_1+I_2+I_3)$
Cl_2 (g, 25 °C) → 2Cl (g, 25 °C)	$\Delta H_5 = 242.851 \pm 0.096$ [58]
Cl (g, 25 °C) + e^{-} → Cl^{-} (g, 25 °C)	$\Delta H_6 = -348.575 \pm 0.003$ [58]
RE (s, 25 °C) + $3/2Cl_2$ (g, 25 °C) → $RECl_3$ (s, 25 °C)	$\Delta H_9 = \Delta H°_{f, el}(RECl_3)$ [49,52]
RE^{3+}(g, 25 °C) + $3Cl^{-}$ (g, 25 °C) → $RECl_3$ (s, 25 °C)	$U(RECl_3)$
$U(RECl_3) = - \Delta H_1 - \Delta H_2 - 3/2\Delta H_5 - 3\Delta H_6 + \Delta H_9$	

Table 4.7 Enthalpies of sublimation (ΔH_{sub}) and ionization ($I_1+I_2+I_3$) of RE elements.

Element	ΔH_{sub} (kJ mol^{-1})	$(I_1+I_2+I_3)$ (kJ mol^{-1})
La	434.5 ± 3.0 [60]	3455 ± 5 [62]
Nd	325.6 ± 2.0 [60]	3694 ± 5 [62]
Gd	406.9 ± 2.0 [60]	3750 ± 5 [62]
Ho	305.5 ± 5.0 [60]	3924 ± 5 [62]
Y	421.3 ± 5.0 [61]	3777 ± 5 [62]
Er	316.1 ± 3.0 [60]	3934 ± 5 [62]
Tm	232.5 ± 1.5 [60]	4045 ± 5 [62]
Yb	152.4 ± 1.0 [60]	4194 ± 5 [62]
Lu	428 ± 3 [60]	3896 ± 5 [62]

Table 4.8 Lattice energies (U) of REOCl, REO$_{1.5}$, and RECl$_3$ calculated from Born–Haber cycles.

Element	U(REOCl) (kJ mol^{-1})	U(REO$_{1.5}$) (kJ mol^{-1})	U(RECl$_3$) (kJ mol^{-1})
La	–5642.5 ± 6.0	–6213.6 ± 5.9	–4279.7 ± 5.8
Nd	–5754.5 ± 5.5	–6351.4 ± 5.6	–4379.1 ± 5.5
Gd	–5876.5 ± 5.6	–6495.1 ± 5.7	–4493.7 ± 5.6
Ho	–5950.0 ± 7.6	–6599.5 ± 8.2	–4545.8 ± 7.5
Y	–5945.3 ± 7.4	–6593 ± 7.5	–4535.3 ± 7.5
Er	–5977.9 ± 6.3	–6628.5 ± 6.7	–4563.1 ± 6.2
Tm	–5997.1 ± 5.7	–6650.5 ± 5.9	–4592.4 ± 5.8
Yb	–6026.0 ± 5.6	–6682 ± 5.9	–4624.5 ± 5.9
Lu	–6030.3 ± 6.5	–6690.8 ± 7.0	–4629.7 ± 6.3

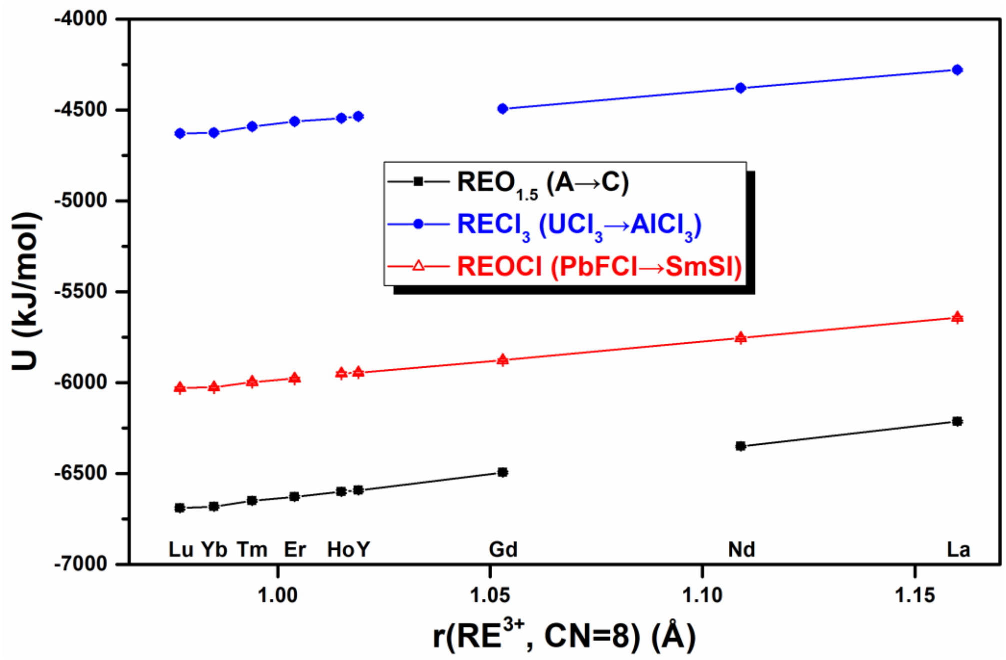

Figure 4.10 Lattice energies (U) of REO$_{1.5}$, RECl$_3$, and REOCls as a function of ionic radii of RE^{3+} in eightfold coordination, in which compounds having the same structure are connected by lines.

4.5 Conclusions

Single-phase REOCl compounds have been synthesized by flux reactions and characterized by PXRD and Raman spectroscopy. With the help of high temperature oxide melt solution calorimetry, formation enthalpies of REOCls were determined, and they give insights into the energetics of 3D and 2D RE materials. The exothermic formation enthalpies indicate the thermodynamic stability of all of these REOCl phases relative to binary oxides and chlorides. Enthalpies of formation become less exothermic with decreasing RE ionic radii. The similar formation enthalpies of REOCls with medium size RE (Ho, Y, and Er) may account for their dimorphism. Lattice energies were calculated by Born–Haber cycles to determine the effects of cation size on the energetics of REOCls with the two crystal structures. For 3D REOCls (PbFCl-type), the lattice contracts from light to heavy RE, reflecting the closer packing of ions in the smaller unit cell and stronger lattice energies. In contrast, the 2D SmSI-type REOCl phases show relatively large volumes with heavier RE but more negative lattice energies. The trend that lattice energies become more exothermic for smaller RE is also observed in these 2D REOCl materials regardless of almost unchanged unit cell volumes. These results reveal that the diverse interactions in SmSI-type REOCls have different effects on volumes and lattice energies, which are dominated by vdW and ionic interactions, respectively. As vdW forces are less sensitive to ionic size, the molecular volume is no longer a good indicator for lattice energies of vdW layered materials. This work lays a foundation for the energetics of 2D RE materials, but more structural and thermodynamic studies are needed for 2D RE and other materials to provide a deeper fundamental understanding of these systems.

4.6 Acknowledgements

The authors acknowledge the use of facilities within the Eyring Materials Center supported in part by NNCI-ECCS-2025490 at Arizona State University. This work was supported by the US Department of Energy Critical Materials Institute (CMI) Hub under the subaward number DE-AC02-07CH11358. We thank Douglas Daniel for help with Raman spectroscopy experiments.

4.7 References

(1) Okamoto, K.; Imanaka, N.; Adachi, G. Chloride ion conduction in rare earth oxychlorides. *Solid State Ion.* **2002**, *154–155*, 577–580.

(2) Nunotani, N.; Misran, M. R. I. B.; Inada, M.; Uchiyama, T.; Uchimoto, Y.; Imanaka, N. Structural environment of chloride ion-conducting solids based on lanthanum oxychloride. *J. Am. Ceram. Soc.* **2020**, *103*, 297–303.

(3) Manoilova, O. V.; Podkolzin, S. G.; Tope, B.; Lercher, J.; Stangland, E. E.; Goupil, J.-M.; Weckhuysen, B. M. Surface acidity and basicity of La_2O_3, LaOCl, and $LaCl_3$ characterized by IR spectroscopy, TPD, and DFT calculations. *J. Phys. Chem. B* **2004**, *108*, 15770–15781.

(4) Podkolzin, S. G.; Stangland, E. E.; Jones, M. E.; Peringer, E.; Lercher, J. A. Methyl chloride production from methane over lanthanum-based catalysts. *J. Am. Chem. Soc.* **2007**, *129*, 2569−2576.

(5) Scharfe, M.; Lira-Parada, P. A.; Amrute, A. P.; Mitchell, S.; Pérez-Ramírez, J. Lanthanide compounds as catalysts for the one-step synthesis of vinyl chloride from ethylene. *J. Catal.* **2016**, *344*, 524–534.

(6) Li, G.; Li, C.; Zhang, C.; Cheng, Z.; Quan, Z.; Peng, C.; Lin, J. Tm^{3+} and/or Dy^{3+} doped LaOCl nanocrystalline phosphors for field emission displays. *J. Mater. Chem.* **2009**, *19*, 8936–8943.

(7) Li, G.; Hou, Z.; Peng, C.; Wang, W.; Cheng, Z.; Li, C.; Lian, H.; Lin, J. Electrospinning derived one-dimensional LaOCl: Ln^{3+} (Ln = Eu/Sm, Tb, Tm) nanofibers, nanotubes and microbelts with multicolor-tunable emission properties. *Adv. Funct. Mater.* **2010**, *20*, 3446–3456.

(8) Kim, D.; Park, S.; Kim, S.; Kang, S.-G.; Park, J.-C. Blue-emitting Eu^{2+}-activated LaOX (X = Cl, Br, and I) materials: crystal field effect. *Inorg. Chem.* **2014**, *53*, 11966−11973.

(9) Renero-Lecuna, C.; Herrero, A.; Jimenez de Aberasturi, D.; Martínez-Flórez, M.; Valiente, R.; Mychinko, M.; Bals, S.; Liz-Marzán, L. M. Nd^{3+}-doped lanthanum oxychloride nanocrystals as nanothermometers. *J. Phys. Chem. C* **2021**, *125*, 19887−19896.

(10) Lee, B.-I.; Jeong, H.; Byeon, S.-H. Oxychloride–hydroxychloride–trihydroxide phase relationships of rare earths in aqueous solution. *Inorg. Chem.* **2014**, *53*, 5212−5221.

(11) Yamamoto, H.; Miyata, M.; Murakami, H.; Furusawa, K.; Uda, T. Hidden nature of the conversion reaction from rare earth chloride to oxychloride and the application to novel separation. *ChemistrySelect* **2018**, *3*, 2998–3002.

(12) Yang, S.; Anderko, A.; Riman, R. E.; Navrotsky, A. Thermochemistry of stoichiometric rare earth oxyfluorides REOF. *J. Am. Ceram. Soc.* **2022**, *105*, 1472–1480.

(13) Yao, Y.; Zhang, Y.; Xiong, W.; Wang, Z.; Sendeku, M. G.; Li, N.; Wang, J.; Huang, W.; Wang, F.; Zhan, X.; et al. Growth and raman scattering investigation of a new 2D MOX material: YbOCl. *Adv. Funct. Mater.* **2019**, *29*, 1903017.

(14) Chen, P.; Han, W.; Zhao, M.; Su, J.; Li, Z.; Li, D.; Pi, L.; Zhou, X.; Zhai, T. Recent advances in 2D rare earth materials. *Adv. Funct. Mater.* **2021**, *31*, 2008790.

(15) Duong, D. L.; Yun, S. J.; Lee, Y. H. van der Waals layered materials: opportunities and challenges. *ACS Nano* **2017**, *11*, 11803−11830.

(16) Wang, X.; Sun, Y.; Liu, K. Chemical and structural stability of 2D layered materials. *2D Mater.* **2019**, *6*, 042001.

(17) Jacob, K. T.; Dixit, A.; Rajput, A. Stability field diagrams for Ln–O–Cl systems. *Bull. Mater. Sci.* **2016**, *39*, 603−611.

(18) Wendlandt, W. W. The thermal decomposition of yttrium, scandium, and some rare-earth chloride hydrates. *J. Inorg. Nucl. Chem.* **1957**, *5*, 118−122.

(19) Wendlandt, W. W. The thermal decomposition of the heavier rare earth metal chloride hydrates. *J. Inorg. Nucl. Chem.* **1959**, *9*, 136−139.

(20) Hölsä, J.; Niinistö, L. Thermoanalytical study on the reactions of selected rare earth oxides with ammonium halides. *Thermochim. Acta* **1980**, *37*, 155−160.

(21) Du, Y.-P.; Zhang, Y.-W.; Sun, L.-D.; Yan, C.-H. Atomically efficient synthesis of self-assembled monodisperse and ultrathin lanthanide oxychloride nanoplates. *J. Am. Chem. Soc.* **2009**, *131*, 3162−3163.

(22) Kort, K. R.; Banerjee, S. Shape-controlled synthesis of well-defined matlockite LnOCl (Ln: La, Ce, Gd, Dy) nanocrystals by a novel non-hydrolytic approach. *Inorg. Chem.* **2011**, *50*, 5539–5544.

(23) Templeton, D. H.; Dauben, C. H. Crystal structures of rare earth oxychlorides. *J. Am. Chem. Soc.* **1953**, *75*, 6069−6070.

(24) Garcia, E.; Corbett, J. D.; Ford, J. E.; Vary, W. J. Low-temperature routes to new structures for yttrium, holmium, erbium, and thulium oxychlorides. *Inorg. Chem.* **1985**, *24*, 494−498.

(25) Song, K.; Kauzlarich, S. M. New intercalation compounds of layered lanthanide oxychlorides LnOCl (Ln = Ho, Er, Tm, and Yb) with pyridine and substituted pyridines. *Chem. Mater.* **1994**, *6*, 386−394.

(26) Wagman, D. D.; Evans, W. H.; Parker, V. B.; Schumm, R. H.; Halow, I.; Bailey, S. M.; Churney, K. L.; Nuttall, R. L. *NBS Tables of Chemical Thermodynamic Properties: Selected Values for Inorganic and C_1 and C_2 Organic Substances in SI Units*; National Bureau of Standards, 1982.

(27) Burns, J. B.; Peterson, J. R.; Haire, R. G. Standard enthalpies of formation for europium, gadolinium, and lutetium oxychlorides, calculated from measured enthalpies of solution. *J. Alloys Compd.* **1998**, *265*, 146–152.

(28) Koch, C. W.; Broido, A.; Cunningham, B. B. The vapor phase hydrolysis of rare earth halides. I. Heat and free energy of the reaction: $LaCl_3(s) + H_2O(g) = LaOCl(s) + 2HCl(g)$. *J. Am. Chem. Soc.* **1952**, *74*, 2349−2351.

(29) Koch, C. W.; Cunningham, B. B. The vapor phase hydrolysis of the rare earth halides. II. Heat and free energy of the reactions: $SmCl_3(s) + H_2O(g) = SmOCl(s) + 2HCl(g)$ and $GdCl_3(s) + H_2O(g) = GdOCl(s) + 2HCl(g)$. *J. Am. Chem. Soc.* **1953**, *75*, 796−797.

(30) Koch, C. W.; Cunningham, B. B. The vapor phase hydrolysis of the rare earth halides. III. Heat and free energy of the reactions $PrCl_3(s) + H_2O(g) = PrOCl(s) + 2HCl(g)$ and $NdCl_3(s) + H_2O(g) = NdOCl(s) + 2HCl(g)$. *J. Am. Chem. Soc.* **1954**, *76*, 1471−1474.

(31) Hisham, M. W. M.; Benson, S. W. Thermochemistry of inorganic solids. 3. Enthalpies of formation of solid metal oxyhalide compounds. *J. Phys. Chem.* **1986**, *90*, 885−888.

(32) Struck, C. W.; Baglio, J. A. Estimates for the enthalpy of formation of rare-earth oxyhalides with the P4/nmm structure. *Thermochim. Acta* **1993**, *216*, 45−79.

(33) Sanchez-Segado, S.; Lectez, S.; Jha, A.; Stackhouse, S. A comparison of methods for the estimation of the enthalpy of formation of rare earth compounds. *Phys. Chem. Chem. Phys.* **2021**, *23*, 24273–24281.

(34) Yang, S.; Anderko, A.; Riman, R. E.; Navrotsky, A. Thermochemistry of sodium rare earth ternary fluorides, $NaREF_4$. *Acta Mater.* **2021**, *220*, 117289.

(35) Yang, S.; Jayanthi, K.; Anderko, A.; Riman, R. E.; Navrotsky, A. Thermochemical investigation of the stability and conversion of nanocrystalline and high-temperature phases in sodium neodymium fluorides. *Chem. Mater.* **2021**, *33*, 9571–9579.

(36) Brandt, G.; Diehl, R. Preparation, powder data and crystal structure of YbOCl. *Mater. Res. Bull.* **1974**, *9*, 411−419.

(37) Beck, H. P. Oxychlorides of the heavy rare earth elements. *Z. Naturforsch. B* **1976**, *31*, 1562−1564.

(38) Navrotsky, A. Progress and new directions in high temperature calorimetry. *Phys. Chem. Miner.* **1977**, *2*, 89–104.

(39) Navrotsky, A. Progress and new directions in high temperature calorimetry revisited. *Phys. Chem. Miner.* **1997**, *24*, 222–241.

(40) Navrotsky, A. Progress and new directions in calorimetry: a 2014 perspective. *J. Am. Ceram. Soc.* **2014**, *97*, 3349–3359.

(41) Afanasiev, P.; Aouine, M.; Deranlot, C.; Epicier, T. Ordered arrays of nanorods obtained by solid−liquid reactions of LaOCl crystals. *Chem. Mater.* **2010**, *22*, 5411–5419.

(42) Huang, Z.; Zhang, H.; Zhang, S. Growth of well-developed LaOCl microplates by chloride salt-assisted method. *CrystEngComm* **2017**, *19*, 2971−2976.

(43) Hölsä, J.; Lahtinen, M.; Lastusaari, M.; Valkonen, J.; Viljanen, J. Stability of rare-earth oxychloride phases: Bond valence study. *J. Solid State Chem.* **2002**, *165*, 48–55.

(44) Shannon, R. D. Revised effective ionic radii and systematic studies of interatomic distances in halides and chalcogenides. *Acta Crystallogr. A* **1976**, *32*, 751−767.

(45) Aitasalo, T.; Hölsä, J.; Lastusaari, M.; Legendziewicz, J.; Lehto, L.; Lindén, J.; Maryško, M. Structural, magnetic and spectroscopic investigations of europium oxychloride, EuOCl. *J. Alloys Compd.* **2004**, *380*, 296−302.

(46) Navrotsky, A.; Rapp, R. P.; Smelik, E.; Burnley, P.; Circone, S.; Chai, L.; Bose, K. The behavior of H_2O and CO_2 in high-temperature lead borate solution calorimetry of volatile-bearing phases. *Am. Mineral.* **1994**, *79*, 1099−1109.

(47) Chase, M. W. J. *NIST-JANAF Thermochemical Tables*, 4th ed.; J. Phys. Chem. Ref. Data, Monograph, 1998; Vol. 9, pp 1–1951.

(48) Mielewczyk-Gryn, A.; Wachowski, S.; Lilova, K. I.; Guo, X.; Gazda, M.; Navrotsky, A. Influence of antimony substitution on spontaneous strain and thermodynamic stability of lanthanum orthoniobate. *Ceram. Int.* **2015**, *41*, 2128–2133.

(49) Konings, R. J. M.; Kovács, A. Thermodynamic Properties of the Lanthanide(III) Halides. In *Handbook on the Physics and Chemistry of Rare Earths*, Vol. 33; Elsevier, 2003; pp 147−247.

(50) Konings, R. J. M.; Beneš, O.; Kovács, A.; Manara, D.; Sedmidubský, D.; Gorokhov, L.; Iorish, V. S.; Yungman, V.; Shenyavskaya, E.; Osina, E. The thermodynamic properties of the f-elements and their compounds. Part 2. The lanthanide and actinide oxides. *J. Phys. Chem. Ref. Data* **2014**, *43*, 013101.

(51) Mielewczyk-Gryn, A.; Navrotsky, A. Enthalpies of formation of rare earth niobates, RE_3NbO_7. *Am. Mineral.* **2015**, *100*, 1578–1583.

(52) Xiang-Yun, W.; Zhu, J. T.; Goudiakas, J.; Fuger, J. Thermodynamics of lanthanide elements IV. Molar enthalpies of formation of Y^{3+}(aq), YCl_3(cr), YBr_3(cr), and YI_3(cr). *J. Chem. Thermodyn.* **1988**, *20*, 1195−1202.

(53) Morss, L. R.; Day, P. P.; Felinto, C.; Brito, H. Standard molar enthalpies of formation of Y_2O_3, Ho_2O_3, and Er_2O_3 at the temperature 298.15 K. *J. Chem. Thermodyn.* **1993**, *25*, 415–422.

(54) Qi, J.; Guo, X.; Mielewczyk-Gryn, A.; Navrotsky, A. Formation enthalpies of $LaLn'O_3$ (Ln′=Ho, Er, Tm and Yb) interlanthanide perovskites. *J. Solid State Chem.* **2015**, *227*, 150–154.

(55) Yang, S.; Powell, M.; Kolis, J. W.; Navrotsky, A. Thermochemistry of rare earth oxyhydroxides, REOOH (RE = Eu to Lu). *J. Solid State Chem.* **2020**, *287*, 121344.

(56) Udayakantha, M.; Schofield, P.; Waetzig, G. R.; Banerjee, S. A full palette: crystal chemistry, polymorphism, synthetic strategies, and functional applications of lanthanide oxyhalides. *J. Solid State Chem.* **2019**, *270*, 569–592.

(57) Glasser, L.; Jenkins, H. D. B. Lattice energies and unit cell volumes of complex ionic solids. *J. Am. Chem. Soc.* **2000**, *122*, 632–638.

(58) Rumble, J. R. *CRC Handbook of Chemistry and Physics*, 101st ed.; CRC Press/Taylor & Francis, 2020.

(59) Atkins, P.; de Paula, J.; Keeler, J. *Atkins' Physical Chemistry*, 11th ed.; Oxford University Press, 2018.

(60) Konings, R. J. M.; Beneš, O. The thermodynamic properties of the f-elements and their compounds. I. The lanthanide and actinide metals. *J. Phys. Chem. Ref. Data* **2010**, *39*, 043102.

(61) Morss, L. R. Thermochemical properties of yttrium, lanthanum, and the lanthanide elements and ions. *Chem. Rev.* **1976**, *76*, 827–841.

(62) Cotton S. *Lanthanide and Actinide Chemistry*; John Wiley & Sons, 2006.

Chapter 5

Thermochemistry of Sodium Rare Earth Ternary Fluorides, $NaREF_4$

Shuhao Yang,[†,‡] Andre Anderko,[‖] Richard E. Riman,[§] Alexandra Navrotsky[*,†]

[†]Navrotsky Eyring Center for Materials of the Universe, School of Molecular Sciences, Arizona State University, Tempe, Arizona 85287, United States

[‡]Department of Chemistry, University of California, Davis, California 95616, United States

[‖]OLI Systems, Inc., Parsippany, New Jersey 07054, United States

[§]Department of Materials Science and Engineering, Rutgers, The State University of New Jersey, Piscataway, New Jersey 08854, United States

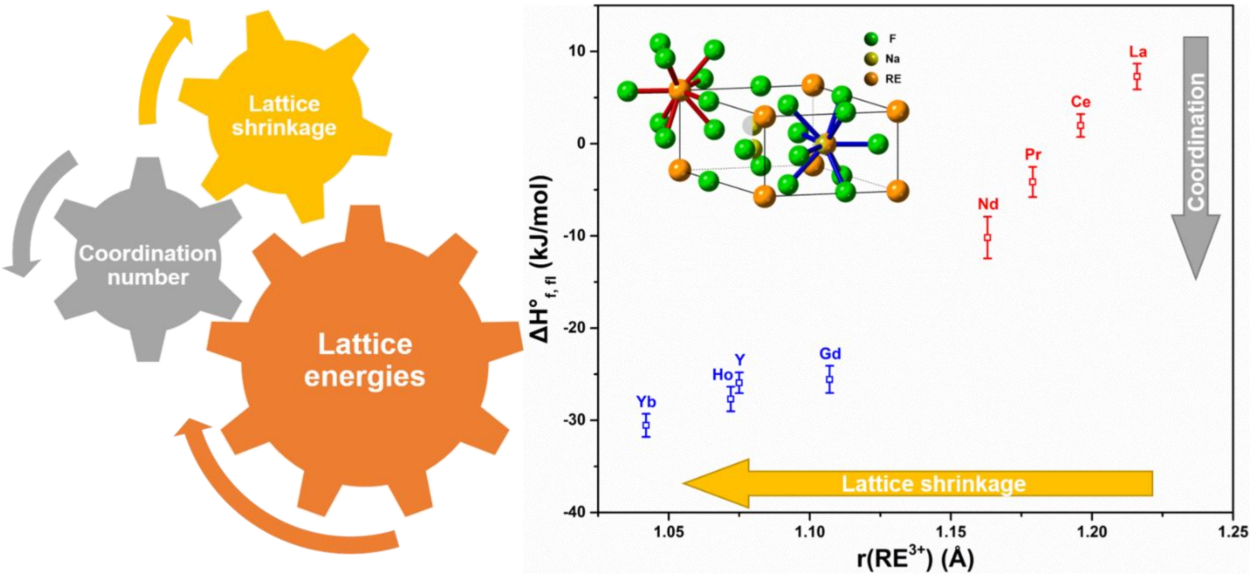

Acta Mater. **2021**, *220*, 117289.

5.1 Abstract

Sodium rare earth fluorides, $NaREF_4$ (RE = rare earth), are used as luminescent materials for light emission and biomedical applications and are important compositions for extracting and separating RE elements. Solution calorimetric measurements of a series of β-structured $NaREF_4$ ($Na_{1.5}RE_{1.5}F_6$) phases with various RE elements determined their heats of formation. Though the lattice contracts from light to heavy RE elements, $NaREF_4$ compounds show more exothermic enthalpies of formation from binary components with the decrease of RE^{3+} radii, contrary to behavior seen in most RE oxide ternary compounds. By constructing Born–Haber cycles, the different slopes of lines relating lattice energies to lattice parameters in binary and ternary fluorides appear to be the reason for this reverse trend, which can be associated with changes in the coordination number of RE cations. These trends and the metastability of sodium light RE fluorides not only reveal the key role of ionic radius in RE compound stability, but also are significant for the design and synthesis of new materials and motivate the more effective utilization of RE.

5.2 Introduction

Sodium rare earth ternary fluorides, $NaREF_4$ (RE = rare earth) draw much interest for their unique photoluminescent properties as promising materials for up-conversion phosphors.[1–3] Although synthesis methods, luminescence, and applications of $NaREF_4$ have been explored extensively,[4] thermodynamic studies are very limited,[5,6] and a comprehensive understanding of their thermodynamic stability along the RE series is absent. The lack of thermodynamic understanding hinders the rational design and synthesis of these and related materials. For example, previous research on $NaREF_4$ mostly focuses on ternary fluorides with heavy RE elements.[7] On the other hand, properties of $NaLaF_4$ are reported minimally.[8]

Not only synthesized in laboratories, RE fluorides are also common precipitates in rare earth mineral processing.[9] For separation and regeneration of RE, it is necessary and useful to know variations of thermodynamic properties of their compounds. Furthermore, because 4f orbitals of RE^{3+} ions are well shielded by 5s and 5p orbitals, not participating in bonding directly, the thermodynamics of RE compounds across the lanthanide series provides a good model to understand the role of cation size in determining the energetics of ionic compounds with different structures. Previous thermodynamic studies of RE compounds mainly revolved around oxides[10–18] and oxysalts[19–24], rarely involving fluoride compounds[25]. Given that F^- anion has only one negative charge and relatively small ionic size, it is possible that RE fluorides display distinct thermodynamic and structural properties from oxides.

In this work, we determined enthalpies of formation of a series of $NaREF_4$ isostructural phases using high temperature oxide melt solution calorimetry, confirming that this well-established calorimetric method can be applied to RE fluoride systems. Lattice energies were calculated from Born–Haber cycles to access the effects of ionic size and coordination of RE cations on thermodynamic stability of $NaREF_4$ with varying RE elements. Considering the crystal structures, it is shown that the coordination number change of RE cations is a major factor defining the trend of energetic stability of RE ionic compounds with respect to ionic size.

5.3 Experimental Methods

5.3.1 Material Preparation

NaF (ACS reagent, ≥ 99%) and Na_2CO_3 (anhydrous, ACS reagent, ≥ 99.5%) were purchased from Sigma-Aldrich. LaF_3 (99.99 %), CeF_3 (99.9 %), PrF_3 (99.9 %), NdF_3 (99.9 %), GdF_3 (99.9 %), HoF_3 (99.99 %), YbF_3 (99.99 %), and YF_3 (99.9 %) were purchased from Alfa-Aesar. All chemicals have been checked by X-ray diffraction and used without further purification.

Ternary sodium rare earth fluorides were prepared by solid state reactions, in which equal molar ratio of NaF and rare earth trifluorides (REF_3) were mixed, pelletized, reacted at 550 °C (or 500 °C for Ho, Yb, and Y) for 24 h, and annealed at 500 °C (or 450 °C for Ho, Yb, and Y) for 24 h in Pt crucibles under N_2 atmosphere. Heating and cooling rates of 5 and 1 °C min^{-1}, respectively, were used. No weight change was observed during the reaction, so the composition of the ternary sodium rare earth fluoride is the same as the precursor, namely $NaREF_4$ or $Na_{1.5}RE_{1.5}F_6$.

5.3.2 Powder X-ray Diffraction

Powder X-ray diffraction (PXRD) patterns were obtained using a Bruker D2 Phaser diffractometer operated with Cu Kα radiation ($\lambda = 1.54184$ Å). The data for $Na_{1.5}RE_{1.5}F_6$ were collected in the 2θ range of 10–120° with a step size of 0.02° and a dwell time of 5 s per step. The PXRD patterns in the 2θ range of 10–100° were analyzed using the Rietveld method implemented in the program GSAS-II.[26] The data for REF_3 were collected in the 2θ range of 10–80° with a step size of 0.02° and a dwell time of 0.45 s per step.

5.3.3 High Temperature Oxide Melt Solution Calorimetry

High temperature oxide melt solution calorimetry experiments were carried out using an AlexSYS Tian-Calvet twin microcalorimeter using methods standard to our laboratory and described previously.[27–29] The calorimeter was calibrated against the heat content of high purity α-Al_2O_3 (99.997 %). Pressed sample pellets (~5 mg) were dropped from ambient temperature into the calorimeter containing the solvent, molten sodium molybdate ($3Na_2O\cdot4MoO_3$), in a Pt crucible at 800 °C. All experiments were flushed with O_2 at 60 mL min^{-1} with bubbling through the solvent at 5 mL min^{-1} to aid dissolution and prevent local saturation of the solvent. The measurement was repeated at least eight times on each sample.

5.4 Results

$NaREF_4$ (RE = La–Nd, Gd, Ho, Yb, and Y) samples were prepared by solid state reactions and characterized by PXRD (Figure 5.1) with Rietveld analysis (Table 5.1, Figure A6–A13). The composition and phase purity of samples was confirmed by the weight consistency during solid state reactions and PXRD patterns. All $NaREF_4$ adopt a hexagonal structure ($P\bar{6}$) termed as the β structure,[30] with the unit cell of $Na_{1.5}RE_{1.5}F_6$ as shown in Figure 5.2, in which there are three cation sites: a one-fold site (RE1) is fully occupied by RE^{3+}, the other one-fold site (Na2/RE2) is occupied by $1/2Na^+$ and $1/2RE^{3+}$, and the two-fold site (Na1) is occupied by the equal proportions of Na^+ and vacancies. For convenience in discussing the relationship between the crystal structure and thermodynamic properties of $NaREF_4$, the formula $Na_{1.5}RE_{1.5}F_6$ is used in the rest of this article unless otherwise stated. From La to Yb, as RE cations become smaller, the lattice parameters decrease (Table 5.2) and unit cell volumes of $Na_{1.5}RE_{1.5}F_6$ shrink following a linear trend versus the ionic radius[31] of RE^{3+} in nine-fold coordination (Figure 5.3). Similar decrease of lattice parameters with increasing atomic number is widespread among RE compounds,[32] indicating that lanthanide contraction dominates the cell size of RE compounds.

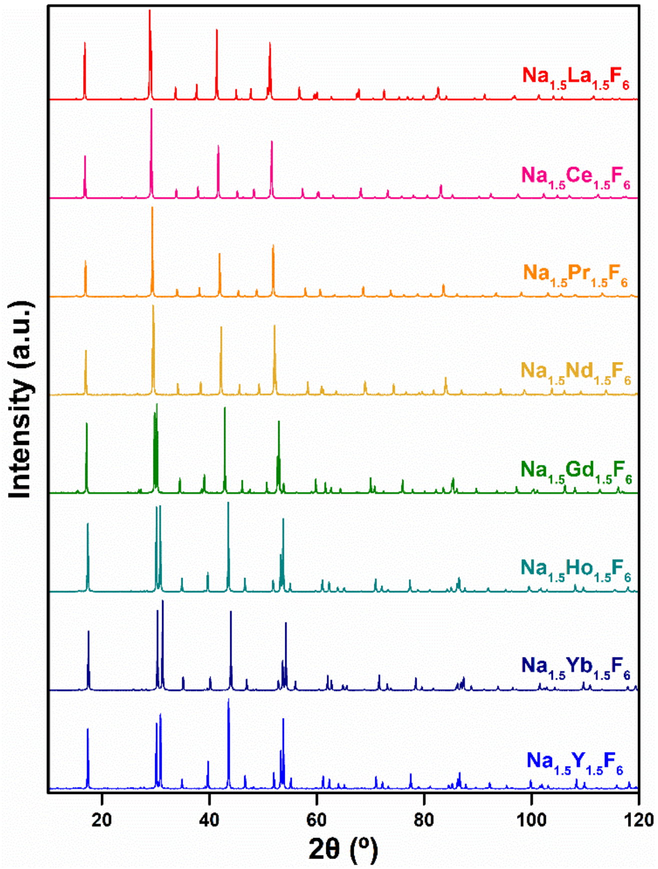

Figure 5.1 PXRD patterns of $Na_{1.5}RE_{1.5}F_6$ (RE = La–Nd, Gd, Ho, Yb, and Y) samples.

Table 5.1 Atomic coordinates and isotropic displacement parameters in $Na_{1.5}RE_{1.5}F_6$ with reliability factors of Rietveld analysis.

Sample	Atom	Wyckoff	x	y	z	SOF	U_{iso}	Reliability factors.
$Na_{1.5}La_{1.5}F_6$	La1	1a	0	0	0	1.000	0.01531	
	Na1	2h	1/3	2/3	0.65482	0.500	0.01439	R = 3.29%
	Na2/La2	1f	2/3	1/3	1/2	0.500/0.500	0.01328	wR = 5.13%
	F1	3j	0.63197	0.06620	0	1.000	0.01889	GOF = 2.61
	F2	3k	0.69959	0.73631	1/2	1.000	0.01073	
$Na_{1.5}Ce_{1.5}F_6$	Ce1	1a	0	0	0	1.000	0.01669	
	Na1	2h	1/3	2/3	0.65931	0.500	0.01289	R = 2.88%
	Na2/Ce2	1f	2/3	1/3	1/2	0.500/0.500	0.00458	wR = 4.16%
	F1	3j	0.63251	0.06616	0	1.000	0.02117	GOF = 2.30
	F2	3k	0.69928	0.73405	1/2	1.000	0.00355	
$Na_{1.5}Pr_{1.5}F_6$	Pr1	1a	0	0	0	1.000	0.01331	
	Na1	2h	1/3	2/3	0.65095	0.500	0.02904	R = 2.38%
	Na2/Pr2	1f	2/3	1/3	1/2	0.500/0.500	0.00816	wR = 3.47%
	F1	3j	0.63150	0.05129	0	1.000	0.01974	GOF = 2.16
	F2	3k	0.69833	0.73073	1/2	1.000	0.01217	

$Na_{1.5}Nd_{1.5}F_6$	Nd1	1a	0	0	0	1.000	0.00953	R = 3.10% wR = 3.19% GOF = 2.26
	Na1	2h	1/3	2/3	0.64019	0.500	0.01870	
	Na2/Nd2	1f	2/3	1/3	1/2	0.500/0.500	0.00869	
	F1	3j	0.63723	0.05225	0	1.000	0.01509	
	F2	3k	0.69640	0.73879	1/2	1.000	0.00259	
$Na_{1.5}Gd_{1.5}F_6$	Gd1	1a	0	0	0	1.000	0.01194	R = 4.85% wR = 8.99% GOF = 2.44
	Na1	2h	1/3	2/3	0.65252	0.500	0.01850	
	Na2/Gd2	1f	2/3	1/3	1/2	0.500/0.500	0.00408	
	F1	3j	0.63760	0.07524	0	1.000	0.01370	
	F2	3k	0.70901	0.73759	1/2	1.000	0.00804	
$Na_{1.5}Ho_{1.5}F_6$	Ho1	1a	0	0	0	1.000	0.01079	R = 5.17% wR = 4.52% GOF = 3.76
	Na1	2h	1/3	2/3	0.64542	0.500	0.02286	
	Na2/Ho2	1f	2/3	1/3	1/2	0.500/0.500	0.00487	
	F1	3j	0.63569	0.07407	0	1.000	0.01900	
	F2	3k	0.70800	0.74124	1/2	1.000	0.00929	
$Na_{1.5}Yb_{1.5}F_6$	Yb1	1a	0	0	0	1.000	0.01232	R = 3.68% wR = 6.45% GOF = 4.71
	Na1	2h	1/3	2/3	0.63641	0.500	0.01570	
	Na2/Yb2	1f	2/3	1/3	1/2	0.500/0.500	0.00288	
	F1	3j	0.63572	0.08052	0	1.000	0.01569	
	F2	3k	0.69792	0.73315	1/2	1.000	0.00836	
$Na_{1.5}Y_{1.5}F_6$	Y1	1a	0	0	0	1.000	0.01770	R = 3.15% wR = 5.57% GOF = 3.66
	Na1	2h	1/3	2/3	0.63210	0.500	0.01968	
	Na2/Y2	1f	2/3	1/3	1/2	0.500/0.500	0.00452	
	F1	3j	0.63744	0.07035	0	1.000	0.01910	
	F2	3k	0.71442	0.73500	1/2	1.000	0.01010	

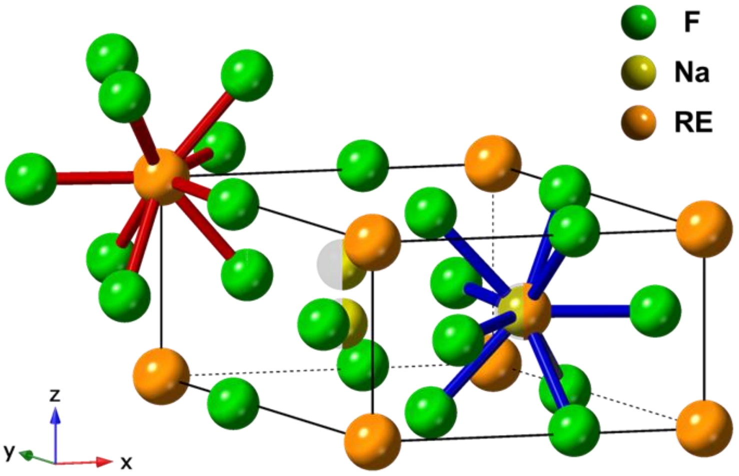

Figure 5.2 The β structure of $Na_{1.5}RE_{1.5}F_6$, in which the two one-fold sites RE1 and Na2/RE2 have 9 coordination (shown in red and blue, respectively), and the two-fold site (Na1) is occupied by the equal proportions of Na^+ and vacancies.

Table 5.2 Lattice parameters of $Na_{1.5}RE_{1.5}F_6$ in the space group of $P\bar{6}$ (Z = 1) obtained from Rietveld refinements of PXRD patterns.

Sample	a (Å)	c (Å)	V (Å^3)
$Na_{1.5}La_{1.5}F_6$	6.1830(3)	3.82819(6)	126.74(1)
$Na_{1.5}Ce_{1.5}F_6$	6.1541(4)	3.78222(7)	124.06(1)
$Na_{1.5}Pr_{1.5}F_6$	6.1295(4)	3.74692(7)	121.92(1)
$Na_{1.5}Nd_{1.5}F_6$	6.1098(4)	3.71776(8)	120.19(1)
$Na_{1.5}Gd_{1.5}F_6$	6.0329(5)	3.61194(9)	113.85(1)
$Na_{1.5}Ho_{1.5}F_6$	5.9843(4)	3.54079(7)	109.81(1)
$Na_{1.5}Yb_{1.5}F_6$	5.9428(3)	3.47937(6)	106.42(1)
$Na_{1.5}Y_{1.5}F_6$	5.9745(3)	3.52959(5)	109.11(1)

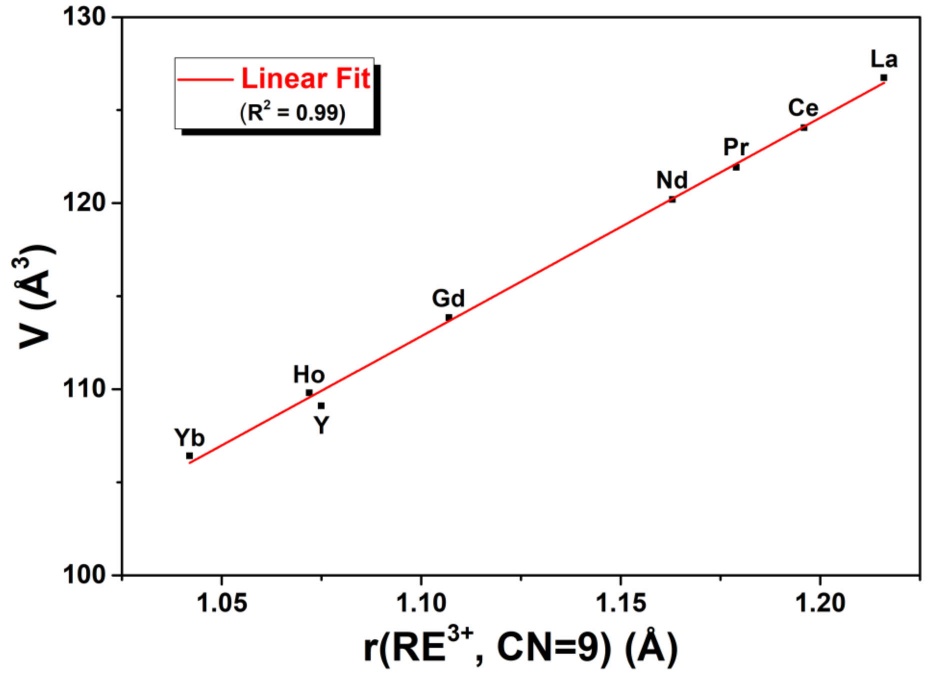

Figure 5.3 Unit cell volumes of $Na_{1.5}RE_{1.5}F_6$ derived from PXRD patterns versus ionic radii of RE^{3+} in 9 coordination with a linear fit in red.

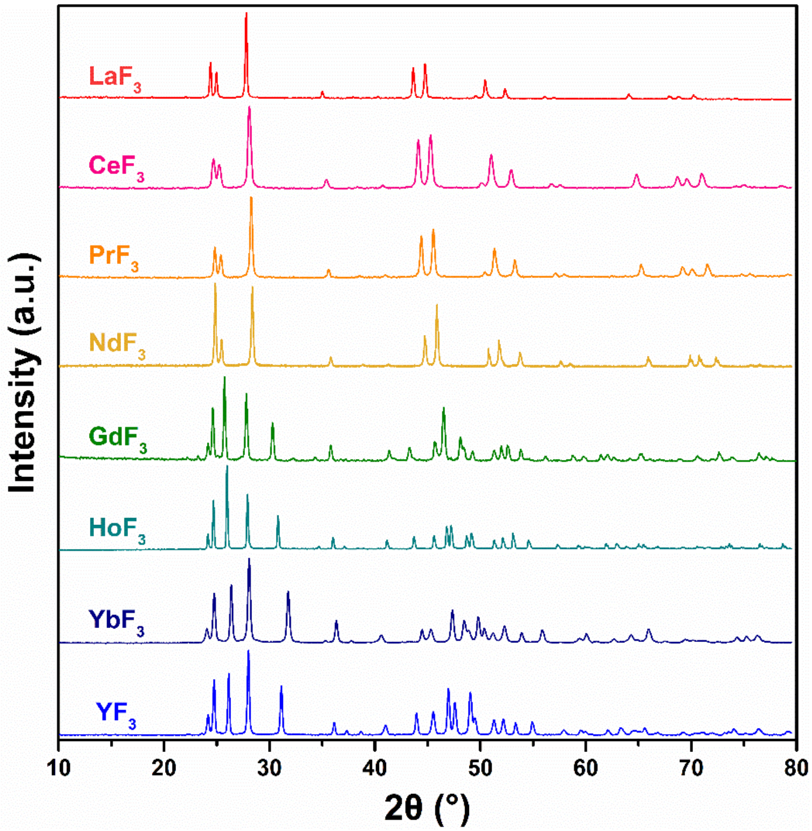

Figure 5.4 PXRD patterns of REF$_3$.

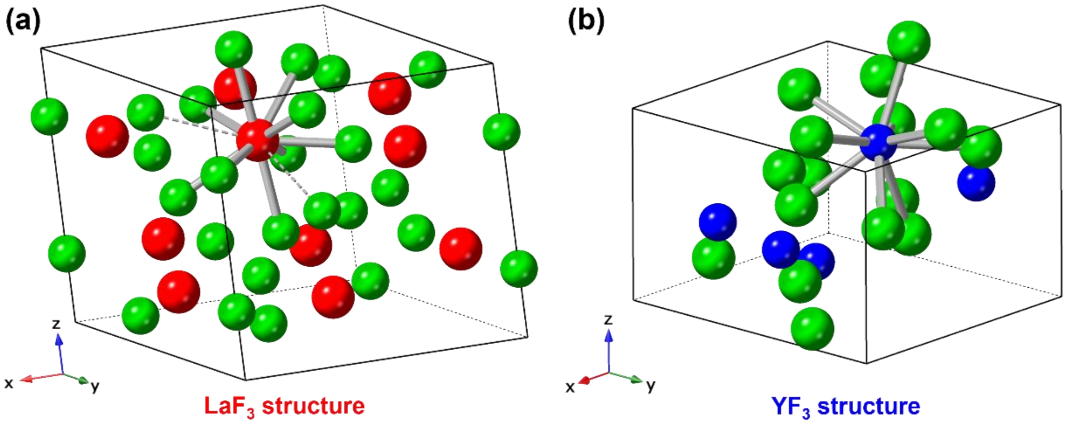

Figure 5.5 Schematic structures of (a) LaF$_3$ and (b) YF$_3$, in which red, blue, and green balls represent light and heavy RE elements and fluorine, respectively. The two longer RE−F bonds in the "LaF$_3$" structure are drawn with dotted lines.

All RE trifluorides were inspected by PXRD to confirm the phase purity (Figure 5.4). They form in two different structures: “LaF3” structure for light RE fluorides (LaF_3, CeF_3, PrF_3, and NdF_3) and “YF3” structure for heavy RE fluorides (GdF_3, HoF_3, YbF_3, and YF_3) (Figure 5.5). Light and heavy RE cations have (9+2) and 9 coordination in these two crystal structures, respectively.

High temperature oxide melt solution calorimetry was used to measure the enthalpy of drop solution (ΔH_{ds}) of fluorides, which is the enthalpy associated with dropping the sample from room temperature and dissolving it in sodium molybdate ($3Na_2O\cdot 4MoO_3$) melt at 800 °C. The data are shown in Table 5.3 and Table 5.4. The enthalpy of formation of the ternary fluorides from the binary fluorides ($\Delta H^\circ_{f,\,fl}$) is based on the following reaction,

$$3/2NaF\ (s, 25\ °C) + 3/2REF_3\ (s, 25\ °C) \rightarrow Na_{1.5}Nd_{1.5}F_6\ (s, 25\ °C) \qquad (5.1)$$

which is calculated directly from the calorimetric data via the thermodynamic cycle shown in Table 5.5.

Table 5.3 Enthalpies of drop solution of REF_3 (ΔH_{ds}-REF_3) and RE_2O_3 (ΔH_{ds}-RE_2O_3) in $3Na_2O\cdot 4MoO_3$ at 800 °C and enthalpies of formation from elements of REF_3 ($\Delta H^\circ_{f,\,el}$-REF_3) and RE_2O_3 ($\Delta H^\circ_{f,\,el}$-RE_2O_3), plus reaction enthalpies of the exchange reactions between NaF and RE_2O_3 from ΔH_{ds} ($\Delta H_{exchange}$) or $\Delta H^\circ_{f,\,el}$ ($\Delta H_{reaction}$).

Element	ΔH_{ds}-REF_3[a] (kJ mol^{-1})	ΔH_{ds}-RE_2O_3[b] (kJ mol^{-1})	$\Delta H^\circ_{f,\,el}$-REF_3 (kJ mol^{-1})	$\Delta H^\circ_{f,\,el}$-RE_2O_3 (kJ mol^{-1})	$\Delta H_{exchange}$ (kJ mol^{-1})	$\Delta H_{reaction}$ (kJ mol^{-1})
La	154.89 ± 0.58 (9)	−221.81 ± 2.25 [33]	−1731.8 ± 5.0 [34]	−1791.6 ± 2.0 [35]	504.91 ± 14.93	525.8 ± 16.9
Ce	134.54 ± 0.62 (8)[c]		−1732.6 ± 4.2 [34]	−1799.8 ± 1.8 [35]		532.4 ± 16.0
Pr	152.45 ± 0.86 (9)		−1712.1 ± 5.0 [34]	−1809.9 ± 3.0 [35]		583.5 ± 17.1

Nd	151.02 ± 1.32 (8)	−156.95 ± 1.05 [15]	−1712.9 ± 4.2 [34]	−1806.9 ± 3.0 [35]	577.51 ± 14.98	578.9 ± 16.2
Gd	145.72 ± 0.66 (8)	−134.48 ± 1.70 [15]	−1713.3 ± 4.6 [34]	−1819.7 ± 3.6 [35]	610.58 ± 14.87	590.9 ± 16.7
Ho	140.89 ± 0.72 (8)	−109.51 ± 1.50 [15]	−1714.2 ± 6.3 [34]	−1883.3 ± 8.2 [35]	645.21 ± 14.86	652.7 ± 20.2
Yb	126.94 ± 0.51 (9)	−90.71 ± 0.40 [24]	−1656.9 ± 10[d] [34]	−1814.5 ± 6.0 [35]	691.91 ± 14.75	698.5 ± 24.9
Y	146.69 ± 0.56 (8)	−116.34 ± 1.21 [15]	−1718.4 ± 3.3 [34]	−1905.0 ± 4.2 [34]	626.78 ± 14.80	666.0 ± 15.6

[a] Value is the mean of the number of experiments indicated in parentheses.

[b] There is no data of enthalpies of drop solution of Ce_2O_3 and Pr_2O_3 in $3Na_2O\cdot4MoO_3$ at 800 °C.

[c] Final state of Ce is Ce^{4+} dissolved in $3Na_2O\cdot4MoO_3$ at 800 °C.

[d] The error is not given in the reference and 10 kJ mol^{-1} is used as the error in the calculation.

Table 5.4 Enthalpies of drop solution (ΔH_{ds}), enthalpies of formation from fluorides ($\Delta H^\circ_{f,\,fl}$) and elements ($\Delta H^\circ_{f,\,el}$) of $Na_{1.5}RE_{1.5}F_6$.

Sample	ΔH_{ds}[a] (kJ mol^{-1})	$\Delta H^\circ_{f,\,fl}$ (kJ mol^{-1})	$\Delta H^\circ_{f,\,el}$[c] (kJ mol^{-1})
$Na_{1.5}La_{1.5}F_6$	340.36 ± 0.98 (10)	7.29 ± 1.4	–2302.2 ± 5.1
$Na_{1.5}Ce_{1.5}F_6$[b]	315.16 ± 0.66 (8)	1.97 ± 1.24	–2306.6 ± 4.4
$Na_{1.5}Pr_{1.5}F_6$	348.14 ± 0.87 (8)	−4.15 ± 1.63	–2290.2 ± 5.2
$Na_{1.5}Nd_{1.5}F_6$	352.03 ± 0.97 (8)	−10.18 ± 2.26	–2295 ± 4.5
$Na_{1.5}Gd_{1.5}F_6$	359.47 ± 0.96 (8)	−25.57 ± 1.47	–2305.6 ± 4.8
$Na_{1.5}Ho_{1.5}F_6$	354.34 ± 0.59 (8)	−27.69 ± 1.33	–2308 ± 6.4
$Na_{1.5}Yb_{1.5}F_6$	336.28 ± 0.85 (8)	−30.55 ± 1.25	–2252.6 ± 10.1
$Na_{1.5}Y_{1.5}F_6$	361.29 ± 0.55 (8)	−25.94 ± 1.12	–2311 ± 3.5

[a] Value is the mean of the number of experiments indicated in parentheses.

[b] Final state of Ce is Ce^{4+} dissolved in $3Na_2O\cdot4MoO_3$ at 800°C.

[c] $\Delta H^\circ_{f,\,el}$ values refer to the chemical formula $NaREF_4$.

Table 5.5 Thermodynamic cycles used to calculate enthalpies of formation from fluorides at 25 °C.

Reaction	ΔH
$Na_{1.5}RE_{1.5}F_6$ (s, 25 °C) → $3/2NaF$ (soln, 800 °C) + $3/2REF_3$ (soln, 800 °C)	$\Delta H_1 = \Delta H_{ds}$
NaF (s, 25 °C) → NaF (soln, 800 °C)	ΔH_2
REF_3 (s, 25 °C) → REF_3 (soln, 800 °C)	ΔH_3
$3/2NaF$ (s, 25 °C) + $3/2REF_3$ (s, 25 °C) → $Na_{1.5}Nd_{1.5}F_6$ (s, 25 °C)	$\Delta H^\circ_{f,\,fl}$
$\Delta H^\circ_{f,\,fl} = -\Delta H_1 + 3/2\Delta H_2 + 3/2\Delta H_3$	

To determine the ΔH_{ds} value of Na_2O in $3Na_2O{\cdot}4MoO_3$ at 800 °C, ΔH_{ds} of Na_2CO_3 under the same condition was measured and another thermodynamic cycle based on the following reaction is used (Table 5.6).

$$Na_2CO_3 \text{ (s, 25 °C)} \rightarrow Na_2O \text{ (soln, 800 °C)} + CO_2 \text{ (g, 800 °C)} \tag{5.2}$$

Table 5.6 Thermodynamic cycles used to calculate the drop solution enthalpy of Na_2O in $3Na_2O{\cdot}4MoO_3$ at 800 °C.

Reaction	ΔH ($kJ\ mol^{-1}$)
Na_2CO_3 (s, 25 °C) → Na_2O (soln, 800 °C) + CO_2 (g, 800 °C)	$\Delta H_1 = \Delta H_{ds}(Na_2CO_3) = 160.77 \pm 0.48$[a]
Na_2CO_3 (s, 25 °C) → Na_2O (s, 25 °C) + CO_2 (g, 25 °C)	$\Delta H_2 = 319.27 \pm 4.20$ [36]
CO_2 (g, 25 °C) → CO_2 (g, 800 °C)	$\Delta H_3 = 37.40$ [36]
Na_2O (s, 25 °C) → Na_2O (soln, 800 °C)	$\Delta H_4 = \Delta H_{ds}(Na_2O)$
$\Delta H_4 = \Delta H_1 - \Delta H_2 - \Delta H_3 = -195.90 \pm 4.23\ kJ\ mol^{-1}$	

[a] The value is based on eight drop experiments.

The enthalpy of formation from the elements ($\Delta H^\circ_{f,\,el}$) is calculated using the enthalpies of formation from the binary fluorides and the literature values of enthalpies of formation of binary fluorides from the elements.

To further check the consistency of the data, we calculated exchange enthalpies between oxides and fluorides for the exchange reaction

$$6NaF\ (s, 25\ °C) + RE_2O_3\ (s, 25\ °C) \rightarrow 3Na_2O\ (s, 25\ °C) + 2REF_3\ (s, 25\ °C) \quad (5.3)$$

based on the thermodynamic cycle shown in Table 5.7.

Table 5.7 Thermodynamic cycles used to calculate reaction enthalpies of the exchange reactions between NaF and RE_2O_3, in which $\Delta H_{exchange}$ and $\Delta H_{reaction}$ are from enthalpies of drop solution (ΔH_{ds}) and enthalpies of formation from elements ($\Delta H°_{f, el}$), respectively.

Reaction	ΔH (kJ mol^{-1})
NaF (s, 25 °C) → NaF (soln, 800 °C)	$\Delta H_1 = 76.88 \pm 0.33$[a]
REF_3 (s, 25 °C) → REF_3 (soln, 800 °C)	ΔH_2
Na_2O (s, 25 °C) → Na_2O (soln, 800 °C)	$\Delta H_3 = -195.90 \pm 4.23$
RE_2O_3 (s, 25 °C) → RE_2O_3 (soln, 800 °C)	ΔH_4
6NaF (s, 25 °C) + RE_2O_3 (s, 25 °C) → $3Na_2O$ (s, 25 °C) + $2REF_3$ (s, 25 °C)	
$\Delta H_{exchange} = 6\Delta H_1 + \Delta H_4 - 3\Delta H_3 - 2\Delta H_2$	
Na (s, 25 °C) + $1/2F_2$ (g, 25 °C) → NaF (s, 25 °C)	$\Delta H_5 = -575.3 \pm 0.8$ [36]
RE (s, 25 °C) + $3/2F_2$ (g, 25 °C) → REF_3 (s, 25 °C)	ΔH_6
2Na (s, 25 °C) + $1/2O_2$ (g, 25 °C) → Na_2O (s, 25 °C)	$\Delta H_7 = -418.0 \pm 4.2$ [36]
2RE (s, 25 °C) + $3/2O_2$ (g, 25 °C) → RE_2O_3 (s, 25 °C)	ΔH_8
6NaF (s, 25 °C) + RE_2O_3 (s, 25 °C) → $3Na_2O$ (s, 25 °C) + $2REF_3$ (s, 25 °C)	
$\Delta H_{reaction} = 3\Delta H_7 + 2\Delta H_6 - 6\Delta H_5 - \Delta H_8$	

[a] The value is based on eight drop experiments.

As demonstrated in Table 5.3, the reaction enthalpies of the exchange reactions between NaF and RE_2O_3 from ΔH_{ds} ($\Delta H_{exchange}$) and from $\Delta H°_{f, el}$ ($\Delta H_{reaction}$) are the same within experimental error. This agreement suggests that the reaction between fluorides and oxygen atmosphere is negligible in the dropping process, and there are no problems with dissolution and no specific interactions between fluoride components in the dilute molten solution. Earlier experiments show that the final state of most RE elements is RE^{3+} when dissolved in molten $3Na_2O{\cdot}4MoO_3$, but Ce^{3+} is oxidized to Ce^{4+}, producing less endothermic values of ΔH_{ds} compared to other light RE fluorides.[37] However, since the same final oxidation state occurs for CeF_3 and $Na_{1.5}Ce_{1.5}F_6$ in an O_2 atmosphere, these oxidation effects cancel out in calculating the heat of formation. The fluorides are completely dissolved and no solid intermediates are visible after dissolution in molten $3Na_2O{\cdot}4MoO_3$. Thus, any transient intermediate reactions during the dissolution of fluorides are included in ΔH_{ds} and cancelled out when any such possible intermediates (for which there is no evidence) dissolve. Furthermore, earlier studies[28] have shown that the molar heat of solution of a given RE fluoride does not depend on its (low) concentration in the melt or on the presence of dissolved NaF. This confirms that interactions between the dissolved fluoride species do not affect the measured enthalpies and the calorimetric cycles used give reliable results.

5.5 Discussion

As shown in Figure 5.6, $\Delta H^{\circ}_{f,\,fl}$ values range from +7.3 to −30.6 kJ mol^{-1}, and most ternary fluorides are energetically stable relative to binary fluorides. Nevertheless, sodium light RE fluorides, especially $Na_{1.5}La_{1.5}F_6$ and $Na_{1.5}Ce_{1.5}F_6$, have small positive enthalpies of formation and must be entropy-stabilized. A positive enthalpy of formation may result from differences in vibrational entropies and, more importantly, from configurational entropies arising from cation disorder. However, these entropy changes cannot be quantified at present. The idea that there is little or no thermodynamic driving force for formation of the La and Ce compounds near room temperature is consistent with their harsh synthetic conditions reported by previous studies,[38] and LaF_3 is often formed instead of $Na_{1.5}La_{1.5}F_6$ at relatively low temperature.[39] In addition, when serving as luminescent host matrices, RE fluorides are usually doped with different RE elements, and the mixing entropy may play a role in stabilizing these solid solution (alloy) materials.[40]

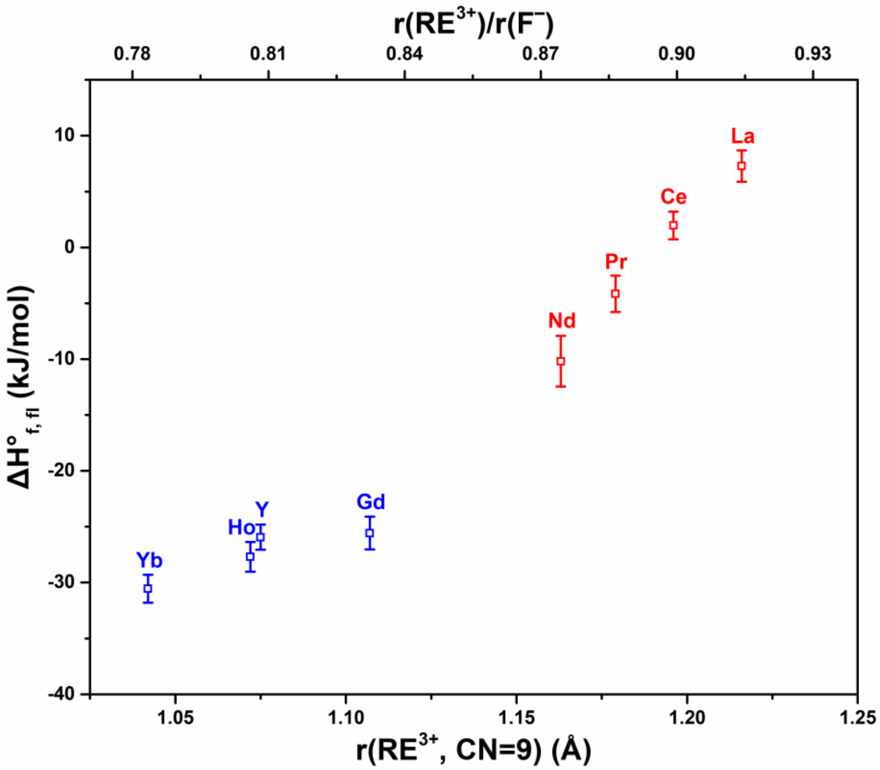

Figure 5.6 Enthalpies of formation from binary fluorides (ΔH°$_{f, fl}$) of $Na_{1.5}RE_{1.5}F_6$ at 25 °C. Light and heavy RE fluorides are shown in red and blue, respectively.

The variation of RE ion size partially explains the difference of thermodynamic stability in ternary fluorides. From La to Yb, the cation-anion radius ratio of RE^{3+}/F^- changes from 0.914 to 0.783, so light RE elements tend to form polyhedra with high coordination in fluorides. In particular, La, Ce, Pr, and Nd form binary fluorides in the “LaF_3” structure with (9+2) coordination, instead of the “YF_3” structure with 9 coordination formed for heavier RE. Ternary fluorides with sodium, in which RE^{3+} has 9 coordination on both RE1 and Na2/RE2 sites, form more favorably with heavy RE elements with smaller ionic radii than those with larger light RE cations. The ionic radius difference is also reflected in the nonuniform contraction of interatomic distances with respect to the overall decrease of lattice parameters. Bond length contraction mainly happens on the relatively loosely packed site (RE1) for light RE elements (La, Ce, Pr, and Nd) and then on the site with mixed occupancy (Na2/RE2) for heavy RE elements (Gd, Ho, Yb, and Y) (Figure 5.7), while the mean distance between the Na1 site and fluoride anions remains relatively constant (Figure 5.8).

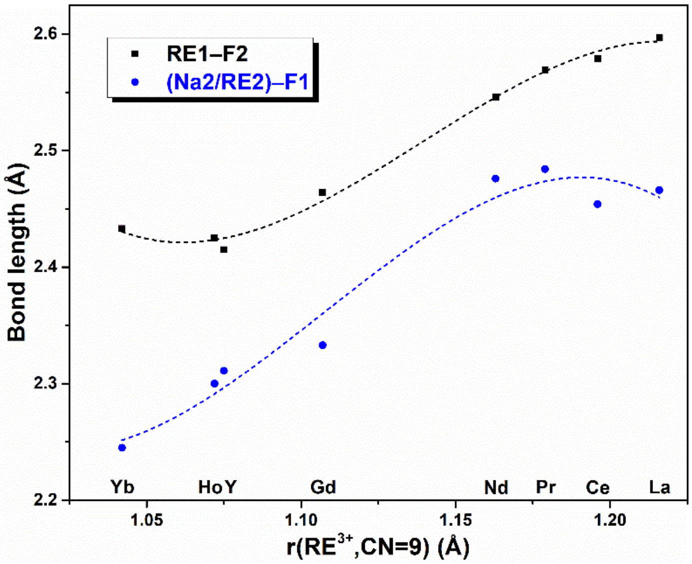

Figure 5.7 Interatomic distances for RE^{3+} versus ionic radii of RE^{3+} in $Na_{1.5}RE_{1.5}F_6$.

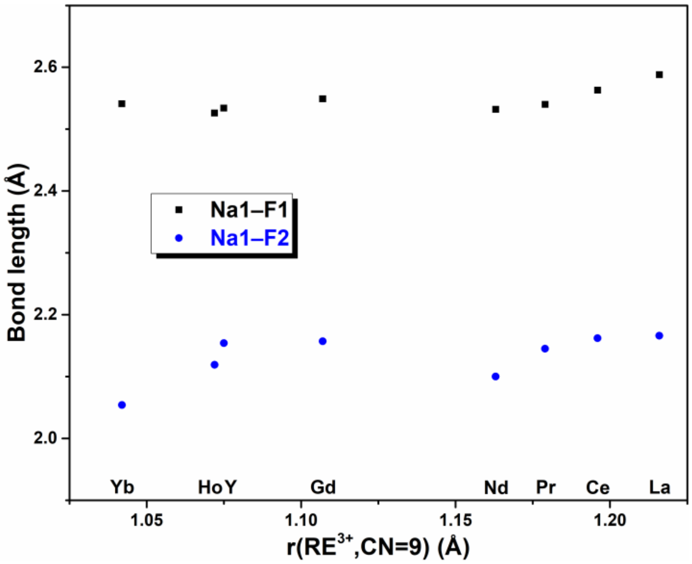

Figure 5.8 Interatomic distances for Na^{+} versus ionic radii of RE^{3+} in $Na_{1.5}RE_{1.5}F_6$.

Compared to most ternary RE oxide compounds,[41] enthalpies of formation from binary components of $Na_{1.5}RE_{1.5}F_6$ follow a reverse trend, namely they become more exothermic with the decreasing RE ionic radii. Based on enthalpies of formation from elements ($\Delta H°_{f,\ el}$), the Born–Haber cycles were used to calculate lattice energies of $NaREF_4$ and REF_3 (Table 5.8–5.10), both of which become more exothermic as the ionic radius of RE^{3+} decreases, as generally expected (Figure 5.9). But different slopes of lattice energies against ionic radii or lattice shrinkage lead to more negative values of lattice energy differences for formation of $NaREF_4$ from NaF and REF_3 for smaller RE cations, supporting the observed trend in enthalpies of formation.

Table 5.8 Summary of reactions in Born–Haber cycles for the formation of $NaREF_4$ and REF_3.

Reaction	ΔH (kJ mol^{-1})
Na (s, 25 °C) → Na (g, 25 °C)	$\Delta H_1 = 107.5 \pm 0.7$ [36]
Na (g, 25 °C) → Na^+ (g, 25 °C) + e^-	$\Delta H_2 = 495.8$ [36]
RE (s, 25 °C) → RE (g, 25 °C)	$\Delta H_3 = \Delta H_{sub}$
RE (g, 25 °C) → RE^{3+} (g, 25 °C) + $3e^-$	$\Delta H_4 = (I_1+I_2+I_3)$
F_2 (g, 25 °C) → 2F (g, 25 °C)	$\Delta H_5 = 158.7 \pm 0.1$ [42]
F (g, 25 °C) + e^- → F^- (g, 25 °C)	$\Delta H_6 = -328.2$ [42]
Na (s, 25 °C) + RE (s, 25 °C) + $2F_2$ (g, 25 °C) → $NaREF_4$ (s, 25 °C)	$\Delta H_7 = \Delta H°_{f,\ el}$-$NaREF_4$
Na^+ (g, 25 °C) + RE^{3+}(g, 25 °C) + $4F^-$ (g, 25 °C) → $NaREF_4$ (s, 25 °C)	U($NaREF_4$)
U($NaREF_4$) = $\Delta H_7 - \Delta H_1 - \Delta H_2 - \Delta H_3 - \Delta H_4 - 2\Delta H_5 - 4\Delta H_6$	
RE (s, 25 °C) → RE (g, 25 °C)	$\Delta H_3 = \Delta H_{sub}$
RE (g, 25 °C) → RE^{3+} (g, 25 °C) + $3e^-$	$\Delta H_4 = (I_1+I_2+I_3)$
F_2 (g, 25 °C) → 2F (g, 25 °C)	$\Delta H_5 = 158.7 \pm 0.1$ [42]
F (g, 25 °C) + e^- → F^- (g, 25 °C)	$\Delta H_6 = -328.2$ [42]
RE (s, 25 °C) + $3/2F_2$ (g, 25 °C) → REF_3 (s, 25 °C)	$\Delta H_8 = \Delta H°_{f,\ el}$-$REF_3$
RE^{3+}(g, 25 °C) + $3F^-$ (g, 25 °C) → REF_3 (s, 25 °C)	U(REF_3)
U(REF_3) = $\Delta H_8 - \Delta H_3 - \Delta H_4 - 3/2\Delta H_5 - 3\Delta H_6$	

Table 5.9 Enthalpies of sublimation (ΔH_{sub}) and ionization ($I_1+I_2+I_3$) of rare earth elements.

RE element	ΔH_{sub} (kJ mol^{-1})	($I_1+I_2+I_3$) (kJ mol^{-1})
La	434.5 ± 3.0 [43]	3455 ± 5 [44]
Ce	424.8 ± 3.0 [43]	3523 ± 5 [44]
Pr	356.6 ± 3.0 [43]	3627 ± 5 [44]
Nd	325.6 ± 2.0 [43]	3694 ± 5 [44]
Gd	406.9 ± 2.0 [43]	3750 ± 5 [44]
Ho	305.5 ± 5.0 [43]	3924 ± 5 [44]
Yb	152.4 ± 1.0 [43]	4194 ± 5 [44]
Y	421.3 ± 5.0 [45]	3777 ± 5 [44]

Table 5.10 Lattice energies (U) of NaF, REF_3 and $NaREF_4$ calculated from Born–Haber cycles.

Fluoride	U (kJ mol^{-1})	Fluoride	U (kJ mol^{-1})
NaF	–927 [46]		
LaF_3	–4874.8 ± 5.8	$NaLaF_4$	–5799.6 ± 7.8
CeF_3	–4933.9 ± 5.8	$NaCeF_4$	–5862.3 ± 7.3
PrF_3	–4949.2 ± 5.8	$NaPrF_4$	–5881.7 ± 7.8
NdF_3	–4986.0 ± 5.4	$NaNdF_4$	–5922.5 ± 7.1
GdF_3	–5123.7 ± 5.4	$NaGdF_4$	–6070.4 ± 7.3
HoF_3	–5197.2 ± 7.1	$NaHoF_4$	–6145.4 ± 9.6
YbF_3	–5256.8 ± 5.1	$NaYbF_4$	–6206.9 ± 11.3
YF_3	–5170.2 ± 7.1	$NaYF_4$	–6117.2 ± 7.9

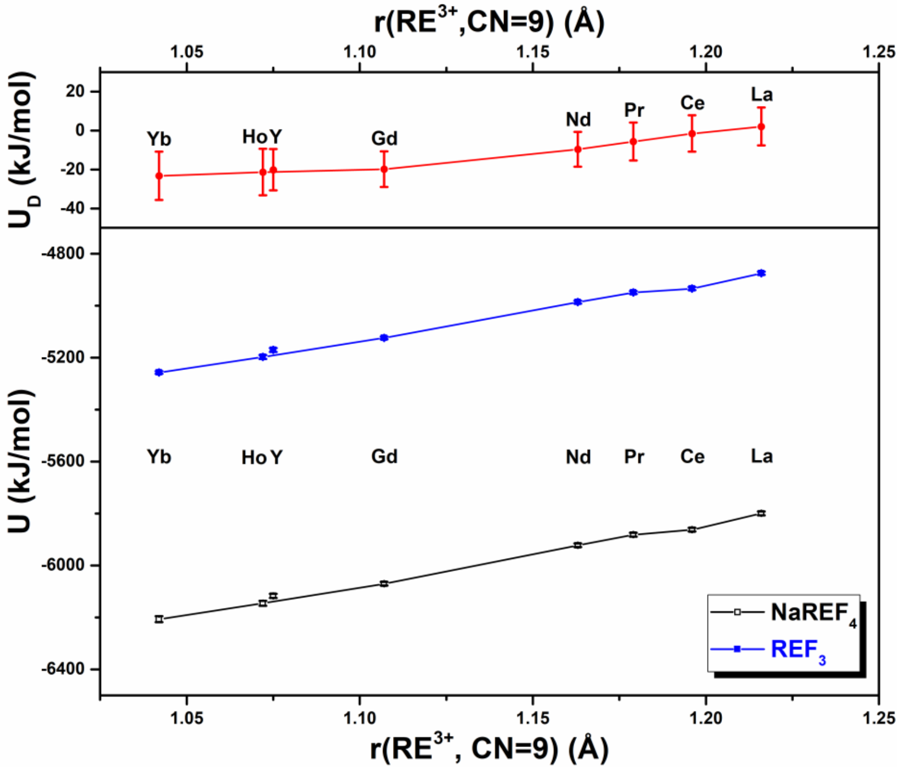

Figure 5.9 Lattice energies (U) of REF_3 and $NaREF_4$ plus differences from REF_3 and NaF to $NaREF_4$ (U_D = U($NaREF_4$) – U(REF_3) – U(NaF)) versus ionic radii of RE^{3+}.

In most oxide compounds, RE^{3+} generally occupies cation sites with coordination numbers ranging from 7 to 12, higher than in corresponding sesquioxides (6 and 7 coordination for C and A type, respectively).[47] The increase of coordination numbers, leading to increasing bond lengths, is in conjunction with the trend of less exothermic enthalpies of formation from oxides ($\Delta H°_{f,\,ox}$) from light to heavy RE elements (Figure 5.10). However, when RE^{3+} has lower coordination in the ternary crystal structure, such as $LaREO_3$[16] and $BaRE_2O_4$[10], $\Delta H°_{f,\,ox}$ becomes more exothermic with heavier RE elements. It is reasonable to link the coordination number of RE cations to the trend of lattice energies versus ionic radii, i.e., higher coordination is accompanied by a slower increase of lattice energies with lattice contraction. In contrast to coordination in oxides, RE^{3+} has relatively high coordination in binary trifluorides, i.e., (9+2) and 9 coordination in “LaF3” and “YF3” structures, respectively. The formation of $Na_{1.5}RE_{1.5}F_6$ from binary fluorides occurs with a decrease or constancy of the coordination number of RE^{3+}, as well as with more exothermic $\Delta H°_{f,\,fl}$ for heavier RE elements. This tendency is more obvious among light RE elements with coordination reduction from REF_3 to $Na_{1.5}RE_{1.5}F_6$, manifesting as more rapid variation of $\Delta H°_{f,\,fl}$ from La to Nd (Figure 5.6). Considering that presently known ternary RE fluorides have the same or lower coordination numbers than REF_3,[48] it is possible that more “reverse” trends of enthalpies of formation exist in other ternary RE fluoride systems.

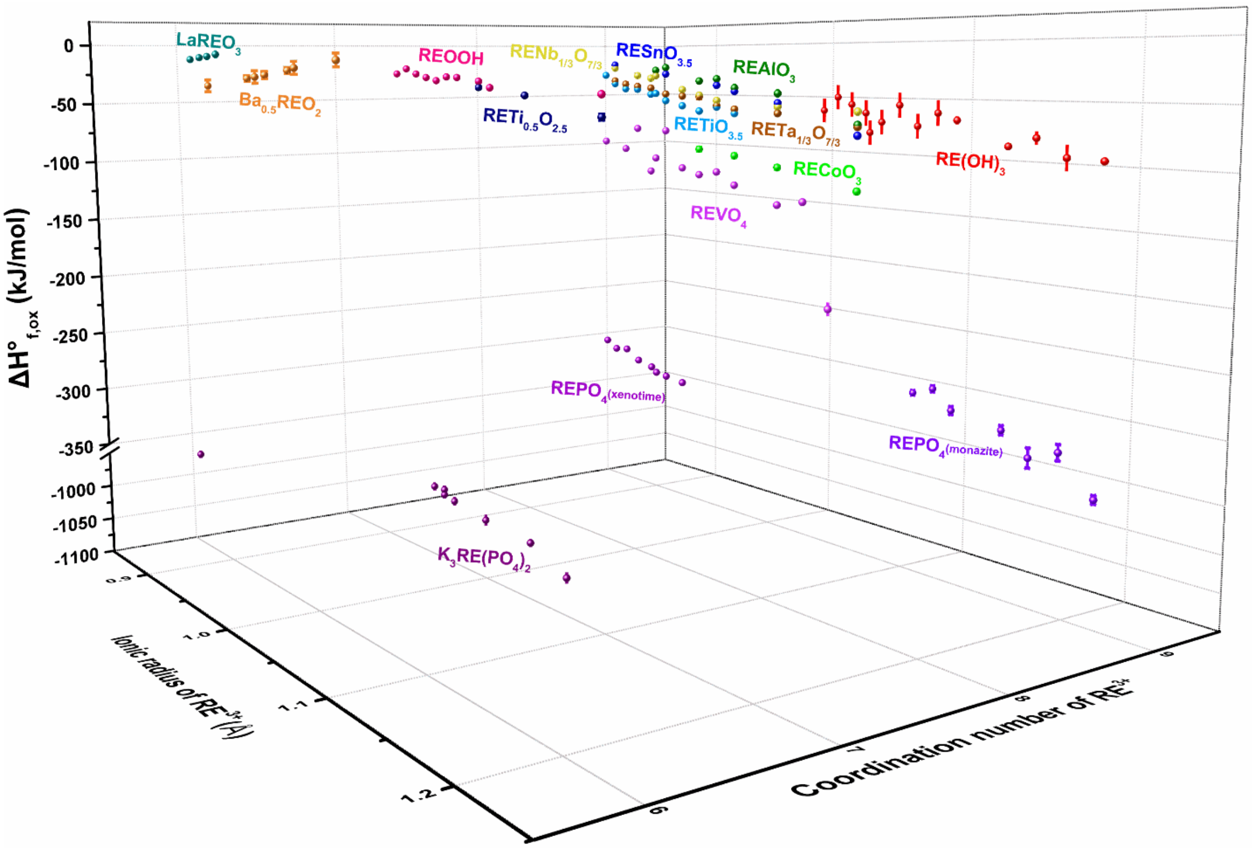

Figure 5.10 Summary of enthalpies of formation from oxides ($\Delta H°_{f,\,ox}$) of ternary RE oxide compounds versus ionic radii of RE^{3+} in various coordination numbers. Data are from References 10–24.

5.6 Conclusions

With the help of high temperature oxide melt solution calorimetry, enthalpies of formation of sodium RE fluorides were determined to investigate thermodynamic stability of $NaREF_4$ in the β structure ($Na_{1.5}RE_{1.5}F_6$) with varying RE elements. These results have important implications in syntheses and applications of $NaREF_4$ materials, particularly from aqueous systems, in which the formation of ternary fluorides is in competition with the formation of binary fluorides. Different from most ternary RE oxide compounds, a reverse trend of enthalpies of formation from binary fluorides were found in this ternary fluoride system. The more exothermic enthalpies of formation from fluorides for heavier RE cannot be explained simply by size difference, and the quantitative assessment of lattice energies by Born–Haber cycles illustrates that coordination of RE ions plays an important role in thermodynamic stability of compounds along the lanthanide series. In opposition to the formation of most RE oxide ternary compounds showing coordination increase from the binaries, the formation of ternary RE fluorides occurs with a decrease or constancy of the coordination number of RE^{3+}, resulting in a faster increase of lattice energies versus lattice contraction and more exothermic enthalpies of formation for smaller RE ions. The coordination number change of RE ions not only gives a new perspective on the energetics of ionic compounds, but also guides predictions of thermodynamic stability of other possible RE compounds. In addition, the reverse trend of RE fluorides compared to oxide compounds may inspire new reaction pathways to recycle RE elements from leachate compositions or to separate RE elements in solutions.

5.7 Acknowledgements

This work was supported by U.S. Department of Energy Critical Materials Institute (CMI) Hub (grant number DE-AC02-07CH11358). We acknowledge the use of facilities within the Eyring Materials Center at Arizona State University supported in part by NNCI-ECCS-2025490. Shuhao Yang would like to thank David Wright and Tamilarasan Subramani for help in sample preparation, Jayanthi Kumar for help in Rietveld analysis, and Albert A. Voskanyan for fruitful discussions.

5.8 References

(1) Wang, F.; Han, Y.; Lim, C. S.; Lu, Y.; Wang, J.; Xu, J.; Chen, H.; Zhang, C.; Hong, M.; Liu, X. Simultaneous phase and size control of upconversion nanocrystals through lanthanide doping. *Nature* **2010**, *463*, 1061–1065.

(2) Han, S.; Deng, R.; Gu, Q.; Ni, L.; Huynh, U.; Zhang, J.; Yi, Z.; Zhao, B.; Tamura, H.; Pershin, A.; Xu, H.; Huang, Z.; Ahmad, S.; Abdi-Jalebi, M.; Sadhanala, A.; Tang, M. L.; Bakulin, A.; Beljonne, D.; Liu, X.; Rao, A. Lanthanide-doped inorganic nanoparticles turn molecular triplet excitons bright. *Nature* **2020**, *587*, 594–599.

(3) Lee, C.; Xu, E. Z.; Liu, Y.; Teitelboim, A.; Yao, K.; Fernandez-Bravo, A.; Kotulska, A. M.; Nam, S. H.; Suh, Y. D.; Bednarkiewicz, A.; Cohen, B. E.; Chan, E. M.; Schuck, P. J. Giant nonlinear optical responses from photon-avalanching nanoparticles. *Nature* **2021**, *589*, 230–235.

(4) Gai, S.; Li, C.; Yang, P.; Lin, J. Recent progress in rare earth micro/nanocrystals: soft chemical synthesis, luminescent properties, and biomedical applications. *Chem. Rev.* **2014**, *114*, 2343–2389.

(5) Thoma, R. E.; Insley, H.; Hebert, G. M. The sodium fluoride-lanthanide trifluoride systems. *Inorg. Chem.* **1966**, *5*, 1222–1229.

(6) Fedorov, P. Systems of alkali and rare-earth metal fluorides. *Russ. J. Inorg. Chem.* **1999**, *44*, 1703–1727.

(7) Mai, H.-X.; Zhang, Y.-W.; Si, R.; Yan, Z.-G.; Sun, L.-D.; You, L.-P.; Yan, C.-H. High-quality sodium rare-earth fluoride nanocrystals: controlled synthesis and optical properties. *J. Am. Chem. Soc.* **2006**, *128*, 6426–6436.

(8) Wang, L.; Li, P.; Li, Y. Down- and up-conversion luminescent nanorods. *Adv. Mater.* **2007**, *19*, 3304–3307.

(9) Haas, J. R.; Shock, E. L.; Sassani, D. C. Rare earth elements in hydrothermal systems: estimates of standard partial molal thermodynamic properties of aqueous complexes of the rare earth elements at high pressures and temperatures. *Geochim. Cosmochim. Acta* **1995**, *59*, 4329–4350.

(10) Gong, W.; Liu, Y.; Xie, Y.; Zhao, Z.; Ushakov, S. V. Thermodynamic assessment of BaO-Ln_2O_3 (Ln = La, Pr, Eu, Gd, Er) systems. *J. Am. Ceram. Soc.* **2020**, *103*, 3896–3904.

(11) Hayun, S.; Navrotsky, A. Formation enthalpies and heat capacities of rare earth titanates: RE_2TiO_5 (RE=La, Nd and Gd). *J. Solid State Chem.* **2012**, *187*, 70–74.

(12) Helean, K. B.; Ushakov, S. V.; Brown, C. E.; Navrotsky, A.; Lian, J.; Ewing, R. C.; Farmer, J. M.; Boatner, L. A. Formation enthalpies of rare earth titanate pyrochlores. *J. Solid State Chem.* **2004**, *177*, 1858–1866.

(13) Kanke, Y.; Navrotsky, A. A calorimetric study of the lanthanide aluminum oxides and the lanthanide gallium oxides: stability of the perovskites and the garnets. *J. Solid State Chem.* **1998**, *141*, 424–436.

(14) Lian, J.; Helean, K. B.; Kennedy, B. J.; Wang, L. M.; Navrotsky, A.; Ewing, R. C. Effect of structure and thermodynamic stability on the response of lanthanide stannate pyrochlores to ion beam irradiation. *J. Phys. Chem. B* **2006**, *110*, 2343–2350.

(15) Mielewczyk-Gryn, A.; Navrotsky, A. Enthalpies of formation of rare earth niobates, RE_3NbO_7. *Am. Mineral.* **2015**, *100*, 1578–1583.

(16) Qi, J.; Guo, X.; Mielewczyk-Gryn, A.; Navrotsky, A. Formation enthalpies of $LaLn'O_3$ (Ln′=Ho, Er, Tm and Yb) interlanthanide perovskites. *J. Solid State Chem.* **2015**, *227*, 150–154.

(17) Sahu, S. K.; Tanasescu, S.; Scherrer, B.; Marinescu, C.; Navrotsky, A. Energetics of lanthanide cobalt perovskites: $LnCoO_{3-\delta}$ (Ln = La, Nd, Sm, Gd). *J. Mater. Chem. A* **2015**, *3*, 19490–19496.

(18) Subramani, T.; Navrotsky, A. Energetics of formation and disordering in rare earth weberite RE_3TaO_7 materials. *Inorg. Chem.* **2019**, *58*, 16126–16133.

(19) Alvero, R.; Bernal, A.; Carrizosa, I.; Odriozola, J. A.; Trillo, J. M. Lanthanide oxides: thermochemical approach to hydration. *J. Mater. Sci.* **1987**, *22*, 1517–1520.

(20) Cordfunke, E. H. P.; Konings, R. J. M.; Ouweltjes, W. The standard enthalpies of formation of hydroxides IV. $La(OH)_3$ and LaOOH. *J. Chem. Thermodyn.* **1990**, *22*, 449–452.

(21) Diakonov, I. I.; Ragnarsdottir, K. V.; Tagirov, B. R. Standard thermodynamic properties and heat capacity equations of rare earth hydroxides: II. Ce(III)-, Pr-, Sm-, Eu(III)-, Gd-, Tb-, Dy-, Ho-, Er-, Tm-, Yb-, and Y-hydroxides. Comparison of thermochemical and solubility data. *Chem. Geol.* **1998**, *151*, 327–347.

(22) Dorogova, M.; Navrotsky, A.; Boatner, L. A. Enthalpies of formation of rare earth orthovanadates, $REVO_4$. *J. Solid State Chem.* **2007**, *180*, 847–851.

(23) Ushakov, S. V.; Helean, K. B.; Navrotsky, A.; Boatner, L. A. Thermochemistry of rare-earth orthophosphates. *J. Mater. Res.* **2001**, *16*, 2623–2633.

(24) Yang, S.; Powell, M.; Kolis, J. W.; Navrotsky, A. Thermochemistry of rare earth oxyhydroxides, REOOH (RE = Eu to Lu). *J. Solid State Chem.* **2020**, *287*, 121344.

(25) Shivaramaiah, R.; Anderko, A.; Riman, R. E.; Navrotsky, A. Thermodynamics of bastnaesite: a major rare earth ore mineral. *Am. Mineral.* **2016**, *101*, 1129–1134.

(26) Toby, B. H.; Von Dreele, R. B. GSAS-II: the genesis of a modern open-source all purpose crystallography software package. *J. Appl. Cryst.* **2013**, *46*, 544–549.

(27) Navrotsky, A. Progress and new directions in high temperature calorimetry. *Phys. Chem. Miner.* **1977**, *2*, 89–104.

(28) Navrotsky, A. Progress and new directions in high temperature calorimetry revisited. *Phys. Chem. Miner.* **1997**, *24*, 222–241.

(29) Navrotsky, A. Progress and new directions in calorimetry: a 2014 perspective. *J. Am. Ceram. Soc.* **2014**, *97*, 3349–3359.

(30) Grzechnik, A.; Friese, K. Crystal structures and stability of $NaLnF_4$ (Ln = La, Ce, Pr, Nd, Sm and Gd) studied with synchrotron single-crystal and powder diffraction. *Dalton Trans.* **2012**, *41*, 10258–10266.

(31) Shannon, R. Revised effective ionic radii and systematic studies of interatomic distances in halides and chalcogenides. *Acta Cryst.* **1976**, *A32*, 751–767.

(32) Kim, P.; Anderko, A.; Navrotsky, A.; Riman, R. E. Trends in structure and thermodynamic properties of normal rare earth carbonates and rare earth hydroxycarbonates. *Minerals* **2018**, *8*, 106.

(33) Mielewczyk-Gryn, A.; Wachowski, S.; Lilova, K. I.; Guo, X.; Gazda, M.; Navrotsky, A. Influence of antimony substitution on spontaneous strain and thermodynamic stability of lanthanum orthoniobate. *Ceram. Int.*, **2015**, *41*, 2128–2133.

(34) Glushko, V. P. *Thermochemical Constants of Substances*; Academy of Sciences of USSR, 1978.

(35) Konings, R. J. M.; Beneš, O.; Kovács, A.; Manara, D.; Sedmidubský, D.; Gorokhov, L.; Iorish, V. S.; Yungman, V.; Shenyavskaya, E.; Osina, E. The thermodynamic properties of the f-elements and their compounds. Part 2. The lanthanide and actinide oxides. *J. Phys. Chem. Ref. Data* **2014**, *43*, 013101.

(36) Chase, M. W. J., *NIST-JANAF Thermochemical Tables*. 4th ed.; J. Phys. Chem. Ref. Data, Monograph, 1998; Vol. 9, pp 1–1951.

(37) Helean, K. B.; Navrotsky, A. Oxide melt solution calorimetry of rare earth oxides. *J. Therm. Anal. Calorim.* **2002**, *69*, 751–771.

(38) Sun, X.; Wang, X.; Chen, B.; Zhao, F.; Xu, X.; Ren, K.; Lu, Y.; Qiao, X.; Qian, G.; Fan, X. Phase and morphology evolution of luminescent $NaLnF_4$ (Ln = La to Yb) micro-crystals: understanding the ionic radii and surface energy-dependent solution growth mechanism. *CrystEngComm* **2019**, *21*, 6652–6658.

(39) Kuznetsov, S. V.; Ovsyannikova, A. A.; Tupitsyna, E. A.; Yasyrkina, D. S.; Voronov, V. V.; Batyrev, N. I.; Iskhakova, L. D.; Osiko, V. V.; Fedorov, P. P. Phase formation in LaF_3–$NaGdF_4$, $NaGdF_4$–$NaLuF_4$, and $NaLuF_4$–$NaYF_4$ systems: synthesis of powders by co-precipitation from aqueous solutions. *J. Fluor. Chem.* **2014**, *161*, 95–101.

(40) McCormack, S. J.; Navrotsky, A. Thermodynamics of high entropy oxides. *Acta Mater.* **2021**, *202*, 1–21.

(41) Navrotsky, A.; Lee, W.; Mielewczyk-Gryn, A.; Ushakov, S. V.; Anderko, A.; Wu, H.; Riman, R. E. Thermodynamics of solid phases containing rare earth oxides. *J. Chem. Thermodyn.* **2015**, *88*, 126–141.

(42) Rumble, J. R. *CRC Handbook of Chemistry and Physics*, 101st ed.; CRC Press/Taylor & Francis, 2020.

(43) Konings, R. J. M.; Beneš, O. The thermodynamic properties of the f-elements and their compounds. I. The lanthanide and actinide metals. *J. Phys. Chem. Ref. Data* **2010**, *39*, 043102.

(44) Cotton, S. *Lanthanide and Actinide Chemistry*; John Wiley & Sons, 2006.

(45) Morss, L. R. Thermochemical properties of yttrium, lanthanum, and the lanthanide elements and ions. *Chem. Rev.* **1976**, *76*, 827–841.

(46) Holbrook, J. B.; Sabry-Grant, R.; Smith, B. C.; Tandel, T. V. Lattice enthalpies of ionic halides, hydrides, oxides, and sulfides: second-electron affinities of atomic oxygen and sulfur. *J. Chem. Educ.* **1990**, *67*, 304–307.

(47) Adachi, G.-y.; Imanaka, N. The binary rare earth oxides. *Chem. Rev.* **1998**, *98*, 1479–1514.

(48) Leblanc, M.; Maisonneuve, V.; Tressaud, A. Crystal chemistry and selected physical properties of inorganic fluorides and oxide-fluorides. *Chem. Rev.* **2015**, *115*, 1191–1254.

Chapter 6

Thermochemical Investigation of the Stability and Conversion of Nanocrystalline and High-Temperature Phases in Sodium Neodymium Fluorides

Shuhao Yang,[†,‡] K. Jayanthi,[†] Andre Anderko,[‖] Richard E. Riman,[§] Alexandra Navrotsky[*,†]

[†]Navrotsky Eyring Center for Materials of the Universe, School of Molecular Sciences, Arizona State University, Tempe, Arizona 85287, United States

[‡]Department of Chemistry, University of California, Davis, California 95616, United States

[‖]OLI Systems, Inc., Parsippany, New Jersey 07054, United States

[§]Department of Materials Science and Engineering, Rutgers, The State University of New Jersey, Piscataway, New Jersey 08854, United States

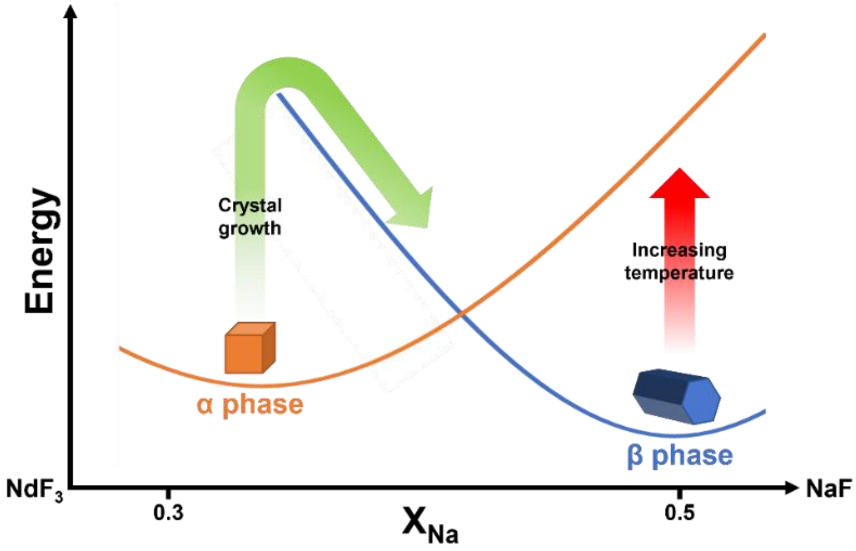

Chem. Mater. **2021**, *33*, 9571–9579.

6.1 Abstract

As important upconversion materials, sodium rare-earth fluorides (nominally $NaREF_4$ in composition but actually often harboring sodium deficiency, especially in nanophase materials) have been subjected to intensive studies, particularly in the synthesis and applications of nanocrystals. However, the mechanisms of the conversion between the two phases (α and β) of $NaREF_4$ nanocrystals during the synthesis are still controversial and lack thermodynamic investigations, which limit the rational design, synthesis, and processing of these materials. In this work, aiming at $NaREF_4$ with light rare-earth elements, the thermochemistry of the NaF–NdF_3 system, including the α and β phases in nanocrystalline/nanophase and bulk stoichiometric samples, is systematically studied by thermogravimetry and differential scanning calorimetry and high temperature oxide melt solution calorimetry. With the help of compositional analysis and structural characterization, a strong Na deficiency is found in nanocrystals with small crystal sizes, which leads to the formation of cubic (α) crystallographic polymorphs at the nucleation stage, possibly because of the relative thermodynamic stability of the α phase compared to the β phase in such compositions. After converting to the hexagonal (β) structure, the crystal growth is accompanied by an increase of Na content in nanocrystals with increasing energetic stability until the formation of the stoichiometric compound (β-$NaNdF_4$). On the contrary, the stoichiometric α phase (α-$NaNdF_4$) is metastable at room temperature but is the intermediate phase as the temperature increases. We show that the $\alpha \rightarrow \beta$ phase conversion in aqueous solution synthesis is distinct from the $\beta \rightarrow \alpha$ transition driven by temperature because of composition differences.

6.2 Introduction

Sodium rare-earth fluorides ($NaREF_4$) have drawn great research interest and are widely used as host materials for a variety of phosphors due to their unique upconversion properties.[1,2] Benefitting from the development of nanotechnology, steady progress has been made in the synthesis and applications of $NaREF_4$ nanocrystals, in particular for bioimaging and therapeutic applications.[3,4] With the emergence of precise control of nanostructures, new photoluminescence (PL) phenomena were also achieved in $NaREF_4$ nanomaterials.[5–7] All these advances not only shed light on the structure–property relationships in the optical field but also motivate the research to understand the structural changes in the synthetic process.

Solvothermal reactions were initially used to synthesize high-quality $NaREF_4$ nanocrystals.[8] However, owing to economic advantages and environmental friendliness, aqueous-phase synthesis, including coprecipitation and hydrothermal reactions, is gradually becoming the mainstream route in the preparation of $NaREF_4$ nanocrystals.[9,10] In aqueous solutions, a number of synthetic factors such as precursors, temperature, and pH have great influence on the phase, size, composition, and morphology of nanocrystals.[11–14] For example, a cubic α phase is usually obtained as nanocrystals with small sizes and transforms to a hexagonal β phase as nanocrystals grow larger when the synthesis time or temperature increases. Many studies involved the $\alpha \rightarrow \beta$ phase conversion for $NaYF_4$ nanocrystals and proposed related crystal growth mechanisms based on the oriented growth of nanoparticles.[12,15,16] However, these theories cannot give a good reason for the appearance of the α phase in the low-temperature range (<200 °C), which occurs as high-temperature solid solutions with less NaF than REF_3 in the phase diagrams.[17,18] In addition, a $\beta \rightarrow \alpha$ transition happens in $NaREF_4$ when the temperature increases,[19,20] indicating the metastability of the α phase of $NaREF_4$ at room temperature. Hence, the energetic relationship between α and β phases in nanocrystals remains unknown, and the thermodynamics of the phase conversion in aqueous solutions needs further research.[21,22]

$NaNdF_4$ nanocrystals can be used as photothermal agents by virtue of the near-infrared absorbing window[23,24] but are more difficult to prepare compared to $NaREF_4$ nanocrystals with heavier RE elements.[25] In our previous work, the thermochemistry of stoichiometric $NaREF_4$ with varying RE elements was systematically investigated, showing that the thermodynamic stability of $NaREF_4$ compounds increases from light to heavy RE elements.[26] Here, to study the energetics of α and β phases in nanocrystals and at different temperatures, especially for $NaREF_4$ with light RE elements, a series of NaF–NdF_3 samples with α and/or β phases were synthesized and characterized.

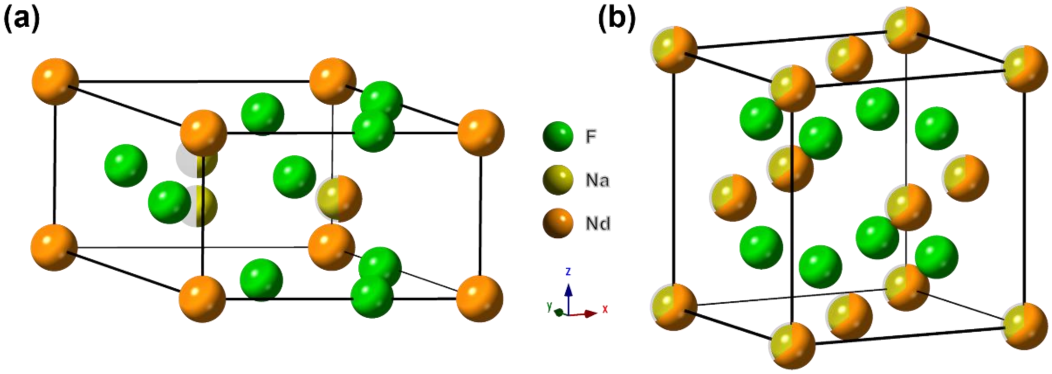

Figure 6.1 Crystal structures of a (a) stoichiometric β-$NaNdF_4$ compound and (b) NaF–NdF_3 solid solution with the α phase structure.

The typical β phase is a stoichiometric compound $NaNdF_4$ or $Na_{1.5}Nd_{1.5}F_6$ with three cation sites in the hexagonal lattice (Figure 6.1a), in which a one-fold site is occupied by Nd^{3+}, the other one-fold site is occupied by $1/2Na^+$ and $1/2Nd^{3+}$, and the two-fold site is occupied by Na^+ and vacancies.[27,28] In contrast, the α phase has a fluorite-type structure, and Na^+ and Nd^{3+} are randomly distributed in the cationic sublattice (Figure 6.1b) with an empirical composition of

$5NaF{\cdot}9NdF_3$ according to the phase diagram.[17] The present work is focused on compositional and structural characterizations, thermal stabilities, and formation enthalpies of various phases in the NaF–NdF_3 system determined by thermogravimetry and differential scanning calorimetry (TG-DSC) and high temperature oxide melt solution calorimetry.

6.3 Experimental Methods

6.3.1 Material Preparation

Sodium fluoride (NaF, 99%, Mallinckrodt), neodymium(III) nitrate hexahydrate ($Nd(NO_3)_3{\cdot}6H_2O$, 99.9%, Alfa Aesar), and neodymium(III) fluoride (NdF_3, 99.9%, Alfa Aesar) were used as precursors without further purification. Nitric acid (HNO_3, 70%, EMD Millipore) and ammonium hydroxide (NH_4OH, 28% NH_3, Alfa Aesar) were used to adjust the pH of the solutions.

Coprecipitation and hydrothermal reactions were employed to synthesize NaF–NdF_3 nanocrystals. In a typical coprecipitation experiment, $Nd(NO_3)_3$ aqueous solution (0.15 M) was added dropwise into a 5-fold excess of saturated NaF solution. After stirring for 3 h, the obtained suspension was separated by vacuum filtration, washed with deionized water, and dried under vacuum at 50 °C overnight. α phase nanocrystals were obtained without adding NH_4OH (pH = 5.9), and β phase nanocrystals were obtained by changing the pH of the solution to 10.3. In a hydrothermal experiment, 22 mL of the as-prepared solution with pH = 10.3 was transferred into a Teflon bottle, sealed within a stainless steel autoclave, and heated at 120, 160, or 200 °C for 24 h. The products were separated by vacuum filtration and collected as described before. To investigate the phase transitions and reactions driven by temperature, part of the NaF–NdF_3

nanocrystals were heated at 550 °C for 1 h, quenched to room temperature, and collected for further structural characterization.

In solid-state (SS) reactions, equal molar amounts of NaF and NdF_3 were ground, pelletized, and heated at different temperatures in a Pt crucible with a lid for 48 h. To get pure β-$NaNdF_4$, a mixture of NaF and NdF_3 in a molar ratio of 1:1 was reacted at 550 °C for 48 h, with heating and cooling rates of 5 or 1 °C min^{-1}, respectively. The other samples were sintered and air-quenched from a specific temperature ranging from 650 to 800 °C.

6.3.2 Powder X-ray Diffraction

Powder X-ray diffraction (PXRD) patterns were obtained using a Bruker D2 Phaser diffractometer operated with Cu Kα radiation ($\lambda = 1.54184$ Å). For phase determination, the data were collected in the 2θ range of 10–80° with a step size of 0.02° and a dwell time of 0.45 s per step. To get XRD patterns for Rietveld refinements, the data were collected in the 2θ range of 10–120° with a step size of 0.01° and a dwell time of 2 s per step. The PXRD patterns were analyzed using the Rietveld method implemented in the program GSAS-II.[29]

6.3.3 Raman and Photoluminescence Spectra

Raman and PL emission spectra were collected at room temperature on a custom-built Raman/PL spectrometer in a 180° geometry. For Raman spectra, the sample was excited using a 50 mW diode laser with a wavelength of 633 nm. The laser beam was focused onto the sample using a 50× APO Mitutoyo microscope objective with a numerical aperture of 0.42. PL emission spectra were obtained by exciting samples using a 20 mW Cobalt Zook laser with a wavelength of 355 nm, which was focused onto the sample using a 50× super long working distance objective (M Plan APO NUV Mitutoyo) with a numerical aperture of 0.42. The signal was discriminated from the laser excitation using a laser Kaiser bandpass filter combined with a Semrock RazorEdge ultrasteep long pass edge filter. The data were collected using an Andor 750 spectrometer combined with an iDus Backthinned CCD detector. Raman spectra were calibrated according to the peak position and intensity of a cyclohexane standard.

6.3.4 Inductively Coupled Plasma Mass Spectrometry

The Na/Nd ratios of the samples were determined by inductively coupled plasma mass spectrometry (ICP–MS) using a Thermo Scientific Quadrupole (iCap-Q) instrument. Samples for ICP–MS measurements were prepared by adding 5 mg of samples to 15 mL of 0.32 M HNO_3 and then shaking vigorously. After resting for several minutes, 1 mL of supernatant was separated and diluted by 0.32 M HNO_3 to make a 1:100 dilution. A previously published microwave digestion procedure was also used to prepare ICP–MS samples,[30] whose results are found to be consistent with the samples prepared by the method described before, confirming the effectiveness of this sample preparation method.

6.3.5 Scanning Electron Microscopy

Secondary electron micrographs were obtained using field emission scanning electron microscopy (SEM) (Philips XL30) at an accelerating voltage of 30 kV. The samples were dispersed in methanol, ultrasonicated, and deposited on silicon wafers.

6.3.6 Thermogravimetry and Differential Scanning Calorimetry

TG-DSC experiments were performed using a Setaram LabSYS EVO instrument. In each measurement, ~30 mg of sample was pressed into a pellet, placed in a Pt crucible, and heated from 30 to 1200 °C (10 °C min^{-1}) under Ar flow (20 mL min^{-1}). A buoyancy correction was performed with an empty crucible prior to the experiment. The water content of samples was obtained from the corresponding weight loss.

6.3.7 High Temperature Oxide Melt Solution Calorimetry

High temperature oxide melt solution calorimetry experiments were carried out using a Setaram AlexSYS Tian-Calvet twin microcalorimeter using methods standard to our laboratory and described previously.[31–33] The calorimeter was calibrated against the heat content of high-purity α-Al_2O_3 (99.997%). Pressed sample pellets (~5 mg) were dropped from ambient temperature into the calorimeter containing the solvent, molten sodium molybdate ($3Na_2O\cdot 4MoO_3$), in a Pt crucible at 800 °C. All experiments were flushed with O_2 at 60 mL min^{-1} with bubbling through the solvent at 5 mL min^{-1} to aid dissolution and purge the evolved water vapor generated by dissolution of samples. The measurement was repeated at least six times on each sample.

6.4 Results and Discussion

As shown in Figure 6.2, a range of NaF–NdF_3 samples containing the two phases (α and β) were prepared by aqueous (AQ) and SS reactions at various temperatures. Their chemical compositions and water contents were determined by ICP–MS and TG-DSC, respectively. The chemical formulas are calculated according to the charge balance as $Na_{3x}Nd_{2-x}F_6$. Since the nanocrystals from aqueous solution synthesis have considerable composition deviations from the stoichiometric compound ($NaNdF_4$), they are called NaF–NdF_3 for differentiation from the bulk samples from SS reactions. Lattice parameters and phase contents were analyzed by Rietveld refinements of PXRD patterns (Table 6.1, Figures A14–A23). All these results are listed in Table 6.2.

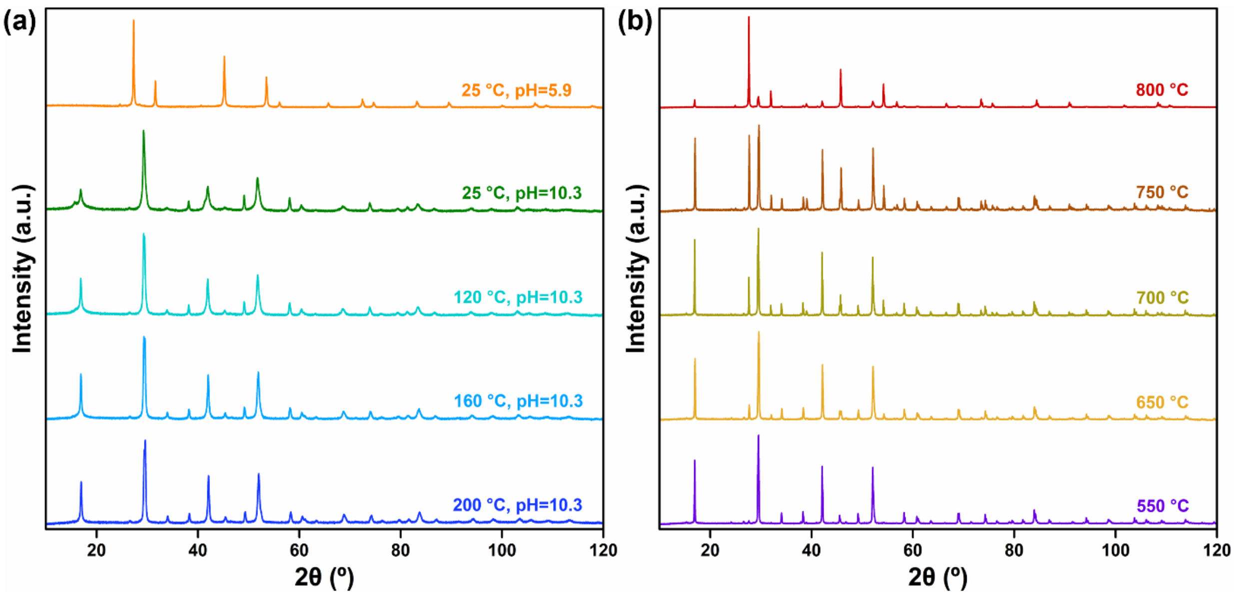

Figure 6.2 PXRD patterns of NaF–NdF_3 samples from (a) aqueous solution synthesis and (b) solid-state reactions at different temperatures.

Table 6.1 Atomic coordination obtained from Rietveld refinements of PXRD patterns.

Sample	Space group	Atomic Coordinates				Reliability factors
		Atom (Wyckoff)	(x, y, z)	Occ	U_{iso}	
AQ1	$Fm\bar{3}m$ (No 225)	Nd (4a)	(0, 0, 0)	0.580	0.00606	R = 3.39 % wR = 5.30 % GOF = 2.44
		Na (4a)	(0, 0, 0)	0.253	0.00606	
		F (8c)	(1/4, 1/4, 1/4)	1.000	0.01000	
AQ2	$P\bar{6}$ (No 174)	Nd1 (1a)	(0, 0, 0)	1.000	0.01931	R = 3.90 % wR = 6.37 % GOF = 2.93
		Na1 (2h)	(1/3, 2/3, 0.6560)	0.275	0.01000	
		Na2/Nd2 (1f)	(2/3, 1/3, 1/2)	0.220/0.780	0.00181	
		F1 (3j)	(0.6337, 0.0429, 0)	1.000	0.01000	
		F2 (3k)	(0.7339, 0.7549, 1/2)	1.000	0.01000	
AQ3	$P\bar{6}$ (No 174)	Nd1 (1a)	(0, 0, 0)	0.973	0.01454	R = 3.97 % wR = 5.78 % GOF = 2.60
		Na1 (2h)	(1/3, 2/3, 0.6450)	0.283	0.01250	
		Na2/Nd2 (1f)	(2/3, 1/3, 1/2)	0.233/0.767	0.01740	
		F1 (3j)	(0.5907, -0.0056, 0)	1.000	0.07021	
		F2 (3k)	(0.7100, 0.7200, 1/2)	1.000	0.07021	
AQ4	$P\bar{6}$ (No 174)	Nd1 (1a)	(0, 0, 0)	0.950	0.01007	R = 3.05 % wR = 4.36 % GOF = 1.98
		Na1 (2h)	(1/3, 2/3, 0.5887)	0.340	0.00896	
		Na2/Nd2 (1f)	(2/3, 1/3, 1/2)	0.280/0.720	0.00921	
		F1 (3j)	(0.6275, 0.0171, 0)	1.000	0.00658	
		F2 (3k)	(0.7308, 0.7479, 1/2)	1.000	0.00658	

AQ5	P$\bar{6}$ (No 174)	Nd1 (1a)	(0, 0, 0)	0.961	0.01292	R = 3.31 % wR = 4.66 % GOF = 2.01
		Na1 (2h)	(1/3, 2/3, 0.6586)	0.335	0.01589	
		Na2/Nd2 (1f)	(2/3, 1/3, 1/2)	0.331/0.669	0.00125	
		F1 (3j)	(0.6064, 0.0152, 0)	1.000	0.01407	
		F2 (3k)	(0.7317, 0.7439, 1/2)	1.000	0.01407	
SS1	P$\bar{6}$ (No 174)	Nd1 (1a)	(0, 0, 0)	1.000	0.00984	R = 2.77 % wR = 3.74 % GOF = 1.70
		Na1 (2h)	(1/3, 2/3, 0.6281)	0.480	0.01000	
		Na2/Nd2 (1f)	(2/3, 1/3, 1/2)	0.500/0.500	0.00916	
		F1 (3j)	(0.6281, 0.0396, 0)	1.000	0.01249	
		F2 (3k)	(0.7264, 0.7475, 1/2)	1.000	0.01249	
SS2	P$\bar{6}$ (No 174)	Nd1 (1a)	(0, 0, 0)	1.000	0.01000	R = 3.33 % wR = 4.68 % GOF = 2.11
		Na1 (2h)	(1/3, 2/3, 0.6281)	0.500	0.01000	
		Na2/Nd2 (1f)	(2/3, 1/3, 1/2)	0.460/0.500	0.00900	
		F1 (3j)	(0.6281, 0.0396, 0)	1.000	0.01200	
		F2 (3k)	(0.7264, 0.7475, 1/2)	1.000	0.01200	
	Fm$\bar{3}$m (No 225)	Nd (4a)	(0, 0, 0)	0.500	0.00600	
		Na (4a)	(0, 0, 0)	0.500	0.00600	
		F (8c)	(1/4, 1/4, 1/4)	1.000	0.01000	
SS3	P$\bar{6}$ (No 174)	Nd1 (1a)	(0, 0, 0)	1.000	0.01000	R = 4.90 % wR = 7.97 % GOF = 3.55
		Na1 (2h)	(1/3, 2/3, 0.6281)	0.500	0.01000	
		Na2/Nd2 (1f)	(2/3, 1/3, 1/2)	0.460/0.500	0.00900	
		F1 (3j)	(0.6281, 0.0396, 0)	1.000	0.01200	
		F2 (3k)	(0.7264, 0.7475, 1/2)	1.000	0.01200	
	Fm$\bar{3}$m (No 225)	Nd (4a)	(0, 0, 0)	0.500	0.00600	
		Na (4a)	(0, 0, 0)	0.500	0.00600	
		F (8c)	(1/4, 1/4, 1/4)	1.000	0.01000	
SS4	P$\bar{6}$ (No 174)	Nd1 (1a)	(0, 0, 0)	1.000	0.01000	R = 5.23 % wR = 8.32 % GOF = 3.57
		Na1 (2h)	(1/3, 2/3, 0.6281)	0.500	0.01000	
		Na2/Nd2 (1f)	(2/3, 1/3, 1/2)	0.460/0.500	0.00900	
		F1 (3j)	(0.6281, 0.0396, 0)	1.000	0.01200	
		F2 (3k)	(0.7264, 0.7475, 1/2)	1.000	0.01200	
	Fm$\bar{3}$m (No 225)	Nd (4a)	(0, 0, 0)	0.500	0.00600	
		Na (4a)	(0, 0, 0)	0.500	0.00600	
		F (8c)	(1/4, 1/4, 1/4)	1.000	0.01000	
SS5	P$\bar{6}$ (No 174)	Nd1 (1a)	(0, 0, 0)	1.000	0.01000	R = 4.96 % wR = 8.45 % GOF = 3.71
		Na1 (2h)	(1/3, 2/3, 0.6281)	0.500	0.01000	
		Na2/Nd2 (1f)	(2/3, 1/3, 1/2)	0.460/0.500	0.00900	
		F1 (3j)	(0.6281, 0.0396, 0)	1.000	0.01200	
		F2 (3k)	(0.7264, 0.7475, 1/2)	1.000	0.01200	
	Fm$\bar{3}$m (No 225)	Nd (4a)	(0, 0, 0)	0.500	0.00600	
		Na (4a)	(0, 0, 0)	0.500	0.00600	
		F (8c)	(1/4, 1/4, 1/4)	1.000	0.01000	

Table 6.2 Summary of the experimental conditions and the corresponding phases, chemical compositions, crystal structures, and lattice parameters of the samples.

Sample	Synthesis method	Synthetic conditions	Observed phase	Chemical composition	Crystal structure	Lattice parameters		
						a (Å)	c (Å)	V (Å^3)
AQ1	Coprecipitation	25 °C pH = 5.9	α	$Na_{0.76}Nd_{1.75}F_6 \cdot 0.24H_2O$	$Fm\bar{3}m$	5.69233(8)		184.447(7)
AQ2	Coprecipitation	25 °C pH = 10.3	β	$Na_{0.77}Nd_{1.74}F_6 \cdot 0.84H_2O$	$P\bar{6}$	6.136(2)	3.7190(3)	121.27(4)
AQ3	Hydrothermal	120 °C pH = 10.3	β	$Na_{0.81}Nd_{1.73}F_6 \cdot 0.68H_2O$	$P\bar{6}$	6.149(1)	3.7281(2)	122.09(3)
AQ4	Hydrothermal	160 °C pH = 10.3	β	$Na_{0.96}Nd_{1.68}F_6 \cdot 0.41H_2O$	$P\bar{6}$	6.1406(6)	3.7211(1)	121.51(1)
AQ5	Hydrothermal	200 °C pH = 10.3	β	$Na_{1.08}Nd_{1.64}F_6 \cdot 0.32H_2O$	$P\bar{6}$	6.1295(6)	3.7126(1)	120.80(1)
SS1	Solid state	550 °C Slow cooling	β	$Na_{1.46}Nd_{1.51}F_6$	$P\bar{6}$	6.1062(2)	3.71476(4)	119.951(5)
SS2	Solid state	650 °C Quenching	β+α	$Na_{1.46}Nd_{1.51}F_6$	$P\bar{6}$ (91.5 %) $Fm\bar{3}m$ (8.5 %)	6.1109(3) 5.6284(2)	3.71784(5)	120.235(7) 178.30(2)
SS3	Solid state	700 °C Quenching	β+α	$Na_{1.46}Nd_{1.51}F_6$	$P\bar{6}$ (87.1 %) $Fm\bar{3}m$ (12.9 %)	6.0908(4) 5.6099(4)	3.70227(7)	118.95(1) 176.55(4)
SS4	Solid state	750 °C Quenching	β+α	$Na_{1.46}Nd_{1.51}F_6$	$P\bar{6}$ (66.9 %) $Fm\bar{3}m$ (33.1 %)	6.0819(6) 5.6010(2)	3.69664(9)	118.42(1) 175.71(2)
SS5	Solid state	800 °C quenching	α+β	$Na_{1.46}Nd_{1.51}F_6$	$P\bar{6}$ (19.8 %) $Fm\bar{3}m$ (80.2 %)	6.087(2) 5.60711(9)	3.7013(3)	118.78(5) 176.286(8)

At room temperature, NaF–NdF_3 nanocrystals with the α or β structure can be coprecipitated from aqueous solutions of $Nd(NO_3)_3$ and saturated NaF at different pH values, which are labeled AQ1 and AQ2, respectively. The phase seen in the nanocrystals is highly correlated with pH values. In an acidic environment (pH = 2.2), NdF_3 instead of NaF–NdF_3 compounds is formed as the precipitate because the release of F^- is not favored in such an acidic system.[34] In neutral conditions without adding HNO_3 or NH_4OH (pH = 5.9), the cubic phase (α) is formed. By adding NH_4OH, the hexagonal phase (β) shows up with an increase of pH to 10.3 (Figure 6.3). The two samples from coprecipitation at room temperature have similar composition with much less Na than Nd, and their Na/Nd ratio is around 0.44. Such a strong Na deficiency in NaF–NdF3 nanocrystals was also reported in previous studies.[25,35] The α → β phase conversion associated with higher pH values may come from the basic environment favoring the selective crystal growth along some preferred orientations, which promotes the transformation from the isotropic unit cell structure of the α phase to the anisotropic unit cell structure of the β phase.[9,13] However, we have no additional evidence for such a proposed mechanism. The phase differences are also manifested in the morphology of nanocrystals, which have polyhedral and rod shapes for α and β phases, respectively (Figure 6.4). However, when the synthesis temperature increases, the α phase starts to decompose in the aqueous solution and NdF3 crystals are formed instead (Figure 6.5).

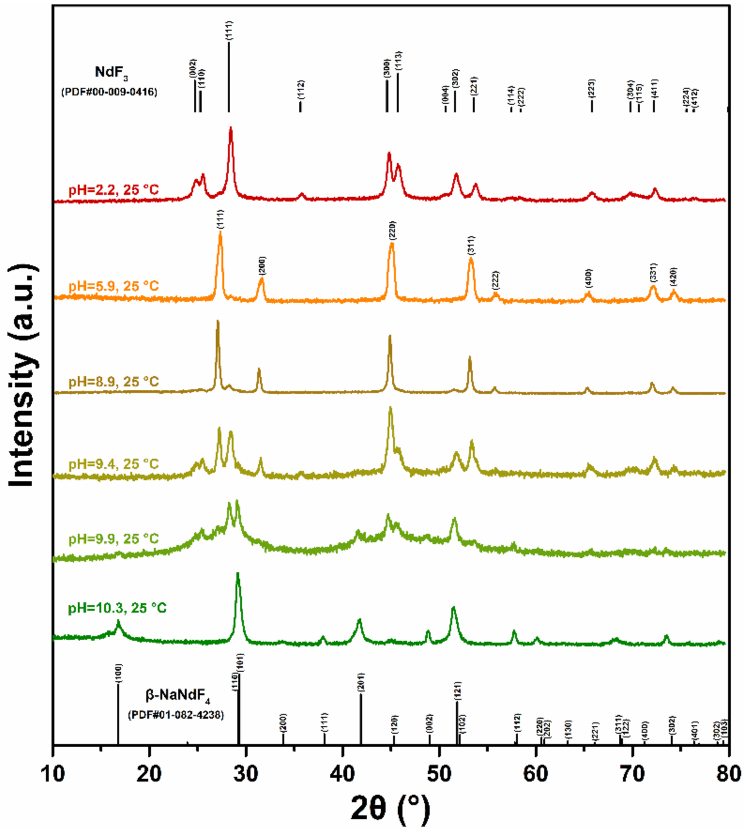

Figure 6.3 PXRD patterns of co-precipitation samples from different pH values compared with ICDD PDF cards.

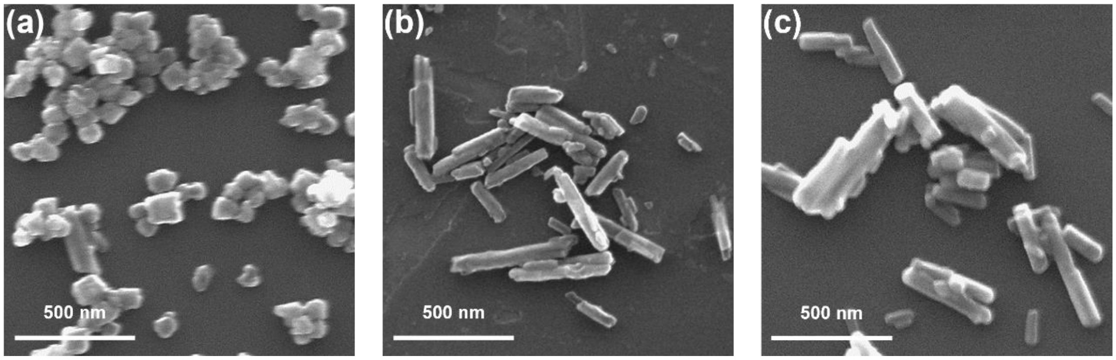

Figure 6.4 SEM images of NaF–NdF_3 samples from aqueous solution synthesis in different conditions: (a) coprecipitation at 25 °C and pH = 5.9 (AQ1), (b) coprecipitation at 25 °C and pH = 10.3 (AQ2), and (c) hydrothermal reaction at 120 °C and pH = 10.3 (AQ3).

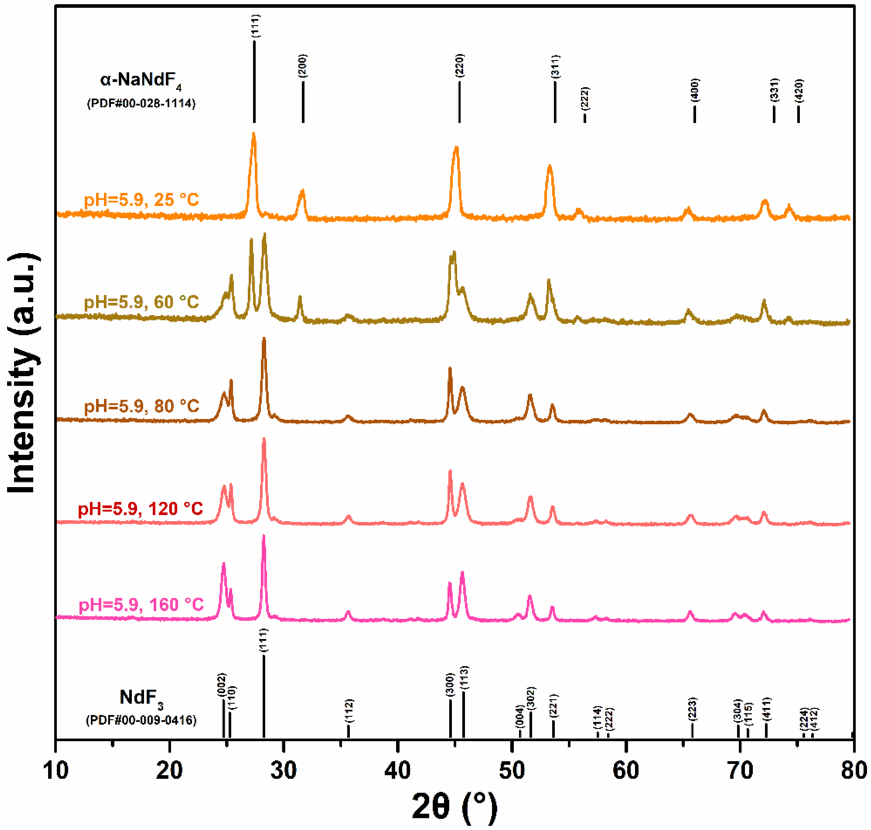

Figure 6.5 PXRD patterns of samples from hydrothermal reactions with different temperatures at pH = 5.9 compared with ICDD PDF cards.

Hydrothermal reactions at different temperatures (120, 160, and 200 °C) were also used to synthesize NaF–NdF_3 nanocrystals, and all the obtained samples (AQ3, AQ4, and AQ5) have the β phase structure (Figure 6.2a). Similar to the samples from coprecipitation, NaF–NdF_3 samples from hydrothermal synthesis show composition deviations from the stoichiometric β-$NaNdF_4$ ($Na_{1.5}Nd_{1.5}F_6$) with Na/Nd ratios increasing from 0.47 to 0.66 when the reaction temperature is raised from 120 to 200 °C. Besides the change of chemical compositions, smaller lattice parameters are seen with the increase of Na contents in the nanocrystals (Table 6.2). It appears that the particle sizes of nanocrystals from hydrothermal reactions are larger than those for samples from coprecipitation (Figure 6.4c). For example, the average particle sizes are 92 nm for AQ1, 58 × 280 nm for AQ2, and 73 × 283 nm for AQ3 based on the SEM images.

Bulk $NaNdF_4$ samples with the stoichiometric composition were prepared by SS reactions between the same molar amount of NaF and NdF_3 at different temperatures (Figure 6.2b). At a relatively low temperature (550 °C) with slow cooling rate, pure β-$NaNdF_4$ was obtained, called SS1. At higher temperatures (650–800 °C), the β → α phase transition happens, and the two phases coexist in the quenched samples (termed as SS2, SS3, SS4, and SS5). The α phase content increases with the temperature from 8.5% for SS2 quenched from 650 °C to 80.2% for SS5 quenched from 800 °C.

The structural differences of samples were further investigated by Raman and PL spectroscopies. As shown in Figure 6.6a, AQ1 shows a broad peak at 360 cm^{-1}, which is consistent with the O_h symmetry for the α phase with the fluorite structure.[36] For samples with the β phase, their Raman spectra have bands at 290, 338, 378, and 406 cm^{-1}, corresponding to the Raman-active modes for the hexagonal $P\bar{6}$ structure.[37] An additional broad band located around 505 cm^{-1} is noted in the spectra of AQ2, which may be associated with the lower symmetry during the crystal growth of nanocrystals.[38] The β → α phase transition driven by temperature in bulk samples is also characterized by Raman spectroscopy (Figure 6.6b). The bands assigned to the β phase diminish accompanying the appearance of the band for the α phase, indicating that more α-$NaNdF_4$ forms as the temperature increases. Although the α phase structure is acquired for both nanocrystals from coprecipitation (AQ1) and high temperature quenching (SS2–SS5), the Raman band of O_h symmetry occurs at higher wavenumber for bulk samples (~400 cm^{-1}), consistent with more Nd than Na existing in the α phase nanocrystals.

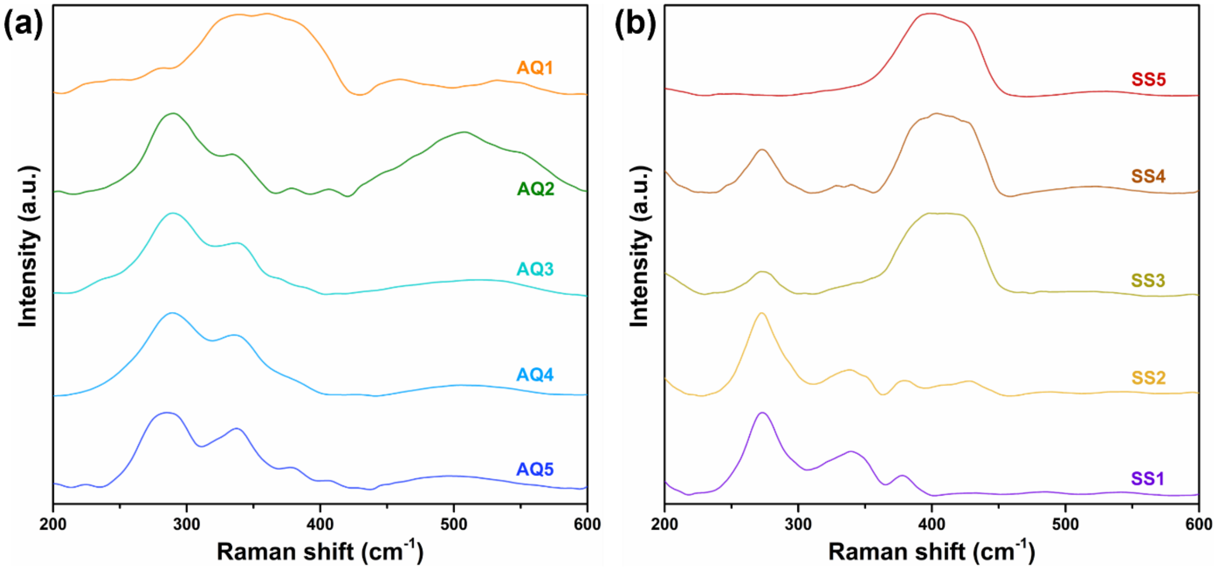

Figure 6.6 Raman spectra of NaF–NdF_3 samples from (a) aqueous solution synthesis and (b) SS reactions.

Figure 6.7 displays the emission spectra of NaF–NdF_3 nanocrystals and the energy-level diagram of Nd^{3+} ions.[39–41] The observed emission peaks at around 740, 790, 860, and 900 nm are attributed to the transitions of $^4F_{7/2} \rightarrow {}^4I_{9/2}$, $^4F_{5/2} \rightarrow {}^4I_{9/2}$, $^4F_{3/2} \rightarrow {}^4I_{9/2}$, and $^4F_{9/2} \rightarrow {}^4I_{13/2}$, respectively. The symmetry difference between α and β phases are also reflected in the PL spectra, in which nanocrystals with the α or β phase have a singlet or a doublet for the $^4F_{5/2} \rightarrow {}^4I_{9/2}$ transition, respectively. Because electric dipole transitions are more sensitive to the local

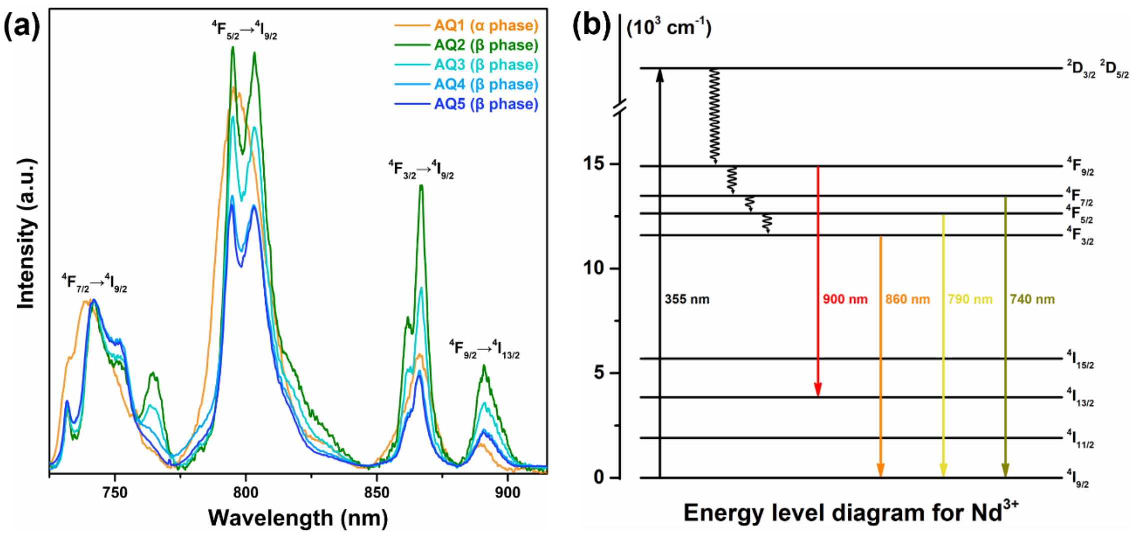

Figure 6.7 (a) PL emission (λ_{ex} = 355 nm) spectra of NaF–NdF$_3$ samples from aqueous solutions (the intensities of peaks are normalized according to the peak at 740 nm) and (b) energy diagram of Nd^{3+} involved in this work.

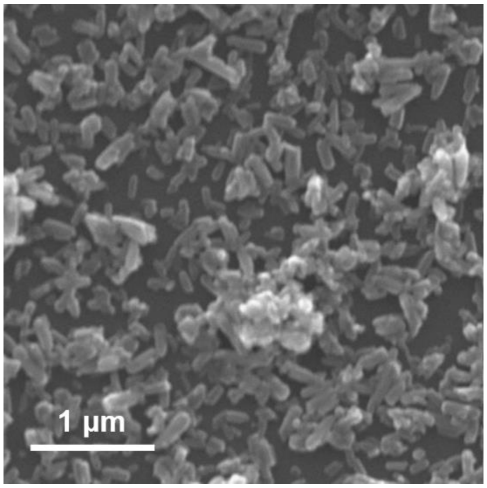

Figure 6.8 The SEM image of the sample AQ4.

symmetry compared to magnetic dipole transitions, electric dipole transitions generally become stronger by decreasing the crystallite size as more atoms are on the surface with lower symmetry.[8] Hence, after normalizing the PL spectra according to the magnetic–dipole transition ($^4F_{7/2} \rightarrow {}^4I_{9/2}$), the relative intensities of electric–dipole transitions ($^4F_{5/2} \rightarrow {}^4I_{9/2}$ and $^4F_{9/2} \rightarrow$

$^4I_{13/2}$) decrease with the increase of synthesis temperatures, implying a great effect of temperature on the size of nanocrystals from aqueous solutions.[12,13] The SEM image (Figure 6.8) also shows that NaF–NdF_3 nanocrystals synthesized at higher temperature have a larger average particle size, such as 94 × 285 nm for AQ4 synthesized at 160 °C.

TG-DSC measurements were used to determine the water contents and study phase transitions driven by temperature for NaF–NdF_3 samples. As shown in Figure 6.9, there are two dehydration steps in the TG profiles, suggesting the existence of two types of water in nanocrystals. Physically adsorbed water on the surface of nanocrystals is lost in the early stages of dehydration (30–200 °C), while crystal water needs higher temperature to be dehydrated (300–400 °C).[42] The number of water molecules per formula in Table 6.2 is calculated based on the total weight loss upon dehydration on the TG curves, in which AQ1 has a weight loss of 1.1 wt % and weight losses range from 1.5 to 3.8 wt % for β phase nanocrystals (AQ2–AQ5).

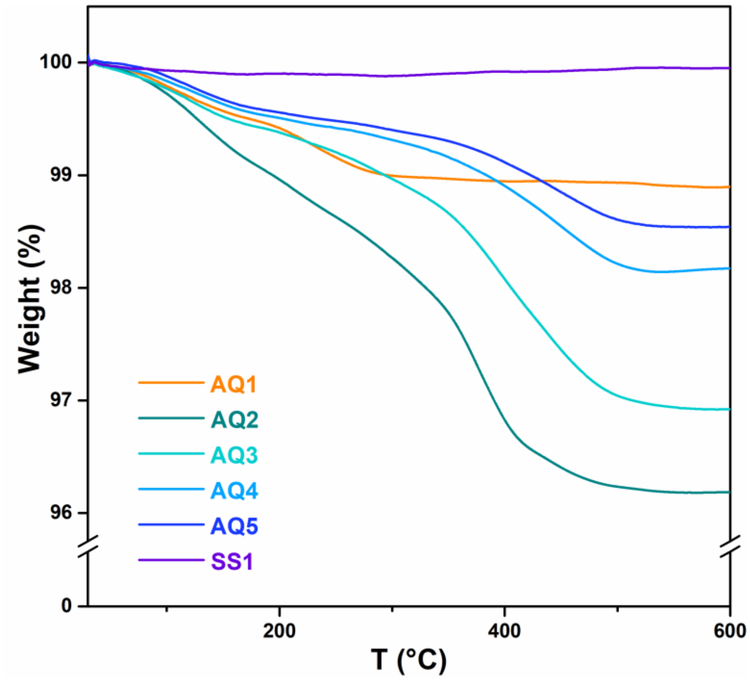

Figure 6.9 TG curves of NaF–NdF_3 samples.

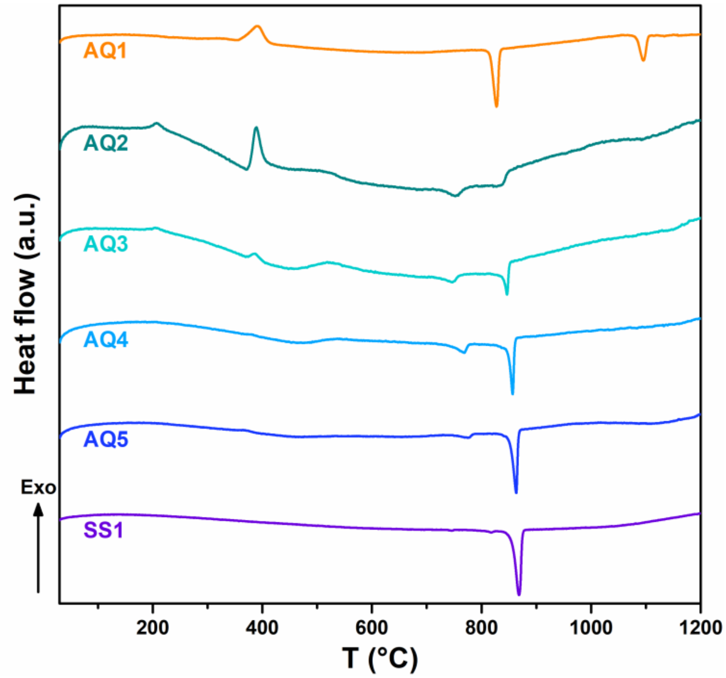

Figure 6.10 DSC curves of NaF–NdF_3 samples.

When NaF–NdF_3 samples are heated, the DSC curves show various exothermic and endothermic peaks (Figure 6.10). For the bulk β phase sample (SS1), a large endothermic peak at ~850 °C and a small endothermic peak at lower temperature correspond to the melting and the β → α phase transition of the stoichiometric $NaNdF_4$, respectively. For nanocrystals of the β phase, besides two endothermic peaks, there are three exothermic peaks on their DSC curves. Although the peaks at ~200 and ~380 °C are associated with the loss of water in nanocrystals and are more obvious for samples with higher water contents, the decomposition of the β phase to form a mixture of α and β phases of NaF–NdF_3 compounds with NdF_3 happens at the same time (Figure 6.11), making the overall heat effects exothermic and different from the typical endothermic dehydration process. Like oxide and hydroxide nanoparticles,[43–45] the presence of water may stabilize the nanosystems, especially the nonstoichiometric NaF–NdF_3 nanocrystals with the β phase structure, but the quantitative study of these effects is out of the scope of this work. The content of the α phase and NdF_3 decreases with increasing synthesis temperature. In contrast, only β-$NaNdF_4$ and NdF_3 exist in sample SS1 annealed at 550 °C. The phase separations of NaF–NdF_3 nanocrystals in the heating processes are associated with the Na insufficiency in compositions and are in accord with the phase diagram of the NaF–NdF_3 system (Figure 6.12).[17,18] Based on this, the two endothermic peaks in the DSC profiles of β phase nanocrystals correspond to the formation and melting of solid solutions with the α phase, while the extra endothermic peak at ~1050 °C on the DSC curve of SS1 is due to the reverse peritectic reaction of the cubic NaF–NdF_3 solid solution.

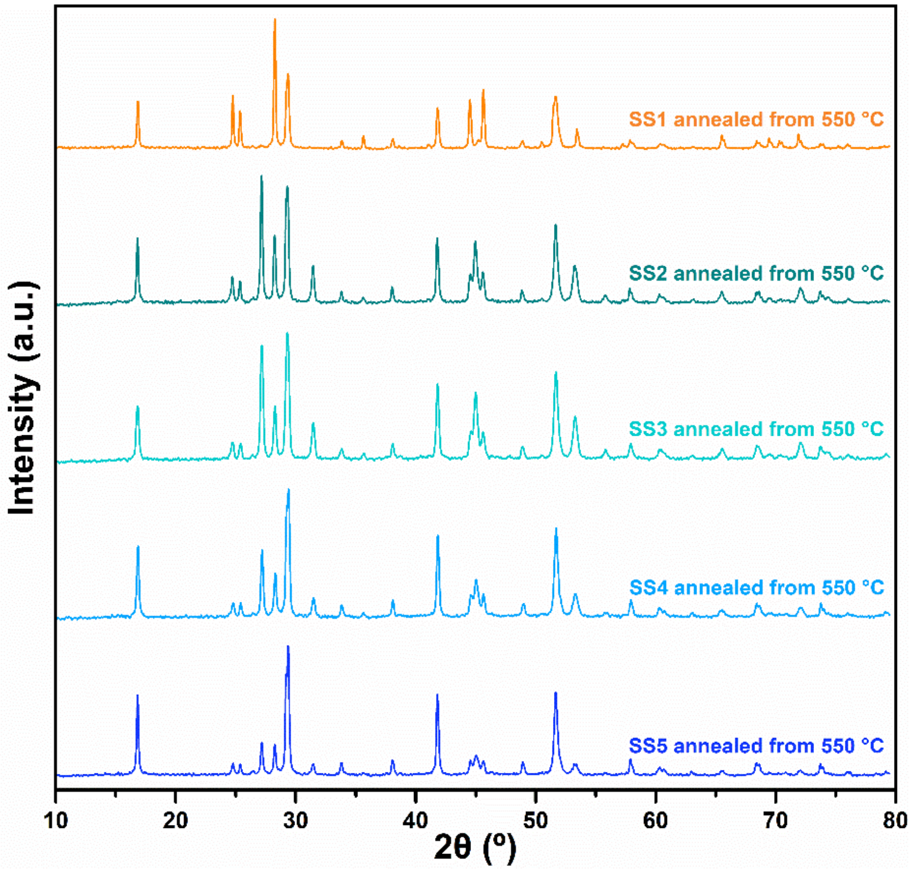

Figure 6.11 PXRD patterns of NaF–NdF_3 samples annealed from 550 °C.

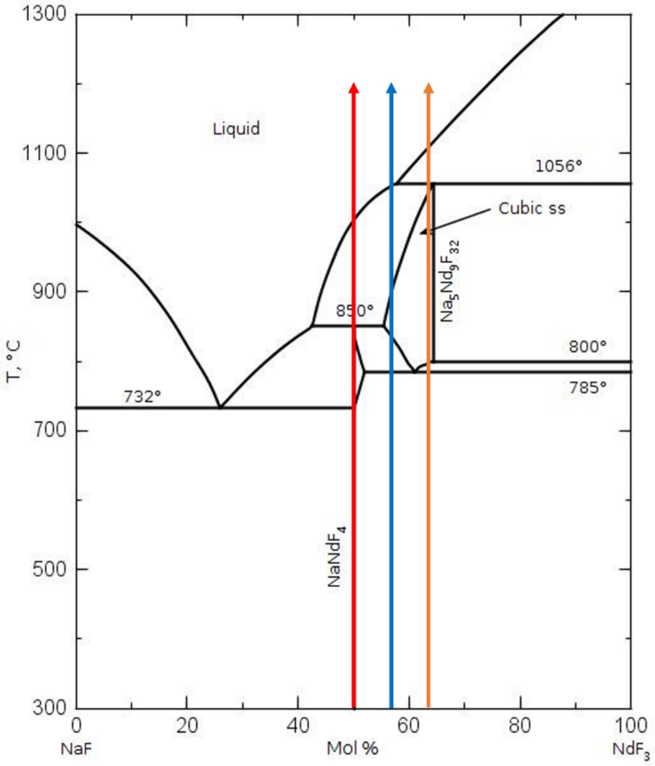

Figure 6.12 The phase diagram of NaF–NdF_3 system.[17] Orange, blue, and red arrows represent the heating processes of the samples AQ1, AQ2–AQ5, and SS1, respectively.

Energetics of NaF–NdF_3 samples were investigated by high temperature oxide melt solution calorimetry employing molten sodium molybdate ($3Na_2O\cdot4MoO_3$) solvent at 800 °C. The formation enthalpies (ΔH_f) from fluorides (or plus water for nanocrystals) at 25 °C are calculated using thermodynamic cycles in Table 6.3. The drop solution enthalpies (ΔH_{ds}) and ΔH_f are listed in Table 6.4. To confirm the consistency and validity of thermodynamic data gained from this method, ΔH_{ds} of NaF or a hydrated NaF sample ($NaF\cdot0.31H_2O$, whose TG-DSC curve is shown in Figure 6.13) and NdF_3 were measured alternatively and have been found to be constant and not affected by fluorides already in the solvent (Table 6.5). The reliability of applying high temperature oxide melt solution calorimetry to RE fluoride compounds was also checked by exchange enthalpies between NaF and RE sesquioxides in our previous study.[26]

Table 6.3 Thermodynamic cycles used to calculate the formation enthalpies (ΔH_f) at 25 °C.

Reaction	ΔH (kJ mol^{-1})
$Na_{3x}Nd_{2-x}F_6 \cdot nH_2O$ (s, 25 °C) → 3xNaF (soln, 800 °C) + (2−x)NdF_3 (soln, 800 °C) + nH_2O (g, 800 °C)	$\Delta H_1 = \Delta H_{ds}$
NaF (s, 25 °C) → NaF (soln, 800 °C)	$\Delta H_2 = 76.88 \pm 0.33$ [26]
NdF_3 (s, 25 °C) → NdF_3 (soln, 800 °C)	$\Delta H_3 = 151.02 \pm 1.32$ [26]
H_2O (l, 25 °C) → H_2O (g, 800 °C)	$\Delta H_4 = 73.05$ [46]
3xNaF (s, 25 °C) + (2−x)NdF_3 (s, 25 °C) + nH_2O (l, 25 °C) → $Na_{3x}Nd_{2-x}F_6 \cdot nH_2O$ (s, 25 °C)	ΔH_f
$\Delta H_f = -\Delta H_1 + 3x\Delta H_2 + (2-x)\Delta H_3 + n\Delta H_4$	
$Na_{3x}Nd_{2-x}F_6$ (s, 25 °C) → 3xNaF (soln, 800 °C) + (2−x)NdF_3 (soln, 800 °C)	$\Delta H_1 = \Delta H_{ds}$
NaF (s, 25 °C) → NaF (soln, 800 °C)	$\Delta H_2 = 76.88 \pm 0.33$ [26]
NdF_3 (s, 25 °C) → NdF_3 (soln, 800 °C)	$\Delta H_3 = 151.02 \pm 1.32$ [26]
3xNaF (s, 25 °C) + (2−x)NdF_3 (s, 25 °C) → $Na_{3x}Nd_{2-x}F_6$ (s, 25 °C)	ΔH_f
$\Delta H_f = -\Delta H_1 + 3x\Delta H_2 + (2-x)\Delta H_3$	

Table 6.4 Drop solution enthalpies (ΔH_{ds}) in $3Na_2O \cdot 4MoO_3$ at 800 °C and formation enthalpies (ΔH_f) at 25 °C of NaF–NdF_3 samples.

Sample	ΔH_{ds} (kJ mol^{-1})[a]	ΔH_f (kJ mol^{-1})
AQ1	309.90 ± 1.18 (8)	29.64 ± 2.60
AQ2	280.15 ± 0.87 (8)	103.77 ± 2.47
AQ3	300.68 ± 0.99 (8)	72.32 ± 2.51
AQ4	322.18 ± 0.90 (8)	34.99 ± 2.42
AQ5	321.03 ± 0.95 (8)	32.91 ± 2.39
SS1	343.20 ± 0.58 (8)	−2.45 ± 2.14
SS3	319.91 ± 1.21 (6)	20.84 ± 2.39
SS4	291.46 ± 1.03 (6)	49.29 ± 2.30
SS5	185.75 ± 0.92 (6)	155.00 ± 2.25

[a] Value is the mean of the number of experiments indicated in parentheses. Two standard deviations are given as errors.

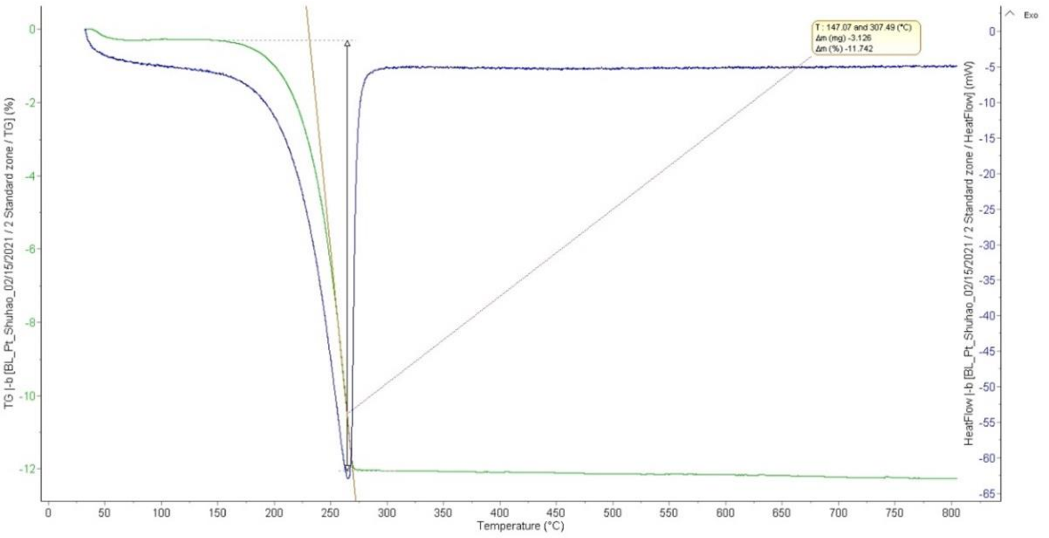

Figure 6.13 TG-DSC curves of the hydrated NaF sample ($NaF \cdot 0.31H_2O$).

Table 6.5 Drop solution enthalpies (ΔH_{ds}) of NaF (or $NaF \cdot 0.31H_2O$) and NdF_3 in $3Na_2O \cdot 4MoO_3$ at 800 °C, in which NaF (or $NaF \cdot 0.31H_2O$) and NdF_3 data are labeled in blue and red, respectively.

Solute being dropped	Solute already in molten	ΔH_{ds} (kJ mol^{-1})
	First batch	
4.453 mg NaF	None	77.46
3.076 mg NaF	4.453 mg NaF	73.97
7.102 mg NaF	7.529 mg NaF	75.80
5.342 mg NaF	14.631 mg NaF	73.64
11.411 mg NdF_3	19.973 mg NaF	154.53
	Second batch	
7.220 mg $NaF \cdot 0.31H_2O$	None	93.31
4.683 mg NdF_3	6.375 mg NaF	152.76
3.685 mg $NaF \cdot 0.31H_2O$	6.375 mg NaF and 4.683 mg NdF_3	92.39
4.429 mg NdF_3	9.629 mg NaF and 4.683 mg NdF_3	152.85
5.386 mg $NaF \cdot 0.31H_2O$	9.629 mg NaF and 9.112 mg NdF_3	91.12
6.504 mg NdF_3	14.385 mg NaF and 9.112 mg NdF_3	152.34
	Third batch	
7.220 mg $NaF \cdot 0.31H_2O$	None	93.31
4.683 mg NdF_3	6.375 mg NaF	152.76
3.685 mg $NaF \cdot 0.31H_2O$	6.375 mg NaF and 4.683 mg NdF_3	92.39
4.429 mg NdF_3	9.629 mg NaF and 4.683 mg NdF_3	152.85
5.386 mg $NaF \cdot 0.31H_2O$	9.629 mg NaF and 9.112 mg NdF_3	91.12
6.504 mg NdF_3	14.385 mg NaF and 9.112 mg NdF_3	152.34

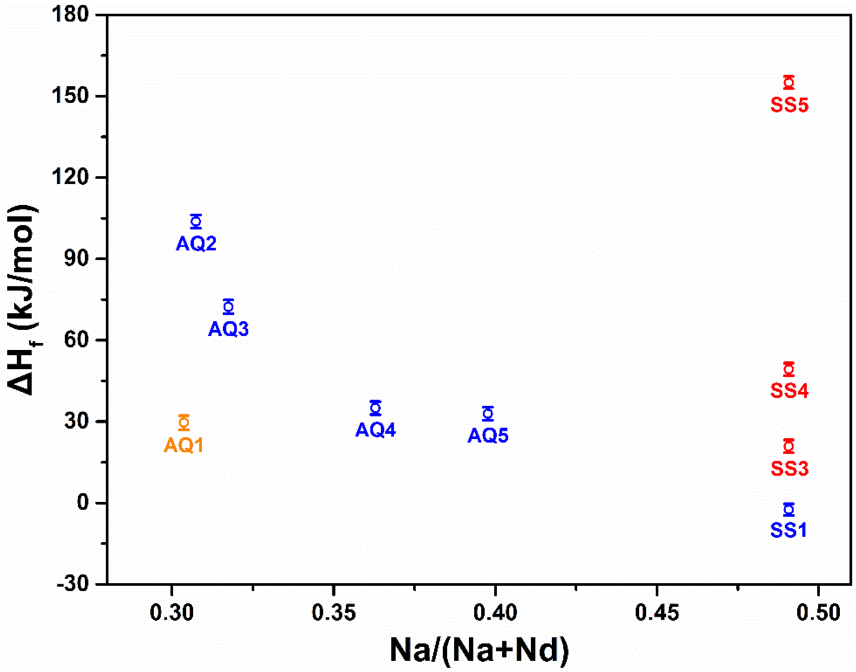

Figure 6.14 Formation enthalpies (ΔH_f) of NaF–NdF_3 samples at 25 °C. Samples with the α phase, the β phase, or a mixture of α and β phases are shown in orange, blue, and red, respectively.

Calorimetric data show that all nanocrystals precipitated from aqueous solutions are not energetically stable compared to binary fluorides and water (Figure 6.14). When having high Na deficiencies, the nanocrystal with the β phase is less stable than the α phase with ΔH_f values of 103.77 ± 2.47 (AQ2) and 29.64 ± 2.60 (AQ1) kJ mol^{-1}, respectively. These are very substantial energetic metastabilities, unlikely to be overcome by entropy contributions near room temperature. However, with increasing Na content, ΔH_f becomes less endothermic for β phase nanocrystals and reaches 32.91 ± 2.39 kJ mol^{-1} for AQ5, and the trend continues to the nearly stoichiometric sample (SS1) with an exothermic ΔH_f value (−2.45 ± 2.14 kJ mol^{-1}). On the other hand, other bulk $NaNdF_4$ samples with the α phase have more endothermic ΔH_f ranging from 20.84 ± 2.39 to 155.00 ± 2.25 kJ mol^{-1} when the α phase content increases from 8.5 to 80.2%. A roughly linear relationship is seen between the ΔH_f values and α phase contents in the quenched samples (Figure 6.15).

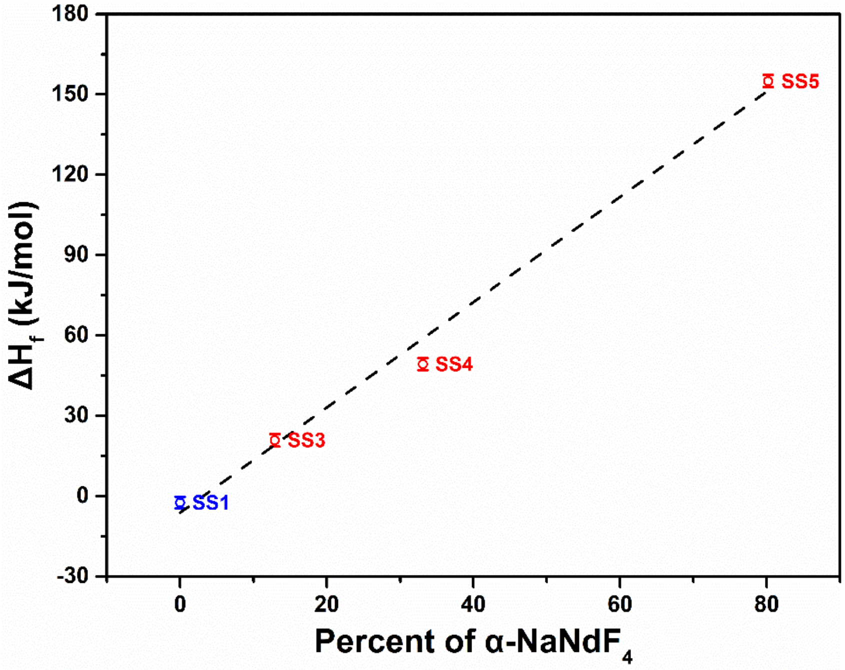

Figure 6.15 Formation enthalpies (ΔH_f) of $NaNdF_4$ samples from solid state reactions versus α phase contents.

The trend of energetic stabilities among NaF–NdF_3 nanocrystals reveals the thermodynamic driving force for the α → β phase conversion in aqueous solutions. At the nucleation stage and/or the early stage of crystal growth, less NaF than NdF_3 precipitates because of the solubility difference, leading to the significant Na inadequacy in nanocrystals and favoring the formation of the α phase for its relatively smaller endothermic ΔH_f. With the growth of crystals, the β phase starts to form, and the energetic stability increases as more NaF is incorporated in nanocrystals. The increasing stability continues until the composition is close to the stoichiometric compound (β-$NaNdF_4$), which has an exothermic ΔH_f. Hence, the appearance of the α phase in small-sized nanocrystals is owing to the Na deficiency at the nucleation stage, and the composition deviation causes the thermodynamic instability of nanocrystals with the β phase, which can be reduced during the crystal growth. Different from the changed stabilities caused by composition variations, the β → α phase transition in the stoichiometric compound gives rise to a metastable α phase (α-$NaNdF_4$) at room temperature with much more endothermic ΔH_f. Despite the same fluorite-type structure, α-$NaNdF_4$ has significant differences in chemical composition and thermodynamic properties compared to the α phase nanocrystals, while the latter is more like the cubic solid solution with less Na than Nd ($Na_{0.5-x}Nd_{0.5+x}F_{2+2x}$) at high temperatures in the NaF–NdF_3 system.

Nucleation and growth processes are governed by the interface energy and Gibbs energies of solids and liquids. Although surface energies of NaF–NdF_3 nanocrystals are not yet known, which are probably similar for α and β phases, the big enthalpy difference between the two phases is very likely the reason for the formation of α phase nanocrystals in the presence of a strong Na deficiency. The α → β transformation of NaF–NdF_3 nanocrystals in aqueous synthesis is essentially a chemical reaction rather than a phase transition like many publications suggested.[21] The formation of the α phase is closely related to the Na deficiency, which may be a result of the much higher solubility of NaF than NdF_3 in water,[47,48] and stoichiometry changes accompany the conversion to the β phase during the crystal growth. A similar phase conversion of $NaYF_4$ due to composition variations was recently observed in oxyfluoride phosphate glass ceramics.[49] The α phase structure can also be acquired by annealing stoichiometric β-$NaNdF_4$, but its chemical and thermodynamic properties are dissimilar to those of α phase nanocrystals because of the composition difference. Considering that upconversion luminescence is sensitive to the phase of the host lattice, this finding may not only guide the synthesis of nanocrystals but also inspire more precise applications taking advantage of phase control.

6.5 Conclusions

The thermochemistry of a series of NaF–NdF_3 samples is studied by thermal analysis and solution calorimetry to reveal the energetic relationship between α and β phases in nanocrystal synthesis and annealing processes. The α → β phase conversion during the nucleation and crystal growth of nanocrystals relates to stoichiometric variations, and the strong Na deficiency causes the formation of the α phase, which is energetically more stable than the β phase with comparable composition. With further crystal growth, more NaF is incorporated in nanocrystals with an accompanying increase in the thermodynamic stability of the β phase until the formation of the stoichiometric compound (β-$NaNdF_4$) as the room-temperature stable phase. Although the α phase structure can be obtained from β-$NaNdF_4$ by increasing the temperature, the stoichiometric α-$NaNdF_4$ is an intermediate phase between the hexagonal β phase and the molten phase, showing great distinctions in chemical compositions and thermodynamic properties compared to α phase nanocrystals. This thermochemical investigation provides a new understanding of the phase conversion in nanocrystals, especially for $NaREF_4$ with light RE elements, and is instructive for the rational design and synthesis of these and related materials.

6.6 Acknowledgements

We acknowledge the use of facilities within the Eyring Materials Center supported in part by NNCI-ECCS-2025490 and the Metals, Environmental and Terrestrial Analytical Laboratory (METAL) at Arizona State University. This work was supported by the U.S. Department of Energy Critical Materials Institute (CMI) Hub under the subaward number DE-AC02-07CH11358. We would like to thank William Petuskey for the use of his laboratory, David Wright for help in sample preparation, and Douglas Daniel, Timothy Karcher, Emmanuel

Soignard, Trevor Martin, Tyler Goepfert, and Gwyneth Gordon for help in sample characterizations.

6.7 References

(1) Haase, M.; Schäfer, H. Upconverting nanoparticles. *Angew. Chem. Int. Ed.* **2011**, *50*, 5808–5829.

(2) Li, X.; Zhang, F.; Zhao, D. Lab on upconversion nanoparticles: optical properties and applications engineering via designed nanostructure. *Chem. Soc. Rev.* **2015**, *44*, 1346–1378.

(3) Wang, F.; Han, Y.; Lim, C. S.; Lu, Y.; Wang, J.; Xu, J.; Chen, H.; Zhang, C.; Hong, M.; Liu, X. Simultaneous phase and size control of upconversion nanocrystals through lanthanide doping. *Nature* **2010**, *463*, 1061–1065.

(4) Gai, S.; Li, C.; Yang, P.; Lin, J. Recent progress in rare earth micro/nanocrystals: soft chemical synthesis, luminescent properties, and biomedical applications. *Chem. Rev.* **2014**, *114*, 2343–2389.

(5) Han, S.; Deng, R.; Gu, Q.; Ni, L.; Huynh, U.; Zhang, J.; Yi, Z.; Zhao, B.; Tamura, H.; Pershin, A., et al. Lanthanide-doped inorganic nanoparticles turn molecular triplet excitons bright. *Nature* **2020**, *587*, 594–599.

(6) Cherniukh, I.; Rainò, G.; Stöferle, T.; Burian, M.; Travesset, A.; Naumenko, D.; Amenitsch, H.; Erni, R.; Mahrt, R. F.; Bodnarchuk, M. I. et al. Perovskite-type superlattices from lead halide perovskite nanocubes. *Nature* **2021**, *593*, 535–542.

(7) Lee, C.; Xu, E. Z.; Liu, Y.; Teitelboim, A.; Yao, K.; Fernandez-Bravo, A.; Kotulska, A. M.; Nam, S. H.; Suh, Y. D.; Bednarkiewicz, A. et al. Giant nonlinear optical responses from photon-avalanching nanoparticles. *Nature* **2021**, *589*, 230–235.

(8) Mai, H.-X.; Zhang, Y.-W.; Si, R.; Yan, Z.-G.; Sun, L.-D.; You, L.-P.; Yan, C.-H. High-quality sodium rare-earth fluoride nanocrystals: controlled synthesis and optical properties. *J. Am. Chem. Soc.* **2006**, *128*, 6426–6436.

(9) Li, C.; Yang, J.; Quan, Z.; Yang, P.; Kong, D.; Lin, J. Different microstructures of β-$NaYF_4$ fabricated by hydrothermal process: effects of pH values and fluoride sources. *Chem. Mater.* **2007**, *19*, 4933–4942.

(10) Fedorov, P. P.; Kuznetsov, S. V.; Mayakova, M. N.; Voronov, V. V.; Ermakov, R. P.; Baranchikov, A. E.; Osiko, V. V. Coprecipitation from aqueous solutions to prepare binary fluorides. *Russ. J. Inorg. Chem.* **2011**, *56*, 1525–1531.

(11) Li, C.; Quan, Z.; Yang, P.; Yang, J.; Lian, H.; Lin, J. Shape controllable synthesis and upconversion properties of $NaYbF_4$/$NaYbF_4$:Er^{3+} and YbF_3/YbF_3:Er^{3+} microstructures. *J. Mater. Chem.* **2008**, *18*, 1353–1361.

(12) Li, C.; Zhang, C.; Hou, Z.; Wang, L.; Quan, Z.; Lian, H.; Lin, J. β-$NaYF_4$ and β-$NaYF_4$:Eu^{3+} microstructures: morphology control and tunable luminescence properties. *J. Phys. Chem. C* **2009**, *113*, 2332–2339.

(13) Zhang, F.; Li, J.; Shan, J.; Xu, L.; Zhao, D. Shape, size, and phase-controlled rare-earth fluoride nanocrystals with optical up-conversion properties. *Chem.─Eur. J.* **2009**, *15*, 11010–11019.

(14) Voß, B.; Nordmann, J.; Uhl, A.; Komban, R.; Haase, M. Effect of the crystal structure of small precursor particles on the growth of β-$NaREF_4$ (RE = Sm, Eu, Gd, Tb) nanocrystals. *Nanoscale* **2013**, *5*, 806–812.

(15) Mai, H.-X.; Zhang, Y.-W.; Sun, L.-D.; Yan, C.-H. Size- and phase-controlled synthesis of monodisperse $NaYF_4$:Yb,Er nanocrystals from a unique delayed nucleation pathway monitored with upconversion spectroscopy. *J. Phys. Chem. C* **2007**, *111*, 13730–13739.

(16) Bard, A. B.; Zhou, X.; Xia, X.; Zhu, G.; Lim, M. B.; Kim, S. M.; Johnson, M. C.; Kollman, J. M.; Marcus, M. A.; Spurgeon, S. R. et al. A mechanistic understanding of nonclassical crystal growth in hydrothermally synthesized sodium yttrium fluoride nanowires. *Chem. Mater.* **2020**, *32*, 2753–2763.

(17) Thoma, R. E.; Insley, H.; Hebert, G. M. The sodium fluoride-lanthanide trifluoride systems. *Inorg. Chem.* **1966**, *5*, 1222–1229.

(18) Fedorov, P. Systems of alkali and rare-earth metal fluorides. *Russ. J. Inorg. Chem.* **1999**, *44*, 1703–1727.

(19) Klier, D. T.; Kumke, M. U. Analysing the effect of the crystal structure on upconversion luminescence in Yb^{3+},Er^{3+}-co-doped $NaYF_4$ nanomaterials. *J. Mater. Chem. C* **2015**, *3*, 11228–11238.

(20) Pin, M. W.; Park, E. J.; Choi, S.; Kim, Y. I.; Jeon, C. H.; Ha, T. H.; Kim, Y. H. Atomistic evolution during the phase transition on a metastable single $NaYF_4$:Yb,Er upconversion nanoparticle. *Sci. Rep.* **2018**, *8*, 2199.

(21) Fedorov, P. P. Comment on "a mechanistic understanding of nonclassical crystal growth in hydrothermally synthesized sodium yttrium fluoride nanowires". *Chem. Mater.* **2021**, *33*, 3859–3861.

(22) Bard, A. B.; Zhou, X.; Xia, X.; Zhu, G.; Lim, M. B.; Kim, S. M.; Johnson, M. C.; Kollman, J. M.; Marcus, M. A.; Spurgeon, S. R. et al. Reply to comment on "a mechanistic understanding

of nonclassical crystal growth in hydrothermally synthesized sodium yttrium fluoride nanowires". *Chem. Mater.* **2021**, *33*, 3862–3864.

(23) Yu, Z.; Hu, W.; Zhao, H.; Miao, X.; Guan, Y.; Cai, W.; Zeng, Z.; Fan, Q.; Tan, T. T. Y. Generating new cross-relaxation pathways by coating prussian blue on $NaNdF_4$ to fabricate enhanced photothermal agents. *Angew. Chem., Int. Ed.* **2019**, *58*, 8536–8540.

(24) Xu, L.; Li, J.; Lu, K.; Wen, S.; Chen, H.; Shahzad, M. K.; Zhao, E.; Li, H.; Ren, J.; Zhang, J. et al. Sub-10 nm $NaNdF_4$ nanoparticles as near-infrared photothermal probes with self-temperature feedback. *ACS Appl. Nano Mater.* **2020**, *3*, 2517–2526.

(25) Naduviledathu Raj, A.; Rinkel, T.; Haase, M. Ostwald ripening, particle size focusing, and decomposition of sub-10 nm $NaREF_4$ (RE = La, Ce, Pr, Nd) nanocrystals. *Chem. Mater.* **2014**, *26*, 5689–5694.

(26) Yang, S.; Anderko, A.; Riman, R. E.; Navrotsky, A. Thermochemistry of sodium rare earth ternary fluorides, $NaREF_4$. *Acta Mater.* **2021**, *220*, 117289.

(27) Burns, J. H. Crystal structure of hexagonal sodium neodymium fluoride and related compounds. *Inorg. Chem.* **1965**, *4*, 881–886.

(28) Grzechnik, A.; Friese, K. Crystal structures and stability of $NaLnF_4$ (Ln = La, Ce, Pr, Nd, Sm and Gd) studied with synchrotron single-crystal and powder diffraction. *Dalton Trans.* **2012**, *41*, 10258–10266.

(29) Toby, B. H.; Von Dreele, R. B. GSAS-II: the genesis of a modern open-source all purpose crystallography software package. *J. Appl. Crystallogr.* **2013**, *46*, 544–549.

(30) Navarro, M. S.; Andrade, S.; Ulbrich, H.; Gomes, C. B.; Girardi, V. A. V. The direct determination of rare earth elements in basaltic and related rocks using ICP-MS: testing the

efficiency of microwave oven sample decomposition procedures. *Geostand. Geoanal. Res.* **2008**, *32*, 167–180.

(31) Navrotsky, A. Progress and new directions in high temperature calorimetry. *Phys. Chem. Miner.* **1977**, *2*, 89–104.

(32) Navrotsky, A. Progress and new directions in high temperature calorimetry revisited. *Phys. Chem. Miner.* **1997**, *24*, 222–241.

(33) Navrotsky, A. Progress and new directions in calorimetry: a 2014 perspective. *J. Am. Ceram. Soc.* **2014**, *97*, 3349–3359.

(34) Yu, S.; Cao, R.; Li, J.; Meng, L. Controlled synthesis of NdF_3 and $NaNdF_4$ micro- or nanocrystals by one-pot microwave-assisted hydrothermal reaction. *J. Fluor. Chem.* **2015**, *178*, 286–290.

(35) Cui, K.; Gao, C.; Cui, X.; She, J.; Peng, B.; Wei, W. Morphology of $NaNdF_4$ nanocrystals from $Nd(C_3H_7COO)_3{\cdot}Phen$ and $Nd(NO_3)_3{\cdot}Phen$ (Phen, 1,10-phenanthroline) as neodymium precursors. *J. Rare Earths* **2011**, *29*, 20–23.

(36) Gee, A. R.; O'Shea, D. C.; Cummins, H. Z. Raman scattering and fluorescence in calcium fluoride. *Solid State Commun.* **1966**, *4*, 43–46.

(37) Lage, M. M.; Moreira, R. L.; Matinaga, F. M.; Gesland, J.-Y. Raman and infrared reflectivity determination of phonon modes and crystal structure of Czochralski-grown $NaLnF_4$ (Ln = La, Ce, Pr, Sm, Eu, and Gd) single crystals. *Chem. Mater.* **2005**, *17*, 4523–4529.

(38) Perera, S. S.; Amarasinghe, D. K.; Dissanayake, K. T.; Rabuffetti, F. A. Average and local crystal structure of β-Er:Yb:$NaYF_4$ upconverting nanocrystals probed by X-ray total scattering. *Chem. Mater.* **2017**, *29*, 6289–6297.

(39) Caspers, H. H.; Rast, H. E.; Buchanan, R. A. Intermediate coupling energy levels for $Nd^{3+}(4f^3)$ in LaF_3. *J. Chem. Phys.* **1965**, *42*, 3214–3217.

(40) Vaishnava, P. P.; Tandon, S. P.; Bhutra, M. P. Energy levels and spectroscopic parameters of neodymium trifluorides. *Spectrosc. Lett.* **1974**, *7*, 515–521.

(41) Wyart, J.-F.; Meftah, A.; Bachelier, A.; Sinzelle, J.; Tchang-Brillet, W.-Ü. L.; Champion, N.; Spector, N.; Sugar, J. Energy levels of $4f^3$ in the Nd^{3+} free ion from emission spectra. *J. Phys. B: At., Mol. Opt. Phys.* **2006**, *39*, L77–L82.

(42) Radha, A. V.; Navrotsky, A. Direct experimental measurement of water interaction energetics in amorphous carbonates MCO_3 (M = Ca, Mn, and Mg) and implications for carbonate crystal growth. *Cryst. Growth Des.* **2015**, *15*, 70–78.

(43) Navrotsky, A. Nanoscale effects on thermodynamics and phase equilibria in oxide systems. *ChemPhysChem* **2011**, *12*, 2207–2215.

(44) Mazeina, L.; Deore, S.; Navrotsky, A. Energetics of bulk and nano-akaganeite, β-FeOOH: enthalpy of formation, surface enthalpy, and enthalpy of water adsorption. *Chem. Mater.* **2006**, *18*, 1830–1838.

(45) Hayun, S.; Shvareva, T. Y.; Navrotsky, A. Nanoceria – energetics of surfaces, interfaces and water adsorption. *J. Am. Ceram. Soc.* **2011**, *94*, 3992–3999.

(46) Chase, M. W., Jr. *NIST-JANAF Thermochemical Tables*, 4th ed.; J. Phys. Chem. Ref. Data, Monograph, 1998; Vol. 9, pp 1– 1951.

(47) Reynolds, J. G.; Belsher, J. D. A review of sodium fluoride solubility in water. *J. Chem. Eng. Data* **2017**, *62*, 1743–1748.

(48) Mioduski, T.; Gumiński, C.; Zeng, D. IUPAC-NIST solubility data series. 100. Rare earth metal fluorides in water and aqueous systems. Part 2. Light lanthanides (Ce–Eu). *J. Phys. Chem. Ref. Data* **2015**, *44*, 013102.

(49) Yu, J.; Hu, L.; Shen, Y.; Ren, J. Phase change of $NaYF_4$:Er crystals in oxyfluoride phosphate upconversion luminescent glass ceramics: an advanced solid-state NMR study. *Inorg. Chem.* **2021**, *60*, 5868–5881.

Chapter 7

Energetics of Anion Excess $Ca_{1-x}RE_xF_{2+x}$ (RE = La, Pr, and Nd) Solid Solutions

Shuhao Yang,[†,‡] Andre Anderko,[‖] Richard E. Riman,[§] Alexandra Navrotsky[*,†]

[†]Navrotsky Eyring Center for Materials of the Universe, School of Molecular Sciences, Arizona State University, Tempe, Arizona 85287, United States

[‡]Department of Chemistry, University of California, Davis, California 95616, United States

[‖]OLI Systems, Inc., Parsippany, New Jersey 07054, United States

[§]Department of Materials Science and Engineering, Rutgers, The State University of New Jersey, Piscataway, New Jersey 08854, United States

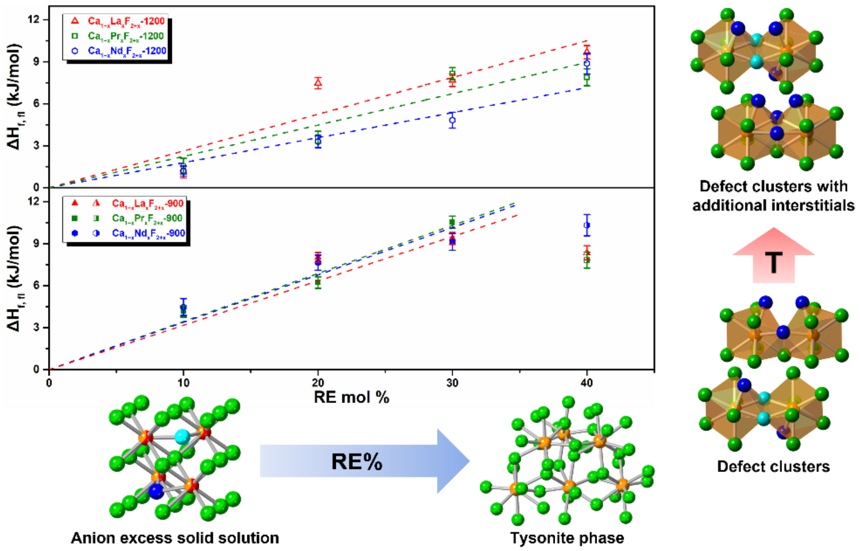

2022, to be submitted.

7.1 Abstract

Rare earth (RE) doped CaF_2 possesses unique optical and ionic transport properties showing widespread applications in solid state lasers, upconversion nanoparticles, and fluorine ion conductors. As a typical anion-excess solid solution, $Ca_{1-x}RE_xF_{2+x}$ (typically $0 \leq x \leq 0.4$) provides intriguing case studies in defect structures containing interstitial anions, on which extensive structural studies have been carried out.[1–18] However, there has been no experimental thermodynamic investigation into these systems, leaving a lack of thermodynamic understanding. By means of high temperature oxide melt solution calorimetry, formation enthalpies of $Ca_{1-x}RE_xF_{2+x}$ (RE = La, Pr, and Nd) over a range of compositions were determined. The formation of fluorite-structured $Ca_{1-x}RE_xF_{2+x}$ is endothermic with respect to binary fluorides, indicating the decisive role of temperature in the formation of these entropy-stabilized materials. Based on solid state nuclear magnetic resonance (SS NMR) and previous research on structure and ionic conductivity, it is evidenced that defect aggregation changes with dopant concentration and annealing temperature, leading to various clusters with different energetic properties. Defect clustering is more preferred in CaF_2 doped with smaller RE ions and is accompanied by less endothermic formation enthalpies, which is consistent with the presence of ordered superstructures in CaF_2–REF_3 systems for heavy RE elements. The thermodynamic assessment of anion-excess solid solutions not only deepens knowledge of solid-state chemistry but also contributes to the rational design, synthesis, and application of these materials.

7.2 Introduction

Calcium fluoride (CaF_2) doped with rare earth (RE) ions shows widespread applications in optical materials[19] and fluoride ion conductors[20] and has attracted extensive research interest.[21–24]

As a typical interstitial defect solid solution, the structural properties of anion-excess CaF_2 have been thoroughly investigated in the past several decades to reveal their defect structures. Despite the simple fluorite structure of the host lattice, complicated defect clusters can be formed by charge-compensating F interstitials with doped trivalent cations and anion vacancies.[25] These local clusters formed by defect aggregation are correlated with RE ionic radii, dopant concentrations, and synthesis temperatures. A variety of structural characterizations, including X-ray and neutron diffraction,[1–9] extended X-ray absorption fine structure (EXAFS),[10,11] and nuclear magnetic resonance (NMR)[12,13] have been applied to gain structural information, especially short-range order in fluorites. Computational simulation,[14–18] thermal depolarization[26,27] and ionic conductivity[28,29] measurements were also performed to have a basic understanding of defect structures and build relationships between structure and properties. Furthermore, as important components in oxyfluoride glass ceramics,[30] $Ca_{1-x}RE_xF_{2+x}$ solid solutions have dramatic impacts on properties and stability of these materials.[31] Unfortunately, experimental thermodynamic studies are absent in these systems, which not only leads to a thermodynamic data gap but also restricts the energetic understanding of anion-excess solid solutions. Accordingly, this work aims to determine the underlying energetics of CaF_2 doped with light RE (La, Pr, and Nd) and shed light on local defect configurations.

As shown in Figure 7.1a, in $Ca_{1-x}RE_xF_{2+x}$ solid solutions, Ca^{2+} and RE^{3+} are mixed on the cation sublattice and vacancies are formed on the anion sublattice with concomitant F^- interstitials. The interstitial F^- ions mainly locate at three sites (labelled F_1, F_2, and F_3): F_1 and F_2 interstitials occupy 48i positions at (1/2, u, u) with $u \approx 0.37$ and 32f positions at (v, v, v) with $v \approx 0.41$, respectively, while F_3 interstitials are considered as relaxed normal anions with the coordinates of (w, w w) and $w \approx 0.31$. It has been widely confirmed that, as the dopant concentration increases (> 1 mol %), defects are no longer isolated but aggregate to form local clusters consisting of substitutional RE^{3+}, anion vacancies, and interstitial F^{-} to stabilize defect structures.[32] Various defect cluster models have been proposed containing different numbers of substitutional doping ions, vacancies, and interstitials (Figure 7.1b). For small RE ions like Y^{3+}, 2:2:2 and 3:4:2 clusters referring to clusters comprising 2 vacancies, 2 F_1 and 2 F_2 interstitials or 3 vacancies, 4 F_1 and 2 F_2 interstitials, respectively, are formed at low dopant concentrations.[1,2] Larger clusters labelled 8:12:1 (8 vacancies, 12 F_1 and 1 F_2 interstitials) and relevant ordered superstructures are observed at high concentrations and after long annealing time.[6,11] On the other hand, large clusters are not favored by CaF_2 doped with light (large) RE ions. Instead, neutral 1:0:3 clusters and charged 2:2:3 and 1:0:4 clusters with interstitial deficient species may form depending on annealing temperature and time.[3–5,10]

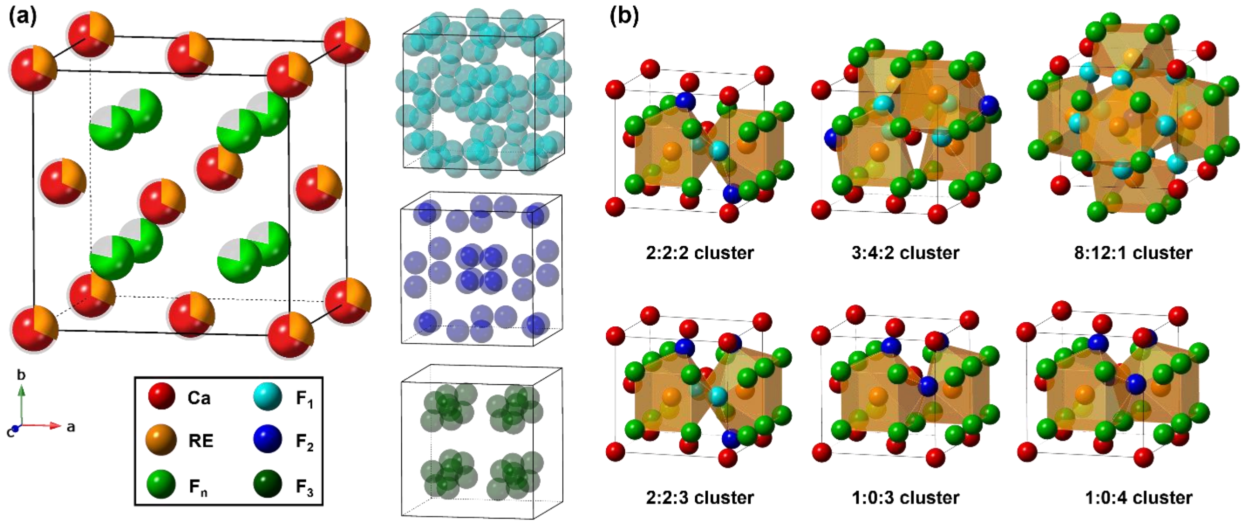

Figure 7.1. (a) The crystal structure of $Ca_{1-x}RE_xF_{2+x}$ and normal (F_n) and interstitial (F_1, F_2, and F_3) sites for F ions, plus (b) potential defect clusters, in which relaxed F ions (F_3) are not shown for clarity.

The thermodynamics of fluorite-structured oxides with cation substitution, such as trivalent RE doped ZrO_2, HfO_2, and CeO_2, have been studied systematically using high temperature oxide melt solution calorimetry.[33–40] The energetics of these anion-deficient solid solutions shows a strong correlation with vacancy–vacancy interactions and defect clusters, which can be related to the ionic conductivity.[41,42] Recently, this well-established calorimetric technique has been extended to fluoride and oxyfluoride compounds.[43–45] In the present work, the thermodynamic stability of $Ca_{1-x}RE_xF_{2+x}$ (RE = La, Pr, and Nd) was determined by high temperature oxide melt solution calorimetry. The effects of dopant radii, concentrations, and annealing temperature on the energetics of defect structures were discussed in light of structural characterizations conducted in the present work, published structural investigations, and conductivity studies.

7.3 Experimental Methods

7.3.1 Material Preparation

$Ca_{1-x}RE_xF_{2+x}$ (RE = La, Pr and Nd) samples were prepared by solid state reactions, in which different molar ratios of CaF_2 (99.95 %, Alfa Aesar) and LaF_3 (99.99 %, Alfa Aesar), PrF_3 (99.9 %, Alfa Aesar) or NdF_3 (99.9 %, Alfa Aesar) were mixed, pelletized, and heated at 900 or 1200 °C in a covered Pt crucible under an Ar atmosphere for 1 day, then fast cooled down to room temperature (within 30 min) and ground into powder. No weight loss was observed during the synthesis, confirming that the composition is the same as the precursor. In hydrothermal experiments, $Ca(NO_3)_2$ (Fisher Scientific, ACS grade), $Pr(NO_3)_3\cdot 6H_2O$ (99.9 %, Alfa Aesar), $Nd(NO_3)_3\cdot 6H_2O$ (99.9 %, Alfa Aesar), and NH_4F (Baker Analyzed, ACS grade) were used to prepare aqueous solutions. 7.5 mL 0.3 M $Ca(NO_3)_2$ and $Pr(NO_3)_3$ or $Nd(NO_3)_3$ solutions in different ratios were stirred with 14 mL 2.0 M NH_4F solutions at room temperature, then transferred into a Teflon bottle, sealed in a stainless steel autoclave, and heated at 160 °C for 1 day. The solid products were separated by vacuum filtration and dried under vacuum at 50 °C overnight. Heat treatments were done by further heating samples obtained from hydrothermal reactions at 1000 °C under an Ar atmosphere for 1 hour, during which heating and cooling rates of 10 and 20 °C min^{-1} were used, respectively.

7.3.2 Powder X-ray Diffraction

Powder X-ray diffraction (PXRD) patterns were obtained using a Bruker D2 Phaser diffractometer operated with Cu Kα radiation (λ = 1.54184 Å). The data for $Ca_{1-x}RE_xF_{2+x}$ samples were collected in the 2θ range of 10–120° with a step size of 0.02° and a dwell time of 5 s per step. The other data were collected in the 2θ range of 10–80° with a step size of 0.02° and a dwell time of 0.45 s per step. Lattice parameters were calculated based on peak positions in the PXRD patterns using MDI Jade software.

7.3.3 Nuclear Magnetic Resonance

The ^{19}F magic-angle spinning (MAS) nuclear magnetic resonance (NMR) measurements were performed on a Varian VNMRS 400 MHz spectrometer with a 1.6 mm T3 High Speed MAS probe. 40 kHz MAS spinning speed was used for the direct ^{19}F MAS experiment. The depth protocol was used to minimize ^{19}F background signals with a 20 second recycle delay. The ^{19}F MAS NMR spectra were calibrated according to a polytetrafluoroethylene (PTFE) standard. All spectra were collected at ambient temperature.

7.3.4 Raman Spectroscopy

Raman spectra were collected at room temperature on a custom-built Raman spectrometer in a 180° geometry. The sample was excited using a 150 mW Coherent Sapphire SF laser with a 532 nm wavelength. The laser power was controlled using a neutral density filter wheel with an initial laser power of 100 mW. The laser beam was focused onto the sample using a 50× APO Mitutoyo microscope objective with a numerical aperture of 0.42. The signal was isolated from the laser excitation using an Ondax SureBlock ultranarrow-band notch filter combined with two optigrate notch filters. The data were collected using an Andor 750 spectrometer combined with an iDus Backthinned CCD detector. Raman spectra were calibrated according to the peak position and intensity of a quartz standard.

7.3.5 High Temperature Oxide Melt Solution Calorimetry

High temperature oxide melt solution calorimetry experiments were carried out using a Setaram AlexSYS Tian-Calvet twin microcalorimeter using methods standard to our laboratory and described previously.[46–48] The calorimeter was calibrated against the heat content of high purity α-Al_2O_3 (99.99%). Pressed sample pellets (∼5 mg) were dropped from ambient temperature into the calorimeter containing the solvent, molten sodium molybdate ($3Na_2O\cdot4MoO_3$), in a Pt crucible at 800 °C. All experiments were flushed with O_2 at 60 mL min^{-1} and bubbled through the solvent at 5 mL min^{-1} to aid dissolution and prevent local saturation of the solvent. The measurement was repeated at least eight times on each sample.

7.4 Results

$Ca_{1-x}RE_xF_{2+x}$ samples were synthesized by solid state reactions at 900 or 1200 °C (termed $Ca_{1-x}RE_xF_{2+x}$-900 or $Ca_{1-x}RE_xF_{2+x}$-1200) and characterized by PXRD (Figure 7.2 to 7.4). The PXRD patterns of all $Ca_{1-x}RE_xF_{2+x}$-1200 show a single cubic fluorite phase up to 40 mol % RE, which is the solubility limit of REF_3 in CaF_2.[49] Trace amounts of REF_3 phases (tysonite structure) are seen in PXRD patterns of samples from 900 °C with 40 mol % RE ($Ca_{0.6}RE_{0.4}F_{2.4}$-900) as the diffuse phase transition in the CaF_2–REF_3 systems primarily occurs around 900 °C

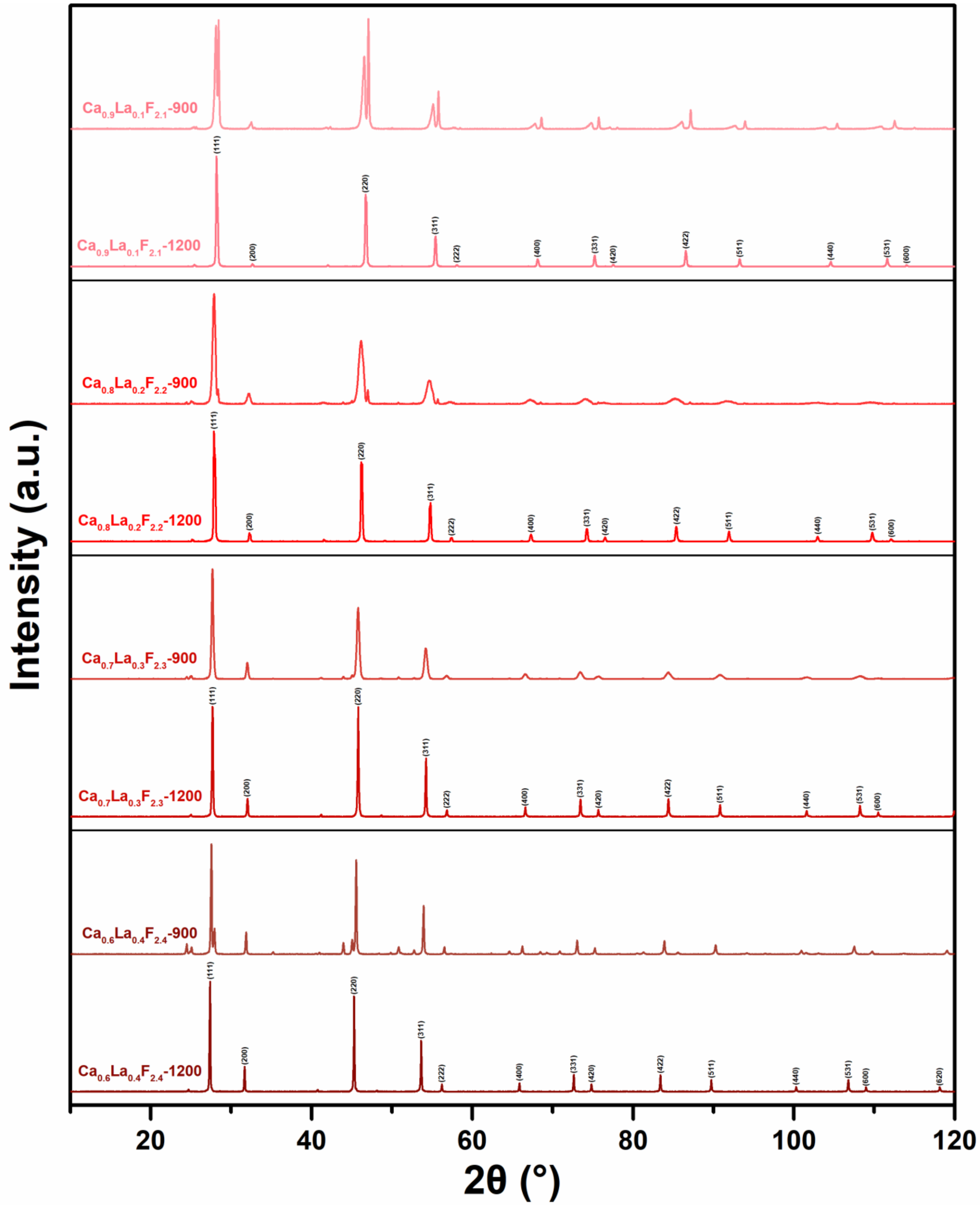

Figure 7.2 PXRD patterns of $Ca_{1-x}La_xF_{2+x}$.

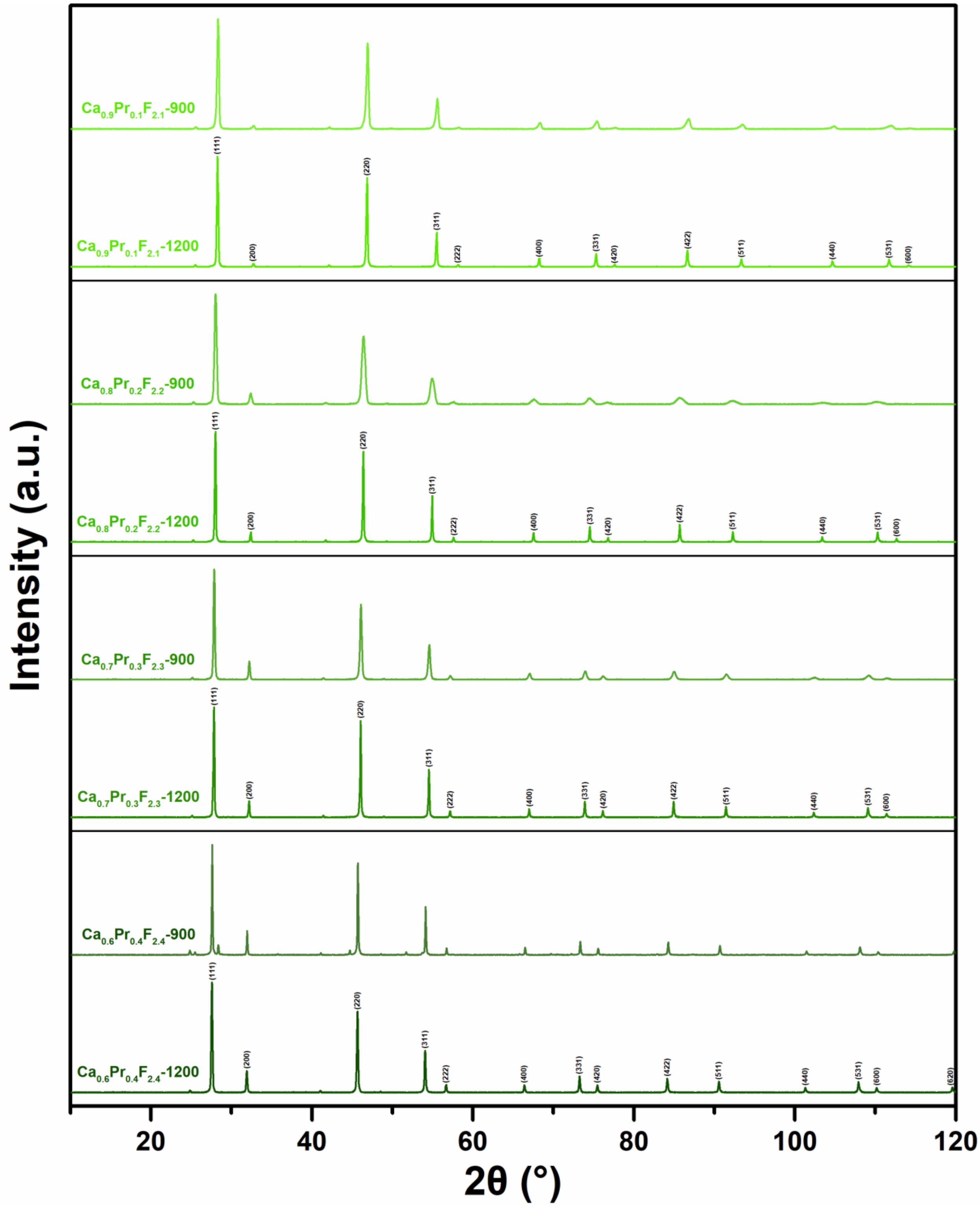

Figure 7.3 PXRD patterns of $Ca_{1-x}Pr_xF_{2+x}$.

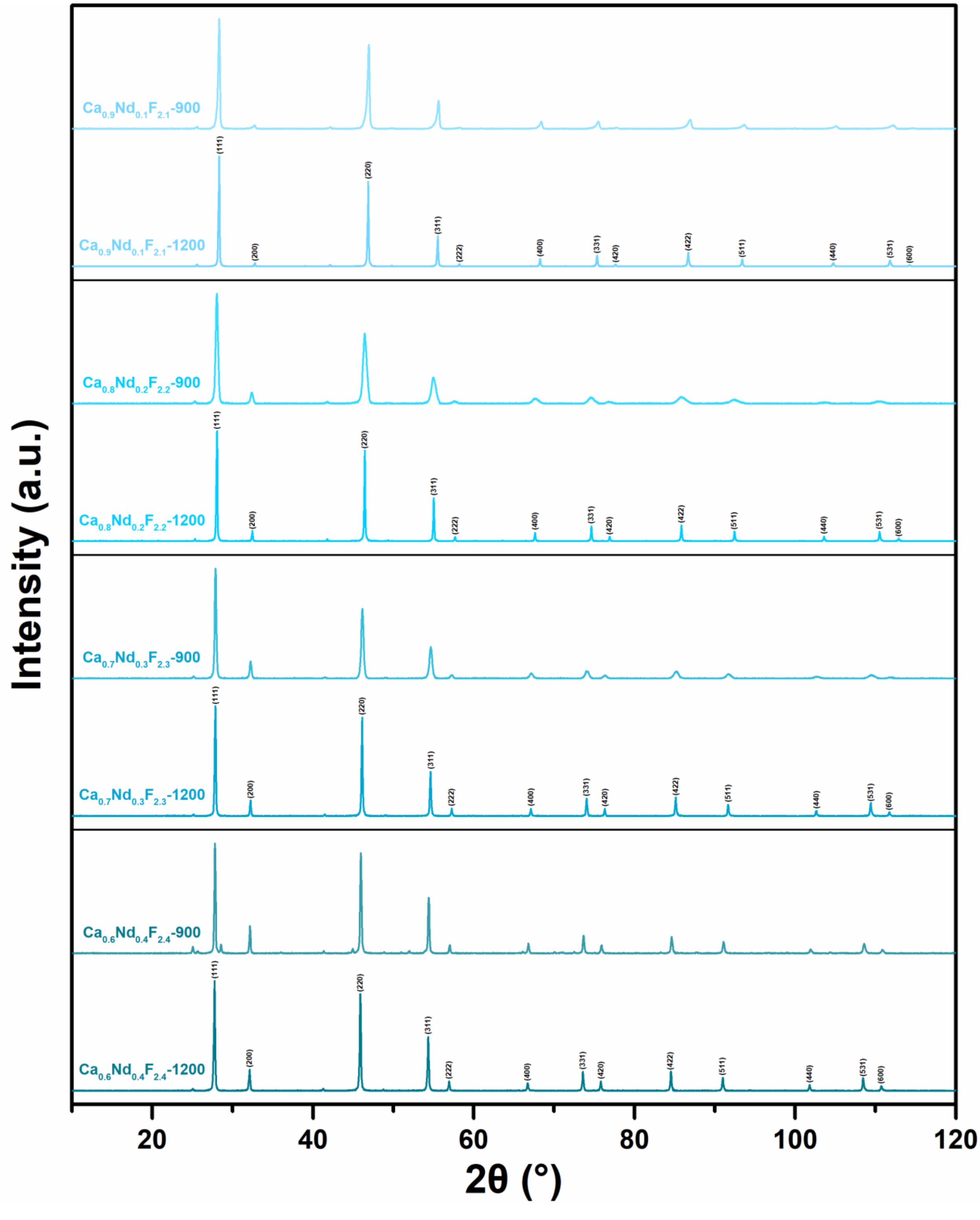

Figure 7.4 PXRD patterns of $Ca_{1-x}Nd_xF_{2+x}$.

leading to a decrease of solubility limit with decreasing temperature.[50] Different from $Ca_{0.9}Pr_{0.1}F_{2.1}$ and $Ca_{0.9}Nd_{0.1}F_{2.1}$, two phases are obtained in $Ca_{0.9}La_{0.1}F_{2.1}$-900, and a small amount of this second phase is also detected in $Ca_{0.8}La_{0.8}F_{2.2}$-900. $Ca_{1-x}RE_xF_{2+x}$-1200 samples have sharper diffraction peaks with different relative intensities compared to samples reacted at 900 °C, implying some structural differences. The lattice parameters of $Ca_{1-x}RE_xF_{2+x}$, refined by whole pattern fitting, are listed in Table 7.1. Figure 7.5 shows that the unit cell volume (V) increases with the RE content and samples from 1200 °C have larger V at room temperature than ones from 900 °C. The abnormal behavior of V for $Ca_{1-x}La_xF_{2+x}$-900 is correlated with the phase separation or the limited LaF_3 solubility at low and high La compositions, respectively.

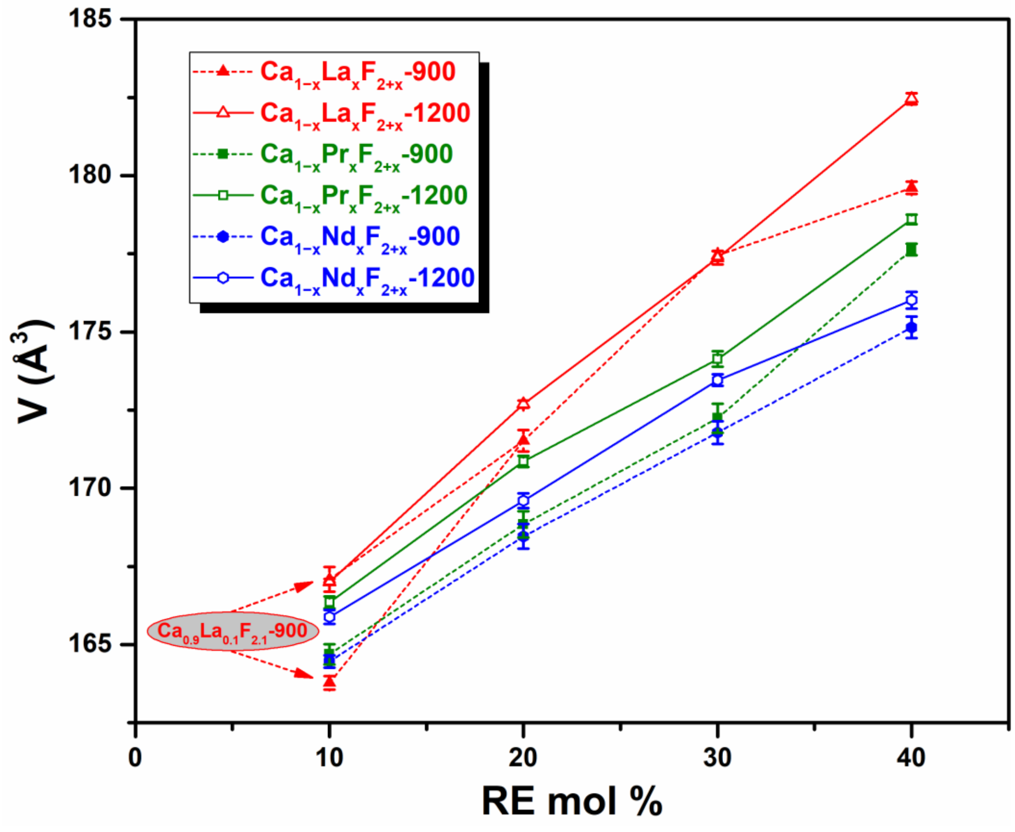

Figure 7.5 Unit cell volumes (V) of $Ca_{1-x}RE_xF_{2+x}$ samples versus RE content.

Table 7.1 Lattice parameters of $Ca_{1-x}RE_xF_{2+x}$ (space group: $Fm\overline{3}m$).

Sample	a (Å)	V (Å^3)
$Ca_{0.9}La_{0.1}F_{2.1}$-900	5.508(4) 5.471(2)	167.1(4) 163.8(2)
$Ca_{0.8}La_{0.2}F_{2.2}$-900	5.556(4)	171.5(3)
$Ca_{0.7}La_{0.3}F_{2.3}$-900	5.619(2)	177.4(1)
$Ca_{0.6}La_{0.4}F_{2.4}$-900	5.642(2)	179.6(2)
$Ca_{0.9}La_{0.1}F_{2.1}$-1200	5.507(1)	167.0(1)
$Ca_{0.8}La_{0.2}F_{2.2}$-1200	5.569(1)	172.7(1)
$Ca_{0.7}La_{0.3}F_{2.3}$-1200	5.619(2)	177.4(2)
$Ca_{0.6}La_{0.4}F_{2.4}$-1200	5.672(2)	182.5(2)
$Ca_{0.9}Pr_{0.1}F_{2.1}$-900	5.481(4)	164.7(3)
$Ca_{0.8}Pr_{0.2}F_{2.2}$-900	5.527(5)	168.8(4)
$Ca_{0.7}Pr_{0.3}F_{2.3}$-900	5.564(5)	172.2(5)
$Ca_{0.6}Pr_{0.4}F_{2.4}$-900	5.621(2)	177.6(2)
$Ca_{0.9}Pr_{0.1}F_{2.1}$-1200	5.500(2)	166.4(2)
$Ca_{0.8}Pr_{0.2}F_{2.2}$-1200	5.549(2)	170.9(2)
$Ca_{0.7}Pr_{0.3}F_{2.3}$-1200	5.584(3)	174.1(2)
$Ca_{0.6}Pr_{0.4}F_{2.4}$-1200	5.632(2)	178.6(2)
$Ca_{0.9}Nd_{0.1}F_{2.1}$-900	5.479(2)	164.5(2)
$Ca_{0.8}Nd_{0.2}F_{2.2}$-900	5.523(4)	168.5(4)
$Ca_{0.7}Nd_{0.3}F_{2.3}$-900	5.559(4)	171.8(4)
$Ca_{0.6}Nd_{0.4}F_{2.4}$-900	5.595(4)	175.1(3)
$Ca_{0.9}Nd_{0.1}F_{2.1}$-1200	5.495(2)	165.9(2)
$Ca_{0.8}Nd_{0.2}F_{2.2}$-1200	5.535(3)	169.6(2)
$Ca_{0.7}Nd_{0.3}F_{2.3}$-1200	5.577(2)	173.5(2)
$Ca_{0.6}Nd_{0.4}F_{2.4}$-1200	5.604(3)	176.0(3)

^{19}F MAS NMR experiments were performed on $Ca_{1-x}La_xF_{2+x}$-900 and $Ca_{1-x}La_xF_{2+x}$-1200 samples with undoped CaF_2 and LaF_3 (Figure 7.6). The spectrum of CaF_2 shows a single resonance at −108 ppm corresponding to the F ions (F_n) occupying normal 8c sites in the fluorite structure. Besides the resonance near −110 ppm (line 1), resonances around −80 (line 2), −70 (line 3), −40 (line 4), and −10 (line 5) ppm are also seen in the ^{19}F MAS NMR spectra of

$Ca_{1-x}La_xF_{2+x}$. The ^{19}F signals at −22 and 26 ppm can be attributed to the existence of LaF_3 phases in $Ca_{0.7}La_{0.3}F_{2.3}$-900 and $Ca_{0.6}La_{0.4}F_{2.4}$-900, which are consistent with the spectrum of LaF_3. The broad and overlapping peaks of LaF_3 phases imply that amorphous nanodomains or small nanocrystals may constitute the main form of LaF_3 phases in $Ca_{1-x}La_xF_{2+x}$-900 samples with over 30 mol % La.[51,52] $Ca_{1-x}Pr_xF_{2+x}$-900 and $Ca_{1-x}Nd_xF_{2+x}$-900 samples also show a shoulder at 400 cm^{-1} on the broad Raman peak of the fluorite structure at 322 cm^{-1} (Figure 7.7). The additional Raman band matches the A_{1g} mode of REF_3 with tysonite structure,[53] which was previously reported in $Ca_{1-x}La_xF_{2+x}$ crystals as a glass-like inclusion.[54]

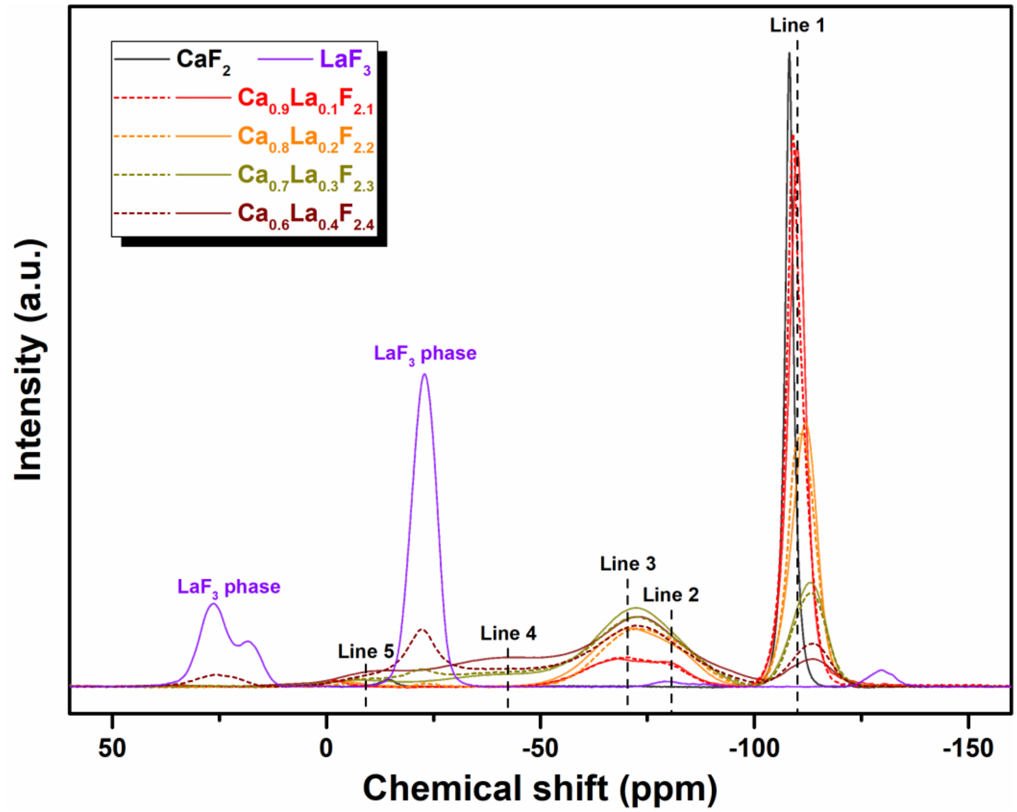

Figure 7.6 ^{19}F MAS NMR spectra of $C_{a1-x}La_xF_{2+x}$ with CaF_2 and LaF_3.

The relative intensities of resonances were estimated by fitting observed data using Gaussian functions. The results are listed in Table 7.2 and plotted in Figure 7.8 as a function of

La content. The relative intensity of line 1 decreases roughly linearly with increasing La content, and line 3 becomes more intense in the range of 10–30 mol % La. The resonance at −80 ppm (line 2) disappears at high La compositions, while two new resonances (line 4 and 5) arise above 30 mol % La. A negative shift of resonances at higher concentrations is seen for all lines as a result of lattice expansion.[13]

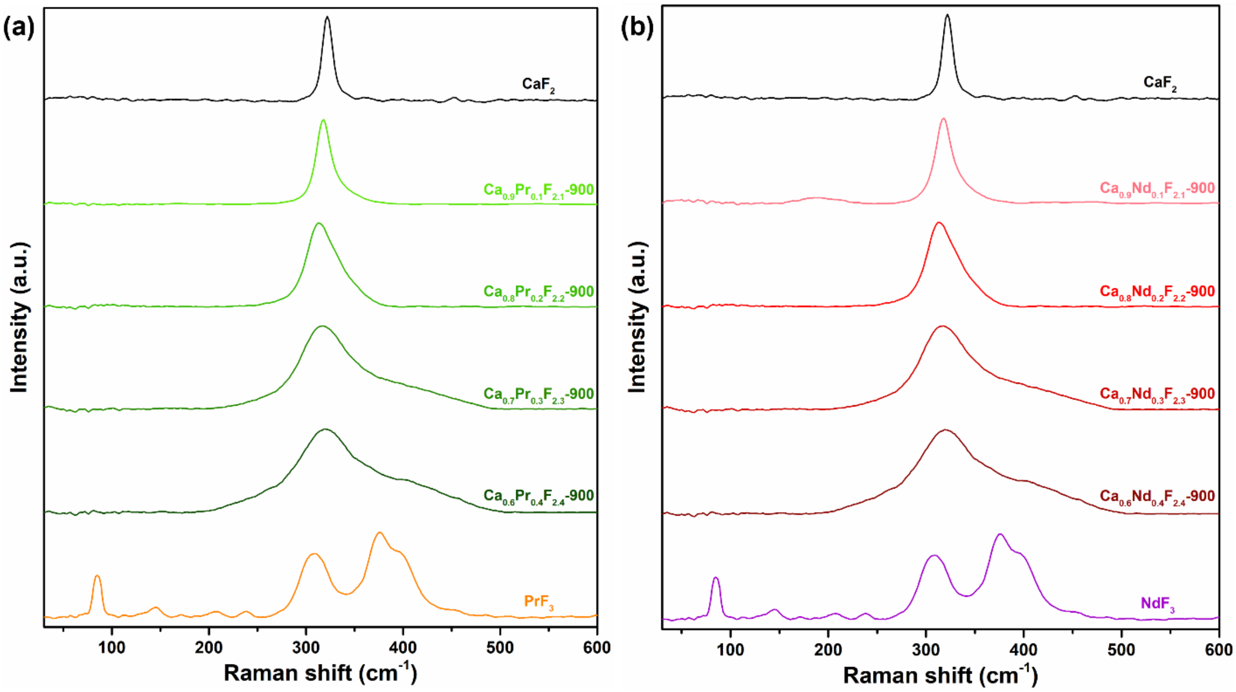

Figure 7.7 Raman spectra of (a) $Ca_{1-x}Pr_xF_{2+x}$-900 and (b) $Ca_{1-x}Nd_xF_{2+x}$-900 with CaF_2 and PrF_3 or NdF_3.

High temperature oxide melt solution calorimetry experiments were conducted to determine the formation enthalpies. The drop solution enthalpies (ΔH_{ds}), corresponding to the heat effects of samples dropped from room temperature and dissolved in molten $3Na_2O{\cdot}4MoO_3$ at 800 °C, are listed in Table 7.3. The thermodynamic cycles in Table 7.4 were used to calculate the formation enthalpies of $Ca_{1-x}RE_xF_{2+x}$ from fluorides ($\Delta H_{f,\,fl}$) or elements ($\Delta H_{f,\,el}$) at 25 °C. The thermochemical data are summarized in Table 7.3 and $\Delta H_{f,\,fl}$ values are presented in Figure 7.9.

Table 7.2 Resonances (ppm) and relative intensities (in parentheses) of the ^{19}F MAS NMR spectra.

Sample	Line 1	Line 2	Line 3	Line 4	Line 5	LaF$_3$ phase
CaF$_2$	−108.1 (100.0%)					
Ca$_{0.9}$La$_{0.1}$F$_{2.1}$-1200	−110.0 (79.0%)	−80.2 (4.0%)	−68.8 (17.0%)			
Ca$_{0.9}$La$_{0.1}$F$_{2.1}$-900	−109.4 (79.0%)	−81.3 (2.9%)	−69.3 (18.1%)			
Ca$_{0.8}$La$_{0.2}$F$_{2.2}$-1200	−111.6 (58.0%)	−83.8 (3.6%)	−71.2 (38.4%)			
Ca$_{0.8}$La$_{0.2}$F$_{2.2}$-900	−111.1 (59.1%)	−83.4 (9.9%)	−71.4 (31.0%)			
Ca$_{0.7}$La$_{0.3}$F$_{2.3}$-1200	−112.7 (29.6%)		−72.8 (55.9%)	−41.0 (10.9%)	−7.6 (3.6%)	
Ca$_{0.7}$La$_{0.3}$F$_{2.3}$-900	−112.9 (27.1%)		−72.8 (53.0%)	−45.2 (6.8%)		−22.0 (13.1%)
Ca$_{0.6}$La$_{0.4}$F$_{2.4}$-1200	−113.0 (10.1%)		−73.0 (56.9%)	−40.9 (20.5%)	−14.4 (12.5%)	
Ca$_{0.6}$La$_{0.4}$F$_{2.4}$-900	−113.2 (13.8%)		−72.9 (48.6%)	−45.2 (7.4%)		−22.3 (25.8%) 25.6 (4.4%)

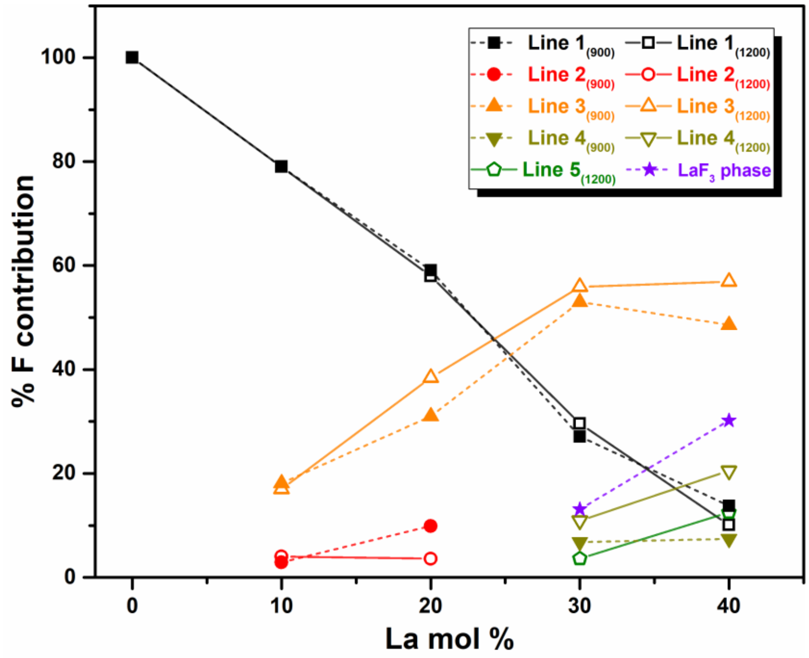

Figure 7.8 The relative intensities of ^{19}F MAS NMR resonances as a function of the La content, in which dashed and solid lines represent samples annealed from 900 and 1200 °C, respectively.

Table 7.3 Drop solution enthalpies (ΔH_{ds}) in $3Na_2O \cdot 4MoO_3$ at 800 °C and formation enthalpies of $Ca_{1-x}RE_xF_{2+x}$ from fluorides ($\Delta H_{f,\ fl}$) or elements ($\Delta H_{f,\ el}$) at 25 °C.

Sample	$\Delta H_{ds}{}^a$ (kJ mol^{-1})	$\Delta H_{f,\ fl}$ (kJ mol^{-1})	$\Delta H_{f,\ el}$ (kJ mol^{-1})
CaF_2	133.29 ± 0.24 (10)		−1225.9 ± 6.3[55]
LaF_3	154.89 ± 0.58[43]		−1731.8 ± 5.0[56]
PrF_3	152.45 ± 0.86[43]		−1712.1 ± 5.0[56]
NdF_3	151.02 ± 1.32[43]		−1712.9 ± 4.2[56]
$Ca_{0.9}La_{0.1}F_{2.1}$-1200	134.34 ± 0.34 (8)	1.11 ± 0.41	−1275.4 ± 5.7
$Ca_{0.8}La_{0.2}F_{2.2}$-900	129.60 ± 0.27 (8)	8.01 ± 0.35	−1319.1 ± 5.2
$Ca_{0.8}La_{0.2}F_{2.2}$-1200	130.14 ± 0.34 (9)	7.47 ± 0.41	−1319.6 ± 5.2
$Ca_{0.7}La_{0.3}F_{2.3}$-900	130.40 ± 0.36 (8)	9.37 ± 0.43	−1368.3 ± 4.7
$Ca_{0.7}La_{0.3}F_{2.3}$-1200	132.09 ± 0.37 (8)	7.68 ± 0.44	−1370.0 ± 4.7
$Ca_{0.6}La_{0.4}F_{2.4}$-900	133.59 ± 0.42 (8)	8.34 ± 0.50	−1419.9 ± 4.3
$Ca_{0.6}La_{0.4}F_{2.4}$-1200	132.25 ± 0.39 (8)	9.68 ± 0.48	−1418.6 ± 4.3
$Ca_{0.9}Pr_{0.1}F_{2.1}$-900	131.05 ± 0.35 (8)	4.16 ± 0.42	−1270.4 ± 5.7
$Ca_{0.9}Pr_{0.1}F_{2.1}$-1200	133.68 ± 0.52 (8)	1.53 ± 0.57	−1273 ± 5.7
$Ca_{0.8}Pr_{0.2}F_{2.2}$-900	130.90 ± 0.32 (8)	6.22 ± 0.41	−1316.9 ± 5.2
$Ca_{0.8}Pr_{0.2}F_{2.2}$-1200	133.51 ± 0.34 (8)	3.61 ± 0.43	−1319.5 ± 5.2
$Ca_{0.7}Pr_{0.3}F_{2.3}$-900	128.50 ± 0.30 (9)	10.54 ± 0.43	−1361.2 ± 4.7
$Ca_{0.7}Pr_{0.3}F_{2.3}$-1200	130.88 ± 0.30 (8)	8.16 ± 0.43	−1363.6 ± 4.7
$Ca_{0.6}Pr_{0.4}F_{2.4}$-900	133.12 ± 0.43 (8)	7.83 ± 0.57	−1412.5 ± 4.3
$Ca_{0.6}Pr_{0.4}F_{2.4}$-1200	133.06 ± 0.47 (8)	7.89 ± 0.60	−1412.5 ± 4.3
$Ca_{0.9}Nd_{0.1}F_{2.1}$-900	130.59 ± 0.56 (8)	4.47 ± 0.61	−1270.1 ± 5.7
$Ca_{0.9}Nd_{0.1}F_{2.1}$-1200	133.86 ± 0.27 (8)	1.20 ± 0.37	−1273.4 ± 5.7
$Ca_{0.8}Nd_{0.2}F_{2.2}$-900	129.20 ± 0.43 (8)	7.64 ± 0.54	−1315.7 ± 5.1
$Ca_{0.8}Nd_{0.2}F_{2.2}$-1200	133.55 ± 0.26 (8)	3.29 ± 0.42	−1320.0 ± 5.1
$Ca_{0.7}Nd_{0.3}F_{2.3}$-900	129.49 ± 0.41 (8)	9.12 ± 0.59	−1362.9 ± 4.6
$Ca_{0.7}Nd_{0.3}F_{2.3}$-1200	133.78 ± 0.36 (8)	4.83 ± 0.56	−1367.2 ± 4.6
$Ca_{0.6}Nd_{0.4}F_{2.4}$-900	130.06 ± 0.53 (8)	10.32 ± 0.76	−1410.4 ± 4.2
$Ca_{0.6}Nd_{0.4}F_{2.4}$-1200	131.50 ± 0.50 (8)	8.88 ± 0.74	−1411.8 ± 4.2

[a] Value is the mean of the number of measurements indicated in parentheses. Two standard deviations of the mean are given as errors.

Table 7.4 Thermodynamic cycles used to calculate formation enthalpies of $Ca_{1-x}RE_xF_{2+x}$ from fluorides ($\Delta H_{f,\,fl}$) or elements ($\Delta H_{f,\,el}$) at 25 °C.

Reaction	ΔH
$Ca_{1-x}RE_xF_{2+x}$ (s, 25 °C) → (1−x)CaF_2 (soln, 800 °C) + xREF_3 (soln, 800 °C)	$\Delta H_1 = \Delta H_{ds}$
CaF_2 (s, 25 °C) → CaF_2 (soln, 800 °C)	ΔH_2
REF_3 (s, 25 °C) → REF_3 (soln, 800 °C)	ΔH_3
(1−x)CaF_2 (s, 25 °C) + xREF_3 (s, 25 °C) → $Ca_{1-x}RE_xF_{2+x}$ (s, 25 °C)	$\Delta H_4 = \Delta H_{f.\,fl}$
$\Delta H_4 = -\Delta H_1 + (1-x)\Delta H_2 + x\Delta H_3$	
Ca (s, 25 °C) + F_2 (g, 25 °C) → CaF_2 (s, 25 °C)	ΔH_5
RE (s, 25 °C) + 3/2F_2 (g, 25 °C) → REF_3 (s, 25 °C)	ΔH_6
(1−x)Ca (s, 25 °C) + xRE (s, 25 °C) + (1+x/2)F_2 (g, 25 °C) → $Ca_{1-x}RE_xF_{2+x}$ (s, 25 °C)	$\Delta H_7 = \Delta H_{f.\,el}$
$\Delta H_7 = \Delta H_4 + (1-x)\Delta H_5 + x\Delta H_6$	

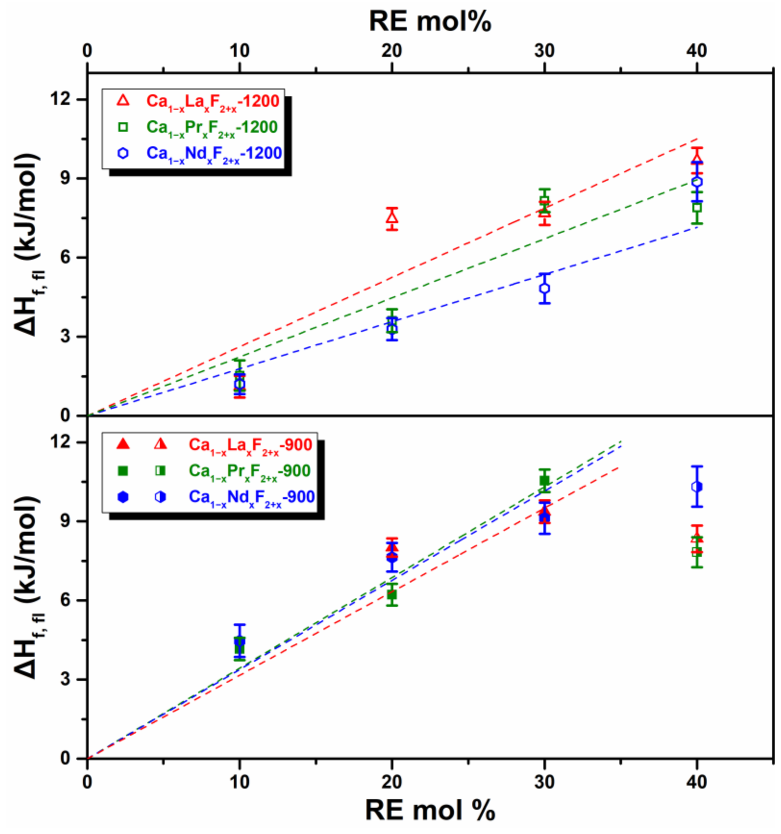

Figure7.9 Formation enthalpies of $Ca_{1-x}RE_xF_{2+x}$ from binary fluorides ($\Delta H_{f,\,fl}$) versus the RE content, in which dash lines are the linear fitting excluding the data of $Ca_{0.6}RE_{0.4}F_{2.4}$-900.

$\Delta H_{f,\,fl}$ values of $Ca_{1-x}RE_xF_{2+x}$ are all endothermic ranging from 1.1 to 10.5 kJ mol^{-1} and generally become more endothermic as the RE content increases. The data show a linear trend with RE compositions except for $Ca_{0.6}RE_{0.4}F_{2.4}$-900. The deviation may be caused by the presence of REF_3 phases. The endothermic $\Delta H_{f,\,fl}$ indicates that light RE doped CaF_2 with fluorite structure is not energetically favored compared to the binary fluorides and must be entropy-stabilized at synthesis temperature. This result is also confirmed by hydrothermal synthesis at relatively low temperature, in which mixtures of CaF_2 and REF_3 were obtained after hydrothermal reactions at 160 °C and were transformed to $Ca_{1-x}RE_xF_{2+x}$ solid solutions having the fluorite structure after annealing at 1000 °C (Figure 7.10).

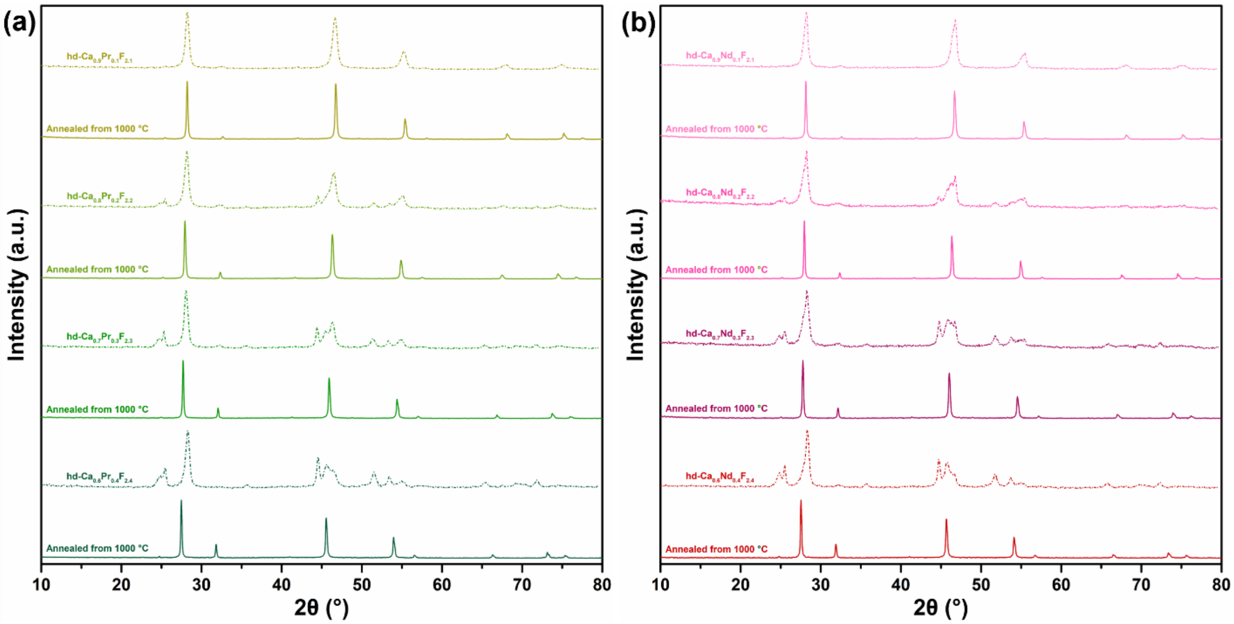

Figure7.10 PXRD patterns of (a) $Ca_{1-x}Pr_xF_{2+x}$ and (b) $Ca_{1-x}Nd_xF_{2+x}$ samples obtained from hydrothermal reactions (dash) and after heat treatments at 1000 °C (solid).

7.5 Discussion

Similar resonances are manifested in the ^{19}F MAS NMR spectra of the two $Ca_{0.9}La_{0.1}F_{2.1}$ samples, suggesting similar short-range structure regardless of different components. There are five F^{-} environments in the fluorite structure resolved in the ^{19}F MAS NMR spectra of $Ca_{1-x}La_{x}F_{2+x}$. In addition to the resonances at −110 ppm contributed by F_n ions, the resonance at −70 ppm (line 3) can be assigned to F_3 interstitials because relaxed F_3 sites have the highest relative intensity of the interstitials in all defect models.[12] Neutron scattering, computational simulation, and EXAFS revealed that 2:2:2 clusters capturing an additional F^{-} interstitial (2:2:3 type) represent the dominant defect cluster structure in 5–10 mol % La doped CaF_2.[3,10] Powder neutron diffraction studies indicated that small 1:0:3 clusters involving two ninefold coordinated La^{3+} are present in $Ca_{1-x}La_{x}F_{2+x}$ ($x = 0.1$–0.38) solid solutions.[4,5] It was also found that F ionic transport in $Ca_{1-x}La_{x}F_{2+x}$ shows drastic changes near $x \approx 0.15$.[28] Based on these structure and conductivity investigations, it is plausible that diverse dimer clusters coexist in $Ca_{1-x}La_{x}F_{2+x}$ at different concentrations. In the ^{19}F MAS NMR spectra, as the La content increases, line 4 (−40 ppm) replaces line 2 (−80 ppm). This alternation can be contributed to F interstitials in the two different cluster structures (such as 1:0:3 and 2:2:2 type), respectively. A new resonance around −10 ppm (line 5) arises for $Ca_{0.7}La_{0.3}F_{2.3}$-1200 and $Ca_{0.6}La_{0.4}F_{2.4}$-1200. By increasing annealing temperature from 900 to 1200 °C, line 3 becomes stronger, indicating that there are more relaxed F^{-} in $Ca_{1-x}La_{x}F_{2+x}$-1200. According to computational simulation, trapping an extra F^{-} in dimer clusters to form negatively charged clusters (1:0:4 and 2:2:3 type) with interstitial deficient species is energetically favored.[16] These cluster reactions may happen more commonly in $Ca_{1-x}La_{x}F_{2+x}$-1200 at high doping levels, producing more relaxed F interstitials. Hence, the additional resonance (line 5) is likely representative of F ions associating with interstitial deficient species with positive charge.

The $\Delta H_{f,\,fl}$ of $Ca_{1-x}RE_xF_{2+x}$ can be regarded as the sum of the transition enthalpy (ΔH_{tr}) of REF_3 from tysonite to fluorite structure and the mixing enthalpy (ΔH_{mix}) between REF_3 and CaF_2 as the fluorite end members. However, the ΔH_{tr} is unknown for REF_3 because the transformation of REF_3 from hexagonal tysonite to cubic fluorite structure has not been observed and apparently cannot be achieved by increasing temperature. Even so, we can speculate that ΔH_{tr} is insensitive to RE concentrations and has similar values for REF_3 containing different light RE elements (La, Pr, and Nd) considering the ΔH_{tr} of A- or C-type $REO_{1.5}$ to the fluorite phase.[35–37] Hence, the ΔH_{mix} associated with defect clustering is likely to be the major factor affecting the trend in $\Delta H_{f,\,fl}$ and may compensate the endothermic ΔH_{tr} to some extent. As shown in Figure 7.9, for $Ca_{1-x}RE_xF_{2+x}$-1200, slopes of the linear fitting of $\Delta H_{f,\,fl}$ against the RE content follow the order: La > Pr > Nd. This trend is in accordance with density functional theory (DFT) calculations,[18] showing that defect clusters are more stable in fluorite structured solid solutions doped with smaller RE ions. In contrast, $\Delta H_{f,\,fl}$ values of $Ca_{1-x}RE_xF_{2+x}$-900 are less affected by RE ionic radii and are more endothermic compared to those of $Ca_{1-x}RE_xF_{2+x}$-1200 with the same RE contents. The energetic difference between $Ca_{1-x}RE_xF_{2+x}$ annealed at 900 or 1200 °C supports the view that clustering, playing a role to stabilize CaF_2–REF_3 systems energetically, mainly emerges at higher temperature. This emergence is probably controlled by kinetics, suggesting high activation energy. The less endothermic $\Delta H_{f,\,fl}$ of $Ca_{1-x}RE_xF_{2+x}$-1200 and defect clusters identified by ^{19}F MAS NMR reveal that the cluster formation and reactions of neutral clusters to form charged clusters and species are kinetically hindered and less likely to take place at the low synthesis temperature, albeit they are more energetically favorable according to computational simulation.[14–17] It has been shown that there is a correlation between formation enthalpies and ionic conductivities at relatively low temperatures in RE doped ceria, i.e., the maximum conductivity is accompanied by the most endothermic formation enthalpy.[42] In CaF_2 doped with light RE elements, increasing ionic conductivities at higher concentrations were found.[28,29] The effects of annealing temperature on ionic conductivities remain to be studied.

The positive $\Delta H_{f, fl}$ and the small ΔH_{mix} compared to ΔH_{tr} suggest that the long-range-ordered superstructures are unlikely in CaF_2–REF_3 systems with light RE elements. In phase diagram research, no ordered stoichiometric compound has been identified in these systems.[49] On the other hand, according to computational simulation, clusters containing small RE ions are more stable and large clusters are more easily formed in fluorite solid solutions doped with heavy RE ions.[17] It is reasonable to infer that the ΔH_{mix} in CaF_2–REF_3 systems is more exothermic for heavy RE elements contributing more thermodynamic stability, since hexamer cluster-based superstructures and ordered phases are more common in CaF_2–REF_3 systems where RE = Ho–Lu.[49,57]

From the structural perspective, RE^{3+} has ninefold coordination in REF_3 phases (9+2 coordination in tysonite structure), higher than eightfold coordination for Ca^{2+} in fluorite structure. The formation of clusters containing interstitials can increase RE coordination to realize coordination conditions similar to those in the structure of their trifluorides.[32] Restricted by limited solubility at low temperatures, REF_3 phases ($RE_{1-y}Ca_yF_{3-y}$) appear in heavily doped CaF_2 samples to stabilize the whole system. The size mismatch of doping ions and lattice cations may be accompanied by substantial stabilization because of defect redistribution as in ZrO_2–$YO_{1.5}$ and HfO_2–$YO_{1.5}$ systems.[33,34] In the RE series, the ionic size of RE^{3+} decreases from light to heavy RE, ranging from a similar radius to Ca^{2+} (1.16 and 1.12 Å for 8-coordinated La^{3+} and Ca^{2+}) to smaller radii (such as 0.985 Å for 8-coordinated Yb^{3+}).[58] Thus, the size variation of RE ions may imply increasing energetic stability of $Ca_{1-x}RE_xF_{2+x}$ from light to heavy RE.

7.6 Conclusions

The formation enthalpies of CaF_2 doped with light RE ions were determined by high temperature oxide melt solution calorimetry. The fluorite structured $Ca_{1-x}RE_xF_{2+x}$ (RE = La, Pr, and Nd) is energetically less stable with respect to a mixture of binary fluorides and is entropy-stabilized at solid state reaction temperatures. Based on diffraction and spectroscopy in this work and previous structure and ionic conductivity studies, defect aggregation is found to be affected by RE ionic size, dopant concentration, and annealing temperature to form different local clusters. Clusters with smaller RE ions are more stable in $Ca_{1-x}RE_xF_{2+x}$ with fluorite structure, resulting in less endothermic formation enthalpies. Reactions forming dimer clusters with additional F^- interstitials and interstitial deficient species are more common at high temperature, which can stabilize the CaF_2–REF_3 system thermodynamically but need higher temperature to overcome kinetic barriers. At relatively low temperatures, REF_3 phases arise at lower concentrations with smaller formation enthalpies. These results provide a fundamental understanding of defect clusters in substitutional solid solutions containing anion interstitials, which can guide the design, synthesis, and functionalization of these materials.

7.7 Acknowledgements

We acknowledge the use of facilities within the Eyring Materials Center supported in part by NNCI-ECCS-2025490 and the Magnetic Resonance Research Center at Arizona State University. This work was supported by the U.S. Department of Energy Critical Materials Institute (CMI) Hub under the subaward number DE-AC02-07CH11358. We thank David Wright for help in sample preparation and Brian Cherry for help in NMR experiments.

7.8 References

(1) Cheetham, A. K.; Fender, B. E. F.; Cooper, M. J. Defect structure of calcium fluoride containing excess anions I. Bragg scattering. *J. Phys. C: Solid State Phys.* **1971**, *4*, 3107–3121.

(2) Steele, D.; Childs, P. E.; Fender, B. E. F. Defect structure of calcium fluoride containing excess anions II. Diffuse scattering. *J. Phys. C: Solid State Phys.* **1972**, *5*, 2677–2688.

(3) Catlow, C. R. A.; Chadwick, A. V.; Corish, J. The defect structure of anion excess CaF_2. *J. Solid State Chem.* **1983**, *48*, 65–76.

(4) Laval, J. P.; Mikou, A.; Frit, B.; Roult, G. Short-range order in heavily doped $CaF_2:Ln^{3+}$ fluorites: a powder neutron diffraction study. *J. Solid State Chem.* **1988**, *28–30*, 1300–1304.

(5) Laval, J. P.; Abaouz, A.; Frit, B. Short-range order in the $Ca_{1-x}La_xF_{2+x}$ solid solution: 1:0:3 or 1:0:4 clusters? *J. Solid State Chem.* **1989**, *81*, 271–277.

(6) Hull, S.; Wilson, C. C. The defect structure of anion-excess $(Ca_{1-x}Y_x)F_{2+x}$ with $x = 0.06$. *J. Solid State Chem.* **1992**, *100*, 101–114.

(7) Grover, V.; Achary, S. N.; Patwe, S. J.; Tyagi, A. K. Synthesis and characterization of $M_{1-x}Nd_xF_{2+x}$ ($M = Sr^{2+}, Ca^{2+}$; $0.00 \leq x \leq 1.00$). *Mater. Res. Bull.* **2003**, *38*, 1413–1422.

(8) Sorokin, N. I.; Karimov, D. N.; Krivandina, E. A.; Zhmurova, Z. I.; Komar'kova, O. N. Ionic conductivity of congruently melting $Ca_{0.6}Sr_{0.4}F_2$ and $Ca_{1-x-y}Sr_yR_xF_{2+x}$ (R = La, Ce, Pr, Nd) single crystals with fluorite structure. *Crystallogr. Rep.* **2008**, *53*, 271–277.

(9) Boiaryntseva, I. A.; Gektin, A. V.; Shiran, N. V. Effect of crystal structure on the luminescence properties of CaF_2-PrF_3 solid solutions. *Inorg. Mater.* **2013**, *49*, 209–213.

(10) Catlow, C. R. A.; Chadwick, A. V.; Greaves, G. N.; Moroney, L. M. Direct observations of the dopant environment in fluorites using EXAFS. *Nature* **1984**, *312*, 601–604.

(11) Catlow, C. R. A.; Chadwick, A. V.; Corish, J.; Moroney, L. M.; O'Reilly, A. N. Defect structure of doped CaF_2 at high temperatures. *Phys. Rev. B* **1989**, *39*, 1897–1907.

(12) Wang, F.; Grey, C. P. Probing the defect structure of anion-excess $Ca_{1-x}Y_xF_{2+x}$ (x = 0.03−0.32) with high-resolution ^{19}F magic-angle spinning nuclear magnetic resonance spectroscopy. *Chem. Mater.* **1998**, *10*, 3081–3091.

(13) Krahl, T.; Scholz, G.; Kemnitz, E. Solid solutions CaF_2–YF_3 with fluorite structure prepared on the sol–gel route: investigation by multinuclear MAS NMR spectroscopy. *J. Phys. Chem. C* **2014**, *118*, 21066–21074.

(14) Catlow, C. R. A. The defect properties of anion-excess alkaline-earth fluorides. I. Low defect concentrations. *J. Phys. C: Solid State Phys.* **1976**, *9*, 1845–1857.

(15) Catlow, C. R. A. The defect properties of anion-excess alkaline-earth fluorides. II. Intermediate and high dopant concentrations. *J. Phys. C: Solid State Phys.* **1976**, *9*, 1859–1869.

(16) Corish, J.; Catlow, C. R. A.; Jacobs, P. W. M.; Ong, S. H. Defect aggregation in anion-excess fluorites. Dopant monomers and dimers. *Phys. Rev. B* **1982**, *25*, 6425–6438.

(17) Bendall, P. J.; Catlow, C. R. A.; Corish, J.; Jacobs, P. W. M. Defect aggregation in anion-excess fluorites II. Clusters containing more than two impurity atoms. *J. Solid State Chem.* **1984**, *51*, 159–169.

(18) Ma, F.; Su, F.; Zhou, R.; Ou, Y.; Xie, L.; Liu, C.; Jiang, D.; Zhang, Z.; Wu, Q.; Su, L.; et al. The defect aggregation of RE^{3+} (RE = Y, La ∼ Lu) in MF_2 (M = Ca, Sr, Ba) fluorites. *Mater. Res. Bull.* **2020**, *125*, 110788.

(19) Doualan, J. L.; Camy, P.; Moncorgé, R.; Daran, E.; Couchaud, M.; Ferrand, B. Latest developments of bulk crystals and thin films of rare-earth doped CaF_2 for laser applications. *J. Fluor. Chem.* **2007**, *128*, 459–464.

(20) Réau, J.-M.; Grannec, J. 12 - Fast Fluorine Ion Conductors. In *Inorganic Solid Fluorides*; Academic Press, 1985; pp 423–467.

(21) Wang, G.; Peng, Q.; Li, Y. Upconversion luminescence of monodisperse $CaF_2:Yb^{3+}/Er^{3+}$ nanocrystals. *J. Am. Chem. Soc.* **2009**, *131*, 14200–14201.

(22) Dong, N.-N.; Pedroni, M.; Piccinelli, F.; Conti, G.; Sbarbati, A.; Ramírez-Hernández, J. E.; Maestro, L. M.; Iglesias-de la Cruz, M. C.; Sanz-Rodriguez, F.; Juarranz, A.; et al. NIR-to-NIR two-photon excited $CaF_2:Tm^{3+},Yb^{3+}$ nanoparticles: multifunctional nanoprobes for highly penetrating fluorescence bio-imaging. *ACS Nano* **2011**, *5*, 8665–8671.

(23) Sun, Z.; Mei, B.; Li, W.; Liu, Z.; Su, L. Effects of Nd concentration on microstructure and optical properties of Nd: CaF_2 transparent ceramics. *J. Am. Ceram. Soc.* **2016**, *99*, 4039–4044.

(24) Xu, B.; He, H.; Gu, Z.; Jin, S.; Ma, Y.; Zhai, T. Improving 800 nm triggered upconversion emission for lanthanide-doped CaF_2 nanoparticles through sodium ion doping. *J. Phys. Chem. C* **2017**, *121*, 18280–18287.

(25) Laval, J. P.; Frit, B. Defect structure of anion-excess fluorite-related $Ca_{1-x}Y_xF_{2+x}$ solid solutions. *J. Solid State Chem.* **1983**, *49*, 237–246.

(26) Stiefbold, D. R.; Huggins, R. A. Dipole reorientation kinetics in rare earth-doped CaF_2. *J. Solid State Chem.* **1972**, *5*, 15–27.

(27) Nauta-Leeffers, Z. C.; den Hartog, H. W. Dipole reorientation of tetragonal charge-compensation centers in $CaF_2:R^{3+}$. *Phys. Rev. B* **1979**, *19*, 4162–4166.

(28) Ivanov-Shits, A. K.; Sorokin, N. I.; Fedorov, P. P.; Sobolev, B. P. Specific features of ionic transport in nonstoichiometric fluorite-type $Ca_{1-x}R_xF_{2+x}$ (R = La–Lu, Y, Sc) phases. *Solid State Ion.* **1990**, *37*, 125–137.

(29) Grandjean, D.; Challier, T.; Jones, D. J.; Vitse, P. Anion-excess fluorite type solid solutions MF_2–NdF_3 and MF_2–UF_4 (M = Ca, Ba): conductivity and EXAFS spectroscopic study. *Solid State Ion.* **1992**, *51*, 297–303.

(30) Fedorov, P. P.; Luginina, A. A.; Popov, A. I. Transparent oxyfluoride glass ceramics. *J. Fluor. Chem.* **2015**, *172*, 22–50.

(31) Imanieh, M. H.; Martín, I. R.; Yekta, B. E.; Gonzalez-Platas, J.; Creus, A. H. Investigation on crystallization and optical properties of $Ca_{1-x}La_xF_{2+x}$ glass-ceramics. *J. Am. Ceram. Soc.* **2014**, *97*, 782–788.

(32) Chernov, S. V.; Gunβer, W.; Murin, I. V. On rare-earth clustering in flourite type solid solutions MF_2–REF_3. *Solid State Ion.* **1991**, *47*, 67–70.

(33) Lee, T. A.; Navrotsky, A.; Molodetsky, I. Enthalpy of formation of cubic yttria-stabilized zirconia. *J. Mater. Res.* **2003**, *18*, 908–918.

(34) Lee, T. A.; Navrotsky, A. Enthalpy of formation of cubic yttria-stabilized hafnia. *J. Mater. Res.* **2011**, *19*, 1855–1861.

(35) Chen, W.; Lee, T. A.; Navrotsky, A. Enthalpy of formation of yttria-doped ceria. *J. Mater. Res.* **2011**, *20*, 144–150.

(36) Chen, W.; Navrotsky, A. Thermochemical study of trivalent-doped ceria systems: CeO_2–$MO_{1.5}$ (M = La, Gd, and Y). *J. Mater. Res.* **2011**, *21*, 3242–3251.

(37) Buyukkilic, S.; Shvareva, T.; Navrotsky, A. Enthalpies of formation and insights into defect association in ceria singly and doubly doped with neodymia and samaria. *Solid State Ion.* **2012**, *227*, 17–22.

(38) Lee, T. A.; Stanek, C. R.; McClellan, K. J.; Mitchell, J. N.; Navrotsky, A. Enthalpy of formation of the cubic fluorite phase in the ceria–zirconia system. *J. Mater. Res.* **2011**, *23*, 1105–1112.

(39) Simoncic, P.; Navrotsky, A. Energetics of rare-earth-doped hafnia. *J. Mater. Res.* **2011**, *22*, 876−885.

(40) Tran, T. B.; Navrotsky, A. Energetics of dysprosia-stabilized bismuth oxide electrolytes. *Chem. Mater.* **2012**, *24*, 4185−4191.

(41) Navrotsky, A.; Simoncic, P.; Yokokawa, H.; Chen, W.; Lee, T. Calorimetric measurements of energetics of defect interactions in fluorite oxides. *Faraday Discuss.* **2007**, *134*, 171–180.

(42) Avila-Paredes, H. J.; Shvareva, T.; Chen, W.; Navrotsky, A.; Kim, S. A correlation between the ionic conductivities and the formation enthalpies of trivalent-doped ceria at relatively low temperatures. *Phys. Chem. Chem. Phys.* **2009**, *11*, 8580–8585.

(43) Yang, S.; Anderko, A.; Riman, R. E.; Navrotsky, A. Thermochemistry of sodium rare earth ternary fluorides, $NaREF_4$. *Acta Mater.* **2021**, *220*, 117289.

(44) Yang, S.; Jayanthi, K.; Anderko, A.; Riman, R. E.; Navrotsky, A. Thermochemical investigation of the stability and conversion of nanocrystalline and high-temperature phases in sodium neodymium fluorides. *Chem. Mater.* **2021**, *33*, 9571−9579.

(45) Yang, S.; Anderko, A.; Riman, R. E.; Navrotsky, A. Thermochemistry of stoichiometric rare earth oxyfluorides REOF. *J. Am. Ceram. Soc.* **2022**, *105*, 1472–1480.

(46) Navrotsky, A. Progress and new directions in high temperature calorimetry. *Phys. Chem. Miner.* **1977**, *2*, 89–104.

(47) Navrotsky, A. Progress and new directions in high temperature calorimetry revisited. *Phys. Chem. Miner.* **1997**, *24*, 222–241.

(48) Navrotsky, A. Progress and new directions in calorimetry: a 2014 perspective. *J. Am. Ceram. Soc.* **2014**, *97*, 3349–3359.

(49) Sobolev, B. P.; Fedorov, P. P. Phase diagrams of thE CaF_2-(Y, Ln)F_3 svstems I. Experimental. *J. Less Common Met.* **1978**, *60*, 33–46.

(50) Fedorov, P. P.; Sobolev, B. P. Phase diagrams of the CaF_2-$(Y,Ln)F_3$ systems II. A discussion. *J. Less Common Met.* **1979**, *63*, 31–43.

(51) Chable, J.; Dieudonné, B.; Body, M.; Legein, C.; Crosnier-Lopez, M.-P.; Galven, C.; Mauvy, F.; Durand, E.; Fourcade, S.; Sheptyakov, D.; et al. Fluoride solid electrolytes: investigation of the tysonite-type solid solutions $La_{1-x}Ba_xF_{3-x}$ ($x < 0.15$). *Dalton Trans.* **2015**, *44*, 19625–19635.

(52) Chable, J.; Martin, A. G.; Bourdin, A.; Body, M.; Legein, C.; Jouanneaux, A.; Crosnier-Lopez, M. P.; Galven, C.; Dieudonné, B.; Leblanc, M.; et al. Fluoride solid electrolytes: from microcrystalline to nanostructured tysonite-type $La_{0.95}Ba_{0.05}F_{2.95}$. *J. Alloys Compd.* **2017**, *692*, 980–988.

(53) Bauman, R. P.; Porto, S. P. S. Lattice vibrations and structure of rare-earth fluorides. *Phys. Rev.* **1967**, *161*, 842–847.

(54) Tu, J.; FitzGerald, S. A.; Campbell, J. A.; Sievers, A. J. Glass-like properties observed in low-frequency Raman scattering of mixed fluorite crystals. *J. Non-Cryst. Solids* **1996**, *203*, 153–158.

(55) Chase, M. W., Jr. *NIST-JANAF Thermochemical Tables*, 4th ed.; J. Phys. Chem. Ref. Data, Monograph, 1998; Vol. 9, pp 1–1951.

(56) Glushko, V. P. *Thermochemical Constants of Substances*; Academy of Sciences of USSR, 1978.

(57) Sobolev, B. P.; Golubev, A. M.; Herrero, P. Fluorite $M_{1-x}R_xF_{2+x}$ phases (M = Ca, Sr, Ba; R = rare earth elements) as nanostructured materials. *Crystallogr. Rep.* **2003**, *48*, 141–161.

(58) Shannon, R. D. Revised effective ionic radii and systematic studies of interatomic distances in halides and chalcogenides. *Acta Cryst.* **1976**, *32*, 751−767.

Chapter 8

Trends in Structure and Energetics of Rare Earth Compounds

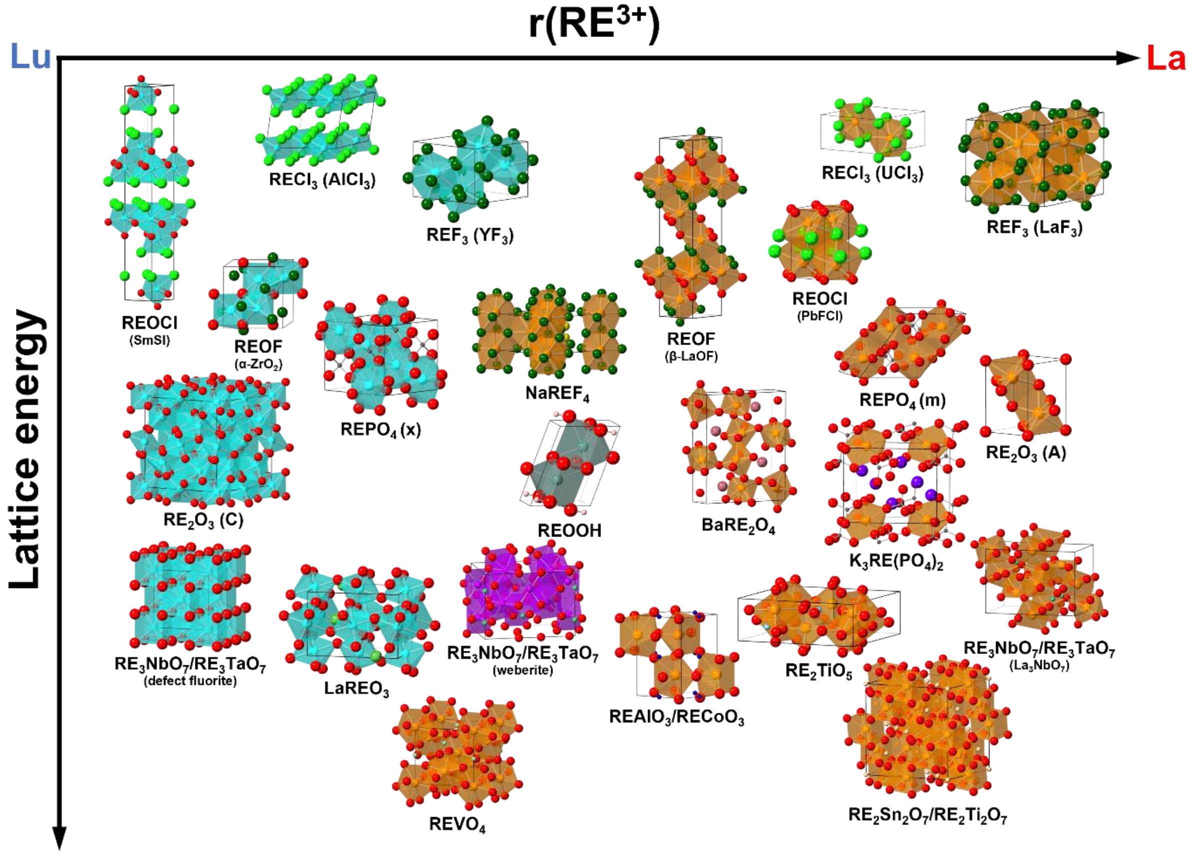

8.1 Introduction

Taking advantage of the development of experimental thermodynamic methods, extensive new thermodynamic data of rare earth (RE) materials have been acquired, which not only enrich the database for thermodynamic modeling and material computation[1] but also provide an opportunity to build a secure basis for a fundamental understanding of the thermodynamics of RE compounds. In this dissertation, energetics of RE oxycompounds and ternary fluorides were studied via direct calorimetric techniques and have been discussed in the preceding chapters. Two remarkable features have been discovered in these RE systems: (i) distinct trends of formation enthalpies or thermodynamic stability relative to binary compounds are manifested in different RE compounds across the RE series; (ii) structural tolerance to variable RE ions differs among RE compounds. Because thermodynamic stability and phase transformations have a dominant position in processing and applications of materials, it is vital to have a fundamental understanding of these phenomena. Lattice energies (U), reflecting the interaction strength between constituent ions in ionic solids, appear to be the entrance to reveal the underlying reason for the trends seen. Some attempts have been made in previous studies,[2–4] but an extensive analysis covering diverse RE systems is needed to reach comprehension on a broader scale. In this chapter, U of RE compounds, including ones studied in this dissertation and RE oxides or oxysalts with published thermodynamic data, were calculated by Born–Haber cycles. Structures of involved RE compounds are also introduced briefly for the convenience of correlating energetics and structures. By combining structural and thermodynamic perspectives, the crucial role of the RE coordination number in the trends of formation enthalpies is identified, which shows a correlation with the slope of U across the RE series. Moreover, the structural consistency of RE compounds throughout RE elements shows an association with the magnitude of U and the ionic strength of RE compounds.

8.2 Lattice Energies of Rare Earth Compounds

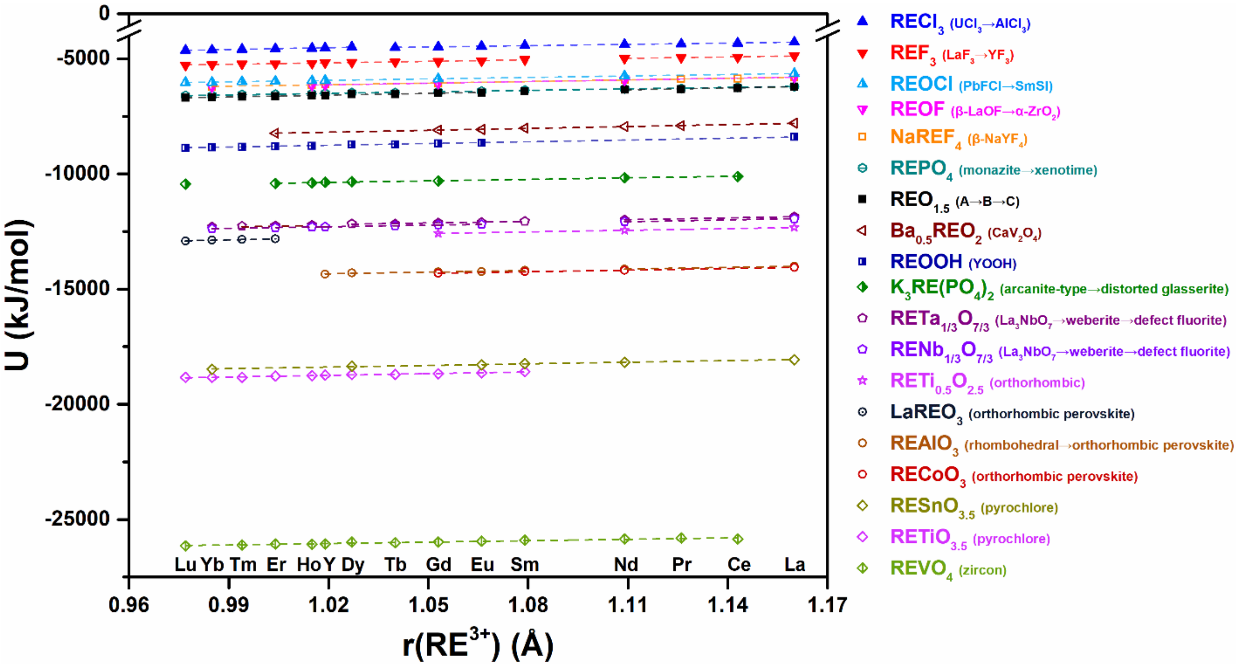

Figure 8.1 Lattice energies (U) of RE compounds as a function of ionic radius (r) of RE^{3+} in eight-fold coordination, in which compounds having the same structure are connected by dashed lines.

To better compare U, the formula of RE compounds is normalized as the composition containing a single RE, which is used in this chapter unless otherwise stated. The U values of RE compounds were calculated using Born–Haber cycles based on the published thermochemical data of binary RE oxides and halides,[5–9] RE oxycompounds,[3,4,10,11] and ternary RE fluorides[2] and oxides[12–21] or oxysalts[22–24]. Except for $REPO_4$ and $K_3RE(PO_4)_2$ which treat PO_4^{3-} as an ion with −3 charge,[25] all U refer to the heat of formation of RE compounds from gaseous mono-ions at standard conditions (298 K and 1 atm). The results are listed in Appendix C and plotted versus ionic radii[26] of RE^{3+} in eight-fold coordination (Figure 8.1).

The U of all RE compounds becomes more exothermic with decreasing RE size. This is consistent with the lattice shrinkage of RE compounds from light to heavy RE elements, giving rise to shorter cation–anion distances and stronger Coulombic interactions. Besides interionic distances or unit cell volumes embodying cation–anion distances in three-dimensional (3D) lattices, the ionic strength (I) has a great effect on U of ionic solids.[27–29] It can be calculated as follows:

$$I = \frac{1}{2}\sum n_i {z_i}^2 \tag{8.1}$$

where n_i is the number of ions with z_i charge in the chemical formula. As shown in Figure 8.2, I values of RE compounds have a similar order of magnitude as that of U, indicating the predominant role of composition and charge number in the energetics of ionic compounds.

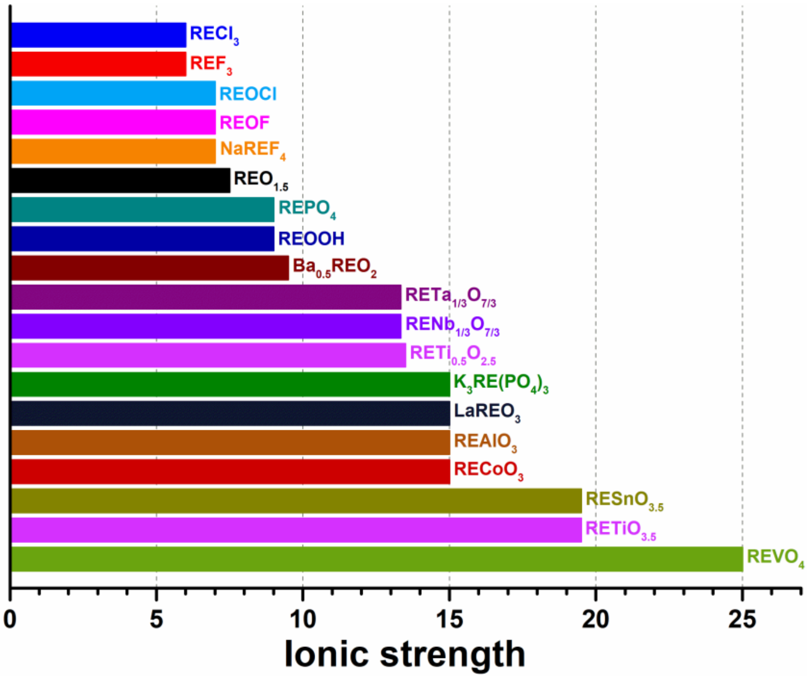

Figure 8.2 Ionic strength of RE compounds.

8.3 Crystal Structures of Rare Earth Compounds

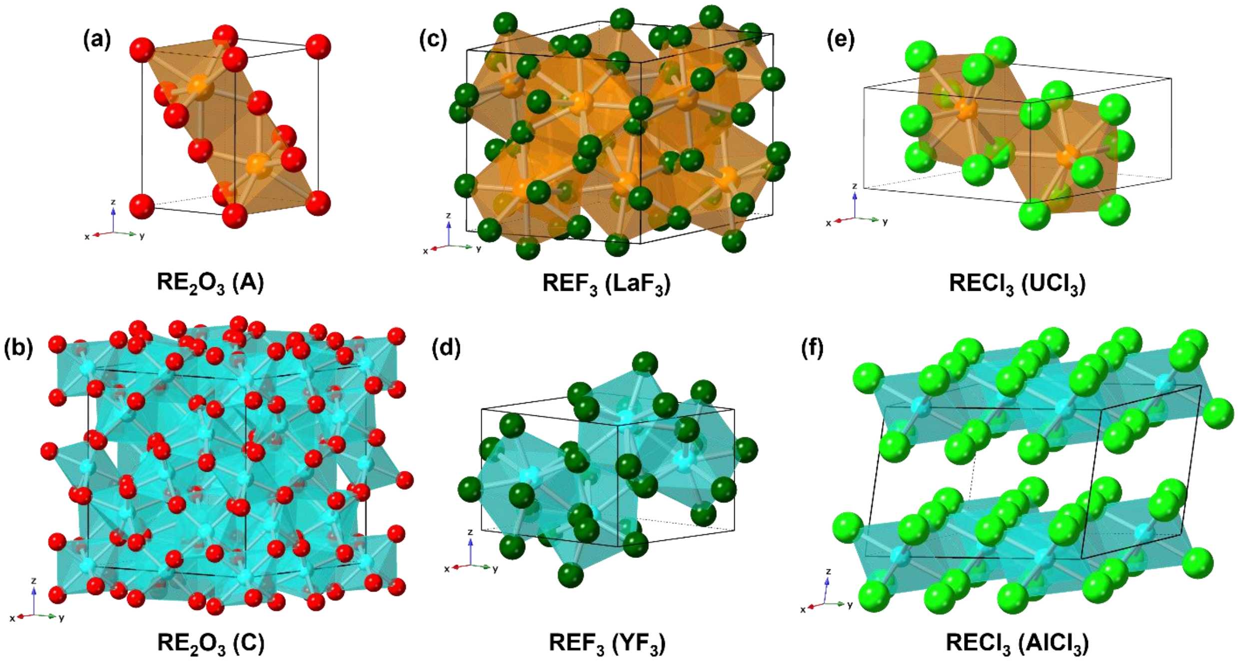

Figure 8.3 Crystal structures of RE binary compounds: (a) A- and (b) C-type structured RE_2O_3, (c) LaF_3 and (d) YF_3 structured REF_3, and (e) UCl_3 and (f) $AlCl_3$ structured $RECl_3$.

The crystal structures of chosen RE compounds are introduced before discussing their correlations with U. For binary oxides, RE sesquioxides (RE_2O_3) adopt A-, B-, and C-type structures as the atomic number increases. Light (La to Nd) and heavy (Eu to Lu plus Y) RE elements prefer the A or C structure, respectively, while the B-type structure is only adopted by Sm_2O_3 as the room temperature stable phase.[30] The A form of RE_2O_3 has the $P\bar{3}m1$ space group where RE ions are in seven-fold coordination (Figure 8.3a), while the C form has a cubic structure (space group: $Ia\bar{3}$) in which RE ions are six-coordinated (Figure 8.3b). The structure variation across the RE series exists in RE trifluorides (REF_3) and trichlorides ($RECl_3$) as well. Light RE fluorides (LaF_3 to NdF_3) have the “LaF_3” (tysonite) structure (space group: $P\bar{3}c1$) with 9+2 coordination of RE ions (Figure 8.3c), and heavy RE fluorides (SmF_3 to LuF_3 plus YF_3)

have the “YF_3” (β-YF_3) structure (space group: Pnma) with nine-fold coordination of RE ions (Figure 8.3d).[31] Anhydrous $RECl_3$ possesses the hexagonal UCl_3 structure (space group: $P6_3/m$) from La to Gd (Figure 8.3e) and the monoclinic $AlCl_3$ structure (space group: C2/m) from Dy to Lu plus Y (Figure 8.3f), where RE ions are in nine-fold or six-fold coordination, respectively.[32,33]

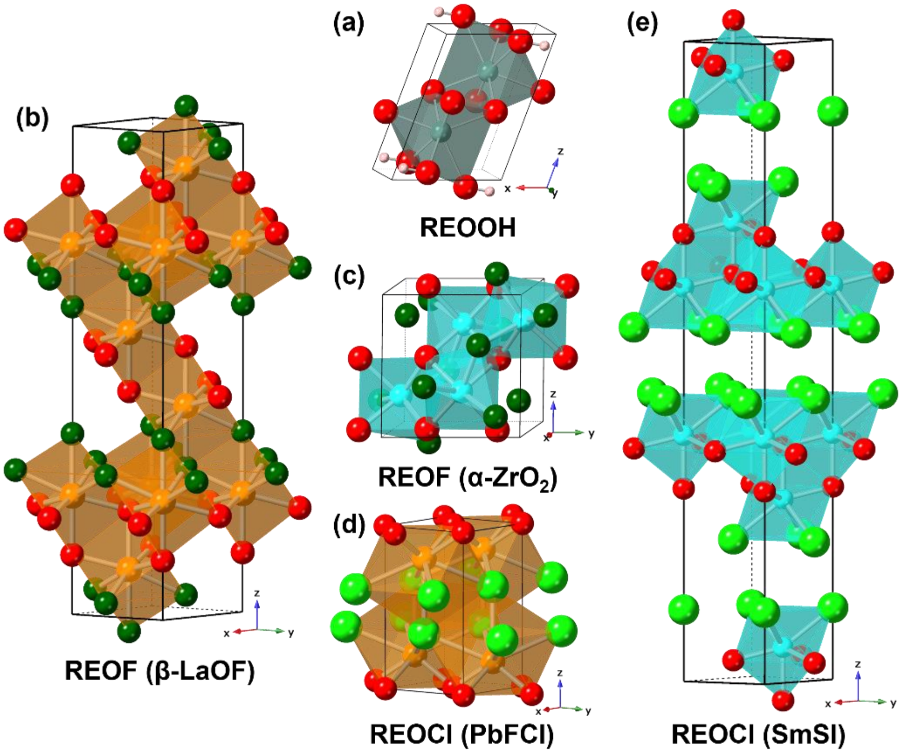

Figure 8.4 Crystal structures of RE oxycompounds: (a) REOOH, (b) β-LaOF and (c) α-ZrO_2 structured REOF, (d) PbFCl-type and (e) SmSI-type structured REOCl.

The crystal structure of REOOH is presented in Figure 8.4a, which is isostructural with YOOH for all lanthanide elements.[34–36] The RE ions are in a distorted monocapped trigonal prism and seven-coordinated with three hydroxyl groups and four O anions, and the structure is not hydrogen bonded.[37] Different crystal structures are adopted by light and heavy RE elements for RE oxyhalides due to the cationic size difference. From La to Er plus Y, REOF has a distorted fluorite structure in the rhombohedral system (space group: $R\bar{3}m$) termed β-LaOF, where RE^{3+} is eight-fold coordinated to four O^{2-} and four F^- in a distorted cube (Figure 8.4b).[38,39] On the other hand, a monoclinic structure is favored by REOF with the last three lanthanide elements (Tm, Yb, and Lu) as the thermodynamic stable phase, which is isostructural to α-ZrO_2 (baddeleyite) and made up of REF_3O_4 polyhedra (Figure 8.4c).[40] A 3D (PbFCl-type, space group: P4/nmm) and a two-dimensional (2D) (SmSI-type, space group: R$\bar{3}$m) structure occur for REOCl with large (La to Ho plus Y) and small (Er to Lu) cations, respectively.[41–43] In the PbFCl-type structure (Figure 8.4d), RE^{3+} is coordinated to four O^{2-} and four Cl^- in the neighboring layers with another Cl^- in the next nearest layer forming an square antiprism. As shown in Figure 8.4e, layers constituted by REO_4Cl_3 polyhedra are held together by van der Waals (vdW) forces in the SmSI-type REOCl.

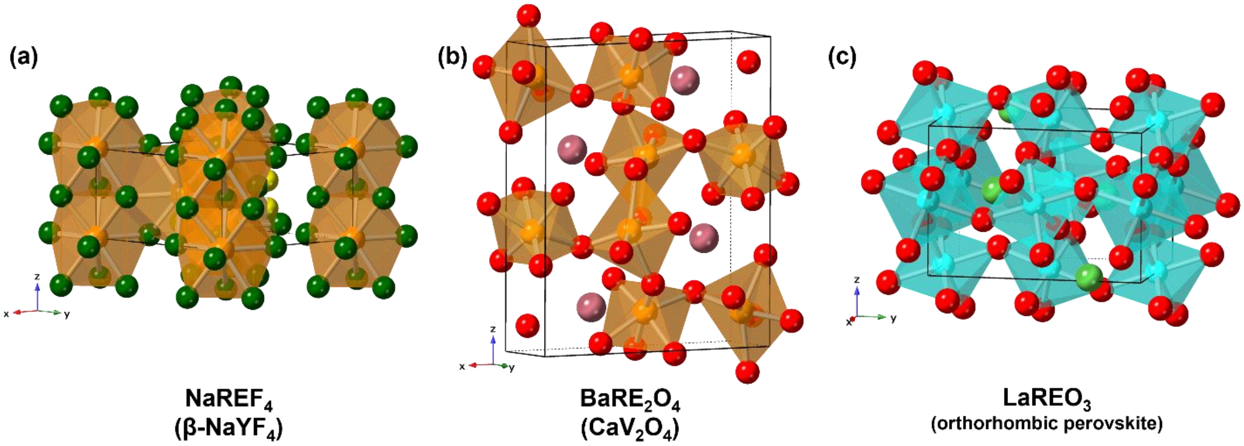

Figure 8.5 Crystal structures of (a) $NaREF_4$, (b) $BaRE_2O_4$, and (c) $LaREO_3$.

Figure 8.5a displays the hexagonal structure of $NaREF_4$ (termed β-$NaYF_4$, space group: P$\bar{6}$) with a mixed cation sublattice.[44] In the unit cell, a one-fold site is completely occupied by RE^{3+}, the other one-fold site is occupied by $1/2Na^+$ and $1/2RE^{3+}$, and the two-fold site is occupied by the equal proportions of Na^+ and vacancies. The one-fold sites are in nine-fold coordination while the two-fold site is surrounded by six F^- ions. As presented in Figure 8.5b, $BaRE_2O_4$

crystallizes in the CaV_2O_4-type structure where RE^{3+} is six-fold coordinated by O^{2-} ions.[45] In interlanthanide perovskites, La and heavy RE (Ho to Lu) ions occupy A and B sites with eight-fold and six-fold coordination, respectively, in the orthorhombic perovskite structure of $LaREO_3$ (Figure 8.5c).[46,47]

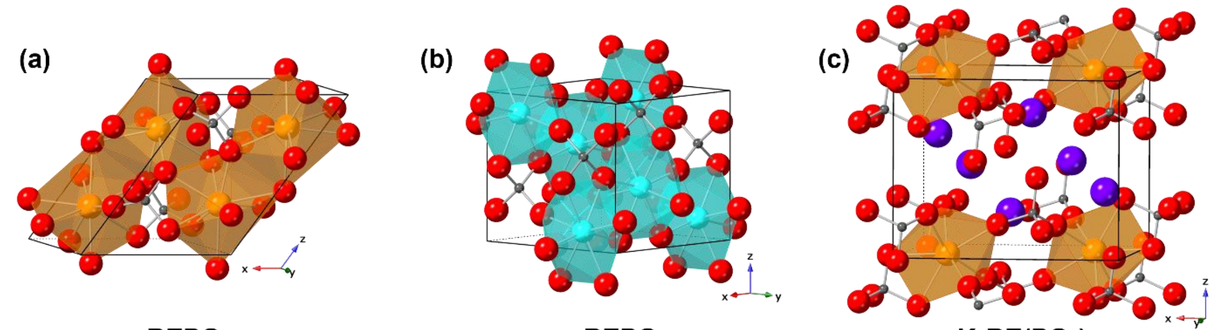

$REPO_4$ (monazite)

$REPO_4$ (xenotime)

$K_3RE(PO_4)_2$ (arcanite-type)

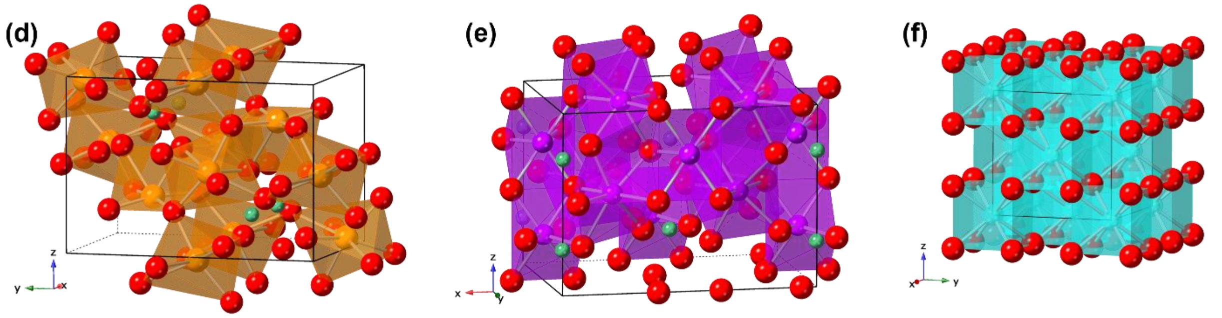

RE_3NbO_7/RE_3TaO_7 (La_3NbO_7)

RE_3NbO_7/RE_3TaO_7 (weberite)

RE_3NbO_7/RE_3TaO_7 (defect fluorite)

Figure 8.6 Crystal structures of (a) monazite and (b) xenotime for $REPO_4$, (c) arcanite-type $K_3RE(PO_4)_2$, and (d) La_3NbO_7, (e) weberite, (f) defect fluorite structured RE_3NbO_7 and RE_3TaO_7.

As the most common RE minerals, $REPO_4$ have two dimorphs, monazite (Figure 8.6a) and xenotime (Figure 8.6b), for light (La to Gd) and heavy (Tb to Lu plus Y) RE elements, respectively. Monazite is monoclinic (space group: $P2_1/m$) composed of REO_9 polyhedra, while xenotime incorporates REO_8 polyhedra in a tetragonal structure (space group: $I4_1/amd$). Most $K_3RE(PO_4)_2$ (RE = La–Yb and Y) exhibit a monoclinic structure (arcanite-type) with the space group $P2_1/m$ (Figure 8.6c),[48] but $K_3Lu(PO_4)_2$ shows a hexagonal $P\bar{3}$ structure (distorted glaserite).[23] These two structures are derived from the glaserite structure: phosphate groups rotate in the distorted glaserite structure, maintaining their six-fold RE coordination, while in the arcanite structure, one $[PO_4]$ tetrahedron shares an edge with the RE polyhedron, increasing the RE coordination number to seven.[49]

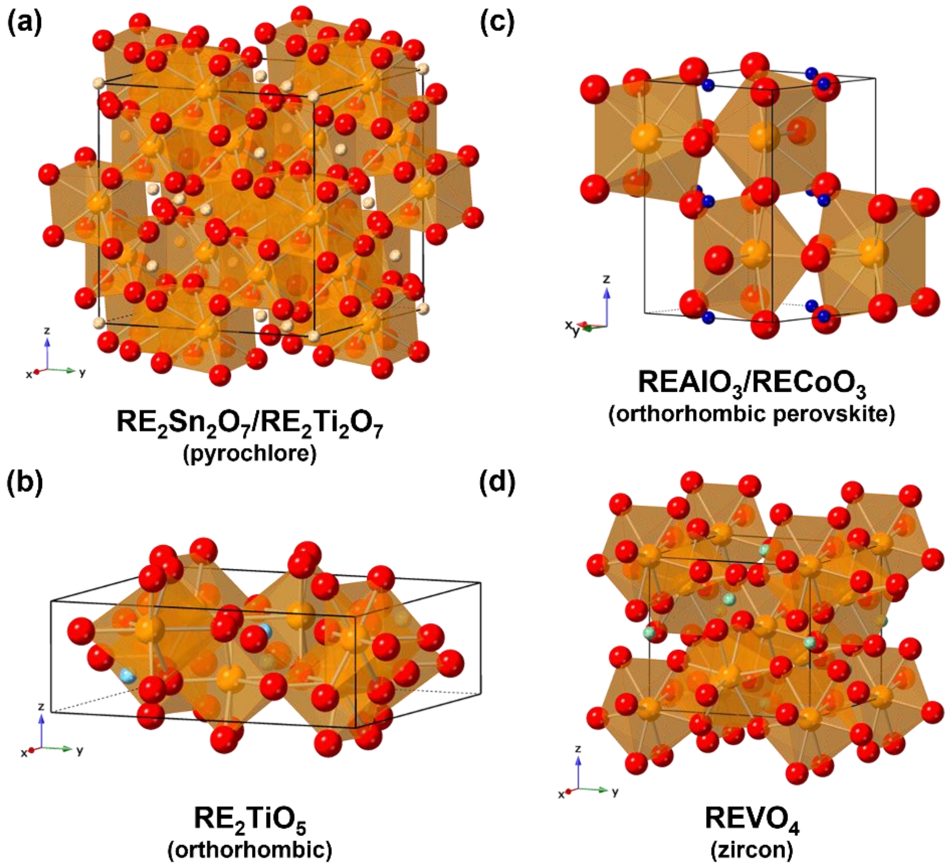

Figure 8.7 Crystal structures of (a) pyrochlore for $RE_2Sn_2O_7$ and $RE_2Ti_2O_7$, (b) orthorhombic RE_2TiO_5, (c) orthorhombic perovskite for $REAlO_3$ or $RECoO_3$, and (d) zircon for $REVO_4$.

Fluorite-derived structures are adopted by RE_3NbO_7, RE_3TaO_7, $RE_2Sn_2O_7$, and $RE_2Ti_2O_7$ having the formula A_3BO_7 or $A_2B_2O_7$. Throughout the RE series, RE_3NbO_7 and RE_3TaO_7 undergo the structure transformation La_3NbO_7 → weberite → defect fluorite as the RE ionic radius decreases.[19,21] The La_3NbO_7 structure (Figure 8.6d) is highly distorted from ideal fluorite structure, evolving into an orthorhombic superstructure (space group: Pnma) and commonly found in the presence of large RE (La to Nd), in which RE ions locate at two sites in seven-fold or eight-fold coordination.[50] Weberite (Figure 8.6e) and pyrochlore (Figure 8.7a) are derivates of the fluorite structure, in which RE ions typically occupy eight-coordinated A sites while part of RE ions make up AO_7 layers in the weberite structure with the formula A_3BO_7. These fluorite-related structures have been summarized elsewhere.[51,52] Defect fluorite (Figure 8.6f) denotes a disordered fluorite structure (space group: $Fm\bar{3}m$) with a mixed cation sublattice and vacancies in the anion sublattice.

Besides $RE_2Ti_2O_7$ (RE = Sm–Lu) with the pyrochlore structure, RE_2TiO_5 represent additional RE titanates with the orthorhombic symmetry for most RE elements (La to Dy plus Y), whose structure is shown in Figure 8.7b with seven-fold RE coordination.[53,54] Figure 8.7c displays the orthorhombic perovskite structure of $RECoO_3$ and $REAlO_3$ (RE = Sm–Lu and Y), in which RE ions occupy A sites in eight-fold coordination.[55,56] The rhombohedral perovskite structure is also reported for $LaCoO_3$ and $REAlO_3$ (RE = La–Nd) with twelve-fold coordinated RE ions.[57,58] Expect $LaVO_4$, all $REVO_4$ crystallize in the zicon-type structure (Figure 8.7d) isostructural with xenotime.[59]

8.4 Correlation between Structures and Energetics of Rare Earth Compounds

Based on the above understanding, the correlation between structures and energetics of RE compounds is discussed in this section. Structural information of RE compounds is summarized in Table 8.1 with I values and the ranges of U.

Table 8.1 Summary of crystal structures, RE coordination numbers (CN_{RE}), ionic strength (I) values, slopes of lattice energies (U) versus ionic radii of RE^{3+} in eight-fold coordination, and ranges of U.

Compound	Crystal structure	CN_{RE}	I	Slope ($kJ\ mol^{-1}$ $Å^{-1}$)	U ($kJ\ mol^{-1}$)
$RECl_3$	$UCl_3 \rightarrow AlCl_3$	9 → 6	6	1870 ± 90 (UCl_3) 2647 ± 190 ($AlCl_3$)	−4280 (La) to −4630 (Lu)
REF_3	$LaF_3 \rightarrow YF_3$	9+2 → 9	6	2029 ± 338 (LaF_3) 2152 ± 113 (YF_3)	−4875 (La) to −5278 (Lu)
REOCl	PbFCl → SmSI	9 → 7	7	2139 ± 27 (PbFCl) 2121 ± 355 (SmSI)	−5643 (La) to −6030 (Lu)
REOF	β-LaOF → α-ZrO_2	8 → 7	7	2386 ± 21 (β-LaOF)	−5804 (La) to −6222 (Yb)
$REO_{1.5}$	A → B → C	7 → 6	7.5	2660 ± 263 (A) 2574 ± 116 (C)	−6214 (La) to −6691 (Lu)
$NaREF_4$	β-$NaYF_4$	9	7	2282 ± 77	−5800 (La) to −6207 (Yb)
REOOH	YOOH	7	9	2535 ± 61	−8403 (La) to −8866 (Lu)
$REPO_4$	monazite → xenotime	9 → 8	9[a]	2092 ± 89 (mon) 2324 ± 189 (xen)	−6206 (La) to −6601 (Lu)
$Ba0_{.5}REO_2$	CaV_2O_4	6	9.5	2743 ± 78	−7802 (La) to −8237 (Er)
$RETa_{1/3}O_{7/3}$	La_3NbO_7 → weberite → defect fluorite	7 or 8	13.333	2283 ± 396 (web) 2497 ± 149 (def)	−11859 (La) to −12295 (Yb)
$RENb_{1/3}O_{7/3}$	La_3NbO_7 → weberite → defect fluorite	7 or 8	13.333	2247 ± 247 (web) 2444 ± 28 (def)	−11941 (La) to −12378 (Yb)
$RETi_{0.5}O_{2.5}$	orthorhombic	7	13.5	2381 ± 35	−12327 (La) to −12581 (Gd)
$K_3RE(PO_4)_3$	arcanite → distorted glasserite	7 → 6	15[a]	2201 ± 96 (arcanite)	−10111 (Ce) to −10443 (Lu)
$LaREO_3$	orthorhombic perovskite	6	15	3127 ± 206	−12822 (Er) to −12908 (Lu)
$REAlO_3$	rhombohedral → orthorhombic perovskite	12 → 8	15	2328 ± 316 (orthorhombic)	−14012 (La) to −14352 (Y)
$RECoO_3$	orthorhombic perovskite	8	15	2362 ± 98	−14059 (La) to −14317 (Gd)
$RESnO_{3.5}$	pyrochlore	8	19.5	2328 ± 103	−18063 (La) to −18479 (Yb)
$RETiO_{3.5}$	pyrochlore	8	19.5	2485 ± 133	−18583 (Sm) to −18836 (Lu)
$REVO_4$	zircon	8	25	2043 ± 139	−25844 (Ce) to −26145 (Lu)

[a] PO_4^{3-} is treated as a single ion with the charge number of 3.

In experimental thermodynamic research, thermochemical data are generally given as standard formation enthalpies ($\Delta H°_f$), referring to the heat of the reaction to form the substance from the most stable constituents at the standard state (typically 298 K and 1 atm). Compared to formation enthalpies from elements ($\Delta H°_{f, el}$) comprising the heat related to the redox of elements, formation enthalpies from binary compounds ($\Delta H°_{f, bc}$) such as formation enthalpies from oxides ($\Delta H°_{f, ox}$) and formation enthalpies from fluorides ($\Delta H°_{f, fl}$), demonstrate the energetic stability relative to the mechanical mixture of binary constituents and serve as a better gauge of the thermodynamic stability of compounds with specific composition and structure. For RE oxycompounds and most ternary RE oxide compounds, $\Delta H°_{f, bc}$ become less exothermic from light to heavy RE elements.[3,4,11,14-24] On the contrary, the reverse trend is observed in $NaREF_4$, $BaRE_2O_4$, and $LaREO_3$, whose $\Delta H°_{f, bc}$ become more exothermic as the RE ionic radius decreases. In fact, as defined by itself, the $\Delta H°_{f, bc}$ embodies the competition between the energetic stability of the substance and the corresponding binary compounds. In RE systems, the change of the thermodynamic stability along the RE series should not be ignored for binary RE compounds. Therefore, U, reflecting the strength of chemical bonding in the lattice, is a more appropriate factor to describe the energetics of RE compounds, which has the relationship with $\Delta H°_{f, bc}$ as

$$\Delta H°_{f,bc} = U_{matter} - \sum U_{bc} \tag{8.2}$$

where U_{matter} and U_{bc} represent the U of the certain material and the corresponding binary compounds, respectively. As U values of RE compounds become more exothermic from light to heavy RE elements, the trend of $\Delta H°_{f, bc}$ throughout the RE series depends on the different slopes of U for ternary and binary compounds. In order to compare various RE compounds, ionic radii of RE^{3+} in eight-fold coordination are used to recognize the lanthanide contraction across the RE series, and the slopes of U against RE ionic radii are obtained by linearly fitting U values of RE compounds with the same structure (Table 8.1). As illustrated in Figure 8.8, the RE size has different effects on energetics of RE compounds with diverse structures, showing a correlation with the RE coordination number, i.e., higher coordination is usually associated with a smaller slope of U. From the structural perspective, higher coordination is generally accompanied by more loosely packing and longer bond distances around larger RE ions, reducing their interaction with surrounding anions. Here, the quantitative analysis further confirms that RE coordination numbers play an important role in the energetics of RE compounds, and it is impressive to see that the slope of U is highly correlated with the RE coordination number.

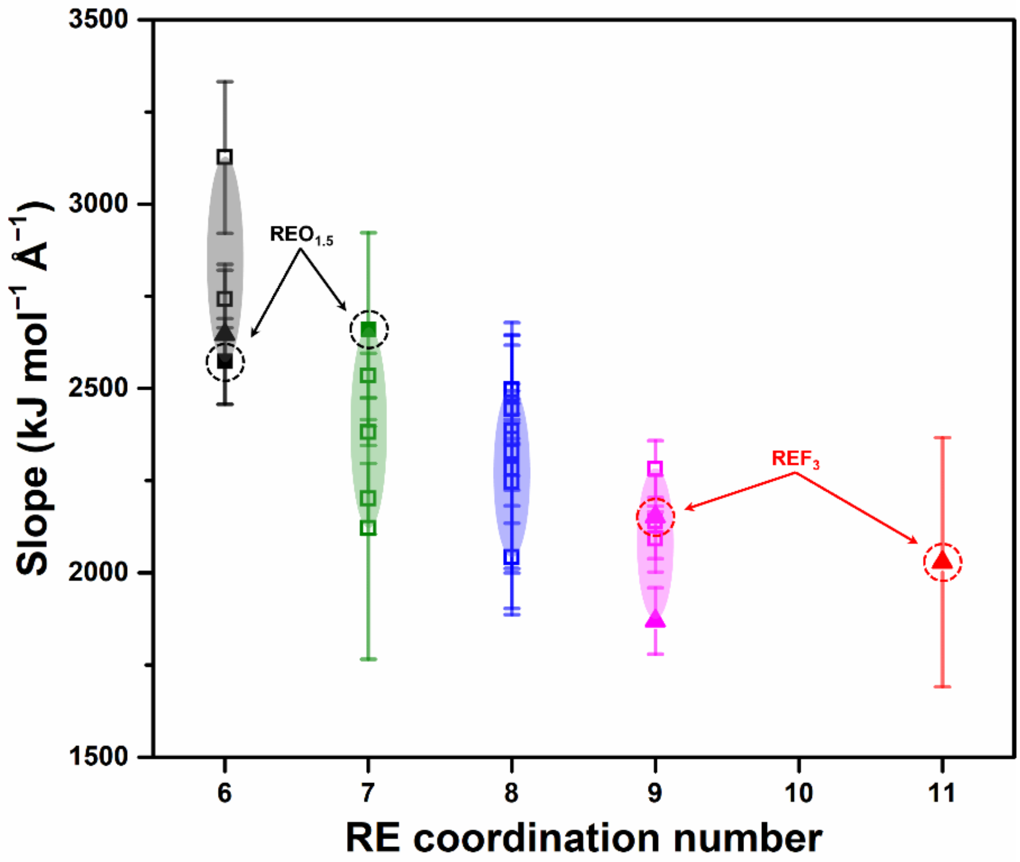

Figure 8.8 Slopes of lattice energies against ionic radii of RE^{3+} in eight-fold coordination for different structures of RE compounds.

Owing to low RE coordination in sesquioxides (6 and 7 for C- and A-type RE_2O_3, respectively), the formation of RE oxide compounds from binary oxides is typically accompanied by an increase of RE coordination with a smaller slope of U through the RE series. Thus, the less exothermic $\Delta H^{\circ}_{f,\,ox}$ or the decreasing thermodynamic stability relative to binary oxides is expected for heavier RE elements. However, different from incorporating small transition metal ions, the introduction of large alkaline earth or RE ions reduces or retains the RE coordination number in the formation reaction of $BaRE_2O_4$ and $LaREO_3$ from binary oxides, contributing to larger slopes of U and the reverse trend of $\Delta H^{\circ}_{f,\,ox}$ compared to most ternary RE oxides and oxysalts. For REOF, despite an increase and a decrease of RE coordination happening together in its formation reaction from RE_2O_3 and REF_3, $REO_{1.5}$ has a much larger slope of U (2660 ± 263 and 2574 ± 116 kJ mol^{-1} $Å^{-1}$ for A and C-type, respectively) compared to that of REOF (2386 ± 21 kJ mol^{-1} $Å^{-1}$ for β-LaOF structure) and REF_3 (2029 ± 338 and 2152 ± 113 kJ mol^{-1} $Å^{-1}$ for LaF_3 and YF_3 structure, respectively). Also, the stoichiometric number of $REO_{1.5}$ is higher than that of REF_3 in the equation of the formation reaction.

$$\frac{2}{3}REO_{1.5} + \frac{1}{3}REF_3 \rightarrow REOF \tag{8.3}$$

Hence, $\Delta H^{\circ}_{f,\,bc}$ of REOF become less negative with the decrease of RE ionic radius, which is consistent with the fact that the RE–O interactions dominate in the energetics of REOF.[3] Despite the 2D structure of SmSI-type REOCl held together by vdW forces wrecking the correlation between unit cell volumes and U, REOCl shows a similar trend in $\Delta H^{\circ}_{f,\,bc}$ from light to heavy RE elements as REOF.[4] In RE fluoride systems, REF_3 have high coordination of RE ions (9+2 and 9 for LaF_3 and YF_3 structures, respectively), which are nine-fold coordinated in $NaREF_4$, leading to a decrease or constancy of RE coordination in the formation of $NaREF_4$ from NaF and REF_3 for light and heavy RE elements, respectively. This difference is in accord with $\Delta H^{\circ}_{f,\,fl}$ of

$NaREF_4$ with varying RE elements: as the ionic radius of RE^{3+} decreases, $\Delta H°_{f, fl}$ values become more exothermic from La to Nd while change slightly from Gd to Yb.[2] Taking into account that presently known RE fluorides possess structures with the same or lower RE coordination than REF_3,[60] it is likely that more "reverse" trends of $\Delta H°_{f, bc}$ will be found in other ternary RE fluorides.

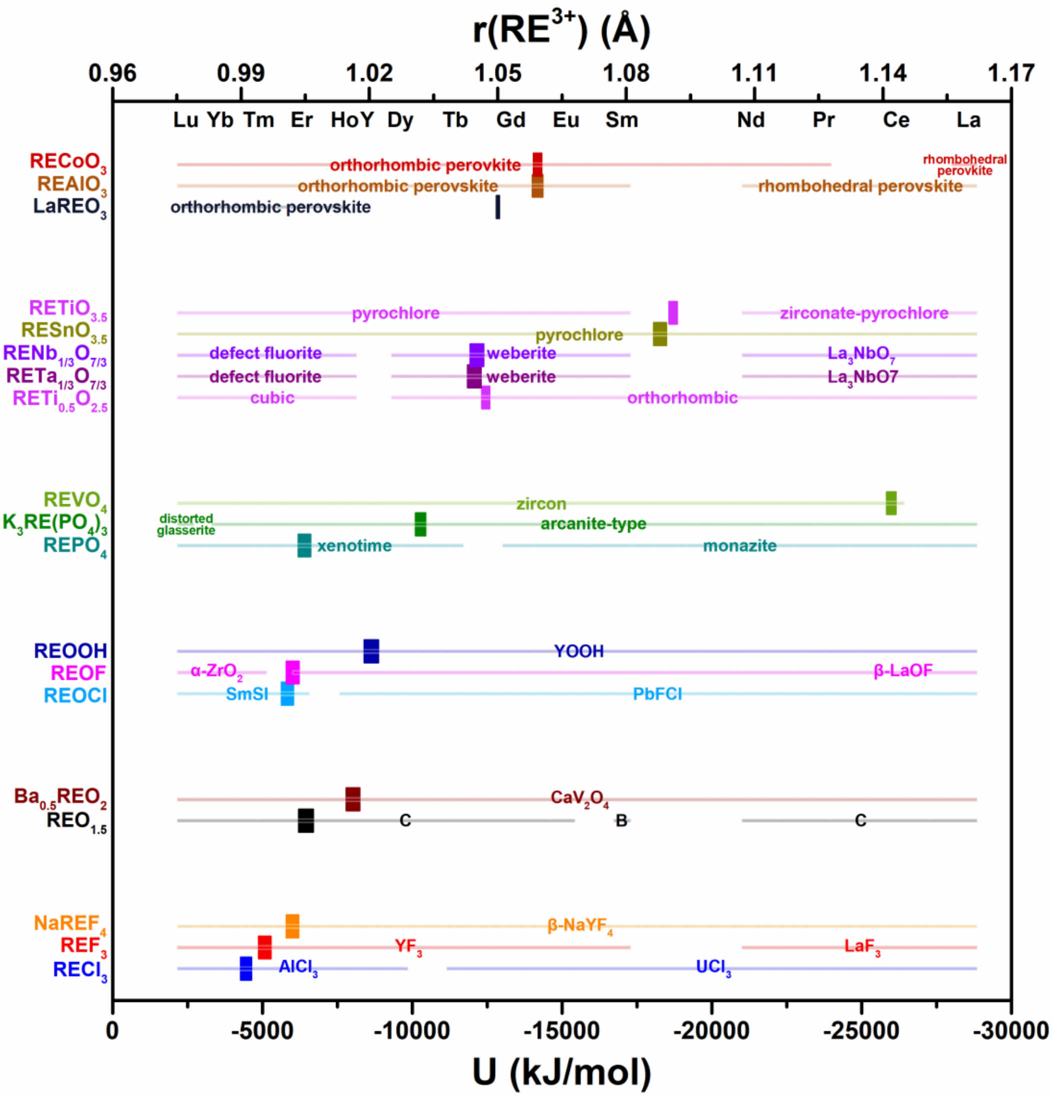

Figure 8.9 The magnitude of lattice energies (U) and the structure distribution across the RE series for various RE compounds, in which bars and lines represent U and crystal structure ranges, respectively.

Another interesting correlation is noted between the structure of RE compounds and the magnitude of U. According to compositions and structures, RE compounds are divided into several groups and their U and crystal structure ranges are presented in Figure 8.9. The I value of RE compounds increases as more ions are integrated in the composition, leading to a larger magnitude of U. Interestingly, the enhanced energetics shows an association with the consistency of the structure across the RE elements, and when RE is varied, the same structure is favored by RE compounds with a high magnitude of U. Among the RE compounds, binary halides have the smallest U and display the phase change $UCl_3 \rightarrow AlCl_3$ ($RECl_3$) or $LaF_3 \rightarrow YF_3$ (REF_3) from light to heavy RE elements.

In contrast, the ternary fluorides $NaREF_4$ adopt the same structure (β-$NaYF_4$) throughout the RE series with larger U values. Likewise, as the RE atomic number increases, the change of structures (PbFCl → SmSI for REOCl and β-LaOF → α-ZrO_2 for REOF) is manifested in RE oxyhalides, while REOOH with more negative U possess the same structure (YOOH) for all RE elements. The similar situation is also seen in $Ba_{0.5}REO_2$, $K_3RE(PO_4)_3$, and $REVO_4$, whose more exothermic U values are accompanied by a wider range of the same structure over the variable RE elements. Besides the number of ions, the U may change because of different charge numbers. Compared to the formula $REM_{1/3}O_{7/3}$, $REMO_{3.5}$ has a higher I value, so $RESnO_{3.5}$ and $RETiO_{3.5}$ have more negative U compared to those of $RETa_{1/3}O_{7/3}$ and $RENb_{1/3}O_{7/3}$. The energetic difference may relate to the structure preference of these fluorite-structured oxides, which adopt the weberite or defect fluorite structure ($REM_{1/3}O_{7/3}$) and the pyrochlore structure ($REMO_{3.5}$), respectively. Considering that the configurational entropy increases in the order pyrochlore < weberite < defect fluorite as disorder in the structure increases, it is possible that entropies compensate the relatively small U of $REM_{1/3}O_{7/3}$ and play a significant part in the thermodynamic stability.[61]

Perovskite structures are known for their big family of derivatives as a treasure chest for solid state chemistry. The orthorhombic perovskite is the most common structure in RE oxides where RE ions typically occupy A sites (e.g., $REAlO_3$ and $RECoO_3$), whereas small RE ions occupy B sites in $LaREO_3$. Other perovskite-related structures such as the rhombohedral perovskite were also reported. Diverse defect, distortion, and ordering modes make up the complexity of perovskite-based structures, and more thermodynamic research is needed to understand the relationship between energetics and structures of these materials.[62,63]

8.5 Conclusions and Outlook

By virtue of thermodynamic studies of RE compounds, an energetic evaluation is made based on lattice energies. The critical role of RE coordination numbers in the trend of formation enthalpies or thermodynamic stability relative to binary compounds is identified, showing a correlation with the slope of lattice energies across the RE series. When varying RE elements, the structure distribution of RE compounds is coupled with the magnitude of lattice energies, which is mainly determined by ionic strength. These findings not only deepen the understanding of the thermodynamics of RE compounds, but also contribute to applications of these materials, for example in the field of nuclear energy.[64] In future work, more attention should be paid to entropies of RE compounds, the other component of thermodynamic stability. Low temperature heat capacity measurements can determine lattice entropies and gain some information of vacancies in compounds,[65] and Gibbs free energies can be calculated according to the third law of thermodynamics. The Gibbs free energy can also be determined by chemical equilibria, such as solubilities in aqueous solutions.[66,67] By comparing the results from the two approaches, configurational entropies coming from the disordering in the lattice can be estimated from the thermodynamic perspective.[68]

Besides bulk materials, RE containing nanocrystals have attracted great interest due to the unique upconversion properties.[69] The nanoscale effects, such as surface energies and adsorbed water, on the thermodynamics and phase equilibria represent an emerging research direction in the development of RE nanomaterials,[70] while some works have been carried out on nano RE oxides[71] and fluorides[72]. More research is needed to better understand the effects of disordering and defect structures on the energetics of RE materials, which are crucial to the long-term use of these materials.

8.6 References

(1) Liu, Z.-K. Computational thermodynamics and its applications. *Acta Mater.* **2020**, *200*, 745–792.

(2) Yang, S.; Anderko, A.; Riman, R. E.; Navrotsky, A. Thermochemistry of sodium rare earth ternary fluorides, $NaREF_4$. *Acta Mater.* **2021**, *220*, 117289.

(3) Yang, S.; Anderko, A.; Riman, R. E.; Navrotsky, A. Thermochemistry of stoichiometric rare earth oxyfluorides REOF. *J. Am. Ceram. Soc.* **2022**, *105*, 1472–1480.

(4) Yang, S.; Anderko, A.; Riman, R. E.; Navrotsky, A. Thermochemistry of 3D and 2D rare earth oxychlorides (REOCl). *Inorg. Chem.* **2022**.

(5) Glushko, V. P. *Thermochemical Constants of Substances*. Academy of Sciences of USSR, 1978.

(6) Xiang-Yun, W.; Zhu, J. T.; Goudiakas, J.; Fuger, J. Thermodynamics of lanthanide elements IV. Molar enthalpies of formation of Y^{3+}(aq), YCl_3(cr), YBr_3(cr), and YI_3(cr). *J. Chem. Thermodyn.* **1988**, *20*, 1195−1202.

(7) Morss, L. R.; Day, P. P.; Felinto, C.; Brito, H. Standard molar enthalpies of formation of Y_2O_3, Ho_2O_3, and Er_2O_3 at the temperature 298.15 K. *J. Chem. Thermodyn.* **1993**, *25*, 415–422.

(8) Konings, R. J. M.; Kovács, A. Thermodynamic properties of the lanthanide(III) halides. In *Handbook on the Physics and Chemistry of Rare Earths*, Elsevier, 2003; Vol. 33, p 147−247.

(9) Konings, R. J. M.; Beneš, O.; Kovács, A.; Manara, D.; Sedmidubský, D.; Gorokhov, L.; Iorish, V. S.; Yungman, V.; Shenyavskaya, E.; Osina, E. The thermodynamic properties of the f-elements and their compounds. Part 2. The lanthanide and actinide oxides. *J. Phys. Chem. Ref. Data* **2014**, *43*, 013101.

(10) Cordfunke, E. H. P.; Konings, R. J. M.; Ouweltjes, W. The standard enthalpies of formation of hydroxides IV. $La(OH)_3$ and LaOOH. *J. Chem. Thermodyn.* **1990**, *22*, 449–452.

(11) Yang, S.; Powell, M.; Kolis, J. W.; Navrotsky, A. Thermochemistry of rare earth oxyhydroxides, REOOH (RE = Eu to Lu). *J. Solid State Chem.* **2020**, *287*, 121344.

(12) Qi, J.; Guo, X.; Mielewczyk-Gryn, A.; Navrotsky, A. Formation enthalpies of $LaLn'O_3$ (Ln′=Ho, Er, Tm and Yb) interlanthanide perovskites. *J. Solid State Chem.* **2015**, *227*, 150–154.

(13) Gong, W.; Liu, Y.; Xie, Y.; Zhao, Z.; Ushakov, S. V.; Navrotsky, A. Thermodynamic assessment of BaO–Ln_2O_3 (Ln = La, Pr, Eu, Gd, Er) systems. *J Am Ceram Soc.* **2020**, *103*, 3896–3904.

(14) Kanke, Y.; Navrotsky, A. A calorimetric study of the lanthanide aluminum oxides and the lanthanide gallium oxides: stability of the perovskites and the garnets. *J. Solid State Chem.* **1998**, *141*, 424–436.

(15) Helean, K. B.; Ushakov, S. V.; Brown, C. E.; Navrotsky, A.; Lian, J.; Ewing, R. C.; Farmer, J. M.; Boatner, L. A. Formation enthalpies of rare earth titanate pyrochlores. *J. Solid State Chem.* **2004**, *177*, 1858–1866.

(16) Lian, J.; Helean, K. B.; Kennedy, B. J.; Wang, L. M.; Navrotsky, A.; Ewing, R. C. Effect of structure and thermodynamic stability on the response of lanthanide stannate pyrochlores to ion beam irradiation. *J. Phys. Chem. B* **2006**, *110*, 2343–2350.

(17) Dorogova, M.; Navrotsky, A.; Boatner, L. A. Enthalpies of formation of rare earth orthovanadates, $REVO_4$. *J. Solid State Chem.* **2007**, *180*, 847–851.

(18) Hayun, S.; Navrotsky, A. Formation enthalpies and heat capacities of rear earth titanates: RE_2TiO_5 (RE=La, Nd and Gd). *J. Solid State Chem.* **2012**, *187*, 70–74.

(19) Mielewczyk-Gryn, A.; Navrotsky, A. Enthalpies of formation of rare earth niobates, RE_3NbO_7. *Am. Mineral.* **2015**, *100*, 1578–1583.

(20) Sahu, S. K.; Tanasescu, S.; Scherrer, B.; Marinescu, C.; Navrotsky, A. Energetics of lanthanide cobalt perovskites: $LnCoO_{3-\delta}$ (Ln = La, Nd, Sm, Gd). *J. Mater. Chem. A* **2015**, *3*, 19490–19496.

(21) Subramani, T.; Navrotsky, A. Energetics of formation and disordering in rare earth weberite RE_3TaO_7 materials. *Inorg. Chem.* **2019**, *58*, 16126−16133.

(22) Ushakov, S. V.; Helean, K. B.; Navrotsky, A.; Boatner, L. A. Thermochemistry of rare-earth orthophosphates. *J. Mater. Res.* **2011**, *16*, 2623–2633.

(23) Ushakov, S. V.; Navrotsky, A.; Farmer, J. M.; Boatner, L. A. Thermochemistry of the alkali rare-earth double phosphates, $A_3RE(PO_4)_2$. *J. Mater. Res.* **2011**, *19*, 2165–2175.

(24) Shelyug, A.; Mesbah, A.; Szenknect, S.; Clavier, N.; Dacheux, N.; Navrotsky, A. Thermodynamics and stability of rhabdophanes, hydrated rare earth phosphates $REPO_4 \cdot n\ H_2O$. *Front. Chem.* **2018**, *6*, 604.

(25) Flora, N. J.; Yoder, C. H.; Jenkins, H. D. B. Lattice energies of apatites and the estimation of $\Delta H_f°(PO_4^{3-}, g)$. *Inorg. Chem.* **2004**, *43*, 2340−2345.

(26) Shannon, R. D. Revised effective ionic radii and systematic studies of interatomic distances in halides and chalcogenides. *Acta Cryst.* **1976**, *32*, 751−767.

(27) Jenkins, H. D. B.; Roobottom, H. K.; Passmore, J.; Glasser, L. Relationships among ionic lattice energies, molecular (formula unit) volumes, and thermochemical radii. *Inorg. Chem.* **1999**, *38*, 3609−3620.

(28) Glasser, L.; Jenkins, H. D. B. Lattice energies and unit cell volumes of complex ionic solids. *J. Am. Chem. Soc.* **2000**, *122*, 632−638.

(29) Jenkins, H. D. B.; Tudela, D.; Glasser, L. Lattice potential energy estimation for complex ionic salts from density measurements. *Inorg. Chem.* **2002**, *41*, 2364−2367.

(30) Adachi, G.-y.; Imanaka, N. The binary rare earth oxides. *Chem. Rev.* **1998**, *98*, 1479−1514.

(31) Greis, O.; Haschke, J. M. Chapter 45 Rare earth fluorides. In *Handbook on the Physics and Chemistry of Rare Earths*, Elsevier, 1982; Vol. 5, p 387−460.

(32) Templeton, D. H.; Carter, G. F. The crystal structures of yttrium trichloride and similar compounds. *J. Phys. Chem.* **1954**, *58,* 940–944.

(33) Morosin, B. Crystal structures of anhydrous rare-earth chlorides. *J. Chem. Phys.* **1968**, *49*, 3007–3012.

(34) Christensen, A. N. On the crystal structures of HoOOH, ErOOH, and YbOOH. *Acta Chem. Scand.* **1965**, *19*, 1391−1396.

(35) Milligan, W. O.; Mullica, D. F.; Hall, M. A. Structural refinement of lutetium hydroxide oxide. *Acta Cryst. B* **1980**, *36*, 3086−3088.

(36) Neumann, A.; Walter, D. The thermal transformation from lanthanum hydroxide to lanthanum hydroxide oxide. *Thermochim. Acta* **2006**, *445*, 200−204.

(37) Christensen, A. N.; Quézel, S. Crystal structure and magnetic structure of TbOOH. *J. Solid State Chem.* **1974**, *9*, 234−241.

(38) Zachariasen, W. Crystal chemical studies of the 5f-series of elements. XIV. Oxyfluorides, XOF. *Acta Crystallogr.* **1951**, *4*, 231–236.

(39) Mann, A. W.; Bevan, D. J. M. The crystal structure of stoichiometric yttrium oxyfluoride, YOF. *Acta Crystallogr. B* **1970**, *26*, 2129–2131.

(40) Taoudi, A.; Laval, J. P.; Frit, B. Synthesis and crystal structure of three new rare earth oxyfluorides related to baddeleyite [LnOF; Ln=Tm,Yb,Lu]. *Mater. Res. Bull.* **1994**, *29*, 1137–1147.

(41) Templeton, D. H.; Dauben, C. H. Crystal structures of rare earth oxychlorides. *J. Am. Chem. Soc.* **1953**, *75*, 6069−6070.

(42) Brandt, G.; Diehl, R. Preparation, powder data and crystal structure of YbOCl. *Mater. Res. Bull.* **1974**, *9*, 411−419.

(43) Hölsä, J.; Lahtinen, M.; Lastusaari, M.; Valkonen, J.; Viljanen, J. Stability of rare-earth oxychloride phases: bond valence study. *J. Solid State Chem.* **2002**, *165*, 48–55.

(44) Grzechnik, A.; Friese, K. Crystal structures and stability of $NaLnF_4$ (Ln = La, Ce, Pr, Nd, Sm and Gd) studied with synchrotron single-crystal and powder diffraction. *Dalton Trans.* **2012**, *41*, 10258–10266.

(45) Besara, T.; Lundberg, M. S.; Sun, J.; Ramirez, D.; Dong, L.; Whalen, J. B.; Vasquez, R.; Herrera, F.; Allen, J. R.; Davidson, M. W.; Siegrist, T. Single crystal synthesis and magnetism of the $BaLn_2O_4$ family (Ln = lanthanide). *Prog. Solid State Chem.* **2014**, *42*, 23–36.

(46) Schneider, S. J.; Roth, R. S. Perovskite-type compounds in binary rare earth oxide systems. *J. Am. Ceram. Soc.* **1960**, *43*, 115−115.

(47) Martinelli, A.; Masini, R.; Artini, C.; Costa, G. A.; Keller, L. DC magnetic susceptibility and neutron powder diffraction analysis of the perovskite-type compounds $LaYbO_3$ and $LaHoO_3$. *J. Phys. Condens. Matter* **2013**, *25*, 426005.

(48) Hong, H. Y. P.; Chinn, S. R. Crystal structure and fluorescence lifetime of potassium neodymium orthophosphate, $K_3Nd(PO_4)_2$, a new laser material. *Mater. Res. Bull.* **1976**, *11*, 421–428.

(49) Farmer, J. M.; Boatner, L. A.; Chakoumakos, B. C.; Rawn, C. J.; Mandrus, D.; Jin, R.; Bryan, J. C. Polymorphism, phase transitions, and thermal expansion of $K_3Lu(PO_4)_2$. *J. Alloys Compd.* **2014**, *588*, 182−189.

(50) Kahn-Harari, A.; Mazerolles, L.; Michel, D.; Robert, F. Structural Description of La_3NbO_7. *J. Solid State Chem.* **1995**, *116*, 103−106.

(51) Subramanian, M. A.; Aravamudan, G.; Subba Rao, G. V. Oxide pyrochlores — A review. *Prog. Solid State Chem.* **1983**, *15*, 55–143.

(52) Cai, L.; Nino, J. C. Complex ceramic structures. I. Weberites. *Acta Crystallogr. B* **2009**, *65*, 269–290.

(53) Shepelev, Y. F.; Petrova, M. A. Crystal structures of Ln_2TiO_5 (Ln = Gd, Dy) polymorphs. *Inorg. Mater.* **2008**, *44*, 1354−1361.

(54) Zhang, F. X.; Wang, J. W.; Lang, M.; Zhang, J. M.; Ewing, R. C. Pressure-induced structural transformations in lanthanide titanates: La_2TiO_5 and Nd_2TiO_5. *J. Solid State Chem.* **2010**, *183*, 2636−2643.

(55) Geller, S.; Bala, V. B. Crystallographic studies of perovskite-like compounds. II. Rare earth alluminates. *Acta Cryst.* **1956**, *9*, 1019−1025.

(56) Alonso, J. A.; Martínez-Lope, M. J.; de la Calle, C.; Pomjakushin, V. Preparation and structural study from neutron diffraction data of $RCoO_3$ (R = Pr, Tb, Dy, Ho, Er, Tm, Yb, Lu) perovskites. *J. Mater. Chem.* **2006**, *16,* 1555–1560.

(57) Marezio, M.; Dernier, P. D.; Remeika, J. P. The crystal structures of orthorhombic $SmAlO_3$ and of trigonal $NdAlO_3$. *J. Solid State Chem.* **1972**, *4*, 11–19.

(58) Lehnert, H.; Boysen, H.; Dreier, P.; Yu, Y. Room temperature structure of $LaAlO_3$. *Z. Kristallogr.* **2000**, *215*, 145–147.

(59) Baglio, J. A.; Sovers, O. J. Crystal structures of the rare-earth orthovanadates. *J. Solid State Chem.* **1971**, *3*, 458–465.

(60) Leblanc, M.; Maisonneuve, V.; Tressaud, A. Crystal chemistry and selected physical properties of inorganic fluorides and oxide-fluorides. *Chem. Rev.* **2015**, *115*, 1191−1254.

(61) Subramani, T.; Voskanyan, A.; Jayanthi, K.; Abramchuk, M.; Navrotsky, A. A comparison of order-disorder in several families of cubic oxides. *Front. Chem.* **2021**, *9*, 719169.

(62) Navrotsky, A. Energetics and crystal chemical systematics among ilmenite, lithium niobate, and perovskite structures. *Chem. Mater.* **1998**, *10*, 2787−2793.

(63) Voskanyan, A. A.; Navrotsky, A. Shear pleasure: the structure, formation, and thermodynamics of crystallographic shear phases. *Annu. Rev. Mater. Res.* **2021**, *51*, 521−540.

(64) Shelyug, A.; Navrotsky, A. Thermodynamics of fluorite-structured oxides relevant to nuclear energy: a review. *ACS Earth Space Chem.* **2021**, *5*, 703−721.

(65) Neilsen, G.; Rosen, P. F.; Dickson, M. S.; Popovic, M.; Schliesser, J.; Hansen, L. D.; Navrotsky, A.; Woodfield, B. F. Quantifying oxygen vacancies in neodymium and samarium doped ceria from heat capacity measurements. *Acta Mater.* **2020**, *188*, 740–744.

(66) Gausse, C.; Szenknect, S.; Qin, D. W.; Mesbah, A.; Clavier, N.; Neumeier, S.; Bosbach, D.; Dacheux, N. Determination of the solubility of rhabdophanes $LnPO_4 \cdot 0.667H_2O$ (Ln = La to Dy). *Eur. J. Inorg. Chem.* **2016**, *2016*, 4615–4630.

(67) Kim, P.; Anderko, A.; Navrotsky, A.; Riman, R. E. Trends in structure and thermodynamic properties of normal rare earth carbonates and rare earth hydroxycarbonates. *Minerals* **2018**, *8*, 106.

(68) McCormack, S. J.; Navrotsky, A. Thermodynamics of high entropy oxides. *Acta Mater.* **2021**, *202*, 1–21.

(69) Dong, H.; Sun, L.-D.; Yan, C.-H. Local structure engineering in lanthanide-doped nanocrystals for tunable upconversion emissions. *J. Am. Chem. Soc.* **2021**, *143*, 20546−20561.

(70) Navrotsky, A. Nanoscale effects on thermodynamics and phase equilibria in oxide systems. *ChemPhysChem* **2011**, *12*, 2207–2215.

(71) Hayun, S.; Shvareva, T. Y.; Navrotsky, A. Nanoceria – energetics of surfaces, interfaces and water adsorption. *J. Am. Ceram. Soc.* **2011**, *94,* 3992–3999.

(72) Yang, S.; Jayanthi, K.; Anderko, A.; Riman, R. E.; Navrotsky, A. Thermochemical investigation of the stability and conversion of nanocrystalline and high-temperature phases in sodium neodymium fluorides. *Chem. Mater.* **2021**, *33,* 9571–9579.

Appendix

A. Rietveld Refinements of Powder X-ray Diffraction Patterns

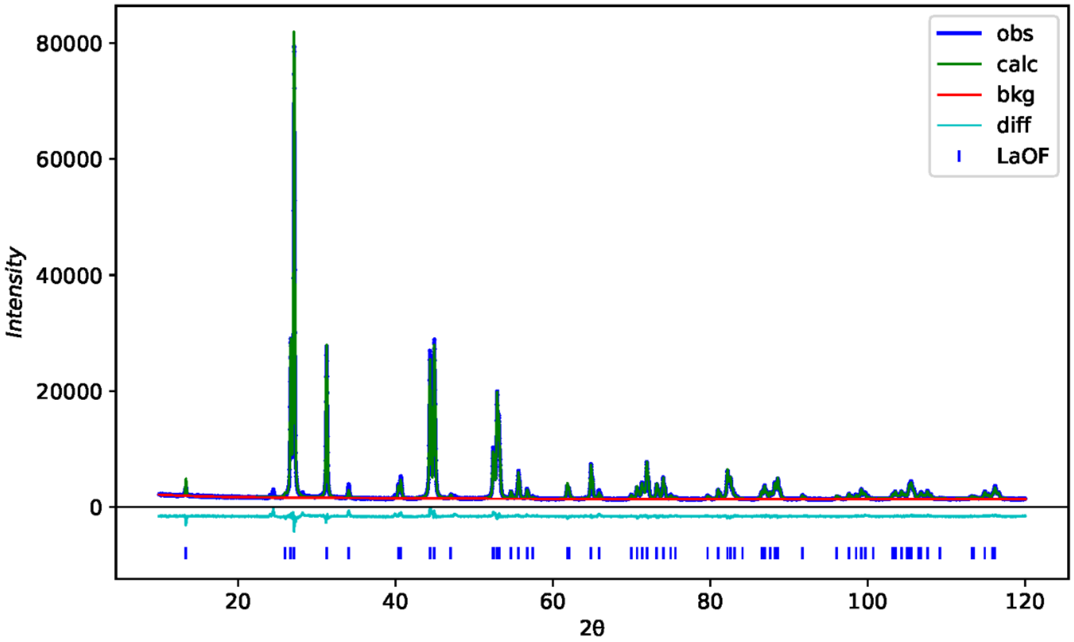

Figure A.1 Rietveld refinement profile of LaOF.

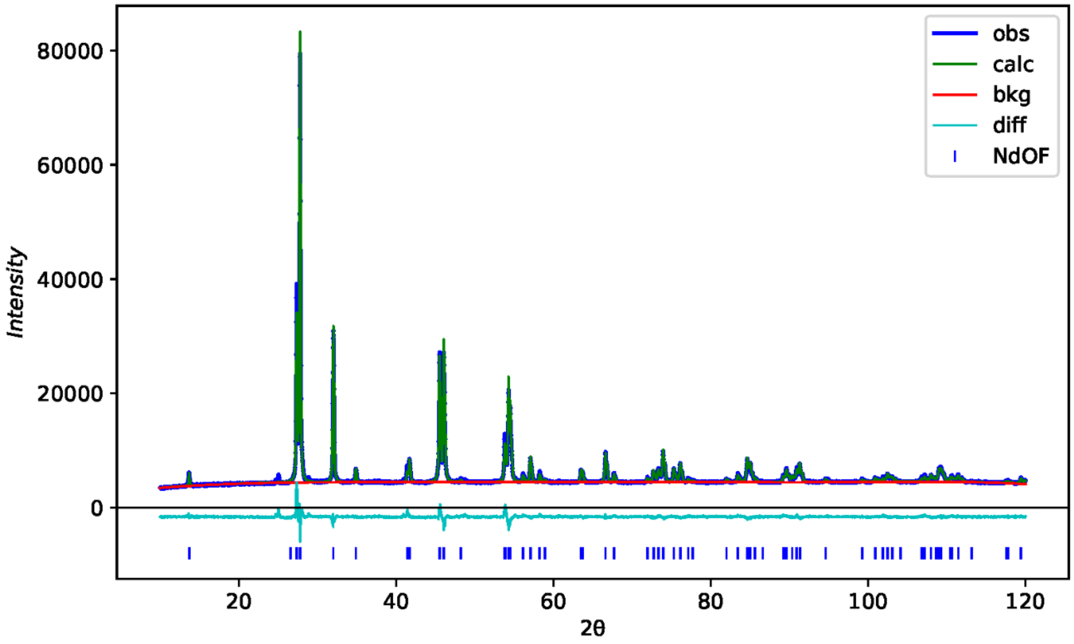

Figure A.2 Rietveld refinement profile of NdOF.

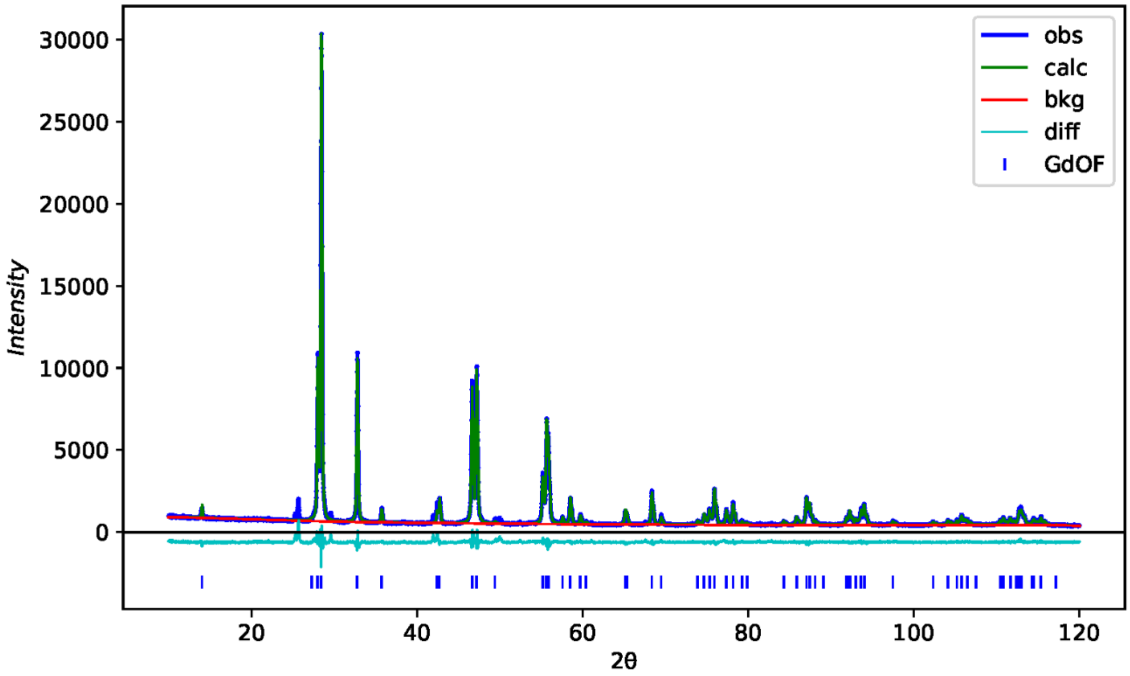

Figure A.3 Rietveld refinement profile of GdOF.

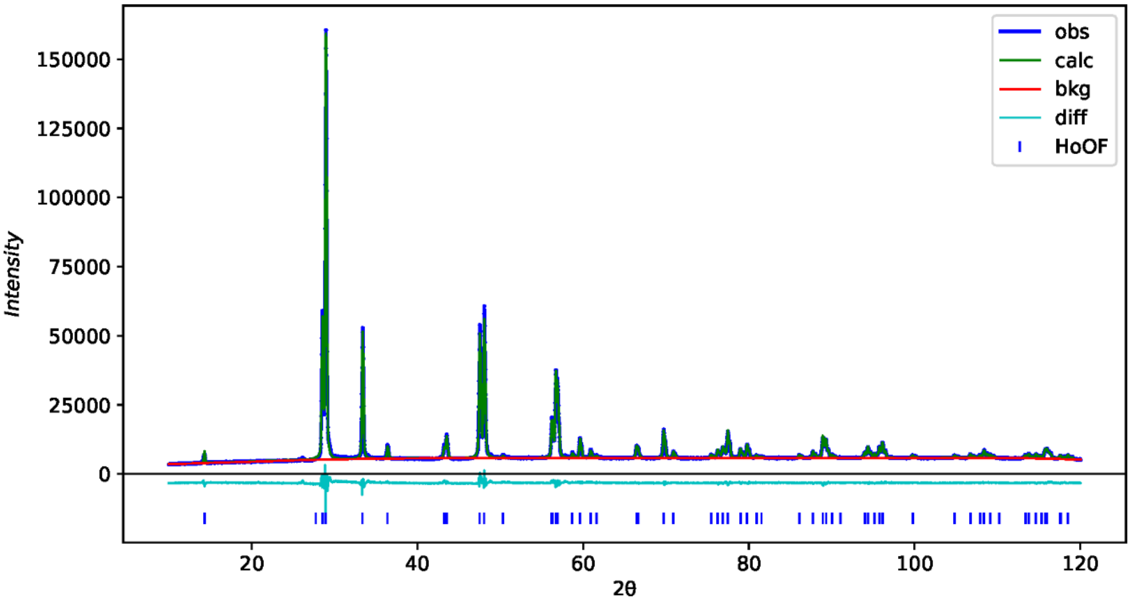

Figure A.4 Rietveld refinement profile of HoOF.

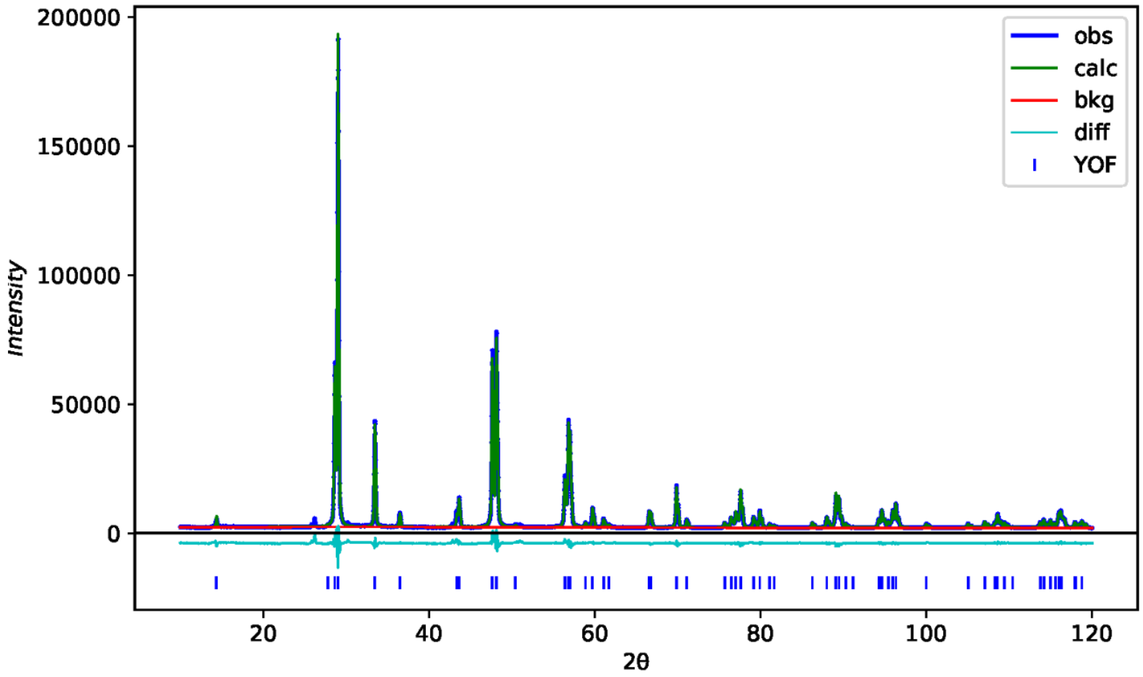

Figure A.5 Rietveld refinement profile of YOF.

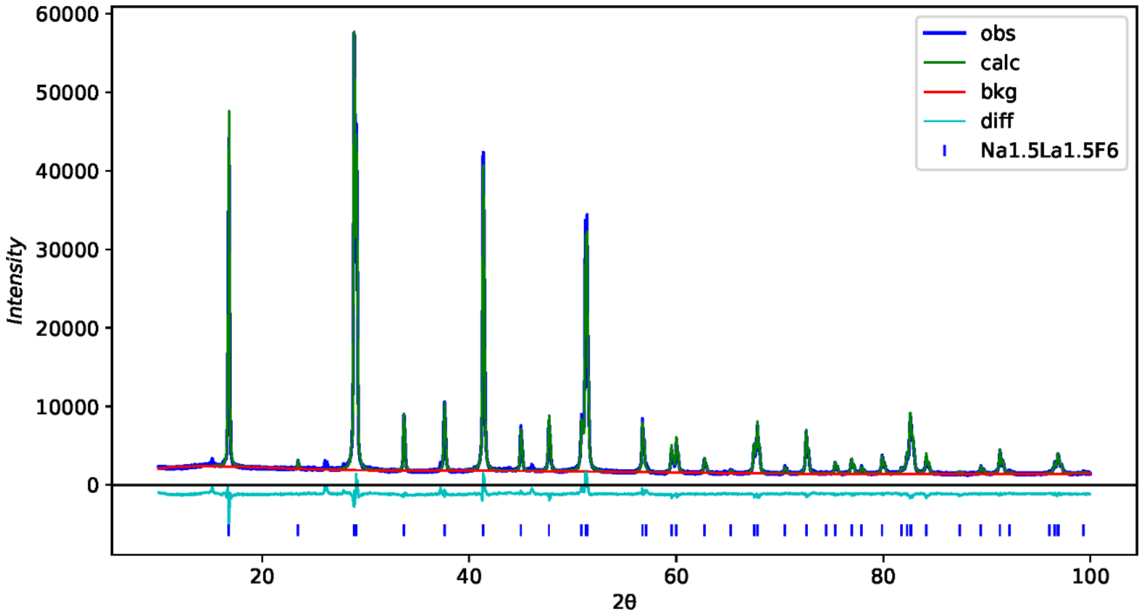

Figure A.6 Rietveld refinement profile of $Na_{1.5}La_{1.5}F_6$.

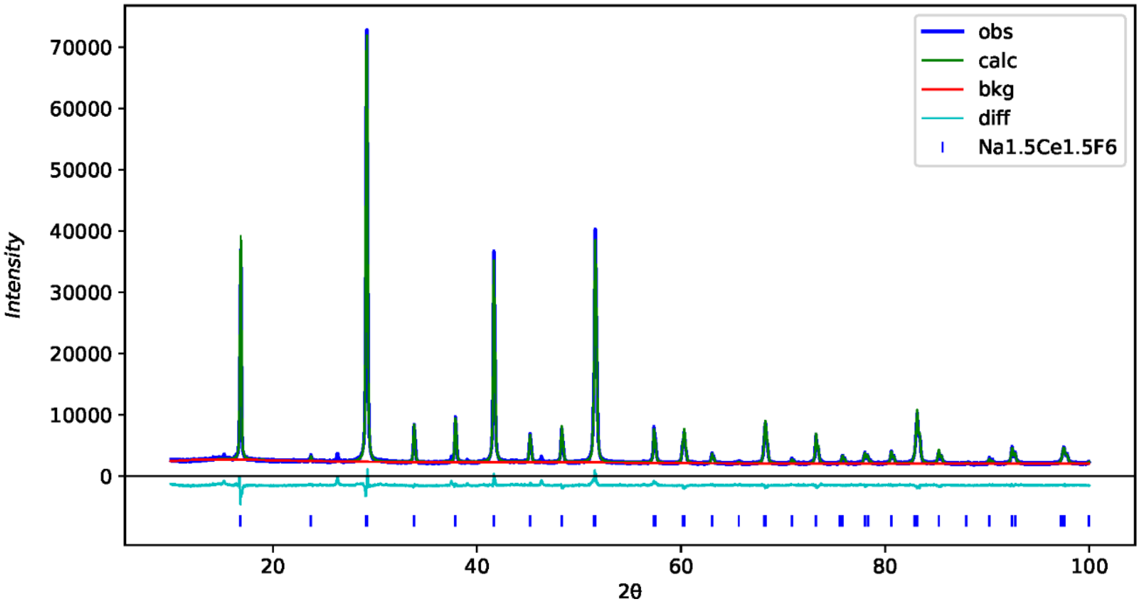

Figure A.7 Rietveld refinement profile of $Na_{1.5}Ce_{1.5}F_6$.

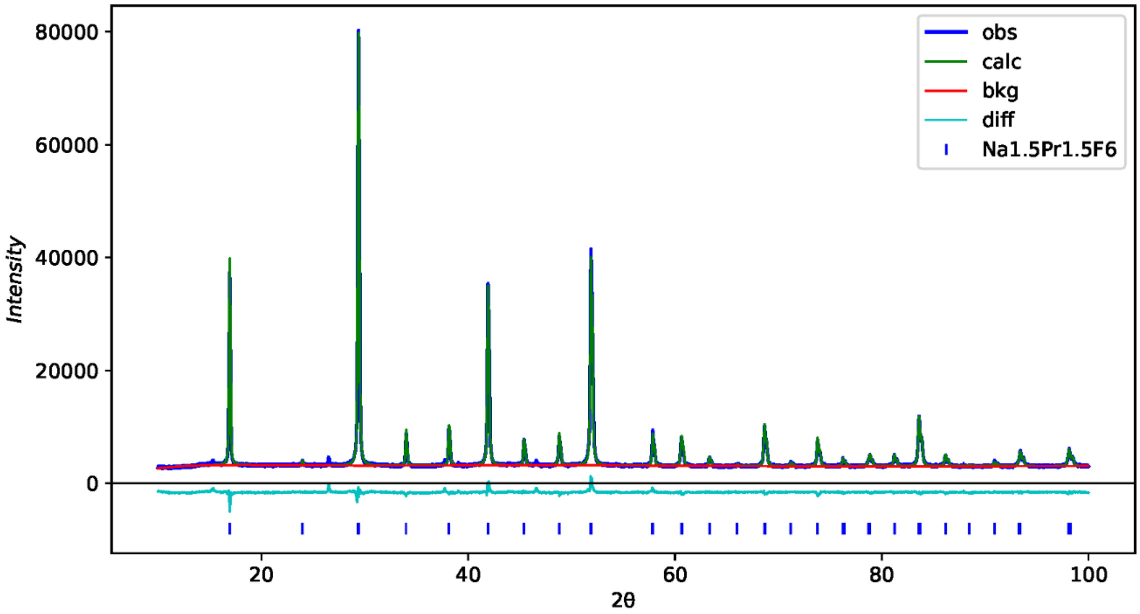

Figure A.8 Rietveld refinement profile of $Na_{1.5}Pr_{1.5}F_6$.

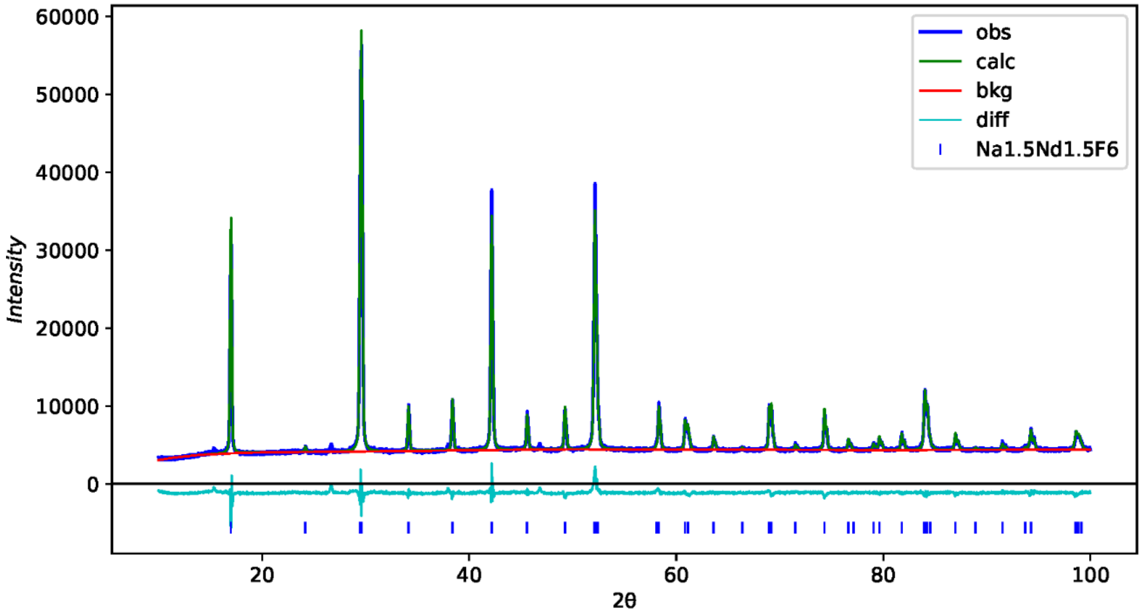

Figure A.9 Rietveld refinement profile of $Na_{1.5}Nd_{1.5}F_6$.

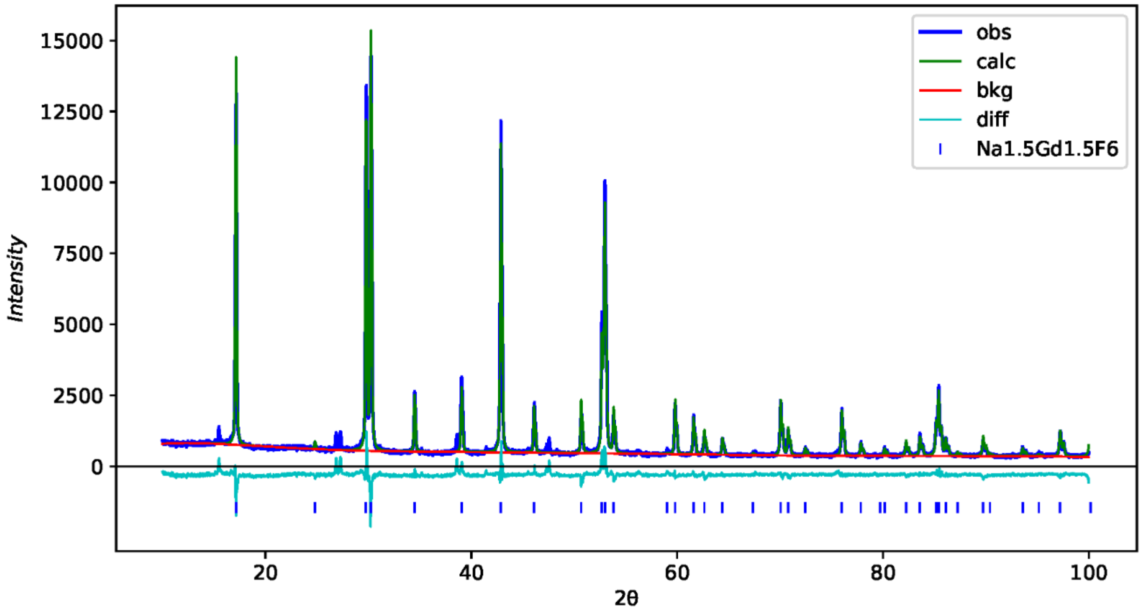

Figure A.10 Rietveld refinement profile of $Na_{1.5}Gd_{1.5}F_6$.

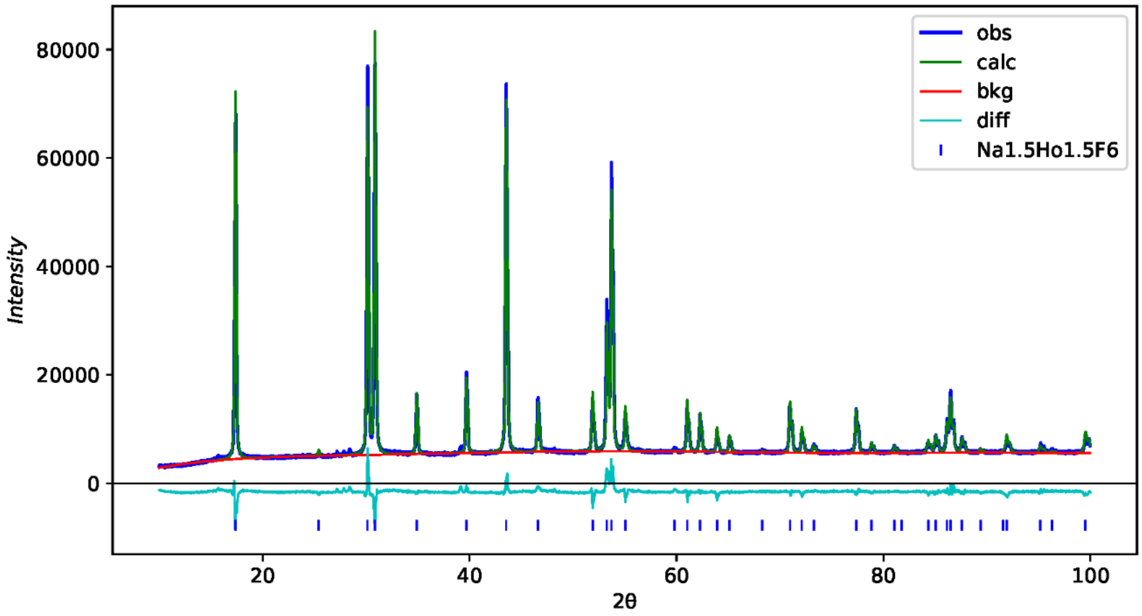

Figure A.11 Rietveld refinement profile of $Na_{1.5}Ho_{1.5}F_6$.

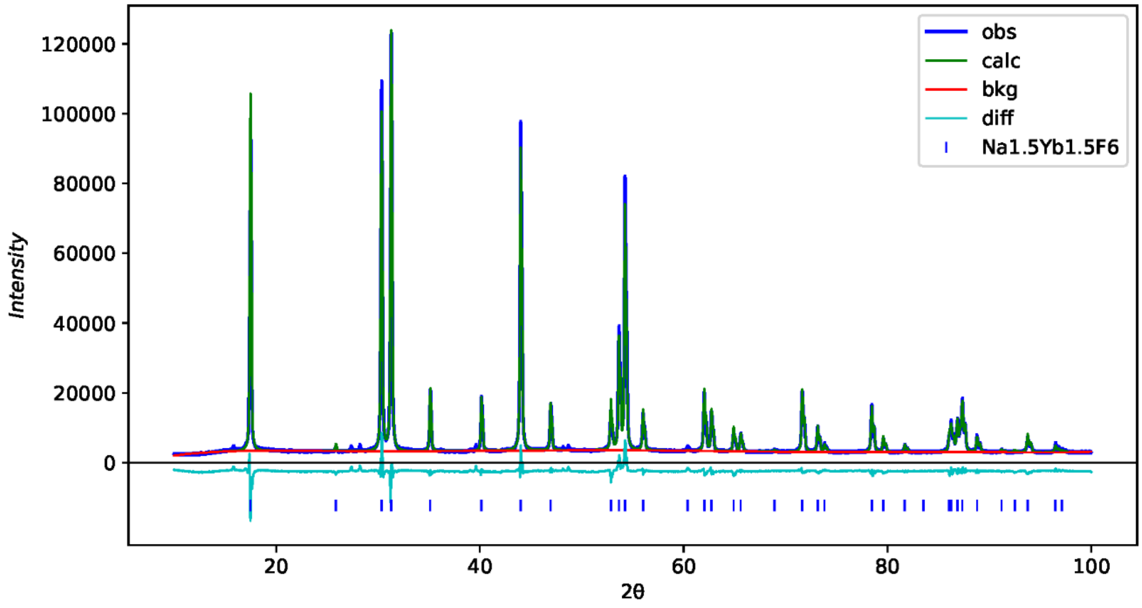

Figure A.12 Rietveld refinement profile of $Na_{1.5}Yb_{1.5}F_6$.

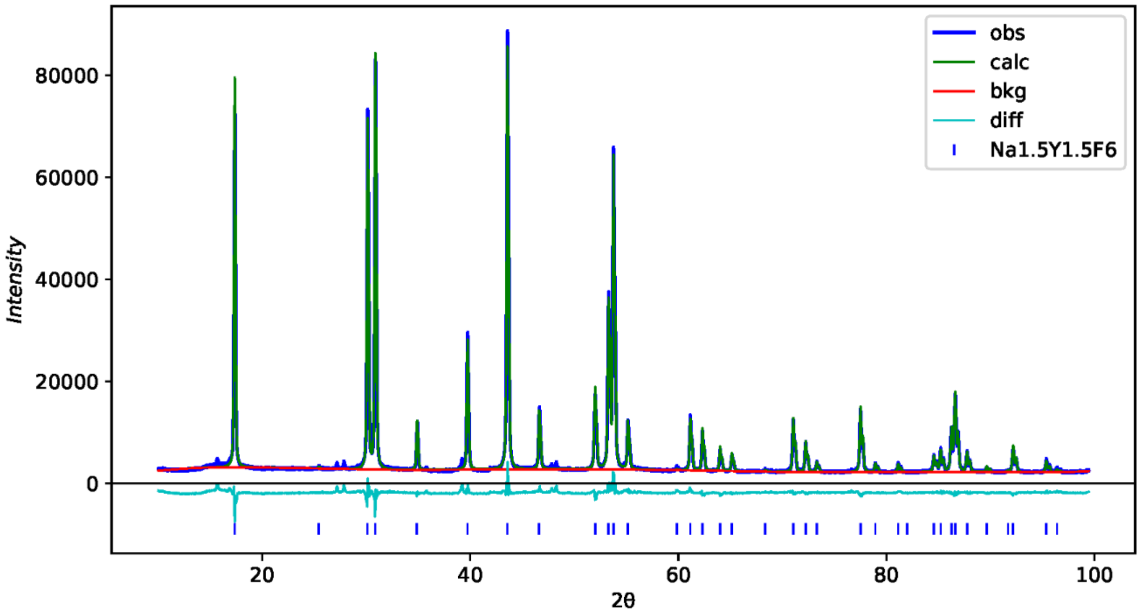

Figure A.13 Rietveld refinement profile of $Na_{1.5}Y_{1.5}F_6$.

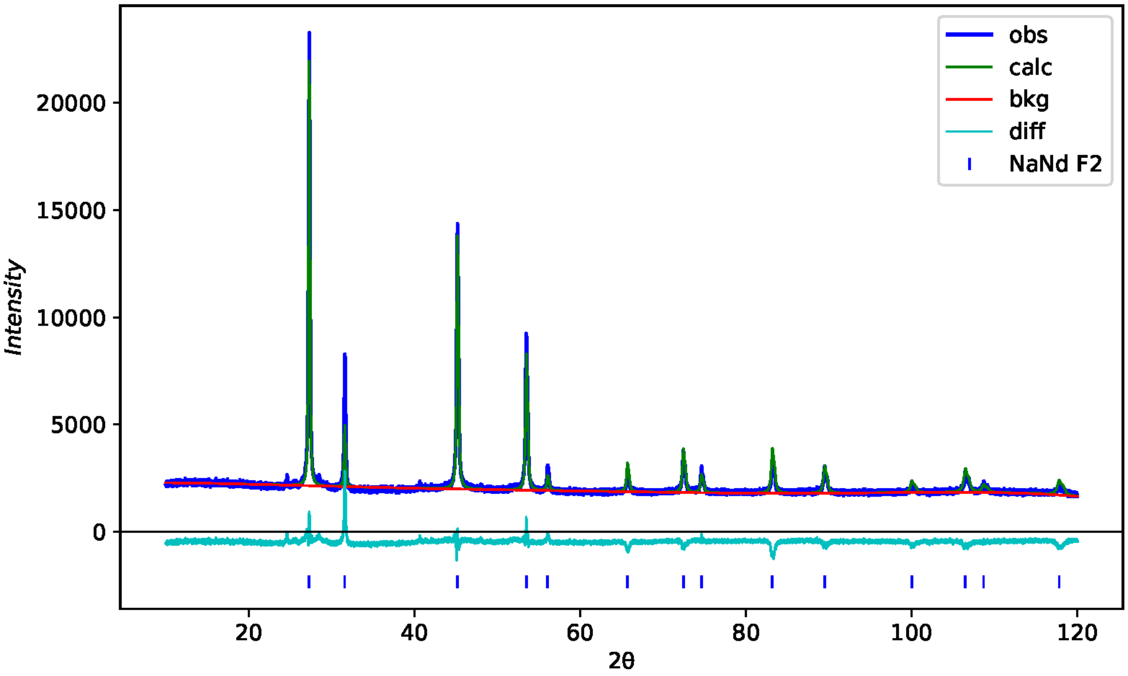

Figure A.14 Rietveld refinement profile of the sample AQ1.

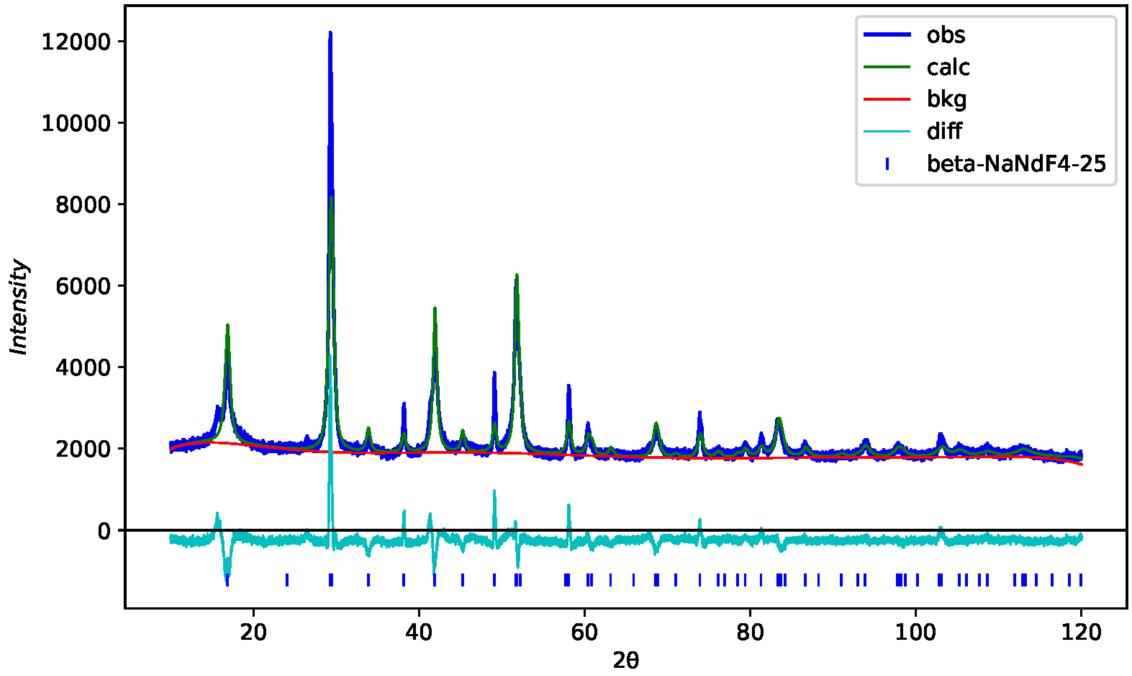

Figure A.15 Rietveld refinement profile of the sample AQ2.

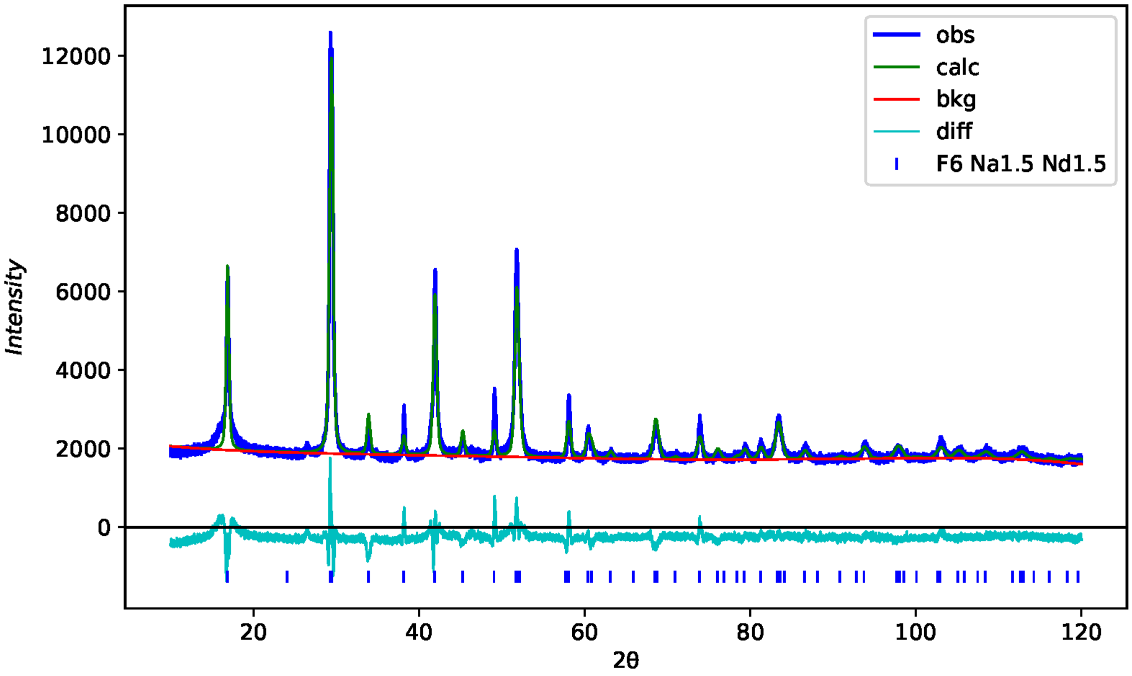

Figure A.16 Rietveld refinement profile of the sample AQ3.

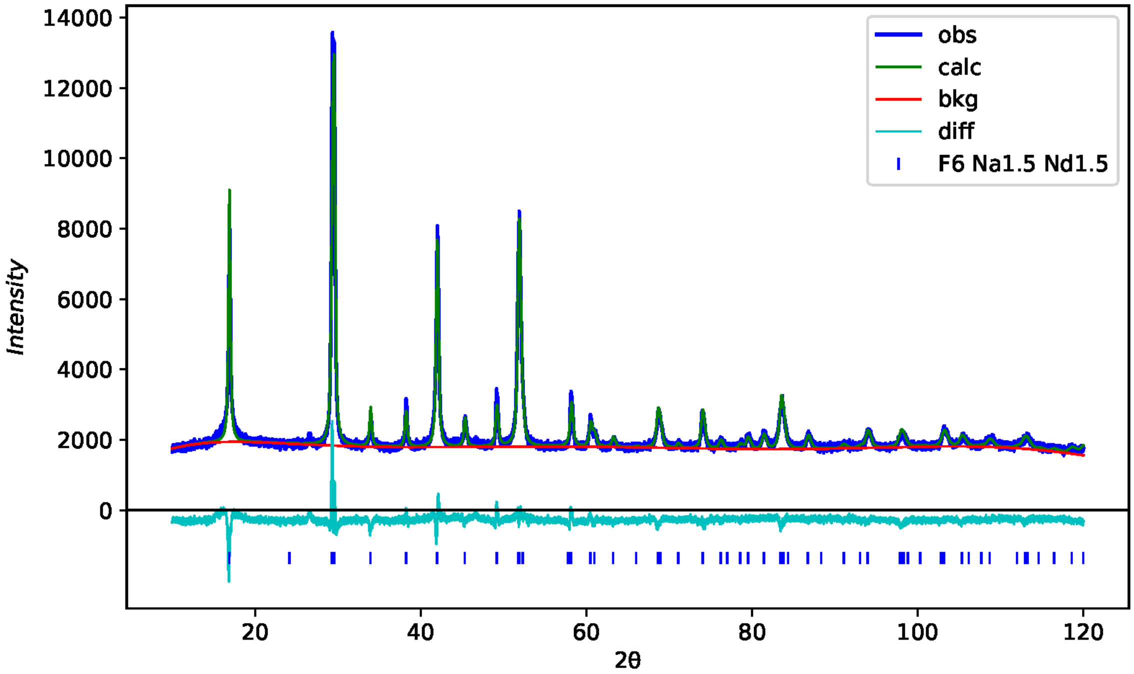

Figure A.17 Rietveld refinement profile of the sample AQ4.

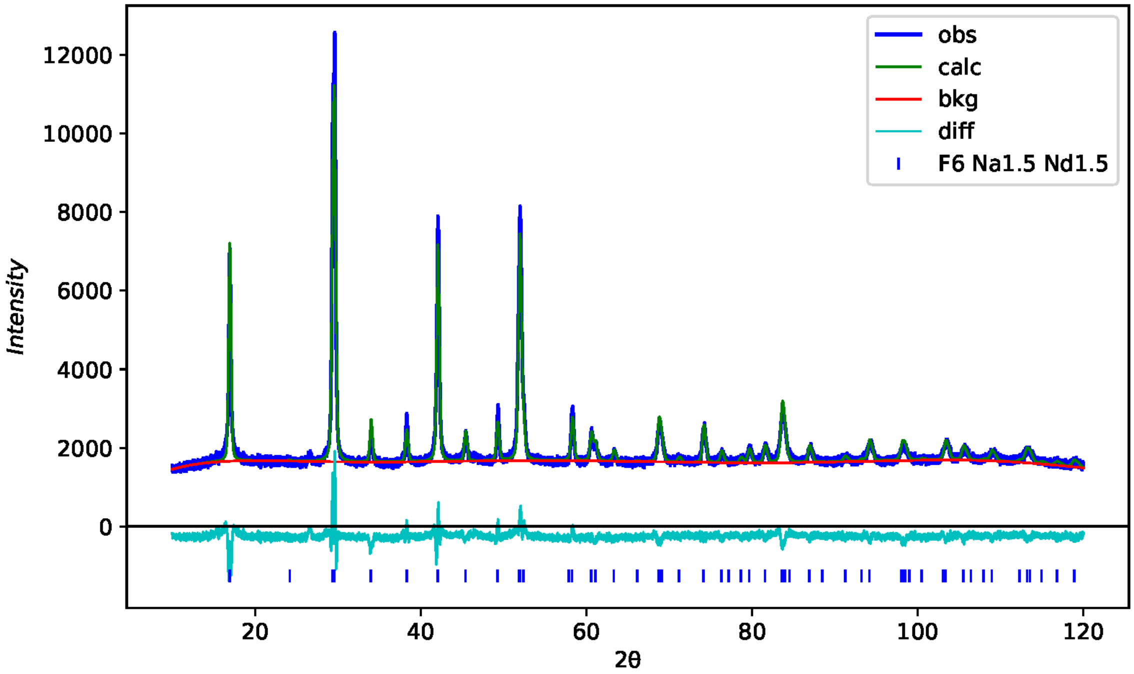

Figure A.18 Rietveld refinement profile of the sample AQ5.

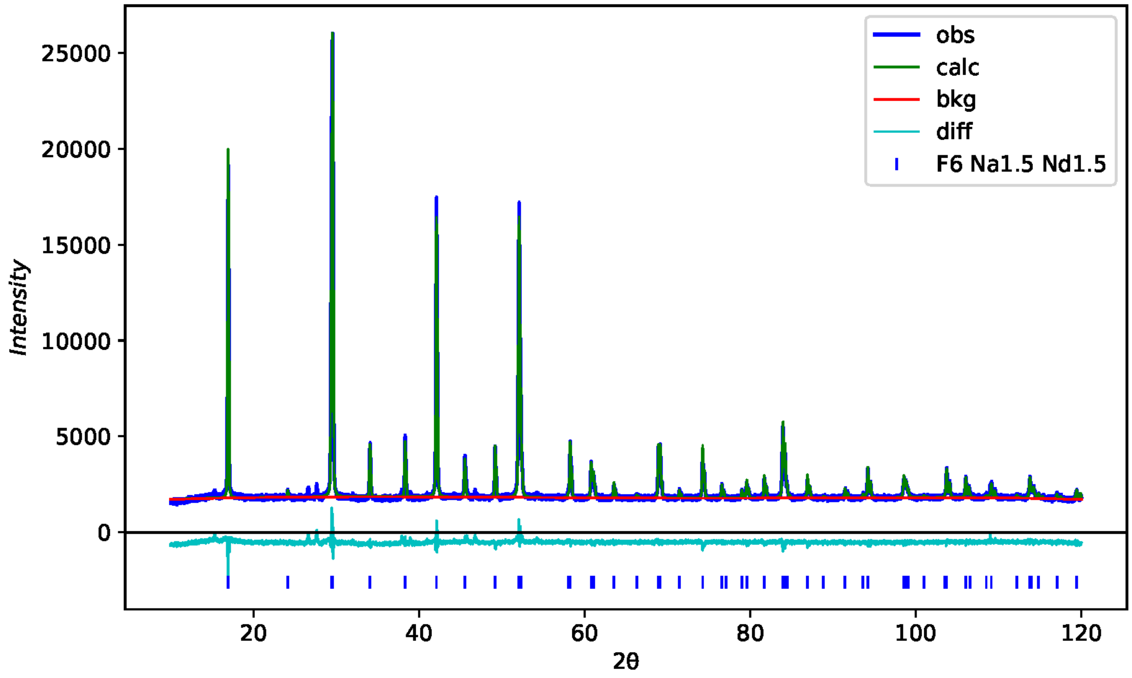

Figure A.19 Rietveld refinement profile of the sample SS1.

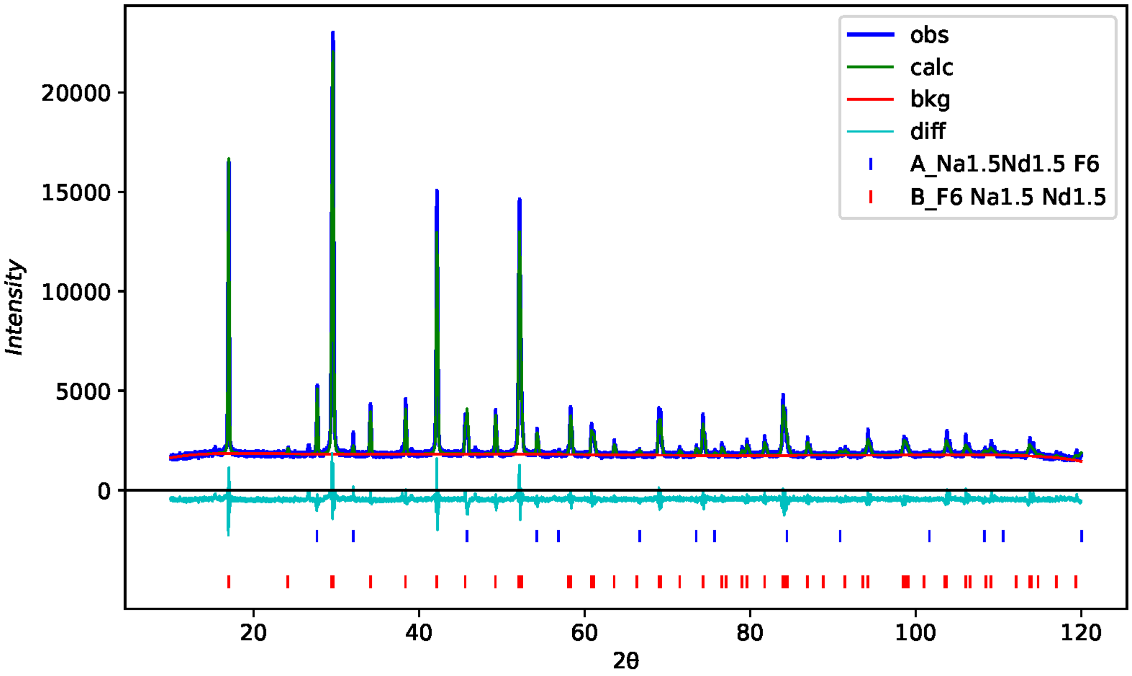

Figure A.20 Rietveld refinement profile of the sample SS2.

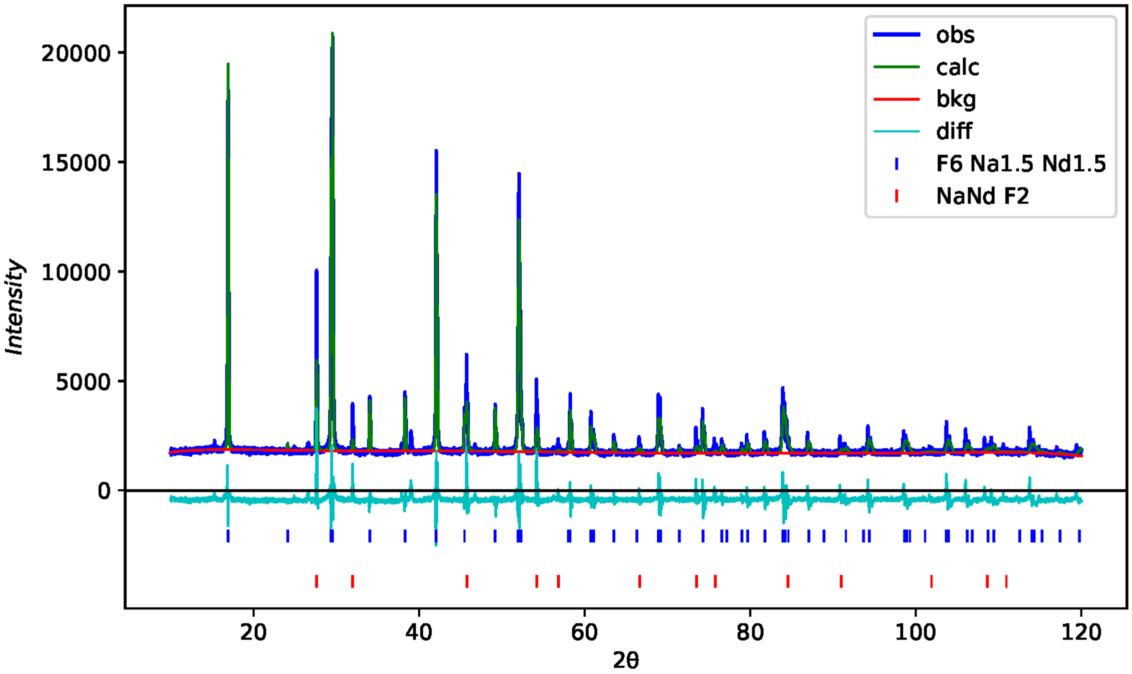

Figure A.21 Rietveld refinement profile of the sample SS3.

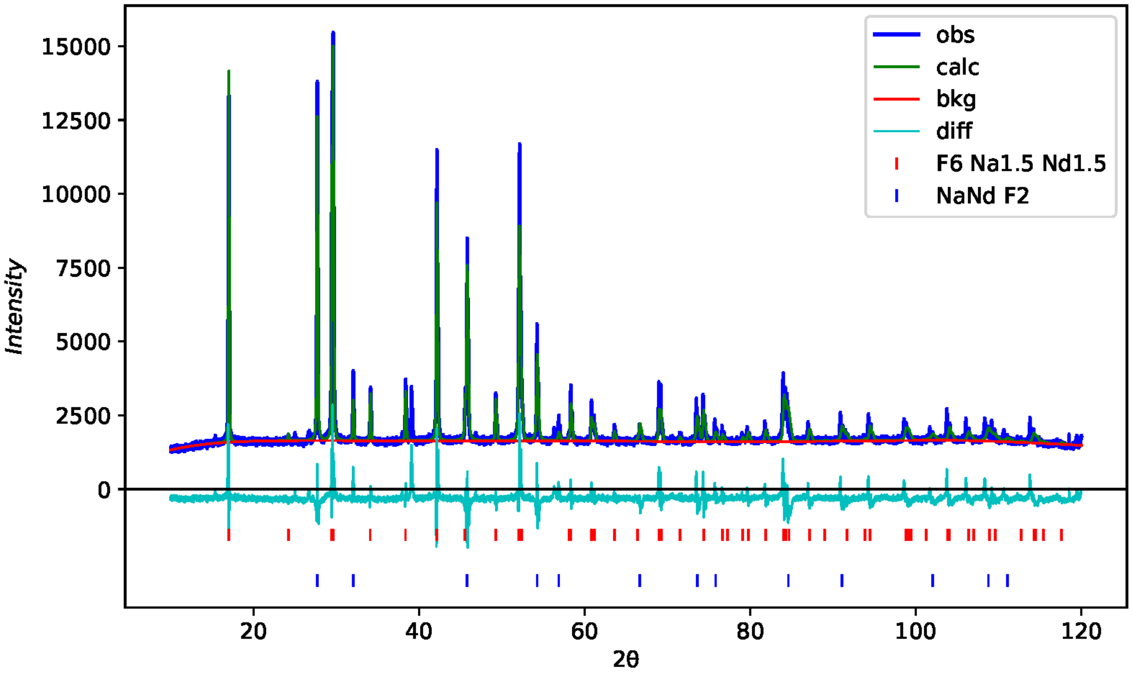

Figure A.22 Rietveld refinement profile of the sample SS4.

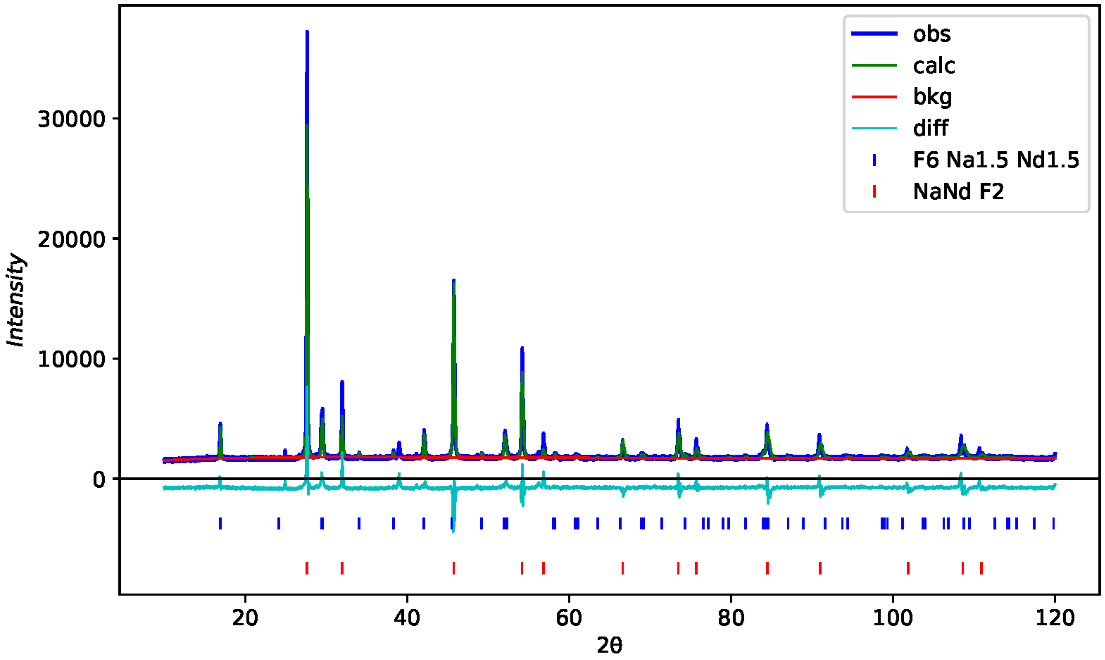

Figure A.23 Rietveld refinement profile of the sample SS5.

B. Raw Data of High Temperature Oxide Melt Solution Calorimetry Experiments

Table B.1 Drop solution enthalpies (ΔH_{ds}) of Yb_2O_3 and Lu_2O_3 in $3Na_2O{\cdot}4MoO_3$ at 800 °C.

No.	Yb_2O_3		Lu_2O_3	
	Mass (mg)	ΔH_{ds} (kJ mol^{-1})	Mass (mg)	ΔH_{ds} (kJ mol^{-1})
1	5.134	–91.16	4.684	–99.07
2	7.832	–90.98	5.691	–99.13
3	5.891	–90.05	5.908	–101.11
4	5.830	–90.07	5.380	–98.91
5	6.935	–90.59	6.039	–98.39
6	4.790	–91.33	5.451	–101.62
7	4.352	–90.13	6.283	–99.95
8	4.971	–91.39	5.252	–101.39
9			6.424	–100.20
Avg.		–90.71		–99.98
2S.D.		0.40		0.79
Error (%)		0.45		0.79

Table B.2 Drop solution enthalpies (ΔH_{ds}) of REOOH in $3Na_2O\cdot4MoO_3$ at 800 °C.

No.	EuOOH		GdOOH		TbOOH		DyOOH	
	Mass (mg)	ΔH_{ds} (kJ mol^{-1})	Mass (mg)	ΔH_{ds} (kJ mol^{-1})	Mass (mg)	ΔH_{ds} (kJ mol^{-1})	Mass (mg)	ΔH_{ds} (kJ mol^{-1})
1	5.625	12.22	5.434	8.05	4.666	7.19	5.556	10.66
2	5.611	11.77	5.962	8.33	3.494	6.67	5.353	11.00
3	6.462	12.28	6.411	8.05	6.031	7.82	7.280	10.79
4	6.293	11.73	5.896	8.67	4.955	6.92	6.371	10.24
5	5.798	11.71	5.520	7.26	2.055	7.08	5.556	10.09
6	5.783	11.68	5.206	6.84	4.779	8.42	6.513	10.86
7	5.481	11.69	7.679	6.96	2.873	7.56	6.310	11.06
8	5.984	11.69	6.928	6.78	4.361	9.50	6.969	10.39
9			6.940	6.88	6.124	9.59		
10					3.243	8.01		
11					3.439	9.58		
Avg.		11.85		7.54		8.03		10.64
2S.D.		0.18		0.49		0.66		0.25
Error (%)		1.49		6.52		8.24		2.39

No.	HoOOH		ErOOH		TmOOH		YbOOH	
	Mass (mg)	ΔH_{ds} (kJ mol^{-1})	Mass (mg)	ΔH_{ds} (kJ mol^{-1})	Mass (mg)	ΔH_{ds} (kJ mol^{-1})	Mass (mg)	ΔH_{ds} (kJ mol^{-1})
1	5.489	13.24	6.032	12.05	5.591	13.04	7.172	13.33
2	5.493	13.18	5.604	11.20	5.819	14.37	5.761	11.60
3	6.399	12.98	4.660	11.05	5.640	13.38	6.198	12.81
4	5.916	12.19	5.254	12.36	5.617	13.15	5.080	12.78
5	5.842	13.48	5.767	12.36	6.904	12.72	6.791	13.25
6	6.240	13.54	6.389	11.27	5.114	13.80	6.087	12.24
7	5.682	13.36	5.865	11.54	5.545	14.02	5.397	12.85
8	6.549	12.49	5.372	11.32	5.935	12.08	5.220	11.68
Avg.		13.06		11.65		13.32		12.57
2S.D.		0.34		0.38		0.52		0.47
Error (%)		2.62		3.25		3.93		3.72

No.	YbOOH		LuOOH	
	Mass (mg)	ΔH_{ds} (kJ mol^{-1})	Mass (mg)	ΔH_{ds} (kJ mol^{-1})
1	7.172	13.33	6.457	12.89
2	5.761	11.60	6.354	12.28
3	6.198	12.81	5.872	11.95
4	5.080	12.78	7.067	11.59
5	6.791	13.25	5.966	12.97
6	6.087	12.24	5.480	12.35
7	5.397	12.85	5.822	12.25
8	5.220	11.68	5.481	12.12
Avg.		12.57		12.30
2S.D.		0.47		0.32
Error (%)		3.72		2.63

Table B.3 Drop solution enthalpies (ΔH_{ds}) of NaF and REF_3 in $3Na_2O{\cdot}4MoO_3$ at 800 °C.

No.	NaF		LaF_3		CeF_3		PrF_3	
	Mass (mg)	ΔH_{ds} (kJ mol^{-1})	Mass (mg)	ΔH_{ds} (kJ mol^{-1})	Mass (mg)	ΔH_{ds} (kJ mol^{-1})	Mass (mg)	ΔH_{ds} (kJ mol^{-1})
1	6.472	77.02	6.932	155.67	5.077	133.12	8.111	151.64
2	6.856	76.82	5.590	154.85	6.555	135.95	5.654	153.27
3	6.862	77.24	6.961	155.22	8.088	134.59	6.243	154.88
4	6.657	76.02	6.890	155.46	6.708	135.54	5.182	150.60
5	5.325	76.43	4.650	153.19	6.331	134.50	7.064	152.72
6	7.419	77.08	7.183	155.21	7.775	134.15	6.828	152.18
7	6.427	76.97	6.239	154.21	6.517	134.17	5.588	151.02
8	7.528	77.50	6.250	155.96	7.263	134.30	6.381	152.90
9			6.773	154.22			7.187	152.81
Avg.				154.89		134.54		152.45
2S.D.				0.58		0.62		0.86
Error (%)				0.37		0.46		0.56

No.	NdF_3		GdF_3		YF_3		HoF_3	
	Mass (mg)	ΔH_{ds} (kJ mol^{-1})	Mass (mg)	ΔH_{ds} (kJ mol^{-1})	Mass (mg)	ΔH_{ds} (kJ mol^{-1})	Mass (mg)	ΔH_{ds} (kJ mol^{-1})
1	6.52	154.59	6.847	146.77	5.749	147.80	8.343	141.82
2	5.77	149.91	7.638	146.50	6.944	147.97	6.008	141.53
3	5.88	150.83	6.754	145.04	7.231	146.34	6.118	139.57
4	9.35	151.89	7.541	146.88	6.874	146.22	7.007	141.87
5	7.19	152.03	7.138	145.01	8.585	146.62	7.779	141.51
6	8.31	150.99	6.348	144.54	6.449	145.87	7.734	141.16
7	5.54	148.68	5.719	146.06	7.391	146.02	5.902	140.40
8	4.83	149.24	6.688	144.96	6.634	146.67	6.926	139.29
9								
Avg.		151.02		145.72		146.69		140.89
2S.D.		1.32		0.66		0.56		0.72
Error (%)		0.88		0.45		0.38		0.51

No.	YbF_3	
	Mass (mg)	ΔH_{ds} (kJ mol^{-1})
1	7.444	127.49
2	6.600	126.98
3	7.459	126.35
4	6.474	126.75
5	5.740	127.48
6	7.487	127.74
7	6.292	125.23
8	6.717	127.35
9	6.995	127.08
Avg.		126.94
2S.D.		0.51
Error (%)		0.40

Table B.4 Drop solution enthalpies (ΔH_{ds}) of Na_2CO_3 in $3Na_2O{\cdot}4MoO_3$ at 800 °C.

No.	Na_2CO_3	
	Mass (mg)	ΔH_{ds} (kJ mol^{-1})
1	5.272	160.74
2	6.158	161.57
3	5.378	161.65
4	4.611	160.01
5	6.241	159.96
6	6.376	160.95
7	4.437	160.10
8	5.856	161.16
Avg.		160.77
2S.D.		0.48
Error (%)		0.30

Table B.5 Drop solution enthalpies (ΔH_{ds}) of REOF in $3Na_2O \cdot 4MoO_3$ at 800 °C.

No.	LaOF		NdOF		GdOF		YOF	
	Mass (mg)	ΔH_{ds} (kJ mol^{-1})	Mass (mg)	ΔH_{ds} (kJ mol^{-1})	Mass (mg)	ΔH_{ds} (kJ mol^{-1})	Mass (mg)	ΔH_{ds} (kJ mol^{-1})
1	8.912	14.90	9.185	27.17	8.998	26.27	12.257	28.19
2	10.709	14.83	8.042	26.98	6.307	26.99	9.230	27.71
3	11.801	13.49	9.827	26.01	11.011	26.97	10.237	27.50
4	11.015	13.56	12.156	26.42	10.500	27.24	8.885	27.00
5	6.389	14.17	10.453	26.85	11.879	26.75	10.422	28.30
6	9.608	14.46	9.432	25.83	11.046	27.33	10.863	27.53
7	9.676	14.32	9.210	27.09	9.746	27.02	10.339	28.33
8	10.891	14.30	10.273	25.47	10.590	26.52	10.257	28.44
Avg.		14.25		26.48		26.89		27.87
2S.D.		0.37		0.45		0.25		0.37
Error (%)		2.56		1.72		0.94		1.31

No.	HoOF		YbOF-mon	
	Mass (mg)	ΔH_{ds} (kJ mol^{-1})	Mass (mg)	ΔH_{ds} (kJ mol^{-1})
1	10.627	30.21	10.275	27.47
2	10.945	30.40	10.513	26.70
3	9.882	29.77	10.205	27.28
4	10.598	29.62	10.350	26.95
5	11.012	30.51	12.101	27.15
6	9.907	30.00	10.926	26.68
7	10.297	29.52	9.963	26.28
8	10.338	29.92	11.924	26.45
Avg.		29.99		26.87
2S.D.		0.25		0.29
Error (%)		0.84		1.09

Table B.6 Drop solution enthalpies (ΔH_{ds}) of NaCl and $RECl_3$ in $3Na_2O \cdot 4MoO_3$ at 800 °C.

No.	NaCl		$LaCl_3$		$NdCl_3$		$GdCl_3$	
	Mass (mg)	ΔH_{ds} (kJ mol^{-1})	Mass (mg)	ΔH_{ds} (kJ mol^{-1})	Mass (mg)	ΔH_{ds} (kJ mol^{-1})	Mass (mg)	ΔH_{ds} (kJ mol^{-1})
1	4.951	76.99	2.957	–16.12	9.041	–26.58	7.371	–48.57
2	4.483	76.91	4.990	–14.07	7.871	–25.05	8.623	–49.70
3	4.426	77.36	1.667	–16.51	6.986	–25.00	4.148	–50.56
4	4.811	77.69	1.672	–16.61	5.330	–26.81	8.576	–49.54
5	5.313	77.66	1.332	–16.65	8.737	–25.88	6.364	–50.51
6	4.411	77.63	5.073	–17.98	8.121	–26.05	5.708	–51.72
7	5.036	77.10	1.651	–17.66	7.739	–26.72	4.245	–49.72
8	5.454	78.07	7.174	–15.69	7.142	–26.92	5.879	–51.62
9	5.392	78.18						
Avg.		77.51		–16.41		–26.13		–50.24
2S.D.		0.30		0.85		0.55		0.76
Error (%)		0.39		5.21		2.09		1.51

No.	YCl_3		$HoCl_3$		$ErCl_3$		$TmCl_3$	
	Mass (mg)	ΔH_{ds} (kJ mol^{-1})	Mass (mg)	ΔH_{ds} (kJ mol^{-1})	Mass (mg)	ΔH_{ds} (kJ mol^{-1})	Mass (mg)	ΔH_{ds} (kJ mol^{-1})
1	2.189	–101.10	2.639	–88.73	2.435	–96.18	0.658	–90.05
2	3.035	–101.74	4.260	–86.65	4.746	–96.34	2.136	–89.43
3	2.556	–100.86	4.963	–88.93	2.976	–97.25	1.230	–89.95
4	2.811	–99.03	1.769	–87.64	2.700	–97.03	0.901	–90.93
5	3.752	–99.01	4.005	–87.96	3.038	–97.58	0.973	–89.13
6	2.663	–99.80	2.268	–87.37	1.350	–97.45	1.202	–90.35
7	1.136	–100.58	4.032	–86.49	2.548	–96.71	2.042	–89.37
8	2.031	–99.27	2.299	–85.03	4.207	–96.26	1.206	–89.02
Avg.		–100.17		–87.35		–96.85		–89.78
2S.D.		0.73		0.91		0.39		0.46
Error (%)		0.73		1.04		0.40		0.52

No.	$YbCl_3$		$LuCl_3$	
	Mass (mg)	ΔH_{ds} (kJ mol^{-1})	Mass (mg)	ΔH_{ds} (kJ mol^{-1})
1	6.525	–89.28	3.051	–71.95
2	5.337	–91.06	1.963	–72.69
3	3.721	–89.58	2.947	–72.63
4	3.024	–90.15	2.204	–71.59
5	3.276	–90.95	1.167	–70.73
6	1.865	–90.77	0.975	–70.04
7	2.057	–90.49	1.707	–70.25
8	1.486	–90.36	1.291	–72.08
Avg.		–90.33		–71.50
2S.D.		0.45		0.73
Error (%)		0.50		1.03

Table B.7 Drop solution enthalpies (ΔH_{ds}) of REOCl in $3Na_2O\cdot4MoO_3$ at 800 °C.

No.	LaOCl		NdOCl		GdOCl		YOCl	
	Mass (mg)	ΔH_{ds} (kJ mol^{-1})	Mass (mg)	ΔH_{ds} (kJ mol^{-1})	Mass (mg)	ΔH_{ds} (kJ mol^{-1})	Mass (mg)	ΔH_{ds} (kJ mol^{-1})
1	5.056	–6.27	4.779	–0.42	4.295	–13.69	6.114	–33.42
2	4.224	–6.05	4.273	–0.53	4.837	–12.80	4.305	–33.55
3	5.056	–6.39	4.211	–0.64	4.529	–12.88	3.600	–34.49
4	4.231	–5.72	4.982	–0.17	3.772	–12.85	3.001	–34.39
5	5.017	–5.80	4.099	–0.82	3.703	–13.73	3.252	–35.63
6	4.366	–5.08	5.055	–0.36	4.564	–12.66	3.999	–33.00
7	4.592	–5.83	4.384	–0.40	4.753	–12.61	3.373	–34.28
8	3.153	–5.85	5.170	–0.81	4.737	–12.74	3.740	–33.31
9			5.011	–0.69				
Avg.		–5.87		–0.54		–13.00		–34.01
2S.D.		0.28		0.15		0.32		0.61
Error (%)		4.81		27.33		2.45		1.78

No.	HoOCl		ErOCl		TmOCl		YbOCl	
	Mass (mg)	ΔH_{ds} (kJ mol^{-1})	Mass (mg)	ΔH_{ds} (kJ mol^{-1})	Mass (mg)	ΔH_{ds} (kJ mol^{-1})	Mass (mg)	ΔH_{ds} (kJ mol^{-1})
1	4.438	–30.28	4.213	–29.34	3.920	–30.26	3.199	–29.76
2	3.825	–29.43	2.582	–30.05	3.251	–31.32	3.608	–30.62
3	4.130	–30.62	4.446	–31.00	2.333	–30.33	3.335	–30.56
4	3.702	–31.08	3.568	–30.99	3.847	–29.60	2.955	–32.06
5	4.736	–30.73	2.439	–29.43	3.465	–29.24	2.852	–29.90
6	3.600	–31.16	4.972	–30.72	2.912	–29.37	3.807	–29.94
7	3.193	–30.57	3.085	–29.61	2.318	–29.64	3.509	–29.93
8	3.736	–30.77	2.760	–30.38	3.049	–30.07	3.509	–31.03
Avg.		–30.58		–30.19		–29.98		–30.48
2S.D.		0.38		0.48		0.48		0.55
Error (%)		1.26		1.60		1.60		1.81

No.	LuOCl	
	Mass (mg)	ΔH_{ds} (kJ mol^{-1})
1	3.052	–32.10
2	3.087	–30.57
3	2.614	–31.44
4	3.131	–30.57
5	2.598	–30.12
6	2.924	–30.58
7	4.020	–29.81
8	3.480	–30.48
Avg.		–30.71
2S.D.		0.52
Error (%)		1.68

Table B.8 Drop solution enthalpies (ΔH_{ds}) of $Na_{1.5}RE_{1.5}F_6$ in $3Na_2O\cdot4MoO_3$ at 800 °C.

No.	$Na_{1.5}La_{1.5}F_6$		$Na_{1.5}Ce_{1.5}F_6$		$Na_{1.5}Pr_{1.5}F_6$		$Na_{1.5}Nd_{1.5}F_6$	
	Mass (mg)	ΔH_{ds} (kJ mol^{-1})	Mass (mg)	ΔH_{ds} (kJ mol^{-1})	Mass (mg)	ΔH_{ds} (kJ mol^{-1})	Mass (mg)	ΔH_{ds} (kJ mol^{-1})
1	9.013	338.70	9.136	314.05	6.694	348.45	6.644	351.21
2	7.870	342.71	7.078	315.24	7.447	345.99	6.879	352.04
3	5.379	342.22	7.011	314.21	6.975	347.50	6.054	350.26
4	6.493	338.25	5.853	315.29	6.147	349.84	7.131	354.95
5	7.349	339.63	6.466	314.19	6.728	347.51	8.119	352.64
6	6.561	341.30	7.038	315.64	6.990	347.94	5.924	352.07
7	6.670	341.29	5.316	316.00	5.840	348.33	6.117	351.35
8	5.747	339.05	6.784	316.62	5.262	349.55	5.851	351.75
9	6.260	339.43						
10	7.882	341.03						
Avg.		340.36		315.16		348.14		352.03
2S.D.		0.98		0.66		0.87		0.97
Error (%)		0.29		0.21		0.25		0.28

No.	$Na_{1.5}Gd_{1.5}F_6$		$Na_{1.5}Y_{1.5}F_6$		$Na_{1.5}Ho_{1.5}F_6$		$Na_{1.5}Yb_{1.5}F_6$	
	Mass (mg)	ΔH_{ds} (kJ mol^{-1})	Mass (mg)	ΔH_{ds} (kJ mol^{-1})	Mass (mg)	ΔH_{ds} (kJ mol^{-1})	Mass (mg)	ΔH_{ds} (kJ mol^{-1})
1	6.379	361.90	8.155	361.07	8.732	354.38	6.916	336.65
2	5.226	360.41	6.349	361.90	6.854	355.89	5.922	336.96
3	6.582	360.24	5.406	361.69	7.059	354.42	8.208	337.51
4	5.989	359.25	6.397	362.00	7.391	354.66	7.035	337.94
5	6.218	358.76	7.214	361.38	6.451	354.68	6.584	334.77
6	5.826	359.32	6.061	360.84	7.007	353.83	7.473	335.29
7	7.462	358.22	5.956	359.66	6.554	352.99	6.773	336.24
8	5.519	357.65	5.950	361.82	8.118	353.86	6.931	334.88
Avg.		359.47		361.29		354.34		336.28
2S.D.		0.96		0.55		0.59		0.85
Error (%)		0.27		0.15		0.17		0.25

Table B.9 Drop solution enthalpies (ΔH_{ds}) of NaF–NdF$_3$ samples in $3Na_2O\cdot 4MoO_3$ at 800 °C.

No.	AQ1 ($Na_{0.76}Nd_{1.75}F_6\cdot 0.24H_2O$)		AQ2 ($Na_{0.77}Nd_{1.74}F_6\cdot 0.84H_2O$)		AQ3 ($Na_{0.81}Nd_{1.73}F_6\cdot 0.68H_2O$)	
	Mass (mg)	ΔH_{ds} (kJ mol^{-1})	Mass (mg)	ΔH_{ds} (kJ mol^{-1})	Mass (mg)	ΔH_{ds} (kJ mol^{-1})
1	6.45	312.53	5.86	279.45	4.84	301.84
2	5.17	311.83	6.14	281.66	4.63	300.81
3	5.223	309.54	6.13	281.65	4.94	301.95
4	4.64	309.95	5.74	277.83	5.37	297.61
5	7.18	308.38	5.82	281.12	5.91	300.42
6	5.93	308.76	6.39	280.97	5.60	300.34
7	6.420	310.47	4.59	279.01	5.81	300.66
8	5.24	307.70	5.88	279.62	4.97	301.77
9			5.58	280.04		
Avg.		309.90		280.15		300.68
2S.D.		1.18		0.87		0.99
Error (%)		0.38		0.31		0.33

No.	AQ4 ($Na_{0.96}Nd_{1.68}F_6\cdot 0.41H_2O$)		AQ5 ($Na_{1.08}Nd_{1.64}F_6\cdot 0.32H_2O$)		SS1 ($Na_{1.46}Nd_{1.51}F_6$)	
	Mass (mg)	ΔH_{ds} (kJ mol^{-1})	Mass (mg)	ΔH_{ds} (kJ mol^{-1})	Mass (mg)	ΔH_{ds} (kJ mol^{-1})
1	4.78	322.48	6.74	321.21	4.33	342.80
2	5.59	321.96	5.66	322.01	8.35	344.22
3	5.23	323.07	5.65	322.09	5.74	342.79
4	5.77	323.84	5.34	319.24	4.93	344.00
5	6.81	321.28	6.17	318.90	6.60	342.01
6	6.23	321.03	4.63	321.15	6.21	342.39
7	7.22	323.50	5.14	320.98	6.58	343.96
8	7.03	320.24	5.61	322.67	6.32	343.44
Avg.		322.18		321.03		343.20
2S.D.		0.90		0.95		0.58
Error (%)		0.28		0.30		0.17

No.	SS3 ($Na_{1.46}Nd_{1.51}F_6$)		SS4 ($Na_{1.46}Nd_{1.51}F_6$)		SS5 ($Na_{1.46}Nd_{1.51}F_6$)	
	Mass (mg)	ΔH_{ds} (kJ mol^{-1})	Mass (mg)	ΔH_{ds} (kJ mol^{-1})	Mass (mg)	ΔH_{ds} (kJ mol^{-1})
1	8.668	321.49	10.231	291.23	5.94	185.18
2	7.955	318.14	7.765	291.78	7.482	185.43
3	7.607	319.67	4.550	291.60	5.339	185.26
4	6.854	319.10	7.50	289.74	4.63	184.68
5	8.550	321.93	6.540	293.58	6.36	186.08
6	7.008	319.15	5.244	290.85	4.894	187.85
Avg.		319.91		291.46		185.75
2S.D.		1.21		1.03		0.92
Error (%)		0.38		0.35		0.49

Table B.10 Drop solution enthalpies (ΔH_{ds}) of CaF_2 in $3Na_2O \cdot 4MoO_3$ at 800 °C.

No.	CaF_2	
	Mass (mg)	ΔH_{ds} (kJ mol^{-1})
1	8.979	133.84
2	4.704	132.95
3	6.199	133.73
4	7.350	132.90
5	6.629	133.09
6	5.039	133.51
7	5.273	133.15
8	5.459	133.51
9	5.087	132.74
10	6.017	133.48
Avg.		133.29
2S.D.		0.24
Error (%)		0.18

Table B.11 Drop solution enthalpies (ΔH_{ds}) of $Ca_{1-x}RE_xF_{2+x}$ in $3Na_2O\cdot4MoO_3$ at 800 °C.

No.	$Ca_{0.9}La_{0.1}F_{2.1}$-1200		$Ca_{0.8}La_{0.2}F_{2.2}$-900		$Ca_{0.8}La_{0.2}F_{2.2}$-1200		$Ca_{0.7}La_{0.3}F_{2.3}$-900	
	Mass (mg)	ΔH_{ds} (kJ mol^{-1})	Mass (mg)	ΔH_{ds} (kJ mol^{-1})	Mass (mg)	ΔH_{ds} (kJ mol^{-1})	Mass (mg)	ΔH_{ds} (kJ mol^{-1})
1	5.551	133.84	5.225	129.63	6.311	129.14	5.605	130.33
2	5.410	134.27	6.347	129.52	5.669	130.43	5.273	130.16
3	6.066	134.82	5.620	130.13	5.363	130.81	4.946	130.31
4	5.998	133.50	5.845	129.93	5.962	130.66	4.590	130.25
5	5.207	134.67	5.229	129.97	5.607	129.90	5.393	131.38
6	5.338	134.79	4.735	129.35	5.445	130.29	5.944	130.82
7	6.215	134.24	5.874	129.16	5.211	129.93	5.058	130.29
8	5.834	134.62	5.492	129.09	5.645	130.33	5.678	129.68
9					5.709	129.79		
Avg.		134.34		129.60		130.14		130.40
2S.D.		0.34		0.27		0.34		0.36
Error (%)		0.25		0.21		0.26		0.27

No.	$Ca_{0.7}La_{0.3}F_{2.3}$-1200		$Ca_{0.6}La_{0.4}F_{2.4}$-900		$Ca_{0.6}La_{0.4}F_{2.4}$-1200		$Ca_{0.9}Pr_{0.1}F_{2.1}$-900	
	Mass (mg)	ΔH_{ds} (kJ mol^{-1})	Mass (mg)	ΔH_{ds} (kJ mol^{-1})	Mass (mg)	ΔH_{ds} (kJ mol^{-1})	Mass (mg)	ΔH_{ds} (kJ mol^{-1})
1	5.466	132.48	5.703	133.41	5.978	132.72	5.703	130.60
2	5.356	132.73	5.933	132.23	5.685	133.10	6.866	130.73
3	5.409	132.39	5.819	133.94	4.972	131.83	6.276	131.39
4	6.073	132.06	5.609	134.03	5.219	131.54	5.244	130.72
5	5.563	132.05	6.040	133.99	5.407	132.50	5.372	131.12
6	6.265	131.64	5.769	133.92	5.274	131.63	5.630	131.71
7	4.902	132.27	5.733	133.61	5.097	132.30	4.793	130.46
8	6.340	131.07	5.303	133.56	5.127	132.41	7.397	131.69
Avg.		132.09		133.59		132.25		131.05
2S.D.		0.37		0.42		0.39		0.35
Error (%)		0.28		0.32		0.29		0.27

No.	$Ca_{0.9}Pr_{0.1}F_{2.1}$-1200		$Ca_{0.8}Pr_{0.2}F_{2.2}$-900		$Ca_{0.8}Pr_{0.2}F_{2.2}$-1200		$Ca_{0.7}Pr_{0.3}F_{2.3}$-900	
	Mass (mg)	ΔH_{ds} (kJ mol^{-1})	Mass (mg)	ΔH_{ds} (kJ mol^{-1})	Mass (mg)	ΔH_{ds} (kJ mol^{-1})	Mass (mg)	ΔH_{ds} (kJ mol^{-1})
1	5.841	132.35	6.385	130.95	5.475	133.72	6.903	128.55
2	5.171	133.83	5.884	130.62	5.149	132.64	5.978	127.76
3	5.471	133.49	6.653	130.92	5.120	133.85	5.767	128.39
4	5.950	133.69	7.132	130.71	5.818	134.26	4.557	127.96
5	5.602	132.95	5.176	131.16	6.061	133.28	6.071	128.44
6	5.260	134.27	4.804	131.13	5.914	133.49	6.033	128.92
7	6.009	134.41	6.026	131.63	5.085	133.33	6.322	128.59
8	5.614	134.46	6.576	130.11	5.153	133.53	6.404	128.65
9							6.617	129.27
Avg.		133.68		130.90		133.51		128.50
2S.D.		0.52		0.32		0.34		0.30
Error (%)		0.39		0.24		0.25		0.24

No.	$Ca_{0.7}Pr_{0.3}F_{2.3}$-1200		$Ca_{0.6}Pr_{0.4}F_{2.4}$-900		$Ca_{0.6}Pr_{0.4}F_{2.4}$-1200		$Ca_{0.9}Nd_{0.1}F_{2.1}$-900	
	Mass (mg)	ΔH_{ds} (kJ mol^{-1})	Mass (mg)	ΔH_{ds} (kJ mol^{-1})	Mass (mg)	ΔH_{ds} (kJ mol^{-1})	Mass (mg)	ΔH_{ds} (kJ mol^{-1})
1	6.125	130.79	6.117	132.81	5.694	133.91	9.524	130.03
2	6.351	131.31	5.715	133.24	6.051	132.59	6.996	130.54
3	5.797	130.17	5.595	133.72	6.088	133.51	7.347	131.03
4	5.874	131.45	5.801	133.22	6.210	132.23	5.849	130.92
5	5.054	131.20	6.706	132.38	5.567	133.01	5.187	130.92
6	6.741	130.91	5.762	132.98	4.948	132.36	7.013	131.96
7	5.574	130.56	7.857	132.46	6.707	132.90	5.675	129.68
8	5.888	130.62	7.376	134.15	6.064	133.94	6.871	129.64
Avg.		130.88		133.12		133.06		130.59
2S.D.		0.30		0.43		0.47		0.56
Error (%)		0.23		0.32		0.36		0.43

No.	$Ca_{0.9}Nd_{0.1}F_{2.1}$-1200		$Ca_{0.8}Nd_{0.2}F_{2.2}$-900		$Ca_{0.8}Nd_{0.2}F_{2.2}$-1200		$Ca_{0.7}Nd_{0.3}F_{2.3}$-900	
	Mass (mg)	ΔH_{ds} (kJ mol^{-1})	Mass (mg)	ΔH_{ds} (kJ mol^{-1})	Mass (mg)	ΔH_{ds} (kJ mol^{-1})	Mass (mg)	ΔH_{ds} (kJ mol^{-1})
1	5.521	133.45	8.739	129.35	6.124	133.29	7.947	129.96
2	5.459	134.26	5.887	128.46	5.796	133.46	6.613	130.47
3	5.254	133.87	7.840	128.08	5.849	133.44	6.380	129.43
4	6.084	133.26	6.044	129.57	5.651	133.02	6.283	129.07
5	5.694	133.63	6.049	129.91	5.399	133.40	6.329	129.54
6	5.630	134.29	4.700	129.36	5.874	134.16	5.804	128.54
7	5.072	134.17	4.996	129.46	5.858	133.76	5.915	129.22
8	5.465	133.95	6.148	129.41	6.015	133.92	5.707	129.69
Avg.		133.86		129.20		133.55		129.49
2S.D.		0.27		0.43		0.26		0.41
Error (%)		0.20		0.33		0.19		0.32

No.	$Ca_{0.7}Nd_{0.3}F_{2.3}$-1200		$Ca_{0.6}Nd_{0.4}F_{2.4}$-900		$Ca_{0.6}Nd_{0.4}F_{2.4}$-1200	
	Mass (mg)	ΔH_{ds} (kJ mol^{-1})	Mass (mg)	ΔH_{ds} (kJ mol^{-1})	Mass (mg)	ΔH_{ds} (kJ mol^{-1})
1	5.532	133.17	4.782	129.85	5.546	132.06
2	5.736	134.34	7.420	130.75	5.898	131.70
3	6.019	133.92	5.169	129.06	5.404	131.85
4	5.755	133.68	5.703	129.48	5.604	132.11
5	5.338	132.97	5.706	131.39	5.911	130.13
6	5.902	133.88	6.491	130.04	6.401	132.09
7	5.673	134.46	6.491	130.35	5.284	130.85
8	5.002	133.82	6.148	129.53	5.635	131.25
Avg.		133.78		130.06		131.50
2S.D.		0.36		0.53		0.50
Error (%)		0.27		0.41		0.38

C. Lattice Energy Data

Table C.1 Lattice energies (U) of rare earth compounds calculated from Born–Haber cycles.

$RECl_3$		REF_3		$REOCl$		$REOF$	
RE	U (kJ mol^{-1})	RE	U (kJ mol^{-1})	RE	U (kJ mol^{-1})	RE	U (kJ mol^{-1})
La	–6213.6 ± 5.9	La	–4874.8 ± 7.7	La	–5642.5 ± 6.0	La	–5803.9 ± 6.2
Ce	–6276.0 ± 5.9	Ce	–4933.9 ± 7.2	Nd	–5754.5 ± 5.5	Nd	–5924.7 ± 5.7
Pr	–6316.9 ± 6.0	Pr	–4949.2 ± 7.7	Gd	–5876.5 ± 5.6	Gd	–6061.1 ± 5.8
Nd	–6351.4 ± 5.6	Nd	–4986.0 ± 6.8	Y	–5945.3 ± 7.4	Y	–6136.5 ± 7.4
Sm	–6416.2 ± 5.7	Sm	–5037.0 ± 11.4	Ho	–5950.0 ± 7.6	Ho	–6151.6 ± 7.9
Eu	–6472.8 ± 6.6	Eu	–5085.9 ± 11.6	Er	–5977.9 ± 6.3	Yb	–6221.7 ± 6.4
Gd	–6495.1 ± 5.7	Gd	–5123.8 ± 7.1	Tm	–5997.1 ± 5.7		
Tb	–6543.8 ± 6.2	Tb	–5144.3 ± 7.4	Yb	–6026.0 ± 5.6		
Dy	–6543.7 ± 6.3	Dy	–5156.8 ± 8.6	Lu	–6030.3 ± 6.5		
Y	–6593.0 ± 7.5	Y	–5170.2 ± 7.8				
Ho	–6599.5 ± 8.2	Ho	–5197.2 ± 9.5				
Er	–6628.5 ± 6.7	Er	–5226.2 ± 8.6				
Tm	–6650.5 ± 5.9	Tm	–5225.5 ± 11.3				
Yb	–6682.0 ± 5.9	Yb	–5256.8 ± 11.2				
Lu	–6690.8 ± 7.0	Lu	–5278.3 ± 7.7				

$NaREF_4$		$REPO_4$		$REO_{1.5}$		$Ba_{0.5}REO_2$	
RE	U (kJ mol^{-1})	RE	U (kJ mol^{-1})	RE	U (kJ mol^{-1})	RE	U (kJ mol^{-1})
La	–5799.5 ± 7.8	La	–6205.7 ± 7.3	La	–6213.6 ± 5.9	La	–7801.6 ± 8.2
Ce	–5862.2 ± 7.3	Ce	–6233.4 ± 11.1	Ce	–6276.0 ± 5.9	Pr	–7910.4 ± 8.3
Pr	–5881.6 ± 7.8	Pr	–6288.9 ± 8.7	Pr	–6316.9 ± 6.0	Nd	–7947.0 ± 6.7
Nd	–5922.4 ± 7.1	Nd	–6306.1 ± 7.5	Nd	–6351.4 ± 5.6	Sm	–8015.3 ± 6.9
Gd	–6070.3 ± 7.3	Sm	–6363.9 ± 7.7	Sm	–6416.2 ± 5.7	Eu	–8073.5 ± 8.7
Y	–6117.1 ± 7.9	Eu	–6405.6 ± 7.7	Eu	–6472.8 ± 6.6	Gd	–8097.2 ± 6.7
Ho	–6145.3 ± 9.6	Gd	–6434.8 ± 9.1	Gd	–6495.1 ± 5.7	Er	–8237.0 ± 8.8
Yb	–6206.8 ± 11.3	Tb	–6473.3 ± 7.2	Tb	–6543.8 ± 6.2		
		Dy	–6473.4 ± 6.5	Dy	–6543.7 ± 6.3		
		Y	–6507.8 ± 7.4	Y	–6593.0 ± 7.5		
		Ho	–6522.9 ± 7.9	Ho	–6599.5 ± 8.2		
		Er	–6548.8 ± 6.3	Er	–6628.5 ± 6.7		
		Tm	–6564.0 ± 7.1	Tm	–6650.5 ± 5.9		
		Yb	–6597.6 ± 7.2	Yb	–6682.0 ± 5.9		
		Lu	–6601.2 ± 7.3	Lu	–6690.8 ± 7.0		

$REOOH$		$K_3RE(PO_4)_2$		$RETa_{1/3}O_{7/3}$		$RENb_{1/3}O_{7/3}$	
RE	U (kJ mol^{-1})	RE	U (kJ mol^{-1})	RE	U (kJ mol^{-1})	RE	U (kJ mol^{-1})
La	–8402.5 ± 6.0	Ce	–10110.9 ± 10.7	La	–11858.5 ± 123.2	La	–11941.1 ± 10.1
Eu	–8658.2 ± 7.1	Nd	–10161.7 ± 8.9	Nd	–11988.1 ± 123.1	Nd	–12076.8 ± 9.9
Gd	–8675.5 ± 6.6	Gd	–10303.0 ± 11.5	Sm	–12050.8 ± 123.1	Eu	–12194.5 ± 10.5
Tb	–8721.3 ± 7.0	Dy	–10339.1 ± 9.9	Eu	–12104.9 ± 123.2	Gd	–12212.8 ± 9.9
Dy	–8720.8 ± 6.7	Y	–10363.6 ± 10.4	Gd	–12120.4 ± 123.1	Tb	–12257.2 ± 10.2
Ho	–8779.7 ± 8.8	Ho	–10390.0 ± 10.3	Tb	–12168.8 ± 123.2	Y	–12295.1 ± 11.1
Er	–8806.1 ± 7.3	Er	–10412.7 ± 9.6	Dy	–12167.2 ± 123.2	Ho	–12303.6 ± 11.5
Tm	–8825.2 ± 6.5	Lu	–10443.1 ± 9.9	Ho	–12218.2 ± 123.3	Er	–12330.5 ± 10.6
Yb	–8852.3 ± 6.3			Er	–12245.9 ± 123.2	Yb	–12377.7 ± 10.0
Lu	–8865.5 ± 7.4			Tm	–12266.1 ± 123.1		
				Yb	–12294.9 ± 123.1		

$RETi_{0.5}O_{2.5}$		$LaREO_3$		$REAlO_3$		$RECoO_3$	
RE	U (kJ mol^{-1})	RE	U (kJ mol^{-1})	RE	U (kJ mol^{-1})	RE	U (kJ mol^{-1})
La	–12326.5 ± 17.9	Er	–12821.5 ± 12.2	La	–14011.7 ± 7.7	La	–14059.3 ± 8.7
Nd	–12451.2 ± 17.6	Tm	–12852.1 ± 10.8	Nd	–14127.6 ± 7.8	Nd	–14183.6 ± 8.4
Gd	–12581.4 ± 17.6	Yb	–12875.0 ± 10.0	Sm	–14188.7 ± 7.9	Sm	–14241.5 ± 8.6
		Lu	–12908.0 ± 10.1	Eu	–14238.2 ± 8.2	Gd	–14316.8 ± 8.5
				Gd	–14262.3 ± 7.7		
				Dy	–14300.0 ± 7.7		
				Y	–14351.6 ± 8.8		

$RESnO_{3.5}$		$RETiO_{3.5}$		$REVO_4$	
RE	U (kJ mol^{-1})	RE	U (kJ mol^{-1})	RE	U (kJ mol^{-1})
La	–18062.7 ± 7.8	Sm	–18582.9 ± 17.7	Ce	–25843.6 ± 10.4
Nd	–18178.0 ± 7.5	Eu	–18638.7 ± 18.3	Pr	–25808.0 ± 10.2
Sm	–18234.5 ± 7.5	Gd	–18670.4 ± 17.7	Nd	–25847.2 ± 10.0
Eu	–18286.4 ± 8.2	Tb	–18710.8 ± 18.1	Sm	–25899.4 ± 10.0
Dy	–18348.5 ± 7.9	Dy	–18710.6 ± 17.9	Eu	–25946.2 ± 10.2
Yb	–18479.0 ± 7.9	Y	–18737.7 ± 18.2	Gd	–25975.2 ± 9.9
		Ho	–18756.0 ± 18.5	Tb	–26015.6 ± 10.0
		Er	–18778.7 ± 17.8	Dy	–25985.3 ± 10.2
		Tm	–18831.5 ± 17.6	Y	–26058.3 ± 10.9
		Yb	–18834.1 ± 17.6	Ho	–26074.9 ± 10.9
		Lu	–18835.8 ± 18.2	Er	–26068.4 ± 10.5
				Tm	–26109.2 ± 9.9
				Lu	–26144.7 ± 10.3